# Nanoscratch Testing - Fundamentals of Wear




Ziyue Shao
Linacre College
University of Oxford

A thesis submitted for the degree of
*Doctor of Philosophy*
Trinity 2024

# Abstract

This thesis investigates wear mechanisms using nanoindentation and nanoscratch techniques. Nanoindentation measures hardness and elastic modulus at the nanoscale, while nanoscratch testing simulates sliding contact and material removal. Atomic Force Microscopy (AFM) is used to study how pile-up formation changes with normal load and how wear tracks develop with repeated scratches, enhancing the understanding of surface structure and abrasion processes.

The research focuses on the early stages of wear in nickel-based alloys, which are used in high-temperature turbines and corrosive environments due to their strength and corrosion resistance. Nanoscratch testing and AFM, which mimic single-asperity contact, explore the factors influencing the scratch formation and the relationship between material properties and scratch resistance.

Indentation and scratch hardness tests were performed on three nickel-based alloys (Ni201, Ni600, and Ni718) with different strengths and compositions. The results show a correlation between hardness profiles and macroscopic yield strength, with scratch hardness exceeding indentation hardness. The orientation of the Berkovich tip affects scratch strength and appearance: tips facing the surface produce higher hardness measurements with wavy grooves, while edge positioning results in straight scratches.

A novel aspect of this study is the AFM analysis of nanoscratch shape changes under increased normal forces, providing insights into material deformation. Multi-pass nanoscratch tests on a single Ni600 grain showed stabilisation in penetration depth with repeated passes. Focused Ion Beam (FIB) and High-Resolution Electron Backscatter Diffraction (HR-EBSD)

analyses identified stress and rotation distributions in the plastic zone, supporting theories of stabilisation.

To connect microscale data with macroscale properties, a machine learning model was developed to predict Johnson-Cook constants based on nanoindentation results. These parameters were used in Abaqus finite element simulations of nanoscratch experiments. Sensitivity analyses examined the impact of factors such as yield stress on indentation outcomes. Simulations matched experimental data in initial passes but deviated in later passes, prompting further investigation.

This research enhances the understanding of nanoscale wear in nickel-based alloys by linking nanoscratch behaviour with macroscale properties through machine learning. Key contributions include explaining penetration depth variations in multi-pass nanoscratch tests and providing detailed AFM characterisation of nanoscratch morphology. The predictive model offers the potential for optimising wear-resistant nickel-based alloys for industrial applications.

## Acknowledgement

Completing this thesis was made possible by the support of a group of excellent and kind people.

First, I would like to thank my mother, 郝绍红 (Hao Shaohong), and my father, 邵春生 (Shao Chunsheng). They created everything almost from scratch, giving me the opportunity to explore the boundaries of knowledge and this beautiful world. Through their own exemplary conduct, they taught me how to be upright and diligent.

I am equally grateful to my two very supportive supervisors, Dr. Anna Kareer and Professor Angus Wilkinson. They guided me step by step in my growth from a student to an independent researcher, constantly encouraging me and providing me with the courage to face the unknowns and challenges in the research process.

I extend special thanks to all my colleagues in the Oxford Mechanics Group (OMG) and my friends in Oxford. The presence of these talented and humorous people made every day of my four years here particularly joyful.

Lastly, I came to Oxford during a special period. Our world has recovered to its current vibrant state because of the sacrifice and tireless efforts of healthcare workers, and I express my heartfelt gratitude to them.

# Table of Contents

**ABSTRACT** ..... **1**
**ACKNOWLEDGEMENT** ..... **3**
**LIST OF FIGURE CAPTIONS** ..... **8**
**1. INTRODUCTION** ..... **15**
**2. LITERATURE REVIEW** ..... **20**
2.1 CONTACT MECHANICS ..... 20
2.1.1 Contact Mechanics in Indentation ..... 20
2.1.2 Contact Mechanics in Scratch Testing ..... 21
2.2 DEFINITIONS OF HARDNESS IN INDENTATION AND SCRATCH TESTING ..... 23
2.2.1 Indentation Hardness ..... 23
2.2.2 Scratch Hardness ..... 23
2.2.3 Correlation Between Indentation and Scratch Hardness ..... 25
2.3 MICROSCALE SLIDING/WEAR TESTING ..... 27
2.4 NANOINDENTATION ..... 32
2.4.1 Nanoindentation Hardness and Contact Area ..... 32
2.5 NANOSCRATCH ..... 38
2.5.1 Nanoscratch Hardness and Contact Area ..... 39
2.6 APPLICATION OF NANOSCRATCH TESTING ..... 42
2.6.1 Material structure ..... 42
2.6.2 Tip Orientations ..... 43
2.6.3 Scratch Speeds ..... 44
2.6.4 Normal Loads ..... 45
2.6.5 Summary ..... 47
2.7 SCRATCH TEST SIMULATION ..... 49
2.7.1 Materials characterization ..... 49
2.7.2 Material Properties Prediction ..... 54
2.7.3 Simulating Nanoscratch Test ..... 57
2.7.4 Summary ..... 62
**3. METHODS** ..... **64**
3.1 EXPERIMENT METHODS ..... 66
3.1.1 Atomic Force Microscopy (AFM) ..... 66
3.1.2 Electron Backscatter Diffraction (EBSD) ..... 69
3.1.3 High Angular Resolution Electron Backscatter Diffraction (HR-EBSD) ..... 71
3.1.4 Nanoindenter ..... 73
3.1.5 Focused Ion Beam ..... 80

3.2 Simulation method ..... 82
3.2.1 Abaqus ..... 82
3.2.2 Machine Learning ..... 83
**4. HARDNESS MEASUREMENT OF NICKEL-BASED ALLOYS ..... 84**
4.1 Introduction ..... 84
4.2 Nanoindentation Measurements ..... 88
4.2.1 Indentation Hardness ..... 94
4.2.2 Elastic Modulus ..... 95
4.2.3 Discussion ..... 97
4.3 Nanoscratch Hardness ..... 99
4.3.1 Berkovich Tip Measurements ..... 99
4.3.2 Discussion ..... 106
4.4 Morphology of scratches with low normal loads ..... 108
4.4.1 AFM Analysis ..... 108
4.4.2 Hardness Measurements ..... 110
4.4.3 HR-EBSD Result ..... 113
4.4.4 Discussion ..... 116
4.5 Scratching at different speeds ..... 118
4.5.1 Hardness Measurements ..... 119
4.5.2 Discussion ..... 121
4.6 Scratching with Different Orientations: ..... 122
4.6.1 AFM Result ..... 123
4.6.2 HR-EBSD Analysis ..... 125
4.6.3 Discussion ..... 129
4.7 General Discussion ..... 133
4.8 Conclusions ..... 134
**5. MULTI-PASS SCRATCHES ..... 135**
5.1 Introduction ..... 135
5.2 Experiment ..... 136
5.2.1 Nanoindenter Output ..... 136
5.2.2 Residual Profiles ..... 141
5.2.3 Discussion ..... 146
5.3 Deformation zone analysis ..... 148
5.3.1 HR-EBSD Output ..... 148
5.3.2 Discussion ..... 156
5.4 General Discussion ..... 160

5.5 CONCLUSIONS ..... 162

**6. RETRIEVING MATERIAL PROPERTIES FROM NANOINDENTATION TESTS WITH MACHINE LEARNING ..... 163**

6.1 NECESSITY OF BESPOKE MACHINE LEARNING MODEL FOR NANOINDENTATION ..... 163

6.2 BUILDING FINITE ELEMENT ANALYSIS (FEA) MODEL ..... 165

6.2.1 Part Geometries and Material Properties ..... 165

6.2.2 Steps ..... 167

6.2.3 Assembly, Boundary Conditions, and Interactions ..... 169

6.2.4 Mesh and Convergence Study ..... 169

6.3 PARAMETRIC STUDY OF JOHNSON-COOK CONSTANTS IN FEA MODEL ..... 171

6.3.1 Influence of Yield Stress (A) ..... 172

6.3.2 Influence of Straining Hardening Exponent (B) ..... 173

6.3.3 Influence of Elastic Modulus (E) ..... 174

6.3.4 Influence of Hardening exponent (n) ..... 175

6.3.5 Influence of Poisson's Ratio (v) ..... 176

6.4 MACHINE LEARNING THEORIES ..... 178

6.4.1 Gaussian Process Regression (GPR) ..... 178

6.4.2 Artificial Neural Network (ANN) ..... 179

6.5 MACHINE LEARNING (ML) MODEL TRAINING ..... 181

6.6 VALIDATION OF THE ARTIFICIAL NEURON NETWORK (ANN) MODEL ..... 185

6.7 GENERAL DISCUSSION ..... 191

6.8 CONCLUSIONS ..... 194

**7. NANOSCRATCH SIMULATIONS ..... 195**

7.1 NECESSITY OF ABAQUS SIMULATIONS ..... 195

7.2 AIM OF ABAQUS SIMULATIONS ..... 197

7.3.1 Model Setup ..... 198

7.3.2 Surface Friction – A parametric study ..... 198

7.3.3 Effect of Normal Loads ..... 206

7.3.4 Comparison of Edge-Forward and Face-Forward Simulations ..... 209

7.4 MULTI-PASS NANOSCRATCH SIMULATIONS ..... 212

7.4.1 Experiment Findings and Simulation Aims ..... 212

7.4.2 Construction of the FEA model ..... 212

7.4.3 Effects of Repeated Passes ..... 213

7.4.4 Effect of Normal Loads ..... 218

7.5 GENERAL DISCUSSION ..... 228

7.6 CONCLUSIONS ..... 231

**8. SUMMARY AND OUTLOOK ..... 232**
**9. REFERENCES ..... 235**

# List of Figure Captions

*Figure 1 A schematic of a scratch process[9].* ..... *23*
*Figure 2 Ratio of scratch hardness $H_s$ to the static indentation hardness $H_c$ as a function of the indenter included angle [11].* ..... *25*
*Figure 3 Secondary electron image showing the unannealed wear scar of Ni-40tit.%Cu gliding on a 440C circle. The ring moved upwards from the bottom in the sliding direction [20].* ..... *29*
*Figure 4 Scanning transmission electron microscopy (STEM) images of OFHC copper under tribological loading after a different number of scratch passes: (a) pristine material before tribological testing; (b) after 1 pass; (c) after 10 passes; (d) after 100 passes [small-angle grain boundary (SAGB) and clusters are marked by white arrows]; (e) after 500 passes [21].* ..... *30*
*Figure 5 a) Usual and unusual indentation size effects vs the hardness trend predicted by conventional plasticity[37], [38], b) $(H/H_0)^2$ vs. 1/h of Berkovich indentation in electropolished iridium.* ..... *35*
*Figure 6 Schematic representing the emission of geometrically necessary dislocation loops during the indentation of a single crystal with a conical indenter, as proposed by Nix and Gao [39]* ..... *36*
*Figure 7 Schematic representation of the Berkovich indenter: different tip orientations, including edge-forward, side-forward and face-forward [35].* ..... *40*
*Figure 8 Diagrams to show: (a) The tip orientation for EF and FF scratches. Lateral force, FL acts in the direction of motion. (b) The total projected area of contact used in the first method, one-third Ap is used for FF and two-thirds Ap is used for the EF (c) [35].* ..... *40*
*Figure 9 Resolved force calculation for forces acting on the facets in contact with material for the EF and FF tip orientation. Calculations based on the geometry of the tip, $F_N$ and $F_L$ were measured from the instrument [35].* ..... *41*
*Figure 10 Scratch depth vs. scratch distance for scratch tests on TiZrHfNb-HE alloy under ramping load mode at scratch speeds of 0.01, 0.1, 0.5 and 1 µm/s. Tip used was a 90° cono-spherical diamond tip with an effective radius ~600 nm [59].* ..... *45*
*Figure 11 a) Normal force vs. lateral force for Berkovich tip nanoscratch tests and b) scratch hardness measured using average penetration depth and projected area on single crystal copper [35].* ..... *46*
*Figure 12 Summary of the descriptors used in the machine learning model, classified in local, structural, and porosity-related descriptors [72].* ..... *55*
*Figure 13 Defect configurations of monocrystalline 3C–SiC with different crystallographic orientations at maximum loading displacement: (a) (010); (b) (110); (c) (111). Blue lines denote dislocation segments [83]…* *59*
*Figure 14 Schematic diagram depicting main components of an Atomic Force Microscope with an optical beam deflection system [90].* ..... *66*
*Figure 15 The MultiMode 8 microscope used in this study. Monitor readings indicate the tip deflection in vertical and horizontal direction, as well as the signal strength.* ..... *68*
*Figure 16 Raster grid on a tilted specimen surface with digital beam scan [91] .* ..... *69*
*Figure 17 Dynamically simulated Si patterns (a) undistorted; (b) distorted with a=10−7 ['pinch in' can be noticed at the pattern edges] [94].* ..... *71*
*Figure 18 The Agilent Nano Indenter G200 and a cross-sectional diagram of the XP-NMAT [96].* ..... *74*
*Figure 19 Three-pass nanoscratch procedure for a constant load scratch test [97].* ..... *78*
*Figure 20 Schematic diagram of a FIB used in junction with an SEM. Manipulators are also commonly found on FIB [99].* ..... *80*
*Figure 21 IPFz (coloured) maps of Ni201, Ni600 and Ni718. Each colour represents a grain of same crystal orientation. Images are taken at central area of sample slices mounted on pin stubs positioned at 70-degree tilt to the EBSD scanner. Rotation axis for tilting and relative position of the sample to EBSD detector are shown on the right.* ..... *86*
*Figure 22 Average grain size of the material tested in this thesis. Grain size is defined as the diameter of a circle with the same area as the measured grain.* ..... *87*
*Figure 23 Load and displacement measurements for CSM indents on Ni201, Ni600 and Ni718 using Berkovich tip with G200 nanoindenter.* ..... *88*

*Figure 24 AFM scans of 1200 nm deep Berkovich nanoindentation mark on Ni201 and Ni600. Graphs on the right show line depth profiles of 1 indentation mark on each material. Lines are taken parallel to the tip edge and pass through the lowest point of indentation mark. 3 indents were made on each material type. ..... 90*
*Figure 25 Berkovich nanoindentation hardness measurement along penetration depth on Ni201, Ni600 and Ni718 using CSM method. To account for pile-up, the penetration depth is multiplied by 1.07 and 1.10 for Ni600 and Ni201 respectively which was determined from AFM nanoindentation pile up height measurements. Displacement into surface is measured with reference to the sample surface level before indentation. Nix-Gao fit has been performed on three materials tested to highlight plasticity size effects (graph b). Ni718 data is uncorrected for pile-up due to instrument constraint. ..... 91*
*Figure 26 Nanoindentation hardness measured for three nickel-based alloys Ni201, Ni600 and Ni718 using 9 Berkovich tip indents for each alloy with G200 nanoindenter. Red line represents the mean value. The blue box shows the 25 to 75 percentile regions, and the black lines indicates the maximum and minimum values. Ni201 and Ni600 are pile-up corrected using AFM measurements with Ni718 uncorrected due to instrument constraint. ..... 94*
*Figure 27 Average elastic modulus obtained for Ni201, Ni600 and Ni718 using Berkovich tip nanoindentation to 2000 nm penetration depths with G200 nanoindenter. 9 indents were made for each alloy and contact areas for Ni201 and Ni600 were corrected using the pile-up measured under AFM scan. Contact areas were uncorrected for Ni718 due to instrument constraint. ..... 95*
*Figure 28 Modulus measurement across 100 – 2000 nm penetration depth with CSM method using Berkovich tip on G200 nanoindenter. Frame stiffness has been manually calibrated until a horizontal line is reached for each material. ..... 96*
*Figure 29 Load vs Scratch Distance and Penetration Depth vs Scratch Distance output from G200 nanoindenter for the 40 μm long nanoscratches (8 μm to 48 μm) on Ni201,Ni600 and Ni718.. Pre-profile, post-profile and final profiles are made at profiling load (30μN) which is shown by the blue line close to x axis. ..... 100*
*Figure 30 a) Final-profile scans of residual groove along the scratch directions of 20 mN normal load edge-forward nanoscratch tests of 40 μm length (8 to 48 μm) on Ni201, Ni600 and Ni718.Penetration depths averaged between black dotted lines, where steady scratch occurs(20 μm after the scratch start to the end of scratch), were used for contact area and subsequent calculations. Scratch start at 8 μm and tip retracts at 48 μm. Maximum dip in depth is reached at 10 μm and the titled line at beginning and the end reflect Berkovich tip geometries) cross-sections of residual groove taken at mid-scratch (shown by the blue dotted lines). ..... 100*
*Figure 31 Schematic of edge-forward and face-forward nanoscratch procedure using Berkovich tip. Cross profile scans are performed at 50% of the scratch distance in a direction perpendicular to the scratch direction at profiling load to determine pile-up heights. ..... 102*
*Figure 32 Schematic of how contact areas are assumed in the edge-forward and face-forward scratches. Projected areas from normal directions are used and in face-forward is one third of the indentation area with two thirds in edge-forward scratches. ..... 103*
*Figure 33 Scratch hardness measured for Ni201, Ni600 and Ni718. Scratches were made for both edge-forward and face-forward directions using Berkovich diamond tip at 20 mN normal load at scratch speed of 1 μm/s for scratch lengths of40 μm. Each direction has been repeated for 4 times for each material. Nanoindentation hardness are displayed on the left to be compared with scratch hardness corrected with pile-up heights obtained from cross-profile scans.Ni718 indentation hardness is not corrected due to instrument constraint. ..... 103*
*Figure 34 Final profiles along the groove direction and across the groove width for 20mN load edge-forward nanoscratches on Ni600. Dotted line indicates the position that the cross-profiles were taken. ..... 105*
*Figure 35 AFM scans of edge-forward Berkovich tip scratches made with 0.5 mN, 2 mN, 10 mN and 20 mN loads using G200 nanoindenter on same Ni600 grain. Dotted lines indicate where the AFM line cross profiles are taken. ..... 109*
*Figure 36 AFM line cross profile of edge-forward scratches made with 0.5 mN, 2 mN, 10 mN and 20 mN loads on Ni600 using G200 nanoindenter. Data are shifted on the y axis so that the lowest points from each scratch coincide and a perfect Berkovich tip is plotted as a reference for the residual groove shape. ..... 109*
*Figure 37 Scratch hardness and average pile-up heights measured for the edge-forward Berkovich scratches on same Ni600 grain under 0.5mN, 2 mN, 10 mN and 20 mN normal load. Contact area is assumed to be 2/3 of the indentation contact area which has been corrected using pile-up measured from cross-section profiles. The*

*error bars denote the variance of hardness measured in repeated experiments at same load. Nanoindentation hardness measurement at the same grain has been displayed on the same map for comparison.* ..... *111*
*Figure 38 Schematics of the lift-outs. a) 'Across' lift-out of an EF scratch, where the lift out is taken perpendicular to the scratch, b) 'Along' lift-out of an FF scratch, c) lift-out to be scanned with BESD (contact region facing downward), d) diagram illustration of lift out, e) schematic for lift-out mounting on the OmniProbe grid and f) positioning of holder relative to EBSD scanner. In this case, only across lift-out was taken.* ..... *114*
*Figure 39 SEM image of a 2 mN Berkovich tip edge-forward lift-out on Ni600. Dark line indicates where the sample surface is. Magnification is at 10000x and image has been rotated for 180 degree for ease of interpretation.* ..... *115*
*Figure 40 HR-EBSD stress output of 2mN Berkovich tip 2 mN edge-Forward scratch on Ni600.* $\sigma_{11}$ *map shows the stress in horizontal direction and σ22 map shows stress in vertical direction.* $\tau_{12}$ *map indicates the rotating shear stress from horizontal to vertical axis. Unit of the scale bar is GPa and the dark line indicates where the sample surface is.* ..... *115*
*Figure 41 a) Penetration depth profiles and b) cross-section profiles of edge-forward Berkovich tip nanoscratch tests with different scratch speed with normal load at 50 mN and scratch length of 50 μm (10 μm to 60 μm) on Ni718 using G200 nanoindenter. Penetration depths and pile-ups measured are from G200 output.* ..... *119*
*Figure 42 Scratch hardness measured for 50 μm long Berkovich edge-forward scratches on Ni718 at 50 mN normal load under scratch speed of 0.1 μm/s, 1 μm/s, 10 μm/s and 20 μm/s with 4 repeated tests for each speed. Error bars suggest the variance of scratch hardness measured in repeated experiments for each scratch speed. Pile-ups are corrected with cross-section scan output from nanoindenter.* ..... *120*
*Figure 43 a) Penetration depth vs scratch distance output from nanoindenter, b) cross-profile output from nanointenter, and c) line profiles along the centreline of residual grooves taken by AFM. Dotted line indicates that position that the cross-section profile was taken. EF stand for edge-forward orientation and FF stands for face-forward orientation. Scratch was performed with 20 mN normal load at 1 μm/s scratch speed on single Ni600 grain using G200 nanoindenter.* ..... *123*
*Figure 44 A comparison of the scratch hardness measured in edge-forward and face-forward Berkovich tip scratches together with nanoindentation hardness. Scratches were made under 20 mN normal load at scratch speed of 1 μm/s on same Ni600 grain. Nanoindentation was made using Berkovich tip and standard CSM method in G200 nanoindenter.4 repeated tests are made for each method.* ..... *124*
*Figure 45 Demonstration of two different lift-outs on residual groove of a Berkovich tip nanoscratch test [80].* ..... *125*
*Figure 46 SEM images and signal quality maps of 20 mN Berkovich tip nanoscratch along lift-outs on same Ni600 grain. Boxed areas are selected for HR-EBSD analysis comparison and dark lines indicate the sample surface. Rotation axis indicate how the sample was titled during EBSD scan (toward out of the page).* ..... *125*
*Figure 47 GND distribution at the bottom of the residual groove of 20mN face-forward and edge-forward Berkovich scratch on same Ni600 grain. Unit is in logarithmic scale and corresponds to* $10^{13}$ *to* $10^{16}$ *Geometrically Necessary Dislocations (GNDs) per square meter. Dotted line indicates where the scratch surface is. Lift-outs were taken from the areas away from the start of the scratch.* ..... *126*
*Figure 48 Stress distribution at the bottom of the residual groove of 20mN face-forward and edge-forward Berkovich scratch on same Ni600 grain. σ11 map shows the stress in horizontal direction and σ22 map shows stress in vertical direction. Unit of the scale bar is GPa. Figure a and c depicts the horizontal components of stress while figure b and d are related to vertical stress. Yellow indicates tensile stress while blue indicates compressive stress.* ..... *127*
*Figure 49 Rotation maps showing rotations from* $x_1$ *axis to* $x_2$ *axis for20mN face-forward and edge-forward Berkovich scratch on same Ni600 grain. In this case, they correspond to the rotation of material along the scratch direction. Unit of scale bar is in radian .Blue colour indicates clockwise rotation toward scratch direction and yellow colour indicates counter-clockwise motion. Dotted lines indicate the position of the deformed sample surface.* ..... *128*
*Figure 50 Schematic representation of the Berkovich indenter with different tip orientations, including edge-forward, side-forward and face-forward [35].* ..... *130*

*Figure 51 Penetration depth profile of repetitive scratch on Ni600 from G200. Scratches were performed with load of 30 mN, scratch speed of 1 um/s at edge-forward orientation. A) is a schematic of the multi-pass nanoscratch process in which the tip load(a), moves loaded laterally(b), unload and returns to start position unloaded (c) and repeat (d). B) is the load vs scratch distance from G200 for 1 pass from a 100 um scratch and C) is the depth vs scratch distance measured by G200 relative to the initial surface for each pass. Scratch length is 50 um in the multi-pass test (10 um to 60 um). Scratches were performed with load at scratch speed of 1 um/s in edge-forward orientation using Berkovich tip. ..... 136*
*Figure 52 A,b,c graphs are depth vs scratch distance profiles measured by G200 relative to the initial surface for each pass for 20mN, 50mN and 80mN normal loads. Scratch length is 50 um in the multi-pass test (10 um to 60 um). Scratch directions are edge-forward using Berkovich tip. ..... 137*
*Figure 53 Average penetration depths during tests from G200 output for each cycle in multi-pass nanoscratch tests under different normal loads. The depths are averaged for the depths recorded after climb-out region (the initial 10 um)Tests were performed with Berkovich tip and Ni600. Tip orientation was edge-forward with scratch speed of 1um/s at length of 50um. ..... 138*
*Figure 54 Scratch hardness after each cycle in multi-pass test. Contact depth is defined as the total penetration depth after each cycle and contact area is 2/3 of the total area from area function calibrated with fused silica. ..... 139*
*Figure 55 A schematic showing how the material extruded by tip apex relocates and rotates to form the pile-up along two trailing edges (yellow region). Scratch direction for the Berkovich tip is out of the page. ..... 140*
*Figure 56 AFM topography maps of 20mN edge-forward Berkovich tip nanoscratch tests with different number of passes using G200 nanoindenter. A, b, c, d correspond to scratch of 1 pass, 2 pass, 5 pass and 10 pass. 0 height plane were adjusted to the lowest point of the scratch groove. While and blue dotted lines indicate the position where AFM line profiles and cross-section profiles are taken. ..... 141*
*Figure 57 Cross profiles and line profiles of repetitive scratches of different passes under 20mN normal load on same Ni600 grain in edge-forward Berkovich tip orientation.Heights have been adjusted to align sample surface and profiles were taken with AFM. ..... 142*
*Figure 58 Comparison of residual groove depth and experiment depth. The difference is due to the elastic recovery of the material. Depth is determined from the undeformed surface and does not include pile-up. ..... 143*
*Figure 59 A schematic showing how contact area is defined for subsequent passes in multi-pass experiments, which are the red regions that mark the difference between the total contact area in current scratch and total contact area in previous pass (grey region). ..... 143*
*Figure 60 Pile-up heights and penetration depths for the 20mN Berkovich tip edge-forward nanoscratch tests measured on single Ni600 grain. Pile-up heights were measured from AFM and penetration depths were recorded by nanoindenter. ..... 144*
*Figure 61 Scratch hardness calculated using contact area defined as the difference between the total contact area of the current pass and the previous pass. Scratches were made with Berkovich tip at 20 mN normal load in edge-forward direction for 1, 2, 5 and 10 repeated scratch pass on same locations. ..... 145*
*Figure 61 SEM images of cross-section lift-outs of 20mN Berkovich tip edge-forward multi-pass nanoscratch experiments on same Ni600 grain. A,b,c,d represents results from 1 pass, 2 pass, 5 pass, 10 pass experiments. Dark dotted lines denote the scratch surfaces and green dotted line represented the axis that the lift-out was rotated around during tilt process for EBSD scan. ..... 148*
*Figure 62 IPFY maps of the lift-outs prepared from multi-pass 20mN edge-forward Berkovich tip scratches on same Ni600 grain. A, b, c, d images were taken from scratch times of 1pass, 2 pass, 5 pass and 10 pass, respectively. Black lines reflected the automated grain boundary selection of HR-EBSD algorithm. Blue box were the referenced area used for cross-referencing (undeformed structure). Dotted lines indicate where the sample surface was. ..... 149*
*Figure 63 Secondary electron image and pattern quality image of the 20mN 2 pass scratch lift-out on single Ni600 grain. Actual scratch edges are less discernible in pattern quality image and other output maps based on it due to severe deformation. Green lines indicate lengths used for plastic zone estimation. White dotted lines indicate the location of sample surface. ..... 150*

*Figure 64 GND density maps of 20mN Berkovich tip scratches under different cycles of loading on same Ni600 grain. A, b, c, d correspond to 1 pass, 2 pass, 5 pass and 10 pass. Unit was in logarithmic scale and corresponded to $10^{13}$ to $10^{16}$ Geometrically Necessary Dislocations (GNDs) per square meter. ..... 151*
*Figure 65 1) Image quality maps of 20mN Berkovich tip scratch lift-outs under different cycles of loading on same Ni600 grain. White colour indicated area with best signal while dark black suggested no signal due to the severe deformation or presence of platinum protection layer. Dotted lines noted the location of the groove surface. 2) Depths of plastic zone plotted against number of scratch cycles measured using quality maps. ..... 152*
*Figure 66 HR-EBSD rotation maps of 20mN Berkovich tip scratches under different cycles of loading on same Ni600 grain. $\omega 21$ maps suggested horizontal rotations around vertical axis. $\omega 13$ maps characterised vertical rotation around $x_2$ axis and $\omega 32$ maps denoted in-plane rotation around $x_1$ axis. Yellow area indicated positive sign rotations while blue area suggested negative rotations. Unit of scale bar was radian. ..... 153*
*Figure 67 Stress distribution of scratches under multiple passes of loadings. $\sigma_{11}$ map showed the stress in horizontal direction and $\sigma_{22}$ map showed stress in vertical direction. $\tau 12$ map indicated the rotating shear stress. Yellow area indicated tensile stress in $\sigma_{11}$ and $\sigma_{22}$ maps anticlockwise shear stress in . $\tau 12$ maps. Blue area suggested compressive and clockwise shear stress. Unit of the scale bar was GPa. ..... 155*
*Figure 68 Schematic of the nanoindentation model with Berkovich tip with base length of 20 μm and height of 2.66 μm and spherical tip of 20 μm nominal radius. Tips and samples are meshed. ..... 166*
*Figure 69 Schematic of the Abaqus model in scratch test ..... 166*
*Figure 70 Mesh convergence studies for 20mN edge-forward Berkovich tip nanoscratch simulation and nanoindentation simulation with Berkovich tip of spherical tip of 20-micron radius. Johnson-Cook constants for Inconel 718 were applied. ..... 170*
*Figure 69 Simulated load/Displacement curves of varying yield stress A. B=748.2MPa, v=0.258, E=104.6 GPa and n=0.419. ..... 172*
*Figure 70 Simulated load/Displacement curves of varying yield stress B. A=212.15MPa, v=0.258, E=104.6 GPa and n=0.419. ..... 173*
*Figure 71 Simulated load/Displacement curves of varying elastic modulus E. A=212.15MPa, B=748.2MPa, v=0.258, and n=0.419. ..... 174*
*Figure 72 Simulated load/Displacement curves of varying hardening exponent n. A=212.15MPa, B=748.2MPa, v=0.258, and E=106 GPa. ..... 175*
*Figure 73 Simulated load/Displacement curves of varying hardening exponent v. A=212.15MPa, B=748.2MPa, n=0.419 and E=106 GPa. ..... 176*
*Figure 74 Schematic diagram of the ANN model [123]. ..... 180*
*Figure 75 Python code to be used as a command for TensorFlow. Variables and functions are highlighted. .. 182*
*Figure 76 Changes of Mean Absolute Error against iteration times in training and validation. ..... 184*
*Figure 77 A comparison of the Johnson-Cook constant predictions from Abaqus simulation results with material properties used. ..... 185*
*Figure 78 Predictions of A, B, n constants are plotted against their input values with dotted line showing perfect predictions. Model is trained with simulations using spherical tip with 20 μm radius and tested on simulations using tip with 20 μm radius. ..... 186*
*Figure 79 Predictions of A, B, n constants are plotted against their input values with dotted line showing perfect predictions. Model is trained with simulations using spherical tip with 20 μm radius and tested on simulations using tip with 16 μm radius. ..... 187*
*Figure 80 Predictions of A, B, n constants are plotted against their input values with dotted line showing perfect predictions. Model is trained with simulations using spherical tip with 20 μm radius and tested on simulations using tip with 24 μm radius. ..... 187*
*Figure 81 Comparison of Ni600 Berkovich nanoindentation experiment with simulation using Johnson-Cook constants predicted by the ANN model. Yellow boxed regions are the near-surface area where Abaqus have limited ability to predict due to the presence of Indentation Size Effect. ..... 188*
*Figure 82 Comparison of 20mN Ni600 Berkovich edge-forward nanoscratch experiment with Abaqus simulation using Johnson-Cook constants predicted by the ANN model from a single grain Ni600 indent. Red box denoted the discrepancy between the simulation and 20mN nanoscratch experiment in initial loading depth. ..... 189*

*Figure 83 Comparison of the residual profiles of 20mN Berkovich edge-forward scratch on Ni600 in Abaqus simulations and from experiment by G200 nanoindenter scanned with AFM. ..... 190*
*Figure 87 Residual von mises stress distributions on simulated edge-forward scratches with different interfacial friction coefficients. Unit of scale is MPa. 20 mN load edge-forward Berkovich tip nanoscratches of 20 µm length were simulated. ..... 199*
*Figure 88 Scratch profile of simulated edge-forward scratches in comparison with the 20mN Berkovich tip edge-forward experiment output by G200 on single Ni600 grain. Measurements were taken during the scratch process. ..... 201*
*Figure 89 Lateral force measurements and overall CoFs against different assumed interfacial friction constants in 20 mN edge-forward Berkovich nanoscratch simulations. ..... 202*
*Figure 90 Residual von mises stress distributions on simulated face-forward scratches with different interfacial friction coefficients. Unit of scale is MPa. 20 mN load face-forward Berkovich tip nanoscratches of 20 µm length were simulated. Boxed regions indicate where the start of the scratch no longer resembles a Berkovich triangle indent. ..... 203*
*Figure 91 Scratch profiles of the simulated 20mN Berkovich tip face-forward scratches using varied interfacial friction coefficients and experiment output from G200 nanoindenter. ..... 204*
*Figure 92 Lateral force measurements and overall CoFs against different assumed interfacial friction constants in 20 mN face-forward Berkovich nanoscratch simulations. A CoF above 1 indicates that the lateral resistance experienced by the tip exceeded the normal load applied. ..... 205*
*Figure 93 A comparison of the cross-section profiles of residual groove in Abaqus simulations and experiments of edge-forward Berkovich nanoscratch at 0.5 mN, 2 mN, 10 mN, 20 mN normal loads on single Ni600 grain. ..... 206*
*Figure 94 Overall Coefficient of Friction for edge-forward Berkovich nanoscratch simulations with 0.5 mN, 2 mN, 10 mN and 20 mN normal loads. ..... 207*
*Figure 95 Top views of the residual von Mises stress distribution. Edge-forward Berkovich tip nanoscratches of 30 µm length under 0.5 mN, 1mN, 10mN and 20 mN normal loads were simulated. ..... 208*
*Figure 96 Stress distribution in two on-going simulated Berkovich tip scratches with 20 mN normal load at 1 µm/s scratch speed.. ..... 209*
*Figure 97 A comparison of the plastic strain component maps from Abaqus simulation with HR-EBSD GND analysis on the residual groove of 20 mN Berkovich nanoscratch tests on single Ni600 grain in edge-forward (EF) and face-forward (FF) orientations. Unit of GND density was in logarithmic scale and corresponded to $10^{13}$ to $10^{16}$ Geometrically Necessary Dislocations (GNDs) per square meter. ..... 211*
*Figure 98 Residual von mises stress distribution at groove surface after different numbers of loading cycles. 20 mN normal load edge-forward Berkovich tip nanoscratches of 30 µm length under 1, 2, 5 and 10 passes of scratch were simulated. ..... 214*
*Figure 99 A comparison of the residual cross profiles of 20 mN Berkovich nanoscratch s in edge-forward orientation after 1, 2, 5 10 passes in both FE simulations and experiment residual profiles on Ni600, scanned by AFM. ..... 215*
*Figure 100 A comparison of average residual groove depth and vertical displacements during FE simulations of 20 mN edge-forward Berkovich nanoscratch tests with changing number of scratch passes on single Ni600 grain. Experiment results are displayed on the right for comparison. ..... 216*
*Figure 101 Change of overall friction coefficient for 20 mN load edge-forward nanoscratch simulations under changing number of passes. ..... 217*
*Figure 102 Changes of lateral resistance on the tip during first and fifth pass of repeated 20 mN load edge-forward Berkovich nanoscratch simulations. ..... 217*
*Figure 103 Change of average penetration depth with different number of passes on edge-forward Berkovich edge-forward nanoscratch simulations on Ni600 described with Johnson-Cook hardening under changing normal loads. Experiments results from G200 nanoindenter measurements are shown on the right for comparison. ..... 219*
*Figure 104 Change of average contact area with number of passes in Berkovich nanoscratch simulations under normal loads of 20 mN, 30 mN and 50 mN. Contact area are obtained differently, in which a) is estimated from*

*total penetration depth , b) is from direct Abaqus output, c) estimated using the difference between the total contact areas in two neighbouring passes, defined as an 'effective contact area' in previous section. ..... 220*
*Figure 105 Change of tip contact area across the scratch distance for first and fifth pass of edge-forward nanoscratch simulation with 20 mN normal load. ..... 221*
*Figure 106 a) change of scratch hardness with increased number of nanoscratch passes under different normal loads. Contact areas used to derive hardness are directly derived from Abaqus Output b) Change of scratch hardness in 20 mN Berkovich tip edge-forward nanoscratch on Ni600. Contact are used are a sum of increment penetration depths and pile-up heights compared to previous pass recorded. Different hardness scales are applied as the range in b is considerably larger than that of a. ..... 222*
*Figure 106 Cross-sections of 20mN Berkovich tip edge-forward nanoscratches at 5th and 6th pass at the same scratch distance. Arrows indicate the positions where the elevated asperities are no longer in contact with the tip in the following pass. ..... 223*
*Figure 107 Cross-section of a 20mN Berkovich tip edge-forward repeated nanoscratch simulation. Frame shown is in the middle of the second pass on same scratch location. ..... 224*
*Figure 108 Comparison of scratch hardness calculated using effective contact area defined in Section 5.2 for a) Abaqus simulation and b) G200 penetration depths measurement for edge-forward Berkovich nanoscratches under 20 mN, 30 mN, 50 mN. For ease of comparison, result for 1 test/simulation for each load was shown. . 225*
*Figure 110 A comparison of the Abaqus plastic strain output and GND map from HE-EBSD on repeated nanoscratch experiment lift-out. Unit of the GND is in logarithmic scale and corresponds to $10^{13}$ to $10^{16}$ Geometrically Necessary Dislocations (GNDs) per square meter ..... 226*

# 1. Introduction

Abrasive wear is a major engineering obstacle in many industries, resulting in material degradation that leads component failure, decreased efficiency, and environmental consequences. Abrasive wear happens when tough particles remove material from a surface via physical force. This type of wear poses a big challenge in high-performance situations where durability and reliability are crucial. Nickel-based alloys, renowned for their exceptional ability to withstand high temperatures and corrosion, are extensively used in the aviation and power generation sectors. Cases where abrasive wear has caused disastrous failures are recorded in reports.

In the nuclear power industry, the wear of nickel-based alloy components has led to critical failures. A notable case is the premature wear of steam generator tubes at the San Onofre Nuclear Generating Station (SONGS) in California. The steam generator tubes, made from Alloy 690 (a nickel-based alloy), experienced unexpected abrasive wear due to flow-induced vibrations and friction against supporting structures. The presence of hard particulate matter in the coolant exacerbated the abrasive wear. This degradation led to a small radiation leak in 2012, which prompted the shutdown of the reactors [1]. Nickel-based superalloys are often used in engine turbine blades, and abrasive wear induced by sand ingestion and other foreign object damage is identified as one of the factors that contribute to their failure. This wear leads to mechanical damage, such as nicking and bending of the blades, affecting the system's balance, and degrading airflow characteristics. Ultimately, this can induce aerodynamically excited vibrations or flutter, which can initiate fatigue failures [2].

The effects of abrasive wear extend beyond component failure. Wear can compromise the efficiency of mechanical systems by increasing friction and reducing the performance of moving parts, which not only leads to higher energy consumption but also necessitates more

frequent maintenance and part replacements, thereby increasing operational costs. Environmentally, the degradation and disposal of worn components contribute to material waste and pollution, while the energy losses associated with inefficient machinery also have a broader environmental impact, further increasing carbon emissions.

Understanding and mitigating abrasive wear necessitates the creation of testing methods and analytical tools. Traditional wear testing techniques, such as pin-on-disk and ball-on-flat configurations, employ tribometers to quantify wear rate, friction coefficient, and changes in surface roughness under controlled conditions. These experimental results provide valuable data but often lack the capability to fully predict wear behaviour under complex, real-world conditions.

It is in this context that wear mechanism maps gain critical importance. Wear maps, pioneered by Michael Ashby [3], offer a powerful framework for the visualisation and comparison of different wear mechanisms (e.g., adhesive wear, abrasive wear, corrosive wear) as functions of key operating parameters like applied load, sliding speed, and temperature. The identification of the dominant wear mechanism under specific conditions and, crucially, the prediction of transitions between different wear regimes is facilitated by these maps. An understanding of these transitions allows for the design of components and the selection of materials that exhibit greater resistance to wear in the intended operating environment.

Quantification and prediction of wear can be further achieved through the application of foundational concepts, such as Archard's Law [4]. This law establishes a fundamental relationship in wear analysis, stating that the volume of material removed due to wear is directly proportional to the applied load and the sliding distance and inversely proportional to the hardness of the softer material. Hardness, in this context, represents a material's resistance to localised plastic deformation, often measured through indentation tests. Archard's Law,

therefore, provides a simplified model for predicting wear volume based on these key parameters.

Despite its usefulness, Archard's law's empirical nature limits its applicability. Both Archard's wear law and conventional wear testing have drawbacks. While macroscale tests can identify various wear causes, their predictive power is limited due to their empirical character. The main difficulty is precisely forecasting wear behaviour, which is complicated by the microscopic interactions between materials. Traditional approaches often overlook the subtleties of asperity interactions and the real-time evolution of surface topography under operating conditions, making it challenging to anticipate wear accurately.

To improve prediction models, it is crucial to understand the microscale mechanics of wear. The small protrusions on surfaces called asperities play a vital role in wear mechanisms. The microscopic characteristics are the primary points of contact when sliding occurs, and their interactions can lead to various wear mechanisms, such as adhesion, ploughing, and cutting. At a small scale, variations known as asperities, which can vary in size, shape, and arrangement, experience intense localized material changes and elimination. The plasticity size effect is important in this context as it shows that materials become harder and stronger when the volume being deformed decreases to the micron or sub-micron scale. This behaviour that varies with the size is caused by factors like strain gradient plasticity and the restricted movement of dislocations in small spaces. The stochastic nature of dislocation nucleation and interaction also plays an important role. At these small scales, the discrete and probabilistic nature of dislocation generation and motion becomes pronounced. The limited number of dislocations within a small asperity, and the statistically varying obstacles they encounter (e.g., grain boundaries, precipitates, other dislocations), lead to fluctuations in the local stress and strain fields. This stochasticity influences the overall deformation response

and contributes to the observed size effect. It is essential to comprehend this phenomenon to analyse microscale deformation and wear processes accurately since it influences the way materials behave during small-scale contacts commonly seen in asperity interactions.

It is important to comprehend the plasticity size effect when extending wear behaviour findings from microscale tests to macroscale uses. The varying nature of roughness characteristics and the continuous formation and breaking of contact points make it even more challenging to predict wear. The difficulty is in connecting small-scale observations with large-scale performance.

This thesis uses nanoindentation and nanoscratch techniques to study the fundamental mechanisms of wear. Nanoindentation enables the evaluation of hardness and elastic modulus on a nanoscale level, offering information on the material's ability to resist deformation. Nanoscratch testing replicates the sliding contact and material removal actions on a small scale. The research outlines how pile-up formation evolves with increased normal load and how wear track formation expands with more scratch passes in the same area using Atomic Force Microscopy (AFM). These observations aid in comprehending the development of surface topography and the significance of asperities in wear mechanisms.

In order to link small-scale observations with large-scale behaviour, this study creates a machine learning model that can forecast Johnson-Cook constants using nanoindentation data. The Johnson-Cook model is frequently utilised to explain the plastic response of materials across different strain rates and temperatures, playing a crucial role in anticipating material behaviour in practical scenarios. The research shows that it is possible to forecast the macroscopic behaviour of materials based on nanoscale indentation test outcomes by linking

nanoscale mechanical characteristics with macroscale constitutive models.

This study improves our knowledge of wear mechanisms by combining small-scale experimental findings with predictive simulation. The study improves the ability to predict wear behaviour by considering the size effect of plasticity and analysing asperity interactions in detail. The accomplishment is in creating a strong connection between small-scale deformation processes and overall material behaviour, resulting in improved predictive models. This will impact the enhancement of durability and efficiency in important parts used for various engineering purposes, leading to lower operational expenses and environmental effects.

# 2. Literature Review

## 2.1 Contact Mechanics

Comprehending the contact mechanics during indentation and scratch testing is crucial for interpreting material behaviour under varying loading conditions. Both methods offer important information regarding a material's ability to resist deformation and wear, although they employ varying mechanisms and analytical methods.

### *2.1.1 Contact Mechanics in Indentation*

The process of indentation testing consists of applying a controlled force to push a known geometric indenter into the surface of a material. Contact mechanics during indentation are controlled by the elastic and plastic deformation of the material under the indenter. Hertzian contact theory explains the connection between the applied load, contact area, and material properties when the contact is purely elastic. It provides a solution for the contact stresses and deformations between two elastic bodies with curved surfaces in contact under a normal load. For a spherical indenter pressing into an elastic half-space, the relationship between the applied load *N*, the contact radius *a*, and the indentation depth $\delta$ is given by:

$$N = \frac{3}{4} \quad E_R R^{\frac{1}{2}} \delta^{\frac{3}{2}} \#(1)$$

where $E_R$ is the effective modulus of elasticity defined as:

$$\frac{1}{E_R} = \frac{1 - v_m^2}{E_m} - \frac{1 - v_i^2}{E_i} \#(2)$$

Here, $E_i$ and $v_i$ are the elastic modulus and Poisson's ratio of the indenter, and $E_m$ and $v_m$ are those of the material. The Hertzian theory hypothesises that the contact is entirely elastic, the surfaces have no friction, and the deformations are significantly smaller than the bodies' dimensions. Yet most indentation experiments require elastic-plastic deformation, particularly when surpassing the material's elastic threshold.

When the applied load exceeds the yield strength of the material, plastic deformation occurs beneath the indenter. The hardness measurement reflects this plastic response. Tabor [5] showed that the indentation hardness $H$ is approximately three times the yield strength $\sigma_y$ for many metals:

$$H \approx 3\sigma_y \#(3)$$

The size of the contact area when indenting is important for determining hardness and is impacted by variables like the shape of the indenter tip and the way the material moves around the indentation. The Oliver and Pharr technique [6] is commonly employed for calculating the contact area and elastic modulus using load-displacement data collected in instrumented indentation tests.

### *2.1.2 Contact Mechanics in Scratch Testing*

Scratch testing consists of sliding an indenter on the material's surface while applying a constant or increasing normal load, creating a scratch or groove. The scratch testing contact mechanics are intricate because of the interaction between normal and tangential forces, resulting in both elastic and plastic deformation, in addition to material removal methods such as ploughing (material is pushed aside by the indenter which involves plastic deformation and displacement of material without significant material removal.) and cutting (material is sheared and removed from the surface as wear debris).

While scratching, the area in front of the indenter endures compression forces, while shear forces are prevalent underneath and surrounding the indenter [7]. Friction between the indenter and the material is important in influencing the lateral force and energy dissipation in the scratch.

The depth of penetration and the shape of the scratch track depend on the applied load, indenter geometry, and material properties. Analytical models for scratch testing often incorporate both normal and tangential forces to describe the material response [8].

Results obtained using the theories suggested above should be interpreted with caution: Hertzian elasticity models, while foundational, oversimplify scenarios by ignoring friction, surface imperfections, and time-dependent behaviour—factors critical for polymers or biomaterials. Oliver-Pharr method's reliance on elastic recovery during unloading may misrepresent materials with significant plasticity or heterogeneities, such as composites. Scratch testing faces analogous challenges: analytical frameworks may neglect progressive damage mechanisms (e.g., microcrack propagation) and thermal effects induced by friction, which alter material responses in multi-pass or high-strain-rate scenarios. These limitations underscore why integrating contact mechanics with other advanced characterisation tools, which will be illustrated in upcoming chapters, is vital.

## 2.2 Definitions of Hardness in Indentation and Scratch Testing

### *2.2.1 Indentation Hardness*

Indentation hardness measures a material's resistance to localised plastic deformation under an applied load. In nanoindentation, hardness $H$ is calculated using the maximum load $P_{max}$ and the contact area $A_c$ and it represents the average pressure exerted by the indenter on the material at peak load normalized by the contact area projected from the normal loading direction.

$$H = \frac{P_{max}}{A_c} \#(4)$$

### *2.2.2 Scratch Hardness*

Scratch hardness quantifies a material's resistance to deformation or removal when subjected to scratching. A typical scratch process is shown in Figure 1where a hard solid particle is scratched on a soft surface. Different methods can be used to define scratch hardness:

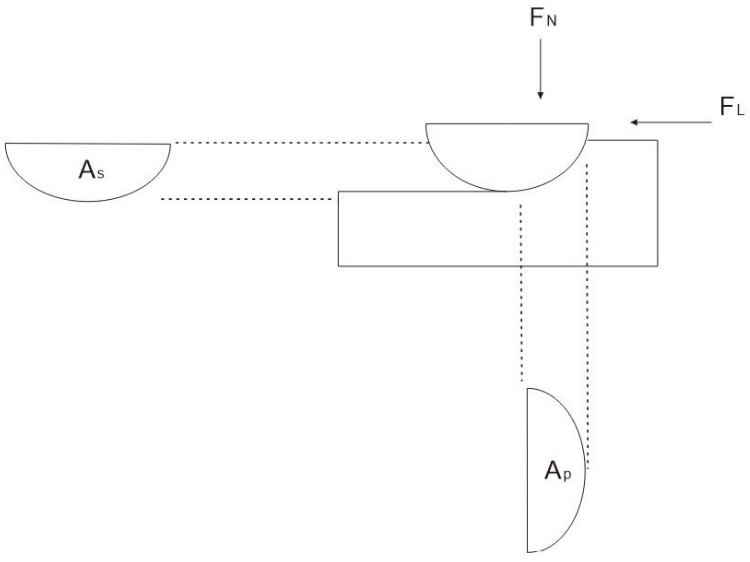



*Figure 1 A schematic of a scratch process [9].*

**Scratch Hardness Number (ASTM G171)**: Defined as the normal force $F_N$ divided by the contact area projected from the normal loading direction $A_p$ of the scratch [9]:

$$H_s = \frac{F_N}{A_p} \#(5)$$

The projected area $A_p$ is calculated based on the width or depth of the scratch track. $H_s$ represents the average normal stress applied to plastically deform the surface and a higher $H_s$ potentially indicates greater resistance to indentation-driven damage (e.g., from hard asperities or particles). However, it simplifies the scratch process by neglecting shear forces.

**Lateral Force-Based Definition:** Accounts for the material's resistance to shear deformation by considering the lateral force $F_L$

$$H_{sL} = \frac{F_L}{A_s} \#(6)$$

where $A_s$ is the contact area projected from the sliding direction of the scratch [10]. It is the mean pressure required to create deformation in the scratch direction. It is likely more sensitive to the material's ability to resist shear-driven wear (e.g., abrasion, microcutting). This approach potentially better reflects dynamic, friction-dominated wear processes but requires precise measurement of lateral forces which some indenters are unable to measure.

### *2.2.3 Correlation Between Indentation and Scratch Hardness*

J.A. Williams used steel, aluminium, and copper, both in annealed and worked conditions, to investigate scratch hardness, which was defined as the normal load applied during the scratch divided by the projected load-bearing area and concluded that scratch hardness is not consistently equal to indentation hardness, as the ratio scratch hardness to indentation hardness varies between materials and depends on factors such as the indenter's geometry and the material's work-hardening characteristics. He found that for ductile metals, the scratch hardness tends to be slightly higher than indentation hardness, but this relationship is complex and influenced by the angle and shape of the indenter used in the tests, as shown in Figure 2 [11].

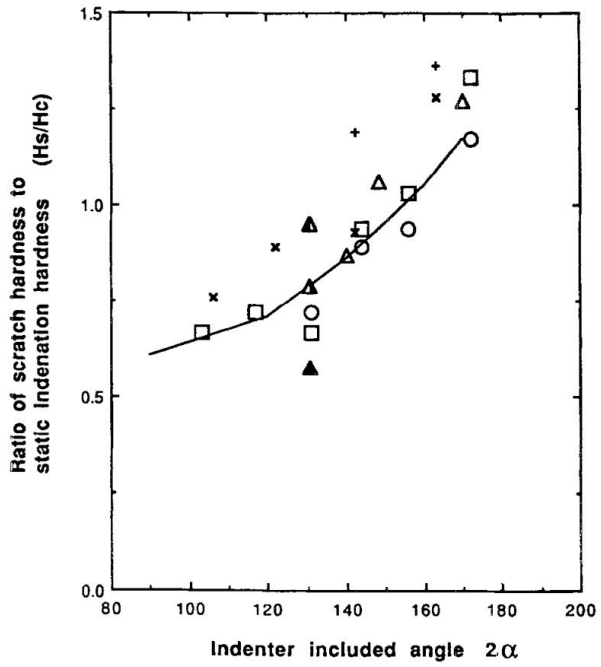



*Figure 2 Ratio of scratch hardness $H_s$ to the static indentation hardness $H_c$ as a function of the indenter included angle [11].*

Graça et al. analysed nickel-cobalt systems and the hardness increase with decreasing contact scale is more pronounced in nanoindentation than in nanoscratch testing - while both tests showed increased hardness at smaller scales, the ratio changed from $H_S$ (scratch hardness)/ $H_I$

(indentation hardness)> 1 (1.16-2.32) at microscale to $H_s/H_i$ < 1 (0.58-1.06) at nanoscale. It was suggested that scratch hardness being lower than indentation hardness is due to native oxide layer being spalled off during the scratch process [12].

Shakhverdova et al. investigated the relationship between nanoindentation hardness ($H_c$) and nanoscratch hardness ($H_s$) in high-carbon nitrogen-doped steel, comparing as-received (nanostructured) and annealed states. They observed that the dissolution of cementite nanowires during annealing significantly reduces both $H_c$ (from ~17.7 GPa to ~3.3 GPa) and $H_s$, with the ratio $H_c/H_s$ decreasing from ~1.27 to ~0.55–0.70. They attributed the higher hardness in the as-received state to nanostructured obstacles (e.g., nanowires) impeding dislocation motion, while annealing eliminates these features, reducing resistance to plastic deformation. The disparity between $H_c$ and $H_s$ was further explained by distinct deformation mechanisms: indentation primarily reflects bulk plastic resistance, whereas scratching involves additional contributions from ploughing (material displacement) and sliding friction, influenced by adhesion forces under ambient conditions. They suggested that $H_c/H_s$ serves as a microstructural indicator, with higher ratios correlating to nanostructured hardening [13].

## 2.3 Microscale sliding/wear testing

Microscale wear refers to wear that occurs at the micron level, typically involving features and phenomena that are in the range of tens to hundreds of micrometres. For friction at this length scale, multiple grains and asperities of contact are usually involved. Researchers like Tabor, Bowden and Ashby have made fundamental contributions to the vast body of knowledge on microscale wear processes. Tabor and Bowden used pin-on-disc and pin-on-flat apparatus to measure the wear rates of different metals and materials under controlled sliding conditions and found that material transfer between contacting surfaces plays a critical role in wear behaviour. Specifically, they noted that when two surfaces slide against each other, strong adhesive bonds can form at asperity contacts, leading to material transfer and eventual wear. This process is particularly pronounced in metals with high ductility and surface energy [14].

Ashby et al. developed several material indices for assessing wear resistance, including hardness ($H$), elastic modulus ($E$), the hardness-to-elastic modulus ratio ($H/E$), and the elastic modulus-to-density ratio ($H/\rho$). These indices integrate key material properties to evaluate a material's ability to resist wear, enabling more effective material selection for wear applications. By systematically analysing the relationships between these properties and wear behaviour, their methodology supports the identification of materials that enhance wear performance in mechanical design [15].

Bhushan and Gupta conducted microscale wear investigations using scratch tests, nanoindentation, and atomic force microscopy (AFM) to explore wear mechanisms across diverse materials. It was demonstrated that adhesive wear, predominant at microscales due to heightened van der Waals interactions, contrasts with abrasive wear mechanisms where

material hardness and indenter geometry dictate transitions between ploughing and microcutting. Surface fatigue, assessed through cyclic nanoindentation, revealed subsurface damage accumulation dependent on the crystallographic structure and loading frequency. They concluded that wear resistance in nanotechnology applications necessitates strategies accounting for scale-specific phenomena, such as tailored surface coatings or optimised lubricants, informed by their integrated microscopy-mechanical testing approach [16].

Holmberg and Matthews' multiscale models integrate microscale tribological phenomena (e.g., asperity adhesion, interfacial crack propagation) with macroscale wear outcomes through 3D finite element analysis and stress intensity factor simulations. It was highlighted that microscale mechanisms—such as hydrogen passivation of dangling bonds in diamond coatings or graphitization of DLC surfaces—suppress macroscale adhesive and abrasive wear by redistributing shear stresses. Surface roughness transitions govern dominant wear modes: asperity interlocking at macro scales ($R_a$ = 0.1–1 μm) versus interfacial shear at nano scales ($R_a$ < 30 nm). They concluded that optimising wear-resistant coatings requires scale-specific strategies, such as gradient layer architectures, to mitigate crack propagation or tailored residual compressive stresses informed by their integrated stress-strain and fracture mechanics framework [17]. Suh's delamination theory reframed wear as a subsurface-driven process governed by cyclic plastic deformation, crack nucleation at inclusions/dislocations, and crack propagation parallel to the surface. This reorientation from surface-centric models revealed that wear resistance hinges on microstructural control of subsurface damage accumulation. Crack initiation depth and propagation rates, influenced by tangential stresses and friction, dictate wear particle geometry (e.g., aspect ratios >10 in ductile metals), with thicker sheets forming under higher friction. Hardness alone proves insufficient for wear

mitigation; materials with coherent precipitates or refined grain boundaries resist crack nucleation better than harder, brittle counterparts [18].

Rigney et al. outlined the sequence of events in sliding wear: the regional contacts cause significant plastic strains in either or both solid components, and the near-surface microstructure is altered by plastic deformation, rendering the material unstable to local shear. This results in the transfer of fragments of deformed material, which are then reshaped and combined with environmental elements or counter-face material to create ultrafine-grained material [19]. By sliding Cu-Ni alloy blocks against rings of 440C stainless steel, Rigney et al. discovered that the Cu-Ni alloys' wear rates decrease as more ring material is transferred and as transfer proceeds, the ring's wear rate rises, as exemplified by Figure 3, which indicates that the friction between two alloys is a dynamic and evolving process and observation of the localised phenomenon is essential for understanding it.

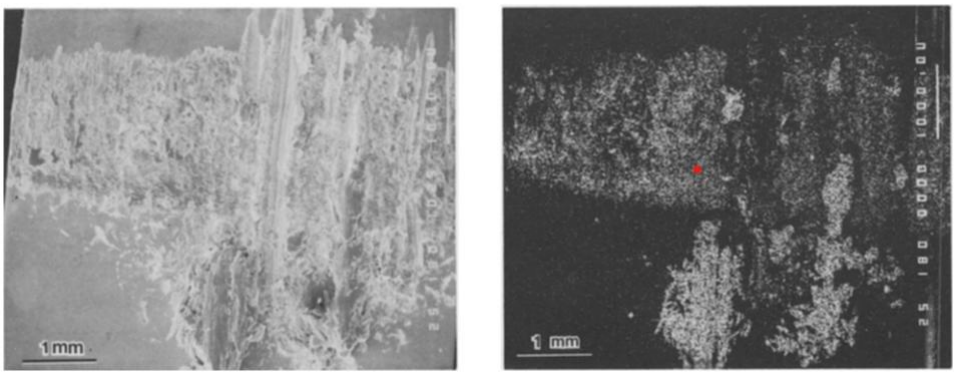



*Figure 3 Secondary electron image showing the unannealed wear scar of Ni-40tit.%Cu gliding on a 440C circle. The ring moved upwards from the bottom in the sliding direction [20].*

They further reported that this procedure frequently results in a transition where the ring sustains significant damage, and the transition can be significantly postponed by removing the loose debris with brushes [20]. Greiner et al. investigated the sequence of stages in the microstructure evolution in copper under mild reciprocating tribological loading and discovered that the sliding contact would form a deformed surface layer with a large number of dislocations that extend deeper with the motion continuing. It would also generate a

straight dislocation trace line that accumulates successive dislocations and an increase in misorientation with increasing cycle number. They further reported that the GND networks would appear in the deformed layer to a depth of several micrometres as the number of pass increases, which eventually evolve into small angle grain boundaries (SAGBs) and form subgrains, as demonstrated by Figure 4 [21].

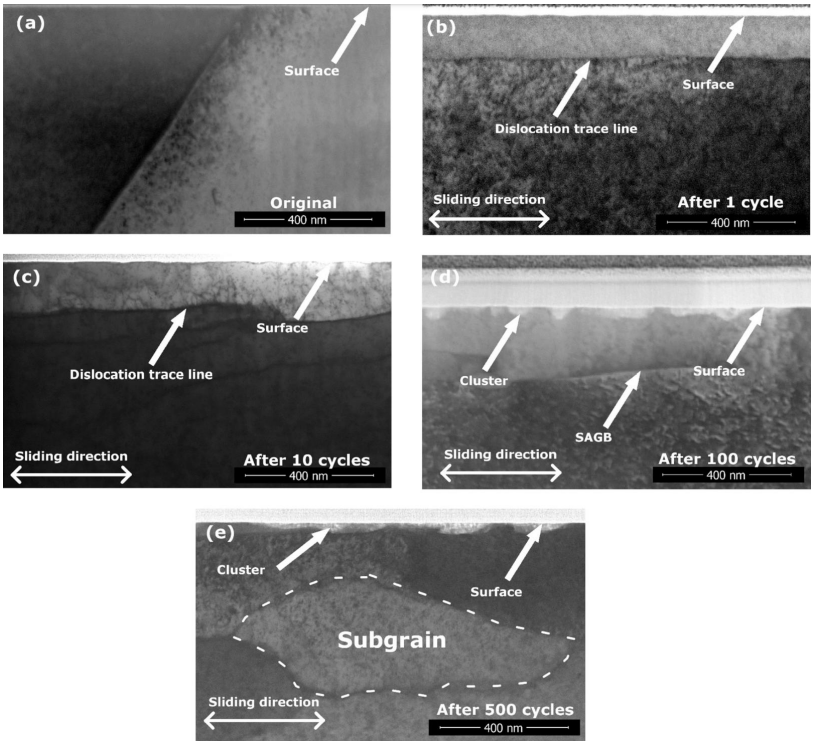



*Figure 4 Scanning transmission electron microscopy (STEM) images of OFHC copper under tribological loading after a different number of scratch passes: (a) pristine material before tribological testing; (b) after 1 pass; (c) after 10 passes; (d) after 100 passes [small-angle grain boundary (SAGB) and clusters are marked by white arrows]; (e) after 500 passes [21].*

Integrating nanoscale tests such as nanoindentation and nanoscratch testing can significantly enhance the understanding of microscale wear processes initially studied by researchers mentioned above by highlighting the single asperity contact at the nanoscale. Nanoindentation can detect changes in hardness and elastic properties within microstructurally complex regions, enabling a more granular understanding of how these properties influence wear resistance. Similarly, nanoscratch testing allows for the evaluation

of wear resistance and scratch hardness at the nanoscale, providing valuable information on the initiation and propagation of wear at extremely fine scales.

This study is not the first to use nanoscratch testing, but it is the first to focus on how individual variables such as the number of scratches and tip orientation influence nanoscale hardness measurements in nickel-based alloys with the aid of a variety of high-resolution characterisation techniques and Finite Element (FE) methods. Before presenting the results, the first part of the literature review will explain how nanoscratch hardness is defined and calculated, how area functions are determined, and how this tool has been used in assessing the mechanical properties (indentation hardness, elastic modulus etc.) of different types of materials. Current efforts in computer simulation will be further discussed to show how simulations and machine learning aid in the interpretation of experimental data and provide a deeper understanding of wear.

## 2.4 Nanoindentation

Nanoindentation testing refers to indenting a hard tip into the surface under either load or displacement control. This method is well used in testing depth-related mechanical properties of the coated and uncoated material systems [22]. Over the last 25 years, nanoindentation testing has increasingly become a conventional nanomechanical characterisation method. By applying a small oscillation and continuously measuring the amplitude and phase of this oscillating force and the resulting displacement response, it can provide depth-related materials properties measurement, known as Continuous Stiffness Measurement (CSM). By limiting the normal load to millinewton range and displacement to micron range, it becomes possible to closely observe how an asperity with known geometry incurs deformation and evolvement of lattice structure within a single grain, which aids the interpretation of overall wear phenomenon at the microscale and macroscale levels.

A typical equipment used in nanoindentation test is a nanoindenter, an instrumented indentation system fitted with either a diamond Berkovich Tip, diamond spherical tip or other custom-made tips. A more detailed introduction of the instrument itself can be found in the Method section.

### *2.4.1 Nanoindentation Hardness and Contact Area*

Tabor classified the definition of hardness into three categories: indentation, scratch, and dynamic hardness, the latest of which more resembles impact tests where a steel ball is dropped on a metal surface instead of the common friction wear [23]. The indentation technique was widely applied in the past century and is the most recognised method for hardness measurement. A permanent indentation mark is created on the sample surface, and

the Meyer hardness is often used, which is the mean pressure defined as the ratio of the load to the projected area of the residual indentation mark[23], [24], [25]. In nanoindentation, the hardness is also defined as the mean pressure but refers to the ratio of the indentation force to the projected area of the in-situ surface contact area between the tip and the sample. The definition of nanoindentation hardness assumes that interfacial shear stress (i.e., friction) does not exist between the surface of the tip and the indented material. Thus, the resultant pressure, *P*, is normal to the indentation surface. The determination of surface area is discussed separately for the spherical tip and Berkovich Tip.

2.4.1.1 Berkovich Tip

For the Berkovich tip, the calculation of the contact area function is usually conducted on fused silica, whose elastic modulus and Poisson's ratio are 72 GPa and 0.17, respectively. Through analysis of the unloading part of a load-depth curve obtained by instrumented indentation, Oliver et al. concluded the relationship between reduced modulus $E_r$, the total compliance of the system $C$, the frame compliance of the instrument $C_f$ and the contact area of the tip $Ac$, is as follow [6]:

$$\sqrt{A_c} = \frac{\sqrt{\pi}}{2\beta(C - C_f)E_R} \#(7)$$

, where $\beta$ is a correction factor with a value depending on the tip geometry [26]. Chicot et al. found with finite element analysis that β = 1.034 for Berkovich tip [27]. $C = \frac{dh}{dP}$ and reflects the compliance of the whole system which is the inverse of the slope of the load ($P$) versus penetration depth ($h$) curve at the beginning of unloading. $C_f$ is meant to remain constant during the indentation process. $E_R$ is correlated with the elastic modulus and Poisson's ratios

of the material and of the tip. The relationship could be described with the Hertzian theory mentioned above [28].

$$\frac{1}{E_R} = \frac{1 - v_m^2}{E_m} - \frac{1 - v_i^2}{E_i} \#(8)$$

, where $E_m$, $v_m$, $E_i$, and $v_i$ refer to the elastic modulus and Poisons ratio of the material and the tip, respectively. For diamond tip, $E_i$ = 1140 GPa and $v_i$ = 0.07, which is the value commonly used but in practice could vary based on factors such as crystallographic orientation, presence of defects, and measurement techniques.

For a perfect Berkovich tip, the projected area $A_c$ is a function of indentation depth $h_c$ and is expressed as [29]:

$$A_c = \pi \cdot \tan^2 \varphi \cdot h_c^2 = 24.56 h_c^2 \#(9)$$

In which $\varphi = 70.32°$ and is the semi-angle of the conical indenter equivalent to the Berkovich tip. To account for the tip bluntness, Oliver et al. further improved the area function of the Berkovich tip as [29], [30] :

$$A_C = 24.56 h_c^2 + C_1 h_c^1 + C_2 h_c^{1/2} + C_3 h_c^{1/4} + \ldots + C_8 h_c^{1/128} \#(10)$$

Where $C_1$ through $C_8$ are constants to be determined in the indentation calibration, the first term depicts a perfect pyramidal tip, while the rest describes the difference from the conical geometry due to tip blunting.

While it's common to assume that $C_f$ remains constant during indentation, in practice, $C_f$ can vary with load, displacement [31], or over time due to instrument creep and thermal drift [32], and using multiple reference materials with different known properties can improve the calibration of frame compliance [33].

### 2.4.1.2 Plasticity Size Effects

It has been observed that nanoindentation and nanoscratch hardness are not fixed values for certain materials but tend to increase as the indent size or scratch size decreases at small scales, which is known as the Indentation Size Effect (ISE) [34] and Lateral Size Effect (LSE) [35]. Figure 5 shows a comparison of hardness measurement from macro-level tests and nanoindentation tests. 'Unusual' ISE refers to the observation that in some materials, the hardness measured in nanoindentation tests increases with the indentation depths [36].

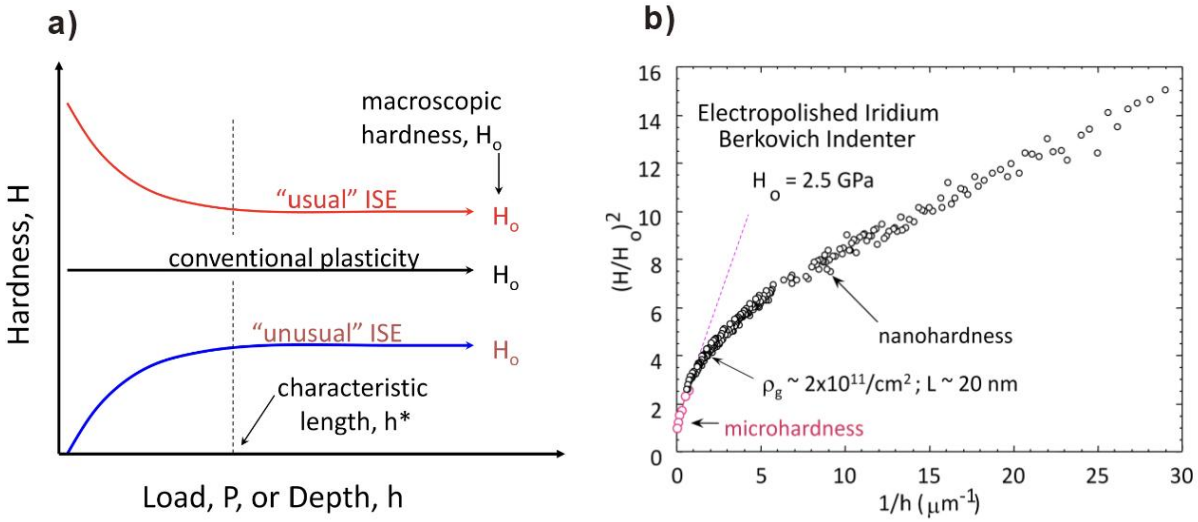



*Figure 5 a) Usual and unusual indentation size effects vs the hardness trend predicted by conventional plasticity[37], [38], b) $(H/H_0)^2$ vs. 1/h of Berkovich indentation in electropolished iridium .*

One of the most recognised explanations of ISE is developed by Nix and Gao, who proposed two types of dislocations that contribute to the hardness/strength during indentation: the statistically illustrated dislocations that occur due to homogeneous strain, and geometrically

necessary dislocations (GNDs) that arise from the strain gradients inherent in small indentations, as illustrated in Figure 6. It was suggested that GNDs became increasingly important as the indentation depth decreased and the strain gradient increased since they were required for the lattice to deform to the shape of the indenter tip [39].

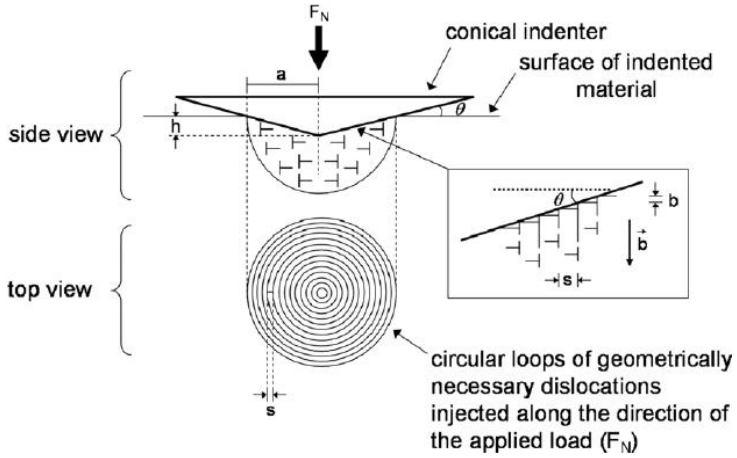



*Figure 6 Schematic representing the emission of geometrically necessary dislocation loops during the indentation of a single crystal with a conical indenter, as proposed by Nix and Gao* [39]

Bull revealed that sample preparation methods can significantly influence the manifestation of ISE [40]. It was suggested that in metallic materials, mechanical polishing generates work-hardened surface layers that artificially elevate measured hardness values at shallow depths, a phenomenon that can be effectively eliminated by removing approximately 1 μm of material through electropolishing. The formation of surface oxides was also another preparation-dependent factor, as most metals develop oxide layers upon environmental exposure that typically exhibit higher hardness than the underlying substrate. It was further suggested that the surface friction effects, while generally minimal for high-angle indenters like Vickers or Berkovich geometries become increasingly significant at very low loads where surface tractions can measurably alter the penetration resistance and become relevant when comparing results across different indenter geometries. Through high-temperature nanoindentations on single-crystal platinum with (110) orientation, Schuh et al. discovered

that initial plasticity is controlled by heterogeneous nucleation sites (with unexpectedly small activation volume ~0.5$b^3$ and low activation energy ~0.28 eV) rather than homogeneous dislocation nucleation as previously believed. It was proposed that the size effect could arise from how the material transitions from this localised, nucleation-dominated deformation behaviour at small scales to bulk plasticity at larger scales, which suggested that the ISE is rooted in the statistical nature and specific mechanisms of initial dislocation nucleation, though the authors acknowledge more research with atomistic simulations including realistic point defect distributions was needed to fully understand this connection [41].

Bolshakov and Pharr [42] studied how the rounding of the indenter tip affects nanoindentation measurements. It was shown that blunt tips result in increased hardness readings at shallower depths, and when the indentation depth is reduced, the impact of the tip radius becomes more noticeable, leading to an overestimation of hardness if the tip shape is not properly considered. Finite element analysis showed that a small tip radius could lead to substantial inaccuracies in hardness measurements when depths are under a few hundred nanometres. Field and Swain [43] also highlighted the significance of considering the indenter tip radius when analysing nanoindentation results. They suggested that the contact area when indenting with a rounded tip is not the same as when using a sharp indenter, which impacts the stress distribution and hardness calculation.

This section highlights the fundamental principles and complexities of nanoindentation testing, particularly its application in characterising mechanical properties at the nanoscale. The discussion of contact area calculations, tip geometry corrections, and size effects provides guidance on the research method design and data interpretation for this thesis on nickel-based alloys.

## 2.5 Nanoscratch

Nanoscratch testing refers to indenting a hard tip into the surface and then moving the stage parallel to it to create a scratch groove. It uses the same instrument and tip-loading procedure as the nanoindentation method, except that later movement is introduced. Compared to Atomic Force Microscopy (AFM), which also applies a limited load on a sharpened tip to characterise or alter sample surface, nanoscratch testing has advantages in measurement stability and avoids excessive tip wear on hard samples. It is also a critical tool in the simulation of single asperity contact in tribological experiments [44].

Commonly used nanoscratch tests include constant load nanoscratch test, ramped load nanoscratch tests and multi-pass repetitive unidirectional constant load nanoscratch tests. Both ramped load tests and constant load tests follow a 'three-pass scratch procedure', in which the first pass profiles the surface topography at a low normal force (20 – 50 μN), the second pass performs the scratch at pre-determined normal load for the length of the scratch and the third pass profiles the surface the again to obtain the residual topography of the surface, as explained in Kareer et al.'s work [35]. The tip shape is determined using nanoindentation calibration methods while the contact area during scratch process will be determined based on the methods illustrated beneath.

### *2.5.1 Nanoscratch Hardness and Contact Area*

Kareer et al. [35] proposed three different methods to calculate the scratch hardness using the Berkovich tip. Method One takes a similar approach to the standard ASTM G171, which defines the scratch hardness number as the normal force of a constant-force scratch divided by the projected area of contact, which is considered as a semicircle with the diameter being the width of the scratch track. In the first method, the scratch hardness is defined as constant normal force $F_N$ divided by the projected area of contact of the indenter with the scratch track. The scratch penetration depth measured from the indenter displacement channel is used to derive the projected contact area of the indenter $A_c$. For the face-forward (FF) orientations shown in Figure 7, the actual contact area is one-third of $A_c$, while for edge-forward (EF) orientation, it is two-thirds of $A_c$. The second method is devised to represent the lateral resistance of the material, where measured lateral force $F_L$ is divided by the lateral area of contact, which remains constant for any given depth for both orientations. The lateral area of contact was assumed to be an isosceles triangle, with height being the scratch depth and base being the side length of the tip. The third method accounts for both normal and lateral load on the tip and derives a resultant force $F_r$; for FF orientation, $F_r$ works on the surface area of a single facet, as shown in Figure 8, while for EF orientation, the force is considered to be equally split between two facets in contact at an in-plane separation angle of 60° as demonstrated in Figure 8 and Figure 9.

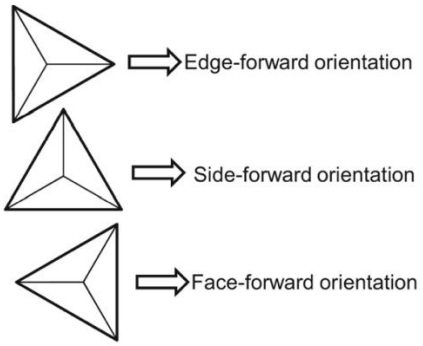



*Figure 7 Schematic representation of the Berkovich indenter: different tip orientations, including edge-forward, side-forward and face-forward [35].*

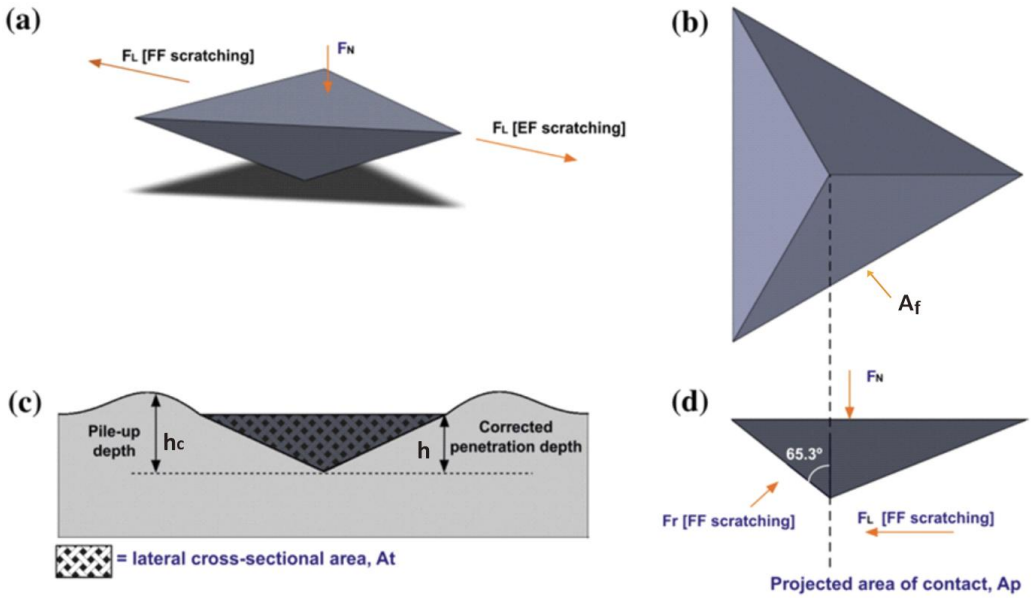



*Figure 8 Diagrams to show: (a) The tip orientation for EF and FF scratches. Lateral force, FL, acts in the direction of motion. (b) The total projected area of contact used in the first method, one-third Ap is used for FF and two-thirds Ap is used for the EF (c) [35].*

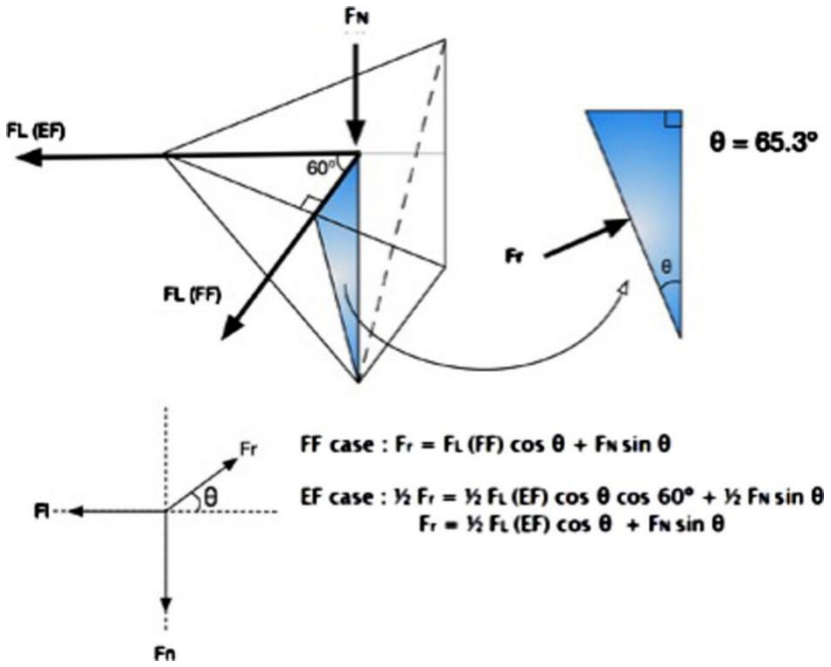



*Figure 9 Resolved force calculation for forces acting on the facets in contact with material for the EF and FF tip orientation. Calculations based on the geometry of the tip, $F_N$ and $F_L$ were measured from the instrument [35].*

It could be concluded from the literature that the correct calibration of tip geometry has a pivotal role in determining the hardness measured as a blunted tip can lead to underestimation of contact area at a given contact depth and requires fewer GNDs to accommodate the stress gradient, which is critical for assessing the Indentation Size Effect for a given material and error in hardness measurement [45].

## 2.6 Application of Nanoscratch Testing

Nanoscratch testing, when being used only on materials without coatings, can reveal how the material properties and microstructures together with scratch mode (i.e. tip orientation) affects the properties measured from nanoscratch testing. Other attempts on using nanoscratch tests to evaluate bulk material property include scratching material with AFM tip.

### *2.6.1 Material structure*

Brazil et al. performed nanoscratch tests on fused silica, aluminium, and nickel. It was discovered that a crucial factor in determining the static coefficient of friction is the additional plastic deformation and sink-in brought on by elevated contact stress. Adsorbates on the surfaces cause the contact to break, which causes the change from static sink-in to kinetic ploughing. The angle at the indent edge was also found to have influence and it is concluded that the initial lateral deformation and the type of transition to full sliding are determined by the $E/H$ ratio, or its inverse, the yield strain $\sim H/E$ [46]. Greiner et al. slid a ruby ball against electropolished bcc iron under an increasing normal load and reported the formation of a dislocation trace line (DTL) similar to those reported on FCC materials. It was concluded that a certain amount of plastic deformation was essential for the formation of the dislocation trace line, and the lateral force could be used as a rough indicator for the onset of ploughing [47]. Prieto et al. conducted reciprocal scratch tests on cryogenically treated stainless steel and postulated that the enhanced mechanical resistance of the cryogenically treated martensite was responsible for the decrease in friction and the marginal decrease in the wear coefficient when compared to conventionally treated steels. They also suggested that wear in the macroscopic test was primarily caused by delamination, driven by ratcheting, whereas wear in the nanoscratch test was primarily abrasive. They did this by comparing the results of the two tests on the same material. It was proposed that because the nanoscratch

test was reciprocal, ratcheting was ineffective and that the carbides contributed only marginally to the material's wear response, which was also attributed to the wear tracks' magnitude being inversely related to carbide's distance from one another. The author believed that the nanoscratch test and nanoindentation were crucial for understanding the martensitic matrix's contribution to the wear resistance of the material, which was not identifiable in macroscopic tests due to the number of tribological interactions involved [48].

In addition to nanoindenters, AFM has been used to conduct nanoscratch tests on magnesium alloys, revealing that the friction and wear characteristics of peak-aged AZ91 Mg alloy are greatly influenced by the local microstructure, such as the types of precipitates and the sliding direction in relation to the precipitate alignment [49]. It was observed that discontinuous precipitate (DP) areas had substantially lower wear than continuous precipitate (CP) regions on average. Additionally, the alignment of DPs in relation to the sliding direction significantly impacted the friction and wear behaviour observed via AFM. Nanoscratch and nanoindentation were employed to assess dislocation nucleation initiation on the surface of the semiconductor Indium Phosphide (InP), revealing that the force required to induce the initial dislocations was half as much during scratching as compared to indentation. The variance was clarified by a mix of precise factors such as the scarce presence of native defects, the non-ideal spherical loading conditions, and the material's anisotropy. It was also mentioned that when loads exceed 2 mN, the shape of the flawed tip begins to influence the situation by creating intense stress at the point of contact, possibly leading to the pop-in occurrence. The findings indicate the need for combining nanoscratch with nanoindentation to completely understand the material wear behaviour and the importance of precisely characterising the tip geometry [50].

### *2.6.2 Tip Orientations*

Youn et al. found that on single-crystal silicon, the tip orientation of the Berkovich tip can have a significant effect on the coefficient of friction (COF) measured, ranging from 0.16 to 0.38 [51], Mulliah et al. also derived a similar conclusion by performing a parallel molecular dynamics simulation of FCC silver (1 0 0), where the COF ranges from 0.37 to 0.57 [52]. Pergande et al. argue that a conical tip is preferred to eliminate any possible directionality [53], but Shikimaka et al. demonstrated that different tip orientations unique to the Berkovich tip could lead to disparate evolution of deformation mechanisms as a function of speed and by changing the scratch speed and normal loading, different strain rate sensitivities of hardness were observed for scratches governed by contrasting mechanisms such as Plastic Flow and Ductile Cutting[54]. Studies above suggest that the Berkovich tip orientation could have a major influence on the deformation formation, and therefore studies on the tip orientation in nanoscratch test should be performed to enhance the understanding of wear formation on nickel-based alloys.

### *2.6.3 Scratch Speeds*

Feng et al. conducted nanoscratch tests on C-plane sapphire using a Berkovich nanoindenter at velocities from 2 to 16 μm/s. The findings indicated that increasing scratch speeds result in greater critical load and depth during the ductile-brittle transition, showcasing improved plastic deformation and surface quality at higher speeds. SEM analysis suggested that lower velocities resulted in increased brittle deformation features such as cracks and chipping, while they are reduced at higher velocities [55]. In research on single-crystal SiC, Tang et al. showed that higher scratch velocity resulted in a delay of the brittle-ductile transition and expansion of the ductile zone. Through analysis of the depth-distance curves and surface morphology, it was noticed that higher scratch speeds resulted in fewer cracks and a smoother scratch process [56].

Gassilloud et al. [57] performed tests on silicon surfaces at two varying speeds: 2 µm/s (slow) and 100 µm/s (fast). At low speeds, the nanoscratch showed a combination of amorphous silicon and Si-XII, whereas at high speeds, the deformed volume consisted entirely of amorphous silicon. The deformation mechanism changed from elastic-plastic to fully plastic as the load increased at low velocities, impacting the hardness values. Hodge and Nieh [58] conducted additional research on the impact of scratch velocity on amorphous alloys and discovered that the speed of the scratch did not have a straightforward relationship with wear resistance in Pd-based alloys. Nevertheless, increased speeds seemed to indicate decreased friction which was considered to be related to pile-up formation but was not explained. Ye et al. investigated the effects of scratch rate on the friction and wear of single-phase equiatomic TiZrHfNb high-entropy alloy using nanoscratch tests which they also discovered that the scratch speed had a negligible effect on the scratch depth, implying that the wear resistance was independent of scratch speed for the alloy tested, shown by Figure 10 [59].

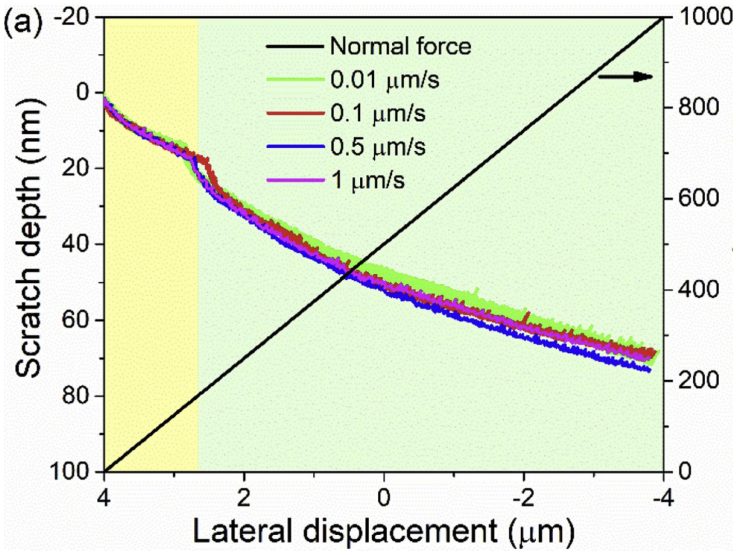



*Figure 10 Scratch depth vs. scratch distance for scratch tests on TiZrHfNb-HE alloy under ramping load mode at scratch speeds of 0.01, 0.1, 0.5 and 1 µm/s. The tip used was a 90° cono-spherical diamond tip with an effective radius of 600 nm [59].*

### *2.6.4 Normal Loads*

Zhang et al. [60] explored the effects of normal load on $Lu_2O_3$ laser crystals and found that with increasing load, surface cracks became more pronounced, and the width of the scratch grooves increased. As the load increased, the deformation transitioned from a smooth surface to one marked by distinct wave patterns and edge cracks, which correlated with an increase in hardness. Tang et al. [56] also examined how changing the load in nanoscratch tests impacts single-crystal SiC and discovered that higher normal loads cause a shift from ductile to brittle material removal. The critical depth for this transition was roughly 212 nm on the C-plane and 105 nm on the Si-plane, with greater loads causing more severe brittle fractures like cracks and chipping. Sanyal et al. [61] performed nanoscratch experiments on Al-Mg-Si alloys with loads ranging from 10 mN to 250 mN and found that greater loads led to increased penetration depth and residual deformation. The hardness decreased as the load increased, but too much loading caused wear and accumulation of plastic deformation, as seen in SEM analysis. Kareer et al. demonstrated with single crystal copper that the lateral resistance experienced by the Berkovich tip increased with normal load in nanoscratch tests, but the scratch hardness calculated using projected areas decreased with increased normal load in both edge-forward and face-forward tip orientations [35], as shown in Figure 11.

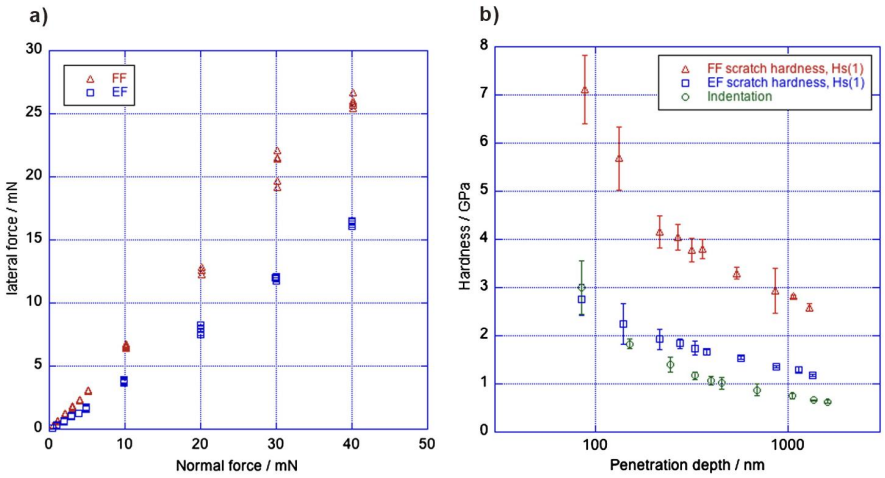



*Figure 11 a) Normal force vs. lateral force for Berkovich tip nanoscratch tests and b) scratch hardness measured using average penetration depth and projected area on single crystal copper [35].*

### *2.6.5 Summary*

Nanoscratch testing offers additional insight into materials compared to nanoindentation testing, thanks to its extra dimension of motion. The transition from a mostly constant process to a dynamic process with friction and rotation occurs when the matrix material moves relative to the tip, with the orientation of the tip becoming important.

According to Rigney's initial microscale test studies, interactions between transferred material, softer and harder bodies, and their collective interactions greatly influence wear rate during scratch experiments, complicating the study of their individual effects. However, in nanoscratch tests, the isolated roughness of the surface allows the separated material to detach as debris (as seen in the brittle cutting of ceramics) or accumulate on the edges of the scratch groove as pile-up, enabling a closer look at the tip's interaction with the strain-hardened matrix separately. Similar to microscale tests, nanoscratch is affected by external variables including temperature, humidity, and surface roughness. Yet, because of a more confined area of research, it is much simpler to create more ideal experimental conditions for nanoscratch tests than for microscale tests.

Nanoscratching in literature is a recent and evolving area, still holding many undisclosed insights into microscale wear mechanics. Even though several studies have utilised nanoscratch testing to assess material properties, the majority focus on determining the strength of coating materials. Nanoscratch tests on bulk materials are mostly single-pass, but real wear processes are typically repeated and develop over time, leading to stress-induced failure from evolving cracks under cyclic loading, as exemplified in the nuclear station incident. At present, there is a lack of research on nickel alloys or repetitive nanoscratching, and there is no research combining the two, even though nickel alloys are extensively used in

applications that experience repeated wear. The lack of adequate research supports the need for conducting repeated nanoscratch tests on nickel-based alloys in this study, with the goal of establishing a foundation for addressing and avoiding wear-induced failures of load-bearing nickel alloy parts in practical applications.

## 2.7 Scratch Test Simulation

Computer simulation has become a prevalent engineering design tool due to its cost-effectiveness and extraordinary mechanical analysis capabilities. Cutting tests represent one of the most heavily researched areas, with substantial efforts made to accurately model the material deformation, heat generation, and stress distribution during the machining process [62]. However, cutting tests performed at the macroscale possess similarities to, but do not completely emulate, nanoscratch testing, as bulk material properties and working conditions dominate cutting test outcomes while nanoscratch tests are heavily influenced by localized material features like dislocations, precipitated phases, and grain orientations as dislocations and contrasting phases often serve as obstacles that inhibit the onset in addition to the propagation of crack formation, while grain orientation also influences the preferred path of crack growth, all of which have vital impact on the life span and safety of mechanical components [63]. Major finite element analysis (FEA) software packages such as Abaqus, Solidworks, and Hyperworks are engineered for macroscale applications, thus warranting investigation into their potential utility for gleaning insights into nanoscratch experimentation and outcomes.

### *2.7.1 Materials characterization*

For the simulation to be accurate, the materials involved must be properly characterized. In Abaqus, for example, the user can manually determine how they want to characterize the material. One can treat the material as purely elastic and put in only one elastic modulus and Poisson's ratio, which is unlikely to represent something that exists in reality but still helpful in understanding how materials behave in the elastic regime. For plasticity, the user can choose to define single yield stress at one given strain or put in a table of stress and strain

values and include rate dependency. However, the stress/strain relationship in this way is represented with discreet values and for the stress/strains that are not defined, the system will have to approximate and could lead to inaccurate outcomes.

One of the popular approaches to describe materials in simulation is the Johnson-Cook model, a constitutive model that is used to describe the flow stress of materials under high strain rate deformation, such as during impact, explosive loading, or ballistic penetration events. The model is commonly written as [64]:

$$\sigma = (A + B\varepsilon^n)\left(1 + C\ln\dot{\varepsilon}^*\right)\left(1 - T^{*^m}\right)\#(11)$$

in which $\sigma$ is flow stress, $\dot{\varepsilon}^* = \varepsilon/\varepsilon_{ref}$ is the dimensionless strain rate with $\dot{\varepsilon}$being the strain rate ($s^{-1}$), $\dot{\varepsilon_{ref}}$ the reference strain rate ($s^{-1}$), and $T^*$ being homologous temperature, expressed as:

$$T^* = \frac{T - T_{ref}}{T_m - T_{ref}}\#(12)$$

where $T_m$ is the melting temperature of the material, $T$ is the experiment temperature, and $T_{ref}$ is the reference temperature ($T \geq T_{ref}$). *A, B, C, n, m* are material properties to be determined from experiments which represent yield stress ($A$), strain hardening exponent ($B$), strain rate hardening coefficient ($C$), strain hardening exponent ($n$) and thermal softening exponent ($m$) respectively. Constant $A$ and $B$ can be determined from room temperature tensile tests while m needs elevated temperature tensile tests, and n can be obtained from orthogonal cutting tests. The analytical cutting force from orthogonal cutting simulations with different feed rates had an excellent match with experiment values, which proved the Johnson-Cook constitutive equation to be a reliable method[65].

However, the original Johnson-Cook model only describes the elastic-plastic flow behaviour up to the point of failure. It does not include a damage evolution law to model the progressive degradation of the material strength due to damage accumulation from plastic deformation and fractures. To add the ability to model material failure and damage accumulation in addition to the flow stress behaviour, an extended version of the Johnson-Cook equation, called Johnson-Cook damage model was developed, which is shown as:

$$\varepsilon_f = \left[D_1 + D_2 \exp\left(D_3\left(\frac{\sigma_m}{\sigma_{eq}}\right)\right)\right]\left[1 + D_4 \ln\left(\dot{\varepsilon_p}^*\right)\right][1 + D_5 T^*] \#(13)$$

Where $\sigma_m$ is known as mean or hydrostatic stress, $\sigma_{eq}$is the von Mises equivalent stress and $D_1$ through $D_5$ are the damage constants that weigh the contribution of different stress components, which can be summarized as [66]

| | |
|---|---|
| $D_1$ | Damage due to equivalent plastic strain |
| $D_2$ | Damage due to hydrostatic pressure stress (mean stress) |
| $D_3$ | Damage due to stress triaxiality |
| $D_4$ | Damage due to strain rate |
| $D_5$ | Damage due to temperature |

*Table 1 Explanation of the damage constants used in Johnson-Cook damage equation.*

The damage of an element is defined based on a cumulative damage law, and it can be shown in a linear way as the equation below.

$$D = \sum\left(\frac{\Delta_\varepsilon}{\varepsilon_f}\right) \#(14)$$

in which $\Delta\varepsilon$ is the equivalent plastic strain increment, and $\varepsilon_f$ is the equivalent strain to fracture under the existing supplied parameters of stress, temperature, and strain rate. At the scene of fracture, the material strength drops during distortion, and the relation of stress for the damage growth can be expressed as:

$$\sigma_D = (1 - D)\sigma_{eq} \#(15)$$

with $\sigma_D$ being the damaged stress state. The stress triaxiality and equivalent stress can be calculated from the observation of the plastic behaviour of undamaged material up to necking

formation. The damage constants have been determined on a variety of commonly used alloys such as Inconel 718 and AISI-1045 medium carbon steel [66]. It has been proven to generate reliable predictions on punch tests, ballistics tests and cutting tests at micro (mm) and macro level (cm and above) [67], [68]. Other methods to describe stress/strain function include Swift law, which is an empirical formula expressed as:

$$\sigma = A\left(\epsilon^{plastic} + \epsilon_0\right)^n \#(16)$$

where $A$ is the stress amplitude, $n$ is the hardening exponent, $\epsilon^{plastic}$ is the plastic strain and $\epsilon_0$ is the strain shift parameter. In many practical applications, the magnitude of plastic strain significantly exceeds the parameter $\epsilon_0$ and hence it becomes a simpler power-hardening law:

$$\sigma = A\epsilon^n \#(17)$$

The modified version includes a parameter that accounts for the effect of strain path change and can describe the evolution of the mechanical behaviour in the reload of prestrained materials, which is then written as:

$$\sigma = A\left(\epsilon + \epsilon_{pre}\right)^n \dot{\varepsilon}^m \#(18)$$

in this case, $\epsilon_{pre}$ is the prior plastic strain at the yield point, $\dot{\varepsilon}$is the strain rate and m is the strain rate sensitivity value. The formula is inherently similar to Johnson-Cook equations except that it did not account the temperature influence and damage.

The methods above are used to characterize the bulk properties of materials and are best suited for simulations representing micro or macro scale experiments such as ballistic impact tests and cutting tests. Other fields of research involved simulation of atomic-scale phenomenon, exemplified by the Molecular Dynamics mentioned above, or of the structural changes at grain levels such as Crystal Plasticity Finite Element Methods (CPFEM).

In CPFEM, the material's microstructure is represented by discretizing it into many finite elements, each assigned a particular crystal orientation. Constitutive laws based on dislocation mechanics govern how these crystalline elements deform. This allows the model to capture the anisotropic material response. With the aid of plugins like UMAT (User Material subroutine), CPFEM can be conducted with Abaqus. To simulate the plastic deformation response of a single crystal, the following parameters may need to be defined[69].

| Parameters | Parameter functions |
|---|---|
| Crystal structure | FCC, BCC etc. Defines available slip systems |
| Lattice orientations | Specifies the initial orientation of the single crystal. |
| Elastic constants | Elastic moduli and compliances of the single crystal. |
| Slip systems | Slip directions and slip plane normals for each slip system. Defines shearing mechanism. |
| Yield surface | The criterion for activation of slip systems, e.g. Schmid law. |
| Rate sensitivity | Model for relating slip rate to resolved shear stress. |
| Critical resolved shear stresses (CRSS) | CRSS values for initial slip resistance of each slip system. |

*Table 2 Parameters defined in CPFEM analysis*

Required parameters could be obtained from EBSD results, literature, and online databases such as MATDAT.

More complex problems include the simulation of polycrystalline structures which requires the definition of inter-grain conditions and properties of dozens of grains which can be too exhaustive to be manually defined. Fortunately, there are tools like MTEX2Gmsh that allow the direct generation of meshes from 2D EBSD data [70].

### *2.7.2 Material Properties Prediction*

While properties of the commonly studied materials can be found in the literature (e.g. Inconel 718), individual samples that researchers have could have been manufactured differently (e.g. rolled or extruded) or experienced additional heat treatment which results in it exhibiting significantly different mechanical properties to the ones used in literature. It is therefore critical to obtain material properties for individual samples to facilitate accurate and reliable simulations. In the previous section, orthogonal cutting and tensile tests are identified as common methods to derive the material constants used in the Johnson-Cook model, but it is not always practical for these tests to be performed (e.g. the sample is too small to be machined). Hence there has been continuous effort to develop machine learning models that can predict properties like elastic moduli, yield strength, hardness, and phase transition temperatures based on a material's composition and structure. Inputs include chemical formulas, crystal structures and microstructural parameters etc [71].

In previous work there has been a volume of descriptors used to train the machine learning model for crystalline material property predictions, ranging from simple geometric and lattice information to complex partial radial distribution functions of the internal coordinates. Evans et al. constructed a model with Gradient Boosting Regressor (GBR) that relied on geometric features only, which were related to the local geometry, structure, and porosity of a zeolite [72]. Their model predicted the elastic response of 590448 hypothetical zeolites, and the outcome offered clear evidence of stability trends in porous materials.

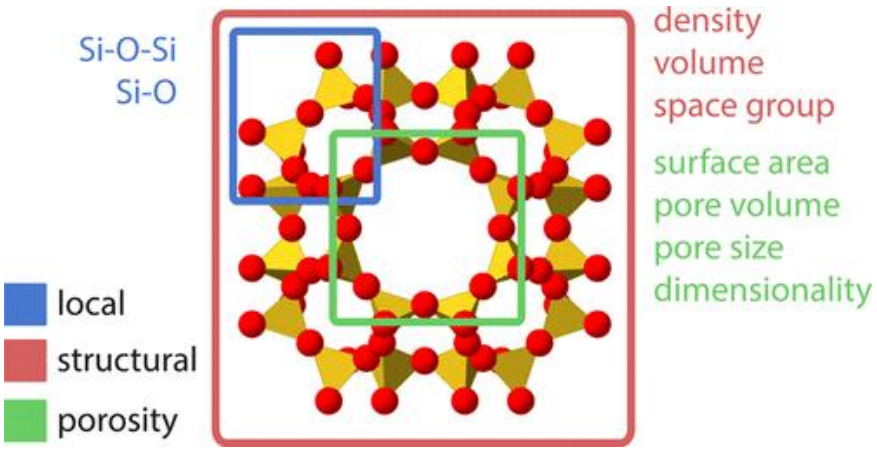



*Figure 12 Summary of the descriptors used in the machine learning model, classified into local, structural, and porosity-related descriptors* [72].

Besides the prediction of molecules or material properties, Machine Learning (ML) can also be used to refine existing computational methods such as improving the exchange-correlation functional in density functional theory (DFT) calculations, for instance, to suggest a better characterization of the weak chemical interactions and highly correlated systems.

The use of machine learning techniques to extrapolate material constants from experimental results represents another promising research direction for predicting material properties. Compared to tensile and cutting tests, indentation experiments can obtain localised, depth-dependent measurements of elastic modulus and hardness using substantially less material. Kim et al. employed an autoencoder neural network trained on finite element methods to predict parameters for the Swift hardening law, a mathematical model used to characterize the strain-hardening behaviour in the regime of large plastic strains, from spherical indentation load-displacement curves [73]. Their approach enabled the extraction of bulk stress-strain behaviour from noisy experimental data. Similarly, Burleigh et al. developed a machine learning model trained with a genetic algorithm to analyse Berkovich nanoindentation load-displacement results. Their model accurately predicted hardness and elastic modulus values for fused silica and aluminium comparable to literature values [74]. It was suggested that when applied to high entropy alloys, the machine learning approach

outperformed traditional least squares fitting, avoiding unphysical contact geometry parameters.

### *2.7.3 Simulating Nanoscratch Test*

2.7.3.1 Macroscale Scratch Test Simulation

Orthogonal cutting simulations prevail among the most extensively modelled scratch test methodologies owing to their prevalence in industrial machining applications. Priyadarshini et al. discovered that variability in the measured Johnson-Cook parameters for AISI 4340 steel could produce up to 68% deviations in predicted cutting forces, with up to 63% and 50% discrepancies in simulated chip morphology and segmentation frequency, respectively [75]. Their analysis also highlighted that friction models exert greater influence on the accuracy of thrust force and temperature predictions at relatively low cutting speeds compared to high cutting speeds. Related research by Daoud et al. determined that adopting a 0° rake angle for measurement of Johnson-Cook constants enables the closest agreement with experimental machining behaviours of Al2024-T3 alloy [76].

In contrast, nanoscratch testing methodologies lack extensive simulation, largely due to their limited direct relevance to industrial processes. However, micromechanical testing combined with simulation on material microstructures offers valuable insights, to help researchers fundamentally comprehend the impacts of grain orientation and phase distribution on mechanical properties and potentially the deformation mechanisms that govern microscale wear.

2.7.3.2 Crystal Plasticity Finite Element Analysis (CPFEM)

CPFEM integrates the crystallographic aspects of individual grains within a polycrystalline aggregate into the finite element framework, thereby enabling the prediction of mechanical behaviour and texture evolution under various loading conditions. Liu et al. developed a fast Fourier transform-based elasto-viscoplastic (EVP-FFT) model to predict micromechanical behaviours and properties of the two-phase α+β microstructures in Ti–6Al–4V alloy [77]. Zhang et al. performed 3D crystal plasticity finite element modelling (CPFEM) to simulate the tensile deformation behaviour of ferritic stainless steels (FSSs). However, their simulations did not capture upper and lower yield points due to excluding dislocation-impurity interactions [78]. Chamani et al. also predicted the adhesive friction coefficient with CPFEM based on the average angle of material flow lines along each side of the contact surface and confirmed that the measurements from the nanoscratch test using the Berkovich tip were highly dependent on the tip orientation [79]. Kareer et al. used CPFEM on (0 0 1) oriented copper single crystals to simulate lattice rotation fields. Their analysis revealed that edge-forward (EF) scratches, face-forward (FF) scratches, and simulated edge-forward scratches produced differing rotation field morphologies and orientations based on the direction of loading relative to tip orientation [80].

2.7.3.3 Molecular Dynamics Modelling

Molecular Dynamics modelling tracks the trajectories of atomic particles by solving their equations of motion and hence is able to simulate more fundamental phenomena such as nucleation of voids and twin grain formation. However, due to the computational resources required, it is often used for simpler experiments such as nanoindentation.

Feichtinger et al. utilized both conjugate gradient and molecular dynamics to analyse spherical indentation on nanocrystalline gold with 5 nm and 12 nm grain diameters. Their work revealed two mechanisms that can provide local stress relief during plastic deformation: 1) Grain boundaries act as reservoirs for dislocations emitted below the indenter; and 2) When the contact area reaches a size equivalent to the grain, grain boundary sliding enables local grain reorganization [81]. Szlufarska et al. also discovered via molecular dynamics that nanoindentation could induce amorphization of silicon carbide, with defect-stimulated growth and coalescence of dislocation loops playing a vital role [82].

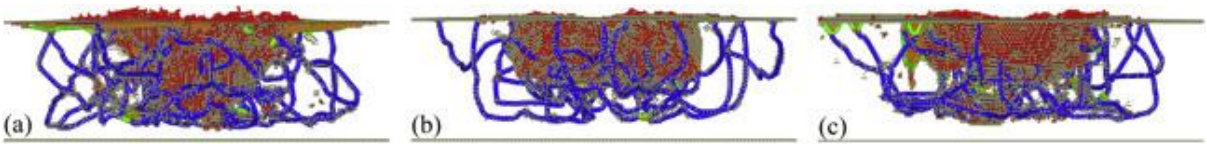



*Figure 13 Defect configurations of monocrystalline 3C–SiC with different crystallographic orientations at maximum loading displacement: (a) (010); (b) (110); (c) (111). Blue lines denote dislocation segments* [83].

The Hall-Petch relationship suggests that the strength and hardness of material would improve with reduced grain size as the interaction between dislocations and grain boundaries during the deformation process intensifies with increased grain boundary density. Nevertheless, theoretical and experimental investigations on polycrystalline diamond and metals with grain size values below the critical value of 10-20 nm have indicated a reverse Hall-Petch relationship [84], [85]. This results from the principal deformation mechanism

shifting from the action of dislocation to grain boundary activities. MD on CuAlNi nanocrystalline showed that with a large grain size, $d$ = 9.55 nm, the propagation of the dislocation and stacking fault mainly took place inside the grain. The dislocations could interact with one another inside the grain to create the network of dislocations or could react with dislocations of the grain boundary. As the abrasive tip further slides, the dislocation can be annihilated by another lattice dislocation or moved into the grain boundary and absorbed, which leads to grain boundary expansion. While with a smaller grain size, $d$ = 4.81nm, the dislocation and stacking fault would not slip inside the grain because of the grain size and the spacing between the grain boundary and the tip is too small [86].

The authors further reported that the average friction coefficient had the downward trend with increasing grain size and average friction coefficient values of polycrystalline CuAlNi alloys were almost larger than the single crystal, which revealed improved adhesion with smaller grain size.

Shugurov et al. performed experimental studies and MD simulation on the polycrystalline Ti, through which they achieved the conclusion that the crystallographic orientation of Ti grains can substantially affect the formation of pile-ups at scratch flanks and residual depth of scratch grooves [87]. It was shown that the most preferred grain orientations in terms of improvement to abrasive wear resistance are those that can promote strain hardening of the material in the scratch groove. It was also concluded that the hardness to elastic modulus ratio ($H/E$ ratio) determined from nanoindentation provided a better agreement with the residual depth of scratch grooves than the $H^3/E^2$ ratio as the strain hardening of the material ahead of the indenter caused by the tangential load is not reflected in the indentation test and higher power would increase the underestimation.

Xu et al. [88] discovered that the deformation phenomena of the superficial layers for both single grain and cross-GB nanocutting was dissimilar to the classic shear-plane theory widely accepted at bigger scales. It was presented that a variable dislocation density would be generated in a progressive manner following the evolution of cutting along a single grain, which was contradictory to the existing knowledge that constant cutting parameters generate constant deformation depth. The authors further demonstrated that the lattice rotation in deformed layers was constrained to a two-dimensional orthogonal plane defined by the normal and cutting directions.

Since molecular simulations involve calculating forces and updating atom positions at femtosecond to picosecond time steps, simulations are generally limited to microseconds or milliseconds of physical time. This requires unrealistically high tip speeds (100 m/s) versus experiments (10 nm/s). Loading rates above certain values in nanoindentation tests were found to significantly impact hardness measurements [89], hence additional scaling laws and theoretical models are needed to interpret simulation results in terms of slower, experimentally relevant speeds.

### *2.7.4 Summary*

Computer simulation has facilitated the understanding of the scratch process by reducing the necessity of time-consuming experiments and providing information that is hard to visualise in real life. Orthogonal cutting simulations can be commonly found in literature but do not fully capture nanoscratch complexity arising from localized material interactions where grain boundary and precipitate phase location (if any), as well as individual grain orientation, are vital to the material's response. Hence nanoscratch lacks comparable extensive modelling, though micromechanical testing provides insights on deformation. At smaller scales, molecular dynamics nanoindentation simulations revealed dislocation movements and grain boundary interactions. However, limitations in computational power restrict molecular dynamics simulations to unrealistic tip speeds. Additional models are needed to translate these outcomes to experimental conditions.

Constitutive equations like the Johnson-Cook model can represent bulk material behaviours for micro- to macro-scale processes. Crystal plasticity finite element modelling (CPFEM) enables explicit simulation of grain-level microstructural interactions for more localized analysis. Accurate modelling requires proper material characterization due to sample variation. Machine learning exhibits the potential for predicting hardening parameters from limited data like nanoindentation curves. This study intends to explore Abaqus's efficacy in simulating nanoscratch experiments combined with machine learning, CPFEM and MD methods, despite their virtues, are time-consuming in nature, which limits their potential in engineering product optimisation, where multiple iterations are often required.

A review of existing literature underscores some pivotal gaps in the application of nanomechanical testing methodologies. While nanoscratch testing has proven valuable for

evaluating thin films and coatings, its application in probing bulk material behaviour—particularly under multi-pass conditions that better replicate repetitive tribological wear—remains underexplored, limiting its relevance to real-world engineering scenarios. It is also noted that, nanoindentation-derived elastic and plastic properties, though fundamental, lack direct compatibility with constitutive models (e.g., Johnson-Cook hardening laws) employed in computational engineering simulations, necessitating empirical approximations that diminish predictive accuracy.

To address these limitations, this thesis proposes a two-sided approach: (1) multi-pass nanoscratch experiments on the bulk nickel-based alloy to understand cyclic wear mechanisms and (2) the integration of machine learning (ML) frameworks to establish correlations between nanoindentation data and plasticity parameters required for finite element analysis (FEA). By coupling advanced nanomechanical testing with ML-driven data translation, this work aims to enhance the interpretability of nanoscale experiments for macro-scale engineering simulations, thereby bridging the gap between fundamental material characterisation and practical tribological or structural applications. The outcomes are anticipated to improve the utility of nanomechanical testing in computational materials design and wear prediction.

# 3. Methods

Wear involves the interaction of several factors, making its study complex and multifaceted. This research begins with the examination of wear at the most fundamental level—single asperity contact, which is crucial for dissecting the intricate dynamics of wear. Nanoindenter is used in this study to control various parameters such as load, sliding speed, direction, and positioning to understand their individual influence on the wear formation.

Atomic Force Microscopy (AFM) is used to characterise the wear tracks which reveals information about the wear mode—whether they are ductile, involving smooth cutting, or brittle, characterized by more abrupt fracturing. This method also accurately measures the depth of the residual wear grooves, which can be subject to inaccuracy in the nanoindenter if surface find is not performed properly.

Focused Ion Beam (FIB) and Lift-out methods are used in conjunction to expose the deformed region beneath the scratch surface without adding mechanical deformation to it. Electron Backscatter Diffraction (EBSD) is applied to gather essential data on the material's grain structure, including orientation, size, and boundary locations. The High-Resolution Electron Backscatter Diffraction (HR-EBSD) extends this analysis to reveal information on the density of geometrically necessary dislocations (GNDs), as well as stress and strain distribution within the material. These insights are indispensable for understanding micro-level mechanisms that underpin the observed macro-level wear phenomena. Abaqus simulations are used to explore Finite Element Analysis’s capability in predicting

nanoscratch experiment outcomes and evaluate variables that can potentially influence scratch formation but are hard to isolate in experiment settings (i.e. tip rotations).

## 3.1 Experiment methods

### *3.1.1 Atomic Force Microscopy (AFM)*

Atomic Force Microscopy (AFM) is a highly versatile technique for imaging and analysing surfaces at the nanoscale. In AFM, a laser beam reflects off the back of the cantilever onto a photodetector that tracks the position of the laser spot. As the tip scans the surface, forces between the tip and sample cause the cantilever to deflect. This deflection leads to a corresponding movement of the laser spot on the photodetector. Typically, the photodetector consists of four quadrants that enable the detection of both vertical and lateral deflections through differential measurements of the laser position on the quadrants. These deflection signals are then converted into tip-sample interaction forces based on the known spring constant of the cantilever. A normal AFM operating software provides different operation modes for the user to select, which often include contact mode and tapping mode.

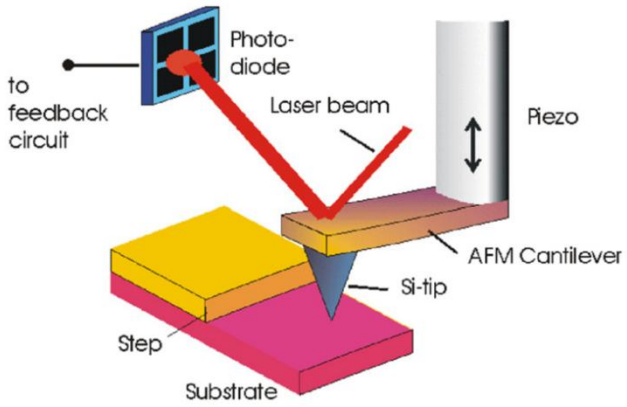



*Figure 14 Schematic diagram depicting main components of an Atomic Force Microscope with an optical beam deflection system* [90].

In tapping mode AFM, the cantilever is driven to oscillate near its resonance frequency by a piezoelectric actuator. As the oscillating tip intermittently contacts the sample surface, tip-sample interactions cause changes in the amplitude and phase of the cantilever oscillation. The photodetector measures the vertical deflection of the laser to track these changes in

amplitude. Additionally, the relative phase of the cantilever oscillation compared to the driving signal can be determined from the deflection signal. Phase shifts to lower values indicate attractive tip-sample interactions, while phase increases signify repulsive interactions. Combining amplitude and phase data enables tapping mode AFM to map topography and distinguish regions of varying composition or mechanical properties.

In contact mode AFM, the tip remains in constant contact with the sample surface during scanning. The static bending of the cantilever is monitored by the photodetector to track topographical changes. Maintaining tip-sample contact enables high resolution profiling of surface features. However, the lateral forces involved can damage soft samples and degrade image quality over time as the tip wears.

ScanAsyst is a proprietary Bruker algorithm that provides automated optimization of imaging parameters and advanced analysis of AFM force curves to map nanomechanical properties. At each pixel, the system fits mathematical models to the approach, contact, and withdraw force segments. This enables extraction of various properties including adhesion, modulus, and electric conductivity. Combining these nanomechanical maps with the topography data provides comprehensive characterization of the sample surface.

While AFM enables exceptional resolution, certain limitations exist. The serial scanning process limits imaging speed and scan sizes. Characterizing deep trenches or steep walls can be difficult. Samples must be mounted well to the stage. Image artefacts can arise from factors like vibration and acoustic noise. Tip-sample interactions induce both elastic and plastic deformations, convoluting measurements. Overall, AFM is best suited for smooth

samples and small scan areas where atomic-scale lateral resolution and pico-Newton force discrimination are required.

The AFM device used in this study is a Bruker MultiMode 8 microscope with a maximum sample size of 15mm diameter x 5mm thickness. The control software is Nanoscope 8.10 provided by Bruker. Tip used is *SCANASYST-AIR* silicon tip on nitride lever with a supported oscillation frequency of 50 to 90 kHz and a spring constant of 0.4 N/m.



*Figure 15 The MultiMode 8 microscope used in this study. Monitor readings indicate the tip deflection in vertical and horizontal directions, as well as the signal strength.*

Owing to constraints related to cantilever bending, the Atomic Force Microscopy (AFM) employed in this investigation is capable of characterizing scratch trenches to a maximum depth of 1.5 µm before the activation of the tip crash protection mechanism. This safety feature limits the maximum normal load that can be applied during experiments. Consequently, this limitation may render the AFM unsuitable for the characterization of scratches that extend through multiple grains vertically.

### *3.1.2 Electron Backscatter Diffraction (EBSD)*

Electron backscatter diffraction (EBSD) is a scanning electron microscopy (SEM)-based microstructural-crystallographic characterization technique that utilizes three main components - a scanning electron microscope, an EBSD detector, and EBSD pattern recognition software. In EBSD, the sample to be analysed is tilted to a high angle, typically 70°, and placed inside the chamber of a scanning electron microscope that is equipped with a field emission gun electron source. This allows for a focused electron beam to strike the tilted crystalline sample surface. When the stationary electron beam interacts with the tilted sample, the diffracted electrons form a pattern that is captured by the EBSD detector, which is usually comprised of a phosphor screen coupled to a low-light camera. The diffraction pattern emitted contains information about the crystal structure and orientation of the phases present in the diffracting volume of the sample. The patterns are then analysed by EBSD pattern recognition software, which identifies the material phases and crystal orientations by matching the experimentally obtained patterns to simulated patterns generated for known crystal structures.

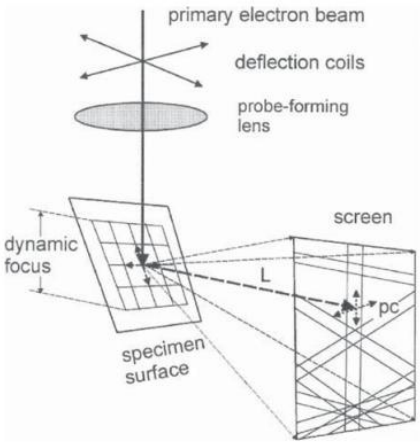



*Figure 16 Raster grid on a tilted specimen surface with digital beam scan* [91] .

By collecting EBSD patterns across a scanning raster on the sample and analysing them via the software, automated acquisition of crystallographic orientation maps over a selected region of interest is enabled. Proper sample preparation is critical for enabling diffraction during EBSD analysis. When the focused electron beam strikes the properly prepared sample surface, the resulting diffraction patterns are captured by the EBSD camera and indexed by the specialized software, allowing crystallographic orientation data to be mapped across the scanned region.

The EBSD devices used in this study are Zeiss EVO and Zeiss Merlin. The EVO is equipped with Bruker Quantax e-Flash1000 high-speed EBSD system that supports a resolution up to 120x120 pixels while the Merlin has a maximum EBSD resolution of 1600 x 1200 pixels. The EVO uses a tungsten source while the Merlin has a field emission gun. Both pieces of equipment use ESPRIT software provided by Bruker that allows automatic recognition of phases and grains.

### *3.1.3 High Angular Resolution Electron Backscatter Diffraction (HR-EBSD)*

HR-EBSD is a novel method to characterize the strain, stress and GND distribution in materials from EBSD patterns. HR-EBSD measures lattice strains and rotations by analysing shifts in EBSD patterns collected across a map, compared to a reference pattern [91].
The EBSD pattern is split into many regions of interest (ROIs) and cross-correlation analysis determines the relative shift of each ROI. By analysing a volume of patterns, the shifts in the ROIs reveal the underlying deviatoric strain tensor and lattice rotations. The reference can be from an unstrained region or a simulation. This analysis transforms the 2D pattern shifts into full 2D strain and rotation tensor fields [92]. The dislocation density can be determined from lattice curvature using Nye's dislocation tensor [93].

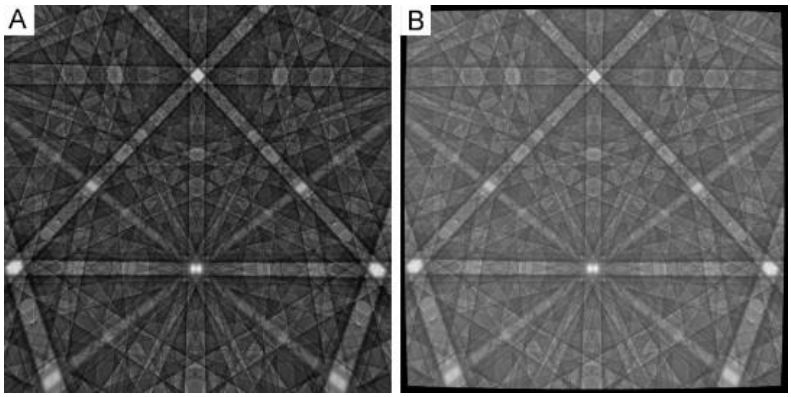



*Figure 17 Dynamically simulated Si patterns (a) undistorted; (b) distorted with a=10−7 ['pinch in' can be noticed at the pattern edges]* [94].

Reported accuracy of HR-EBSD strain mapping attains elastic strain sensitivity around $10^{-4}$ [95]. The spatial resolution depends on the EBSD step size which can be chosen based on the user's feature of interest. A coarse step size would help quickly assess the overall crystal texture, while a smaller step size together with longer exposure time may better suit the

analysis of fatigue crack path, which requires higher sensitivity in intragranular misorientation measurement.

### *3.1.4 Nanoindenter*

3.1.4.1 Instrument Design

A nanoindenter is an instrument that can perform indentation and scratch testing with millinewton and nanometre measurement accuracy. The design and functionality vary with producer and models. The G200 and XP used in this study are both manufactured by KLA and come in similar layout.

In G200, all of the electronic connectors necessary to run the instrument are panel-mounted on the gantry, which is manufactured to be extremely rigid and provides the system with high load stiffness (LFS). Enclosed in the gantry assembly are head assembly, sample tray, motion system and aperture levers that can adjust the view of sample surface.

In the head assembly, the loading column is surrounded by a coil assembly consisting of electromagnetic coils that move the column up and down using magnetic force. The loading column does not contact the coils directly. Instead, it is connected to the outer frame by a parallel leaf spring system. This allows the column to move axially while being laterally stiff, guiding the indenter tip perpendicular to the sample surface. Capacitance gauges are located above and below the loading column to monitor its displacement. As the column moves, the capacitance changes, enabling displacement measurement with sub-nanometre resolution. The tip is located at the bottom of the load column and can be Berkovich, spherical or custom-designed. As it penetrates the surface, the displacements are recorded by the gauges and used for load-displacement curve generation.

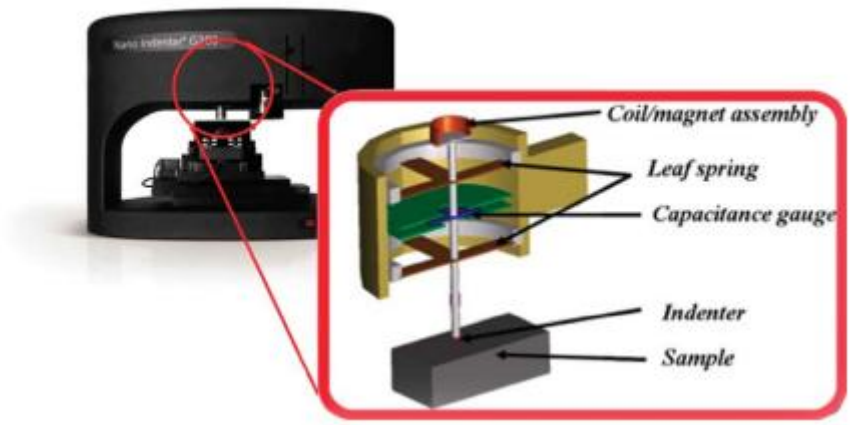



*Figure 18 The Agilent Nano Indenter G200 and a cross-sectional diagram of the XP-NMAT [96].*

The sample tray is driven by a motorized X-Y stage with lead screw drives to position the specimen underneath the indenter tip. Stepper motors allow movement down to sub-micron accuracy. The environment temperature is maintained at 18 degrees Celsius, and the gantry assembly is enclosed in a noise and thermal isolating chamber to minimise the thermal drift and vibration.

### 3.1.4.2 Nanoindentation Process

Nanoindentation tests have been employed to derive localised hardness and elastic modulus. Continuous Stiffness Measurement (CSM) which superimposes a small oscillation on the primary loading signal and measures the amplitude and phase of the oscillation during the indentation process. As the indenter tip presses into the material, the contact area increases, which increases the stiffness. By measuring the change in oscillation amplitude during loading and unloading, G200 can provide measurements of the sample modulus across penetration depth.

A standard nanoindentation follows a five-step procedure [97].

0. The indenter slowly approaches the test surface at the specified surface approach velocity until contact is detected based on an increase in stiffness relative to the support springs.
1. The indenter pushes into the surface up to the maximum load. The loading rate is determined from the time taken to reach max force and the value of the max force.
2. The maximum force is held constant for peak hold time. This allows materials to stabilize creep before unloading.
3. The indenter is withdrawn at the same rate as loading until the force decreases to 10% of the maximum.
4. This reduced force is held to measure the drift rate.
5. The indenter is fully retracted from the sample.

The list of inputs required in G200 indentation setup is provided:

| | |
|---|---|
| Surface approach velocity (μm/sec) | Speed of indenter movement during surface approach stage |
| Delta x, y for test locations (μm) | Indentations are made in the 'Indenter to scope calibration' step to accurately position the tip relative to the optical scope. |
| Maximum load (mN) | The maximum load the indentation will reach before unloading. |
| Allowable drift rate (nm/sec) | Thermal stability criteria that is required to be met before initiating testing, usually defined at 0.5 nm/second. |

| | |
|---|---|
| Peak hold time (sec) | Length of time that maximum load is held. |
| Time to load (sec) | Length of time for loading segment |
| Surface approach distance (μm) | The distance above the surface that the indenter begins “looking” for the surface. |
| Surface approach sensitivity (N/m) | The criterion that the indenter uses to decide if it has contacted the surface |
| Poisson's ratio | Of the sample |

*Table 3 Required inputs for nanoindentation setup [97].*

The area function of the Berkovich tip is calibrated using Oliver and Pharr method [6] shown in section 2.4.1.2,

$$\sqrt{A_c} = \frac{\sqrt{\pi}}{2\beta(C - C_f)E_R} \#(19)$$

and the frame compliance $C_f$ can be deducted from contact stiffness and load-displacement data using equation:

$$S = \frac{dP}{d\delta} = \frac{1}{\frac{d\delta}{dP} - C_f} \#(20)$$

For materials like fused silica, where Poisson's ratio is known, the actual contact area can be corrected by accounting for lateral deformation shown by equation below. The actual material response of the tested material considering pile-up or sink in can be observed with other techniques exemplified by AFM.

$$A_{true} = A_{measured} \times (1 - v^2) \#(21)$$

Where $A_{true}$ is the corrected contact area, $A_{measured}$ is the initially calculated area and $v$ is the Poisson’s ratio of the material.

The frame compliance and area function are derived by indenting fused silica and the Berkovich tip used in this study has a tip modulus of 1141 GPa with Poisson's ratio of 0.07. The frame has a stiffness of 7.65 x $10^6$ N/m, and the area function of the tip used is determined as

$$A_C = 24.5h_c^2 - 588.36h_c^1 + 22579h_c^{1/2} + 32942h_c^{1/4} \#(22)$$

The first term being 24.5 suggests that this tip is relatively undamaged.

Calibration on multiple materials is preferred as fused silica may not represent the behaviour of harder, softer, or more ductile materials, which was not completed in this study due to time constraint.

3.1.4.3 Nanoscratch Process

Nanoscratch is similar to nanoindentation process except that the tip moves laterally after the maximum load has been reached with a first profile and final profile made based on the three-pass procedure mentioned in section 2.5. Before and after the scratch segment, a pre-scan and a post-scan equal to 20% of the scratch length to align the position of each segment. Nanosuite software will obtain 'penetration depth' based on the difference between z-displacements in the first profile and z-placements in the scratch segment. Inputs required and visualisation of the complete process are given below.

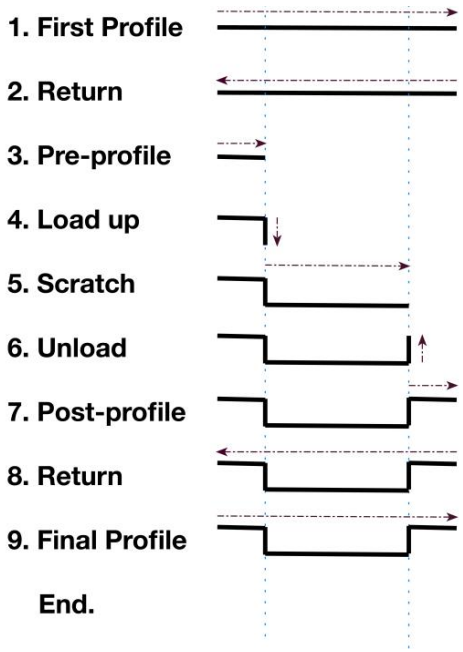



*Figure 19 Three-pass nanoscratch procedure for a constant load scratch test [97].*

| | |
|---|---|
| Scratch length (μm) | The total length of the scratch |
| Scratch velocity (um/s) | Speed of scratch |
| Scratch orientation (deg) | The angle of the scratch from 0° to 360° where zero is a vertical scratch starting at the top of the sample |
| Maximum scratch load (mN) | Load applied during the scratch |
| Cross profile length (μm) | Length of the profile perpendicular to the scratch position |
| Profiling velocity (μm/s) | Speed of the indenter during the profiling |
| Profiling load (μN) | Force for the profile segments |
| Number of cycles | Number of times that the scratch will be repeated at the same position |

*Table 4 Required inputs for nanoscratch setup.*

During the multi-pass test, surface find will be performed before the onset of each full cycle to ensure that the penetration depth is always calculated based on the distance to the original surface instead of the residual groove from the last cycle.

At the end of the nanoscratch test, side profiling can be performed to capture the cross-sectional profile of the residual scratch. This is done by scanning the surface with the same indenter tip. The scan is conducted perpendicular to the scratch direction at a user-specified location, typically at 50% of the total scratch length, though this can be adjusted based on the test requirements. A profiling load, typically $\leqslant 0.1$ mN, is applied during the profiling scan to minimise additional deformation on the surface. The resulting cross-sectional profile provides measurements of residual depth and pile-up height on both sides of the scratch, which are used for further analysis of deformation and material flow behaviour.

### *3.1.5 Focused Ion Beam*

The focused ion beam (FIB) instrument resembles a scanning electron microscope except that a heavy ion source is used instead of accelerated electrons for imaging and processing of the sample surface. Gallium is the common ion source as it has a melting point close to room temperature and does not vaporise easily. Due to Gallium's atomic weight, it can physically sputter away atoms from the sample through momentum transfer which allows milling with nanometre precision [98].

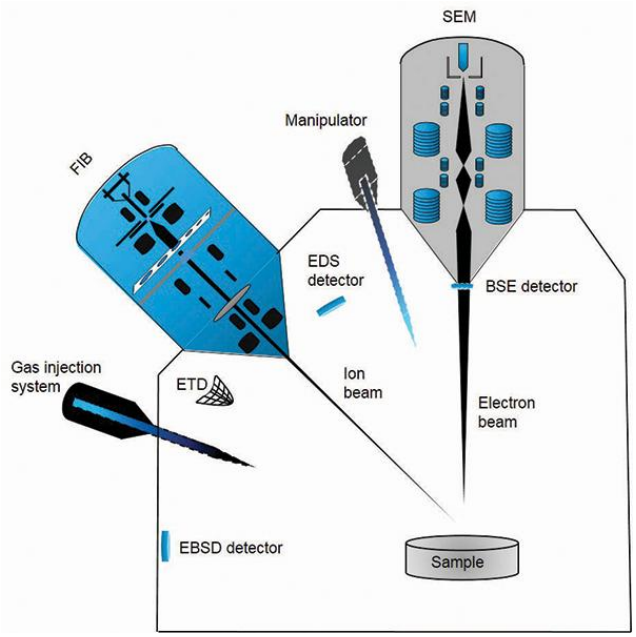



*Figure 20 Schematic diagram of a FIB used in junction with an SEM. Manipulators are also commonly found on FIB [99].*

A typical FIB system consists of an ion source, ion column, sample stage, detectors, and gas injection systems. The gas injection system contains sources like Platinum and Carbon that can be deposited on the sample surface to increase electric conductivity and protect the desired features from being damaged by the ion source.

The FIB used in this work is a Zeiss Auriga equipped with a Gemini electron column operating between 100V and 30kV, capable of resolutions of 1.0 nm at 15 kV. The SEM

column is coupled with a Gallium source FIB that operates between 1kV and 30kV with a range of ion beam currents between 1pA and 20nA. It is also equipped with an OmniProbe nanomanipulator that allows micron-size samples to be collected from the material surface. Lift-out is prepared by creating a ‘slice’ of material containing the deformed area by annihilating the surrounding material with FIB and retrieving it with the OmniProbe nanomanipulator. Settings and a more detailed operation procedure will be further explained in the experiment section.

## 3.2 Simulation method

### *3.2.1 Abaqus*

Abaqus, developed by Dassault Systems, is a software suite for finite element analysis and computer-aided engineering. It has been widely applied in industries including aerospace, automotive, and biomechanics.

Key components of Abaqus include:

- **Step**: This defines phases in a simulation, such as loading or thermal changes. Steps organize the analysis, allowing for specific conditions and analysis types (e.g., linear or nonlinear) to be applied to different stages of the simulation.
- **Sections**: These define material and geometric properties in different regions of the model. Sections allow for the representation of varied material properties and geometries, crucial for simulating in-homogenous and anisotropic materials.
- **Field Outputs**: The results from simulations, including stress, strain, and temperature distributions. Field outputs are vital for identifying potential failure points and optimizing design for performance and safety.

Abaqus's framework, with Steps, Sections, and Field Outputs, provides a suitable toolset for nanoscratch simulations as it allows the users to gradually increase the complexity of the system, for example taking friction heat into consideration, and to fully understand the influence of individual variables before incorporating them together to mimic experiment settings. It also allows the visualisation of the information that is hard to be observed experimentally (i.e. equivalent plastic strain).

### *3.2.2 Machine Learning*

This work also uses machine learning to explore the possibility of recognising material's strain hardening behaviour directly from nanoindentation results. The training process is performed with TensorFlow platform developed by Google.

TensorFlow operates on the principle of dataflow graphs, where a graph represents the computational architecture of a machine learning model. In this context, nodes represent mathematical operations, ranging from simple arithmetic operations to more complex functions. Edges symbolize the tensors (multi-dimensional arrays of data) that flow between these operations. Tensors are the core data structure in TensorFlow, designed to efficiently represent and manipulate large datasets typical in machine learning.

In this study the TensorFlow platform is used to train Artificial Neuron Network (ANN), and the user only puts in the design parameters (number of layers, activation type, training batch sizes etc.) and then the TensorFlow would conduct trainings and optimisation automatically.

# 4. Hardness Measurement of Nickel-based Alloys

## 4.1 Introduction

Nickel-based alloys are extensively used in various industries owing to their corrosion resistance. This section examines the nanoindentation and nanoscratch properties of different nickel-based alloy grades to investigate the relationship between their tensile strength, indentation hardness, and scratch hardness. The materials examined in this study were commercially pure nickel (Ni201), oxidation-resistant nickel alloy (Ni600), and nickel-based superalloy Inconel 718 (Ni718). Ni201 and Ni600 were obtained in 10 mm diameter round bars, with the Ni600 having undergone additional annealing at 800°C for 3 hours for grain size growth. Ni718 was acquired in 4 cm diameter round bars. Ni201 and Ni600 were sectioned into 3 mm thick slices using an IsoMet low-speed saw with IsoCut fluid to minimize heat generation during cutting and preserve the original crystal structure. Due to its size and hardness, Ni718 was cut into 3 mm slices using high-speed table saws and subsequently divided equally into 4 fan-shaped samples. All three types of nickel alloys were acquired from Special Metal Alloys.

Ni201 is a commercially pure nickel product that has at least 99.6% nickel, along with small quantities of carbon (≤0.15%), manganese (≤0.35%), silicon (≤0.35%), sulphur (≤0.01%), copper (≤0.25%), and iron (≤0.40%) as per ASTM B162 standards [100]. The material features a single-phase FCC crystal structure and a uniform microstructure made of equiaxed grains. Ni201 is processed by undergoing hot rolling between 1100 °C and 1200 °C, then annealed within the same temperature range to reduce internal stresses and achieve consistent grain size distribution. This process of annealing leads to a reformed microstructure which

promotes uniform mechanical properties throughout the material. Ni201 has a yield strength of 400 MPa, according to the manufacturer's spec sheet.

Inconel 600, referred to as Ni600 in this study, is composed of about 72% nickel, 14–17% chromium, and 6–10% iron, along with small amounts of carbon (≤0.15%), manganese (≤1.0%), silicon (≤0.5%), copper (≤0.5%), and sulphur (≤0.015%) [101]. Adding chromium improves resistance to oxidation and corrosion, while iron increases mechanical strength and has a yield strength of 637 MPa [101]. Ni600's microstructure consists of a sole-phase FCC solid solution in which chromium is evenly dispersed within the nickel matrix. During annealing or ageing, chromium tends to migrate and combine with carbon, leading to the formation of chromium-rich carbides, particularly $Cr_7C_3$ and $Cr_{23}C_6$. The heat treatment procedure includes hot rolling at temperatures between 1000 °C and 1150 °C, then solution annealing within the range of 1000 °C to 1100 °C, and finally quick quenching [102].

Ni718 (Inconel 718) is a nickel-based superalloy strengthened by precipitation, consisting of 50–55% nickel, 17–21% chromium, 4.75–5.5% niobium and tantalum, 2.8–3.3% molybdenum, 0.65–1.15% titanium, 0.2–0.8% aluminium, with the remainder being iron (about 17%). Trace elements consist of carbon (<0.08%), manganese (<0.35%), silicon (<0.35%), phosphorus (<0.015%), sulphur (<0.015%), cobalt (<1.0%), copper (<0.3%) and boron (<0.006%) [103]. The microstructure is often made up of a gamma (γ) matrix which is strengthened by gamma prime (γ′—$Ni_3$(Al, Ti)) and gamma double prime (γ″—$Ni_3Nb$) precipitates dispersed in the matrix. The Inconel 718 used in this study experienced standard heat treatment provided by the manufacturer which it was solution annealed at around 1050°C followed by rapid water cooling, with precipitation hardening at 760°C for 10 hours, furnace cooled to 649°C and held at the same temperature for a total ageing time of 20 hours,

followed by air cooling. The volume fraction of the precipitate and its distribution have not been measured due to equipment constraints.

For surface preparation, all samples were first ground with SiC papers (Grade 120 to Grade 2500) to flatten the surface, then polished with diamond solutions (particle size from 9 μm to 1 μm) to remove defects, and finally re-polished with colloidal solution to obtain an extremely flat, deformation-free surface for EBSD analysis. As noted by Li et al., surface undulation and impurity can significantly influence indentation size effects [104], so a flat and clean sample surface was critical for subsequent testing.

EBSD scans at 200x magnification were performed for undeformed sample surfaces with Zeiss Merlin, shown in Figure 21. The grain size is defined as the Equivalent Circle Diameter (ECD), which is the diameter of a circle with the same area as the measured grain. The average grain sizes are 20 μm, 100 μm, and 8 μm for Ni201, Ni600, and Ni718, respectively, as shown in Figure 22.

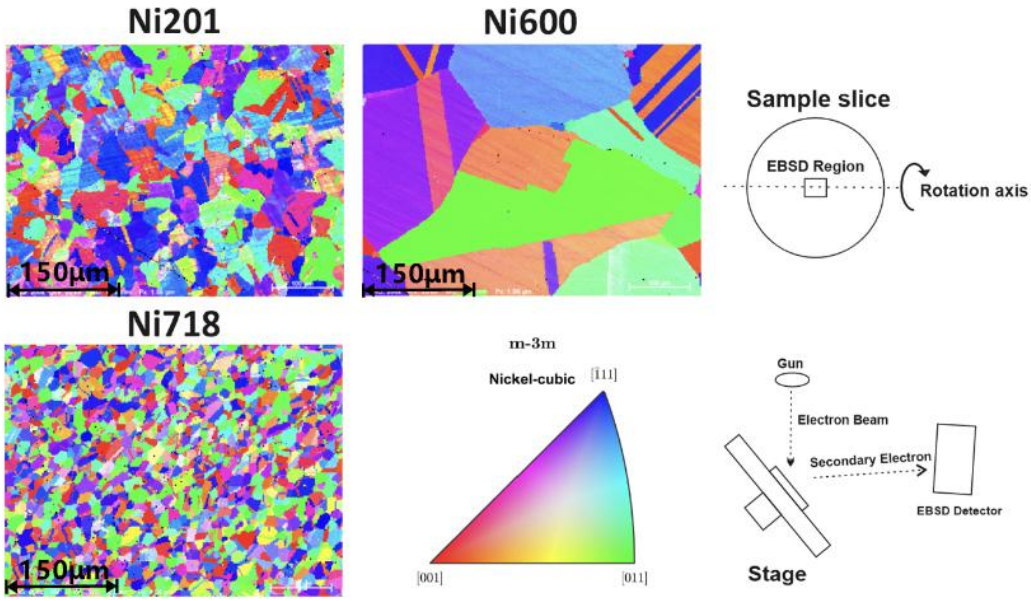



*Figure 21 IPFz (coloured) maps of Ni201, Ni600 and Ni718. Each colour represents a grain of same crystal orientation. Images are taken at central area of sample slices mounted on pin stubs positioned at 70-degree tilt to the EBSD scanner. Rotation axis for tilting and relative position of the sample to EBSD detector are shown on the right.*

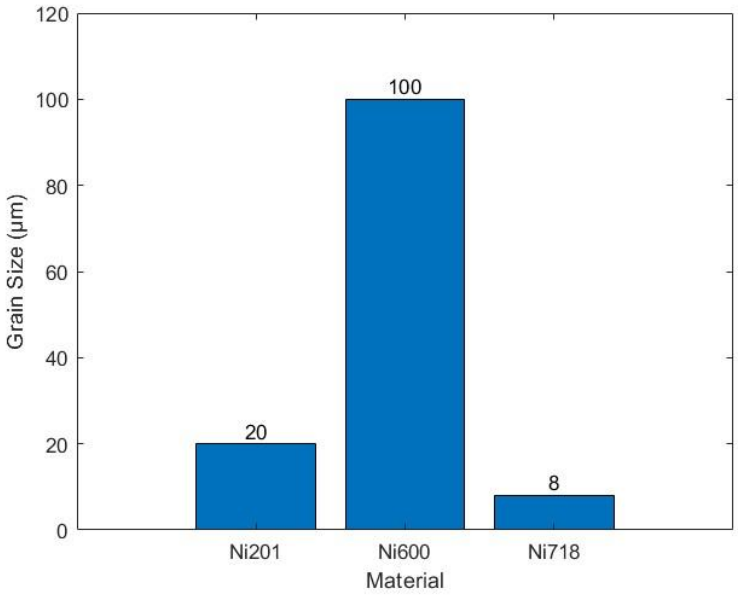



*Figure 22 Average grain size of the material tested in this thesis. Grain size is defined as the diameter of a circle with the same area as the measured grain.*

## 4.2 Nanoindentation Measurements

Nanoindentation hardness testing was conducted using XP and G200 instruments with continuous stiffness measurement (CSM) and a Berkovich tip at a strain rate of 0.05/s. The surface approach velocity was set to 10 nm/s from 1000 nm above the surface, and the depth was limited to 2000 nm. The harmonic displacement targets were 2 nm with a frequency target of 45 Hz, which was the default Nanosuite software configuration. Poisson's ratios were obtained from manufacturer data sheets, with a value of 0.31 used for Ni201[100] , and 0.29 used at room temperature for Ni600 and Ni718 [101], [103]. Nine indents arranged in a 3 x 3 grid were performed on each material with a spacing of 50 µm. Adequate spacing was necessary to prevent the plastic deformation from one indent from affecting subsequent measurements.

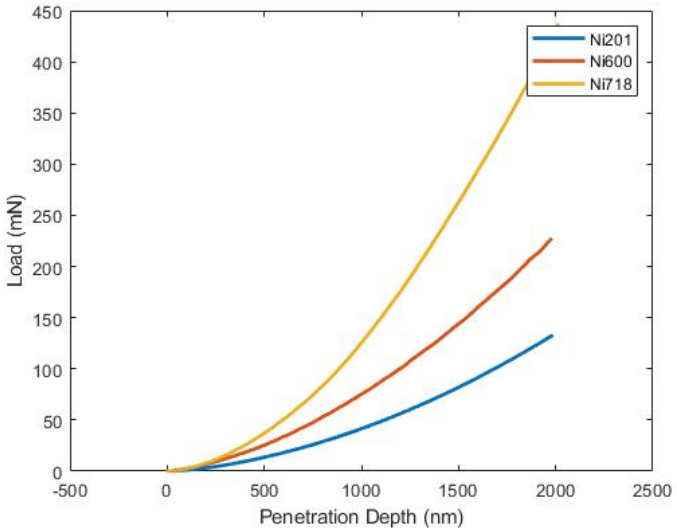



*Figure 23 Load and displacement measurements for CSM indents on Ni201, Ni600 and Ni718 using Berkovich tip with G200 nanoindenter.*

In Figure 23, it can be observed that the average maximum loads at 2000 nm penetration depth were 140 mN for Ni201, 219 mN for Ni600 and 435 mN for Ni718.

Prior to nanoindentation hardness calculations, the pile-up height needs to be measured. Failure to account for pile-up leads to an underestimation of the contact area and, subsequently, an overestimation of the hardness value since indentation hardness is calculated as the applied load divided by the contact area. The penetration depth from the nanoindenter output is measured using the surface height found in the 'surface find' step. The material extruded above the initial surface (pile-up) is also part of the contact area and provides support to the tip.

To measure the pile-up profile in nanoindentation, 1200 nm indents were made on each of the materials. The indentation depth used for pile-up correction is better set at the same depth used for measurement (2000 nm), but it exceeds the height measurement range of the AFM used in this study and therefore an indentation depth at the maximum range has been selected. However, only the AFM scans from Ni600 and Ni201 could be obtained for pile-up correction as the Ni718 sample used was too bulky to fit into the AFM machine. The AFM machine was available after the sample preparation and measurements were completed and its size constraint regrettably has not been anticipated during the sample preparation process. 3 indents were made on each of the materials, and 2 line profiles were taken on each indent.

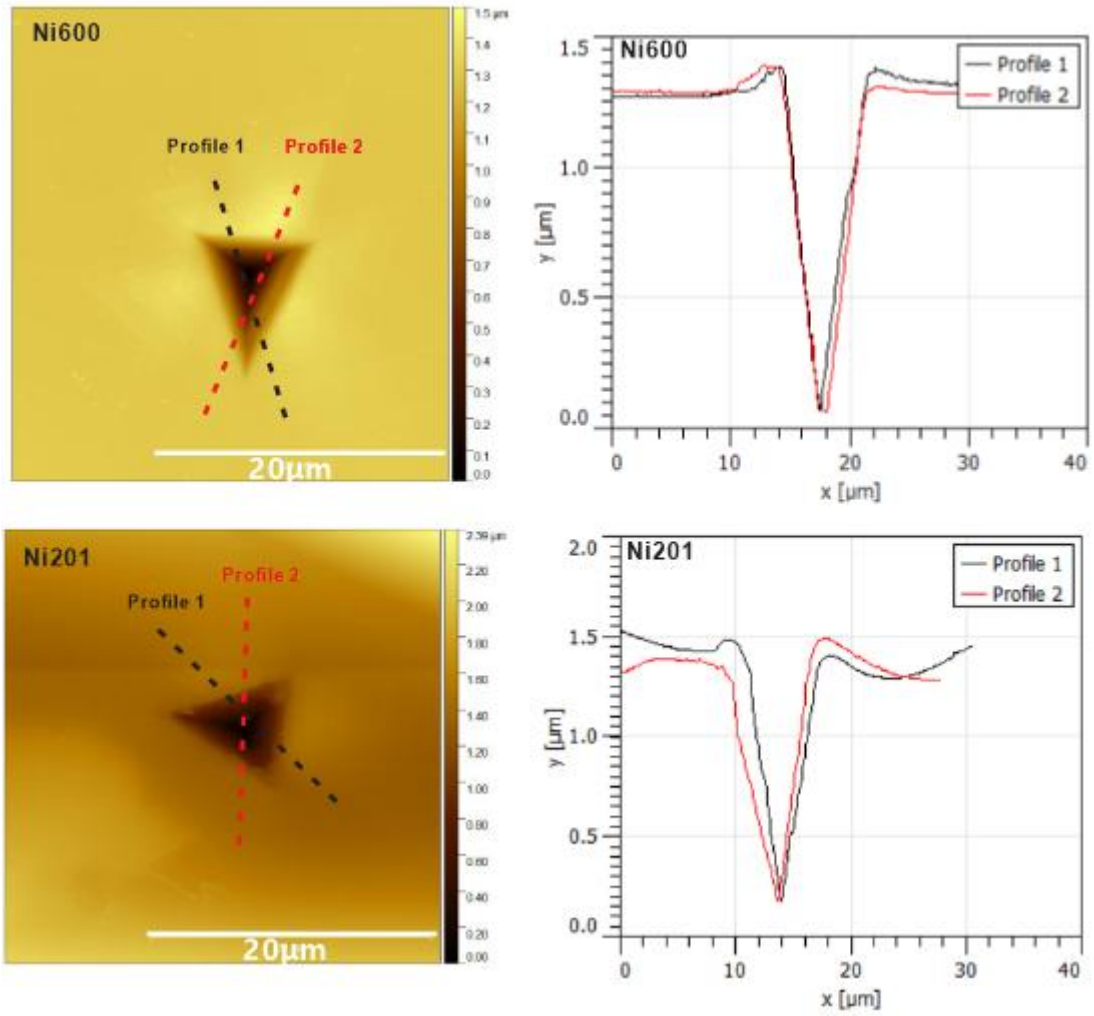



*Figure 24 AFM scans of 1200 nm deep Berkovich nanoindentation mark on Ni201 and Ni600. Graphs on the right show line depth profiles of 1 indentation mark on each material. Lines are taken parallel to the tip edge and pass through the lowest point of indentation mark. 3 indents were made on each material type.*

30 × 30 µm AFM scans were performed on 1200 nm-deep Berkovich indents made on Ni201 and Ni600 as shown in Figure 24. Pile-ups can be clearly observed on all three sides, appearing as bright regions rising above the sample surface. Line profiles were taken parallel to the indentation edges, crossing the tip apex location (the lowest point). Since grain orientation can affect pile-up formation in different directions, the pile-up-to-depth ratio was calculated using the average pile-up height from the three sides and indentation on different grains. The recorded mean pile-up heights were 89 nm and 132 nm with standard deviations

of 32 nm and 46 nm, which gives depth correction ratios of 1.08 ( $\frac{1200+89}{1200}$) and 1.11 ($\frac{1200+132}{1200}$) for Ni600 and Ni201 respectively.

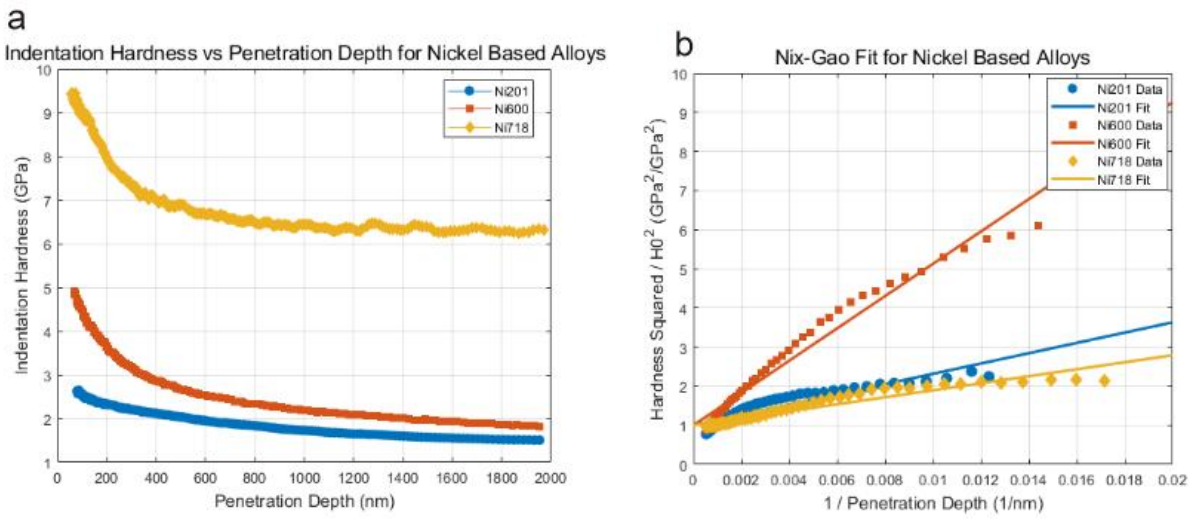



*Figure 25 Berkovich nanoindentation hardness measurement along penetration depth on Ni201, Ni600 and Ni718 using CSM method. To account for pile-up, the penetration depth is multiplied by 1.08 and 1.11 for Ni600 and Ni201 respectively which was determined from AFM nanoindentation pile up height measurements. Displacement into surface is measured with reference to the sample surface level before indentation. Nix-Gao fit has been performed on three materials tested to highlight plasticity size effects (graph b). Ni718 data is uncorrected for pile-up due to instrument constraint.*

Area function of the Berkovich tip used was obtained using CSM indentations on fused silica, shown by:

$$A_C = 24.5h_c^2 - 588.36h_c^1 + 22579h_c^{\frac{1}{2}} + 32942h_c^{1/4} \#(23)$$

However, as fused silica does not form pile-up [35], the indentation depths on Ni600 and Ni201 were corrected using depth correction ratios of 1.08 and 1.11, respectively. The pile-up corrected nanoindentation hardness (Ni201, Ni600) and uncorrected hardness (Ni718) measured across a 2000 nm penetration depth range are shown in Figure 25a.

In Figure 25a, similar nanoindentation hardness changes have been observed for all three alloys tested. The average hardness output from nanoindenter measurements was 6.9 GPa,

2.5 GPa, and 1.95 GPa. Nix and Gao fits have been performed on three alloys, as shown in Figure 25b. The $H_0$ (indentation hardness at infinite depth), which reflects the material's hardness when the indentation depth is large enough that the hardness no longer increases with depth, for Ni718, Ni600, and Ni201 was 6.345 GPa, 1.957 GPa, and 1.659 GPa, respectively. The characteristic lengths *h*, representing the depth below which the indentation size effect is significant, were 89.5 nm, 412.8 nm, and 131.5 nm for Ni718, Ni600, and Ni201, respectively. Results suggest that the indentation size effect diminished at relatively shallow depths for simple Ni201 and Ni718 while it persisted to a higher depth for Ni600. For other single crystal metals in literature, Silver has an $H_0$ ranging between 0.34 GPa to 0.36 GPa with characteristic length *h* between 430 nm to 750 nm and Copper has an $H_0$ ranging between 0.581 GPa to 0.834 GPa with *h* ranging between 464 nm to 1600 nm depending on their prior heat treatments and crystal orientations [39]. A threshold of 20% deviation from the depth-independent hardness ($H_0$) was applied to evaluate the threshold depth at which the ISE becomes less significant. and the threshold depths calculated for Ni201, Ni600 and Ni718 were 299.029 nm, 938.294 nm, and 203.419 nm respectively.

Differences in composition, phase distribution, grain sizes, and plasticity size effects are potentially the main factors affecting nanoindentation hardness trends and indentation size effects among the three alloys tested. Ni718 showed the highest hardness potentially due to its precipitation-hardening phases, which effectively hinder dislocation movement, along with its small grain size of 8 μm, creating an abundance of grain boundaries that serve as obstacles to deformation. Ni600, having fewer strengthening precipitates and a grain size of 100 μm, displayed a stronger indentation size effect with a higher peak-to-stabilized hardness ratio; the larger grains minimized the impact of grain boundaries at greater depths. Ni201, characterized by its high-purity nickel composition and a moderate grain size measuring 20

μm, demonstrated the lowest hardness levels. The sudden rise in hardness at low penetration depths for all alloys was because of the plasticity size effect, in which greater strain gradients near the indenter tip result in more geometrically necessary dislocations [93], thus increasing hardness.

### *4.2.1 Indentation Hardness*

The average hardness and modulus of three alloys were obtained using the measurements from the 100 nm to 2000 nm region, which was assumed to be away from the region affected by the plasticity size effects, surface roughness and contaminants. Nine indents with 50 μm spacing were made on Ni201 and Ni718. Spacing was increased to 100 μm for Ni600 due to significantly larger grain sizes. Contact area corrections were applied. Shown in Figure 26, Ni201 had a mean hardness of 1.94 GPa with a standard deviation of 0.08 GPa. Ni600 had a mean hardness of 3.58 GPa with a standard deviation of 0.18 GPa. Ni718 had a mean hardness of 6.72 GPa and a standard deviation of 0.19 GPa. Ni201 exhibited a smaller variance in nanoindentation hardness due to its simpler composition (nearly pure nickel) and more uniform microstructure, while the indentation hardness for Ni718 likely was overestimated as lacking pile-up correction potentially underestimated the true area of contact.

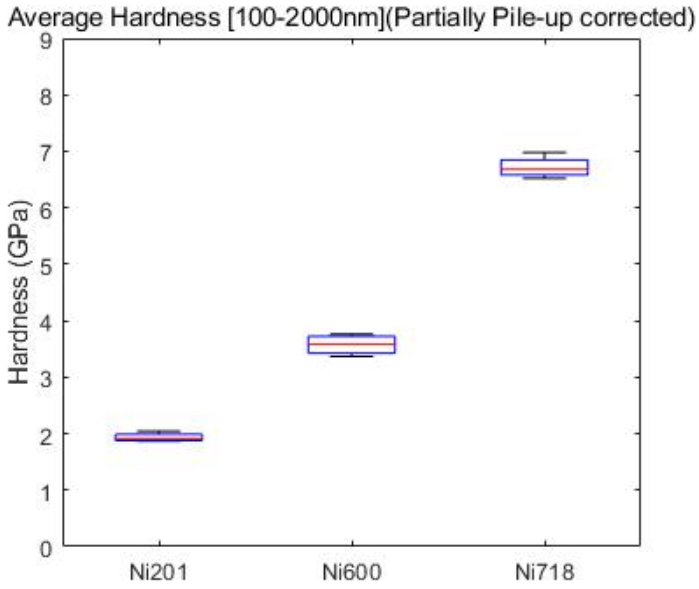



*Figure 26 Nanoindentation hardness was measured for three nickel-based alloys, Ni201, Ni600 and Ni718, using 9 Berkovich tip indents for each alloy with G200 nanoindenter. Red line represents the mean value. The blue box shows the 25 to 75 percentile regions, and the black lines indicates the maximum and minimum values. Ni201 and Ni600 are pile-up corrected using AFM measurements with Ni718 uncorrected due to instrument constraint.*

### *4.2.2 Elastic Modulus*

Presented in Figure 27, the mean modulus measured for Ni201, Ni600 and Ni718 after pile-up corrections were 204.8 GPa, 212.2 GPa and 227.0 GPa with standard deviations of 7.65 GPa, 6.22 GPa and 9.1 GPa, respectively. Values from the manufacturer data sheet are 207 GPa for Ni201 [100], 206.8 GPa for Ni600 [101] and 200 GPa for Ni718 [103]. Compared to literature values, the mean values from G200 nanoindentation were 1.1 % smaller, 2.6% and 11.35% bigger for Ni201, Ni600 and Ni718 respectively. Overestimation of Ni718 modulus potentially indicated that pile-ups were formed during the indentation tests and the contact areas were underestimated.

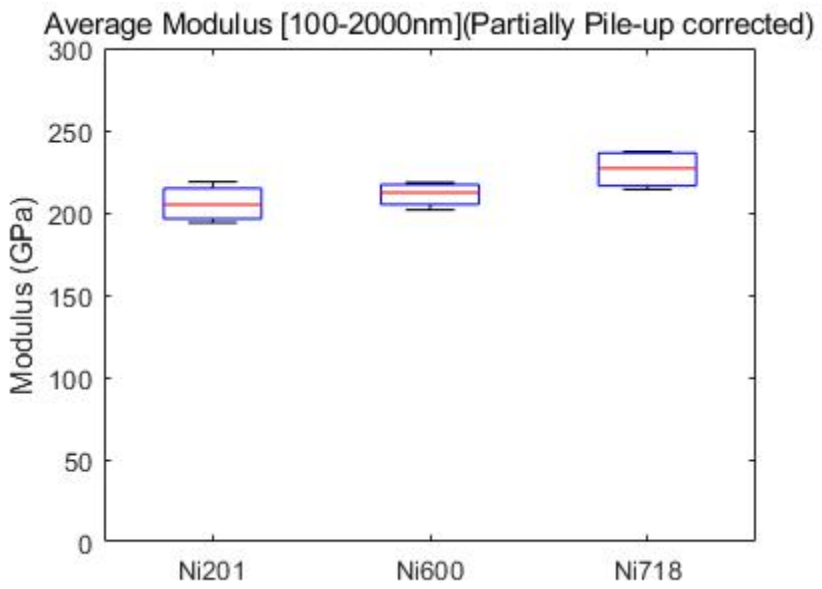



*Figure 27 Average elastic modulus was obtained for Ni201, Ni600 and Ni718 using Berkovich tip nanoindentation to 2000 nm penetration depths with G200 nanoindenter. 9 indents were made for each alloy and contact areas for Ni201 and Ni600 were corrected using the pile-up measured under AFM scan. Contact areas were uncorrected for Ni718 due to instrument constraints.*

The frame stiffness was also corrected for each test until a horizontal line was obtained for the measurements at regions away from the surface (frame stiffness corrections used range from 2950000N/m to 4250000N/m). This correction was essential as the frame stiffness was calibrated using fused silica mechanically mounted to the stage while the sample was bonded

with resin to sample mount, which is compliant, and the compliance was subject to thickness variation. As shown in Figure 28, modulus measurements were higher for Ni718 than the other two materials, which was likely due to a lack of pile-up correction, as suggested above. Modulus measured between 0 nm to 100 nm was excluded as they were subject to the fluctuations caused by the tip blunting, surface contaminants, oxide layer and surface roughness which did not reflect the elastic properties of the substrate material.

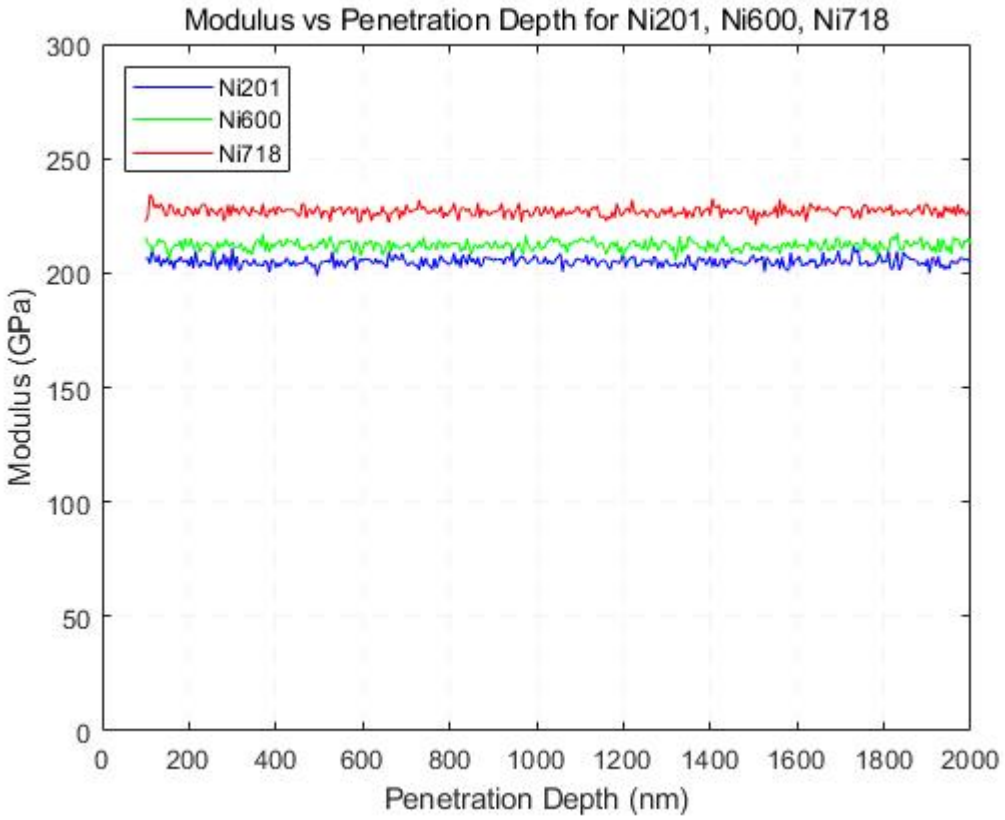



*Figure 28 Modulus measurement across 100 – 2000 nm penetration depth with CSM method using Berkovich tip on G200 nanoindenter. Frame stiffness has been manually calibrated until a horizontal line was reached for each material.*

### *4.2.3 Discussion*

Nanoindentation of the Ni201, Ni600 and Ni718 alloys revealed indentation size effects - hardness decreased with greater penetration depths, aligning with the Nix-Gao model [39] that relates size dependence to strain gradient mechanisms where shallow contacts exhibit higher geometrically necessary dislocation densities. The order of indentation hardness is Ni201, Ni600, Ni718, going from softest to hardest, aligning with the yield strengths provided in the manufacturer's spec sheet: 400 MPa for Ni201, 637 MPa for Ni600, and 1275 MPa for Ni718 [100], [101], [103]. This aligns with what is expected from material strengthening mechanisms: pure nickel (Ni201) has the lowest hardness when indented because it lacks alloying elements and phases that help strengthen it. Ni600, which is a blend of nickel with chromium and iron, exhibits greater hardness compared to pure nickel due to solute strengthening, in which the additional elements cause distortion in the nickel crystal lattice and enhance resistance to dislocation movement. Ni718 gains strength from both solute strengthening from key alloying elements such as chromium, molybdenum, and niobium—and potentially phase strengthening, caused by the precipitation phases that effectively block dislocation movement, although the phase strengthening mechanism is subject to further verification as the distribution and volume percentage of the precipitate phases were not observed in this study.

The stabilised modulus measurement across tested penetration depths for all three materials can be explained by the nickel matrix’s dominant role in governing elastic behaviour. The elastic modulus, determined primarily by the face-centred cubic nickel matrix’s atomic bonding, should remain largely unaffected by precipitates or dilute solid-solution atoms due to their relatively low percentage. It should be recognised again that the distribution of the precipitate phase has not been measured, which would require characterisation tools of higher

resolution. This stability does not contradict the pronounced hardness difference in materials tested caused by solute/precipitate effects because hardness reflects localised resistance to plastic deformation—where obstacles like precipitates disrupt dislocation motion—while modulus characterises bulk elastic stiffness, which depends on collective atomic interactions that remain coherent across the matrix-dominated microstructure despite these localised strengthening features. The variance in modulus measurements across different locations potentially arises from experimental factors such as surface roughness, oxide layers, or contaminants at shallow indentation depths that can distort contact mechanics. Clustered precipitates or solute-rich regions may transiently elevate modulus in specific indents.

It should also be noted that the pile-up corrections used are subject to improvement, as the indentations for pile-up correction made on Ni201 and Ni600 were made at 1200 nm depth which was the maximum depth that the AFM used in this study can probe while they should be at the same indentation depth used for indentation hardness measurements. Failing to consider pile-up would underestimate the true contact area and result in an overestimation of the modulus and indentation hardness shown in Ni718 measurements.

## 4.3 Nanoscratch Hardness

### *4.3.1 Berkovich Tip Measurements*

20 mN normal load single-pass scratches were performed for the three alloys to obtain scratch hardness for both edge-forward and face-forward tip orientations. Loads need to be sufficient to penetrate deep enough into the surface and minimise the effect of surface unevenness caused by grain morphology variation. Scratches were repeated 4 times in each alloy at a scratch speed of 1 μm/s at the length of 40 μm.

For each nanoscratch pass, the normal load was increased to the set value at the pre-determined starting point and the stage would be driven by the rotor at user-set speed and scratch angle to initial lateral movement. After the scratch is finished, the tip would unload at the endpoint and retract. Figure 29 shows the load vs scratch distance together with penetration depth vs scratch distance output from nanoindenter for the 20mN edge-forward tests for 3 materials. A pre-profile at profiling load (30 μN) with 20% of the scratch distance (8 μm) was made, after which the tip was loaded to the desired load at 8 μm and started moving laterally for 40 μm to a total distance of 48 μm and retract to profiling load, then a post-profile with profiling load at 30 μN is performed for another 8 μm (20% of scratch distance) to a total distance of 56 μm. After the scratch procedure completes, the tip returns to the start position at 0 and carries a final profile scan of total distance (56 μm) to characterise the residual groove along the scratch direction. A schematic of this complete process has been given in the method section.

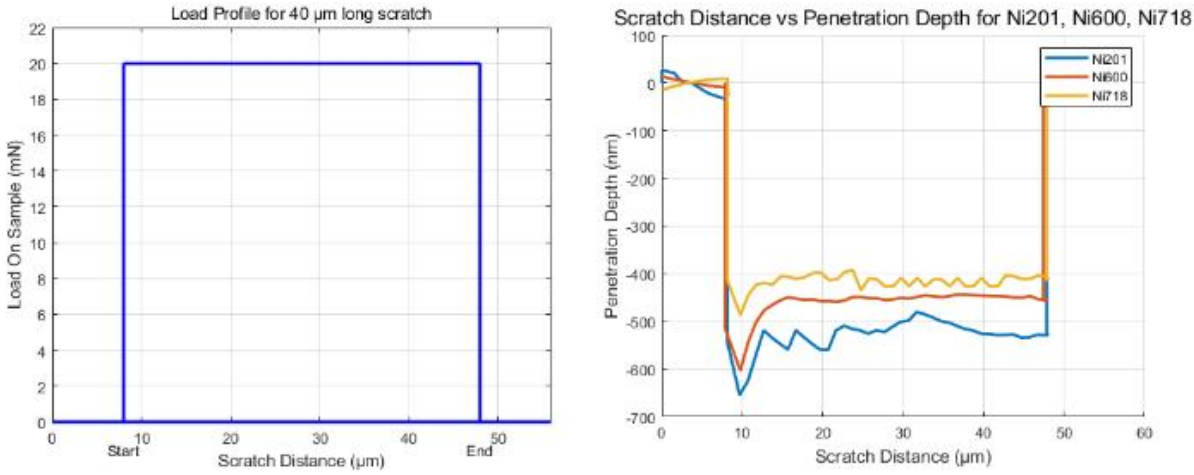



*Figure 29 Load vs Scratch Distance and Penetration Depth vs Scratch Distance output from G200 nanoindenter for the 40 µm long nanoscratches (8 µm to 48 µm) on Ni201, Ni600 and Ni718. Pre-profile, post-profile and final profiles are made at profiling load (30µN), which is shown by the blue line close to the x-axis.*

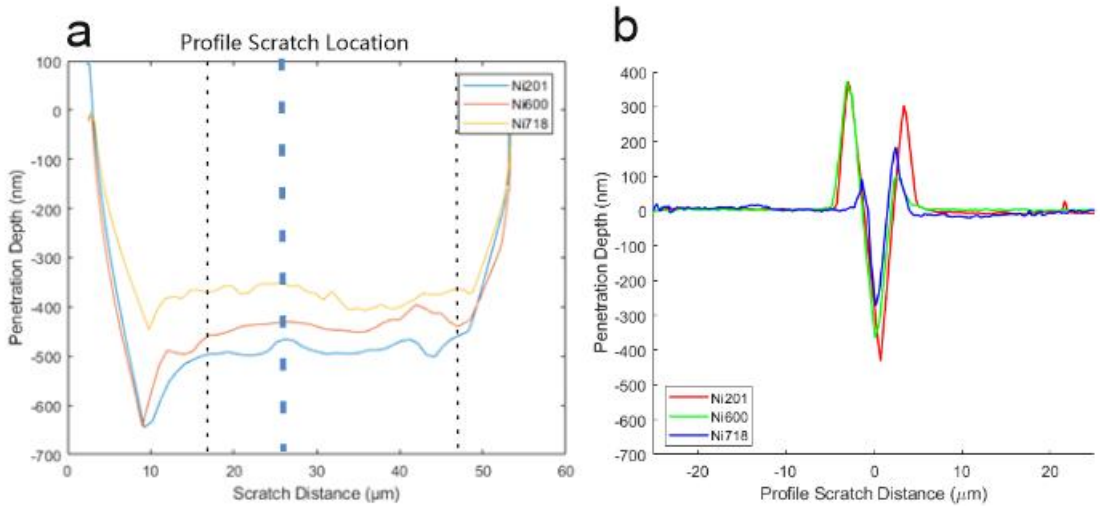



*Figure 30 a) Final-profile scans of residual groove along the scratch directions of 20 mN normal load edge-forward nanoscratch tests of 40 µm length (8 to 48 µm) on Ni201, Ni600 and Ni718.Penetration depths averaged between black dotted lines, where steady scratch occurs(20 µm after the scratch start to the end of scratch), were used for contact area and subsequent calculations. Scratch starts at 8 µm, and tip retracts at 48 µm. Maximum dip in depth is reached at 10 µm and the titled line at the beginning and the end reflect Berkovich tip geometries) cross-sections of residual groove taken at mid-scratch (shown by the blue dotted lines).*

Figure 30 shows the final-profile scans of the Berkovich tip edge-forward nanoscratches made on alloys tested. With the same 20 mN normal load, the tip penetrates the deepest in Ni201 and shallowest in Ni718, a trend similar to that found in indentation tests. The average penetration depths were 410 nm, 465 nm, and 583 nm for Ni718, Ni600 and Ni201. However, this average depth from Nanosuite output includes the depth from the loading section, which is indeed an indentation depth. To isolate the scratch depth from the indentation depth, the

depths after the tip ‘climb-out’ from the indentation mark were used for scratch hardness calculation, a method that was also adopted by Kareer et al. [35], which means that the penetration depths used for following scratch hardness calculations are taken from 10 μm after the scratch start, as marked by the region between dotted lines in Figure. To illustrate more clearly, for a scratch of 40 μm long, the region between 10 μm to 40 μm would be used for calculation while it is 10 μm to 100 μm for a 100 μm long scratch. The climb-out phenomenon is present in nanoscratch tests as when the indenter tip starts moving laterally, the back of the tip loses contact with the substrate, and the tip has to penetrate deeper to maintain the support.

Similar to nanoindentation hardness measurement, the nanoscratch hardness measured needs to be corrected for pile-up which forms additional resistance to the tip movement during the scratch process. Pile-ups have been measured by performing cross-profile scans on the residual groove of the scratches, in which the indenter tip starts moving laterally at profiling load at the middle of the scratch groove. It should be noted that only one cross profile can be performed for each of the scratches in the nanoindenter, which may not reflect the changes in the pile-up height along the scratch direction while the penetration depths used were averaged. As the scratch is repeated 4 times for each direction on each material, cross-profiles are equivalently sampled at different grains, which would reflect the grain variations. A schematic of how edge-forward and face-forward scratches are performed and where cross-profiles are taken is shown in Figure 31

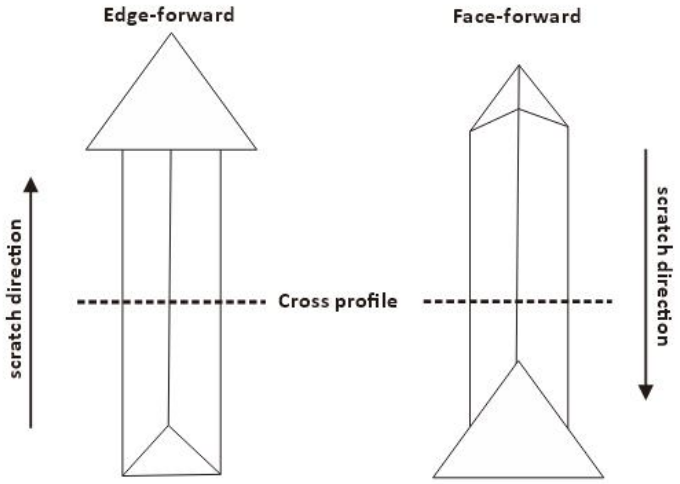



*Figure 31 Schematic of edge-forward and face-forward nanoscratch procedure using Berkovich tip. Cross-profile scans are performed at 50% of the scratch distance in a direction perpendicular to the scratch direction at profiling load to determine pile-up heights.*

This study applies the projected area in the normal direction to determine the contact area as the nanoindenter does not have a lateral force output, which the projected area in the scratch direction would be more pertinent to. In edge-forward scratches, two front facing facets are assumed to be in contact with the material ahead while it is only one facet for face-forward

scratches, which makes contact area 2/3 of the contact area used in indentation tests for edge-forward scratches and 1/3 of the indentation contact area in face-forward scratches, as illustrated in Figure 32.

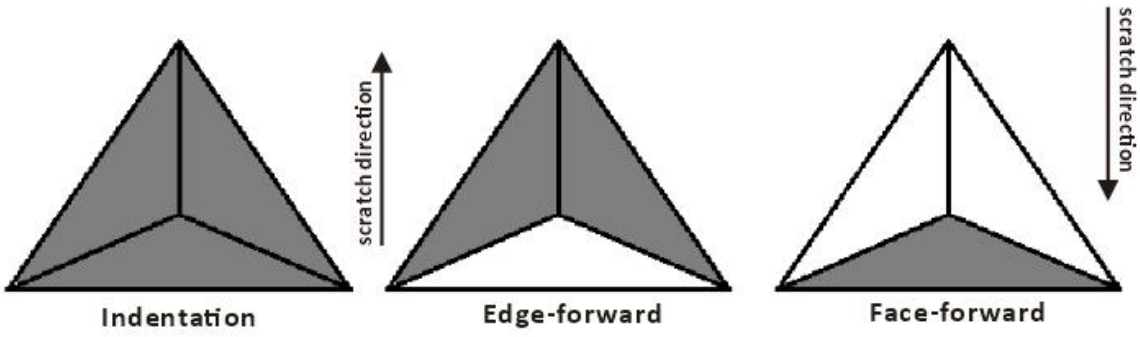



*Figure 32 Schematic of how contact areas are assumed in the edge-forward and face-forward scratches. Projected areas from normal directions are used, and face-forward is one-third of the indentation area with two-thirds in edge-forward scratches.*

Pile-up corrections were made with a similar method to nanoindentation tests in which the pile-up heights on two sides of the groove obtained from the cross-profile scan were averaged and added to the average penetration depth to obtain a total depth that would be used to project area calculations. To illustrate, in Figure 30, for 20mN edge-forward scratch on Ni201, the total penetration depth was 893 nm (583 nm + 310 nm) while it was 775 nm and 547 nm for Ni600 and Ni718 and corrected contact area was 2/3 of the indentation projected area derived with area function.

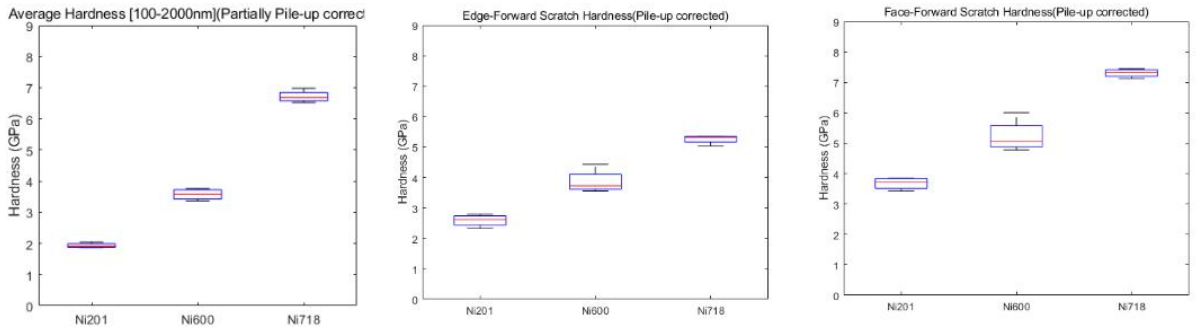



*Figure 33 Scratch hardness measured for Ni201, Ni600 and Ni718. Scratches were made for both edge-forward and face-forward directions using Berkovich diamond tip at 20 mN normal load at scratch speed of 1 μm/s for scratch lengths of40 μm. Each direction has been repeated for 4 times for each material. Nanoindentation hardness are displayed on the left to be compared with scratch hardness corrected with pile-up heights obtained from cross-profile scans.Ni718 indentation hardness is not corrected due to instrument constraint.*

Presented in Figure 33, the mean hardness values for edge-forward and face-forward 20 mN normal load nanoscratches of Ni201, Ni600, and Ni718 alloys were calculated. For edge-forward scratches, the mean hardness of Ni201 was 2.66 GPa with a standard deviation of 0.15 GPa, Ni600 had a mean hardness of 3.70 GPa with a standard deviation of 0.29 GPa, and Ni718 showed a mean hardness of 5.31 GPa with a standard deviation of 0.14 GPa. For face-forward scratches, Ni201 exhibited a mean hardness of 3.56 GPa with a standard deviation of 0.26 GPa, Ni600 had a mean hardness of 5.03 GPa with a standard deviation of 0.32 GPa, and Ni718 showed a mean hardness of 7.29 GPa with a standard deviation of 0.17 GPa. An increase in scratch hardness was observed when transitioning from edge-forward to face-forward scratches across all tested alloys.

Generally, compared to nanoindentation hardness, scratch hardness values remained higher for all three materials, while the difference is bigger for face-forward scratches. For Ni201, the EF scratch hardness was approximately 33.1% higher, and FF was 63.5% higher than the nanoindentation hardness. For Ni600, the EF hardness showed a 13.6% increase, while FF exhibited a 40.9% increase. However, for Ni718, the edge-forward scratch hardness was approximately 21.0% lower than the nanoindentation hardness, whereas the face-forward hardness was 8.5% higher. A smaller difference between the EF scratch hardness and nanoindentation hardness was expected as both mainly involve the tip extruding the surrounding material, while FF involves the tip traversing through the strain-hardened material formed at the front facet. Ni600 exhibited higher variability in both indentation hardness and scratch hardness compared to the other two materials. This was attributed to its significantly larger grain size. Over a scratch length of 40 microns or an indentation depth of 2000 nm, the measurements for Ni600 reflected the characteristics of only a few grains

locally. In contrast, for Ni201 and Ni718, the testing region encompassed a larger number of grains, thus more accurately reflecting the overall material properties. As for the observation that the indentation hardness of Ni718 was higher than its edge-forward scratch hardness, this was likely because the pile-up correction for Ni718 was not performed during the indentation tests due to instrument constraints. This lack of correction may have resulted in an underestimation of the actual contact area, leading to an overestimated indentation hardness value.

Figure 34 shows final profiles along the scratch direction for 20 mN scratch tests on Ni600 in both edge-forward and face-forward directions. Smaller side pile-ups were observed for face-forward scratches. A more detailed comparison of groove formation in both directions will be presented in later

chapters.

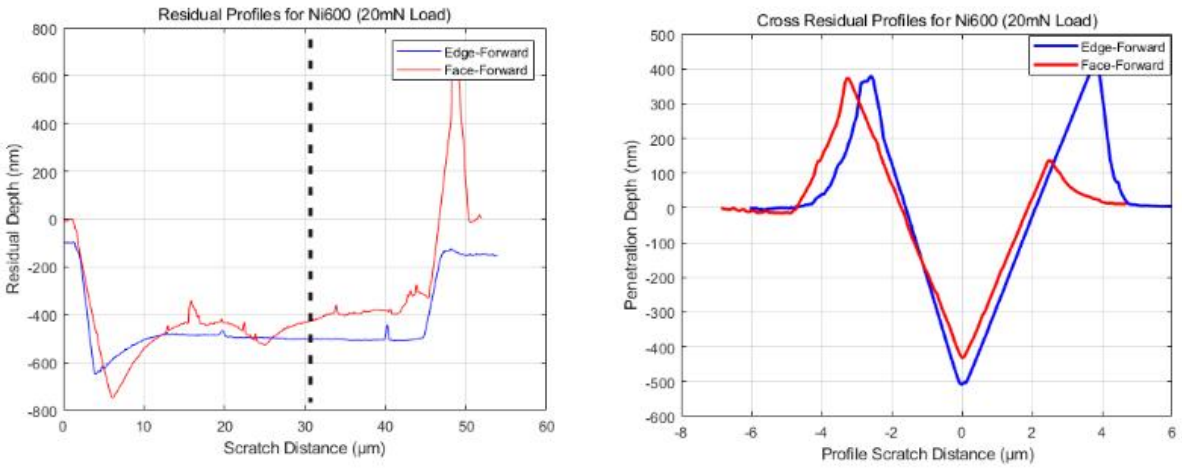



*Figure 34 Final profiles along the groove direction and across the groove width for 20mN load edge-forward nanoscratches on Ni600. Dotted line indicates the position that the cross-profiles were taken.*

### *4.3.2 Discussion*

Scratch hardness is found to be higher than indentation hardness for both tip orientations due to the variances in the deformation mechanisms that are activated. During the nanoscratch test, the material experiences significant plastic deformation and work hardening along the scratch line, while the nanoindentation test mainly assesses the material's reaction to a concentrated force on a small surface area. The face-forward scratch orientation with a Berkovich tip shows greater scratch hardness than the edge-forward orientation because of variations in contact area and pressure distribution. When focusing on the front-facing direction, only one-third of the surface is considered when determining hardness, resulting in increased pressure in a specific area and hence, a higher recorded scratch hardness. On the other hand, the edge-forward positioning uses 2/3 of the contact surface, leading to a greater contact area, reduced localized pressure, and subsequently decreased measured scratch hardness. The variation in how the material rotates around the tip also impacts the difference in measured hardness: for face-forward tip orientation, the material is mainly pushed to the two sides of the tip and doesn't hinder subsequent movement, while in edge-forward orientation, the material rotates beneath the tip, requiring the tip to traverse through the hardened material.

Side pile-up heights are found to be higher in edge-forward than face-forward, with both being significantly higher than the pile-up in nanoindentation tests, in which the pile-up heights were about one-tenth of the penetration depth. This result aligns with expectations, as only material extrusion occurs on three sides during indentations, while the material is relocated to two sides during the scratch process. Scratch formation mechanisms could vary due to differences in alloy composition and the applied normal loads. While the pile-up was assumed to conform to the Berkovich indenter shape during the dynamic scratch process, it is

possible that more complex geometries are involved, such as hemispherical formations or material flow revolving to the rear of the tip.

## 4.4 Morphology of scratches with low normal loads

It is well known that stress distribution is influenced by the geometries of load-bearing components due to the differences in stress-concentrating factors. Plastic strain $\varepsilon_p$ is related to the indenter angle and in the scenario of Berkovich edge-forward scratches, the tip apex is expected to have higher stress concentration than the flat sides walls on top of it, and for shallower indents/scratches, this stress-concentrated region is relatively closer to the stress-free surface and it is worth investigating whether this could change the groove morphology.

### *4.4.1 AFM Analysis*

On the same Ni600 grain, 4 sets of 4 edge-forward scratches under different loads were made. Scratches were made parallel to each other. Loads used were 0.5 mN, 2 mN, 10 mN and 20 mN. AFM scans were performed on one of the scratches in each load at a 1hz scan rate and 256 x 256 resolution.

AFM scan results shown in Figure 35 suggest that edge-forward scratches at all four loads exhibit sharp uniform groove edges on both sides. AFM cross profiles shown in Figure 36 indicates that the residual grooves maintain the self-resemblance of a perfect Berkovich tip, and a sharp triangle was still observed at the bottom 100 nm region.

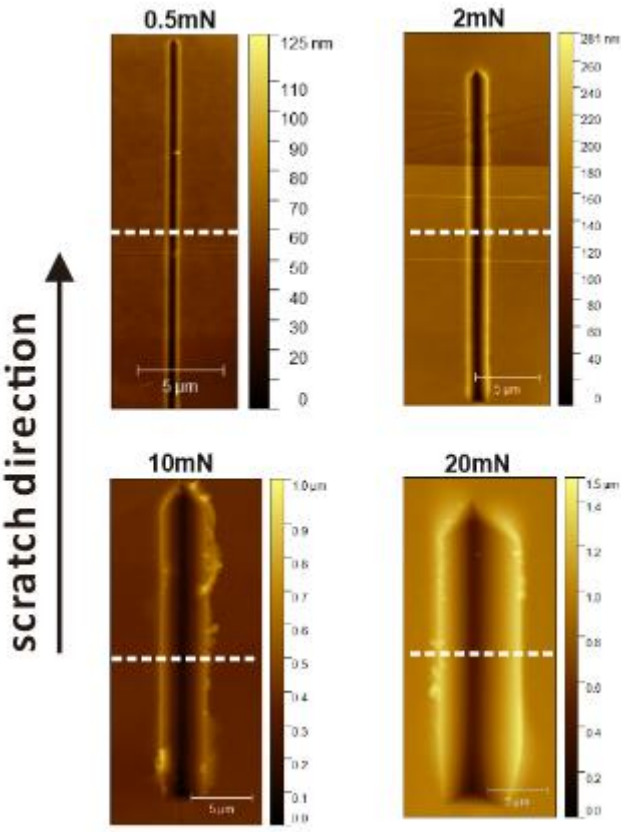



*Figure 35 AFM scans of edge-forward Berkovich tip scratches made with 0.5 mN, 2 mN, 10 mN and 20 mN loads using G200 nanoindenter on same Ni600 grain. Dotted lines indicate where the AFM line cross profiles are taken.*

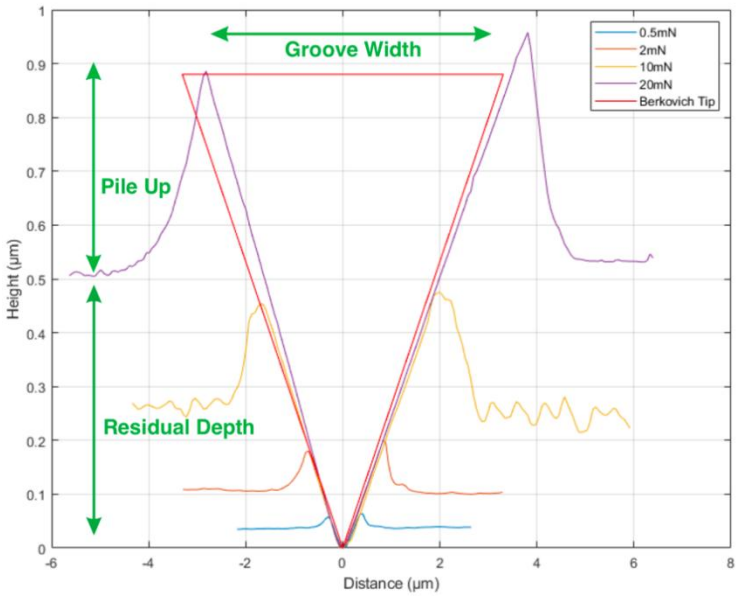



*Figure 36 AFM line cross profile of edge-forward scratches made with 0.5 mN, 2 mN, 10 mN and 20 mN loads on Ni600 using G200 nanoindenter. Data are shifted on the y-axis so that the lowest points from each scratch coincide and a perfect Berkovich tip is plotted as a reference for the residual groove shape.*

It was also observed in Figure 35 and Figure 36 that the pile-ups on the right-hand side of the groove were consistently higher, which could be caused by tip not being perfectly vertical to the sample surface and grain being anisotropic.

### *4.4.2 Hardness Measurements*

The average penetration depths for 0.5 mN, 2 mN, 10 mN and 20 mN edge-forward scratches are 31.7 nm, 97.5 nm, 276.3 nm, and 494.8 nm, respectively. The average penetration depths are obtained by averaging the depth after the climb-out region from the nanoindenter output and averaged again for repeated experiments at the same scratch load. Pile-up heights are obtained from the cross-profile scan in the nanoindenter and averaged for the 4 scratches performed under the same load, for which the mean values were 29 nm, 77 nm, 222 nm, and 415 nm, respectively. Scratch hardness was calculated using the same method illustrated earlier in which the averaged penetration depths are added to their corresponding pile-up heights to obtain a corrected indentation contact area and assumed two-thirds of them as scratch contact area in edge-forward directions [97]which led to an average scratch hardness of 7.8 GPa, 6.4 GPa, 5.3 GPa and 4.0 GPa respectively as shown in Figure 37a. A decrease of scratch hardness with increased penetration depths was observed, similar to the Indentation Size Effect observed in nanoindentation tests shown in section 4.2. Figure 37 indicates that the EF scratch hardness exceeds the indentation hardness measured at the same depths on the same grain, consistent with the findings in previous sections.

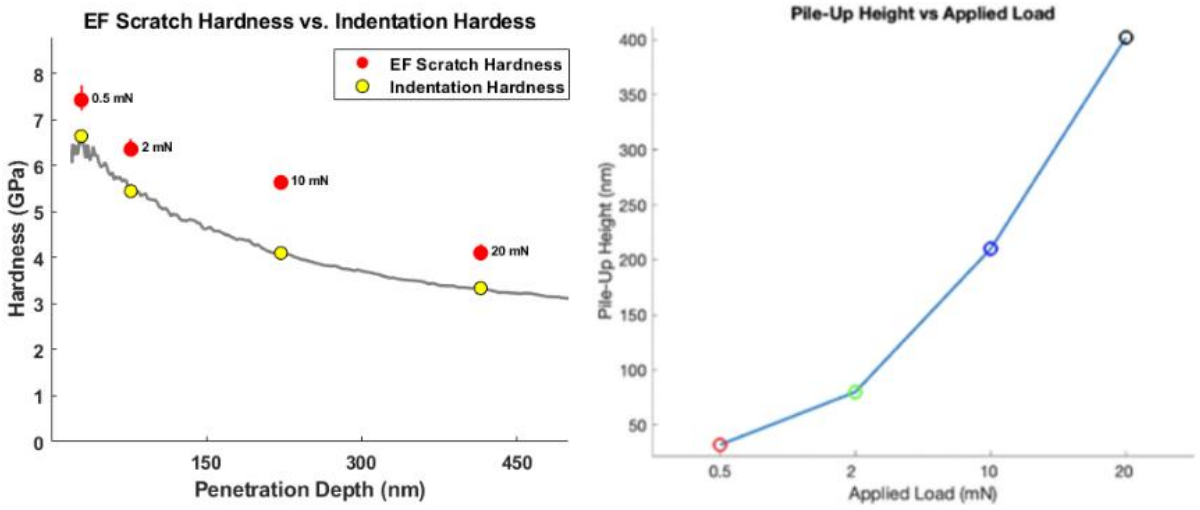



*Figure 37 Scratch hardness and average pile-up heights measured for the edge-forward Berkovich scratches on same Ni600 grain under 0.5mN, 2 mN, 10 mN and 20 mN normal load. Contact area is assumed to be 2/3 of the indentation contact area which has been corrected using pile-up measured from cross-section profiles. The error bars denote the variance of*

*hardness measured in repeated experiments at the same load. Nanoindentation hardness measurement at the same grain has been displayed on the same map for comparison.*

### *4.4.3 HR-EBSD Result*

It was previously discovered that under 10 mN loading, the region closest to the scratch groove was already too deformed for Kikuchi pattern to be properly recognised and to perform HR-EBSD analysis. It was expected that with low normal loads such as 0.5 mN and 2 mN, the material would be less deformed so that there would not be a region that is too deformed to be analysed within HR-EBSD within the plastic zone. Therefore, cross-section lift-out for 2 mN edge-forward scratches was prepared with the aim to observe the stress and strain distribution in deformed region closest to the groove surface. Lift-out was prepared using the same set-up aforementioned: 2 x 20 μm platinum coating were deposited on the scratch groove at a voltage of 30 kV and current of 240 pA. Two 15 μm deep trapeziums were trenched on top and bottom sides of the lift out with 16 nA Gallium current at 54° tilt and subsequently polished with 4 nA, 2 nA and 1 nA current until only the 2 x 20 um platinum layer was left. The stage was then adjusted to 0°, and three 1.5 μm wide cuts were made at the other three sides to have the lift-out picked up with OmniProbe. The lift-out is then attached to a copper OmniProbe grid and finally polished with 600 pA Gallium current at the side to be scanned with EBSD. An illustration of how lift-out was prepared and positioned in the SEM chamber is presented in Figure 38.

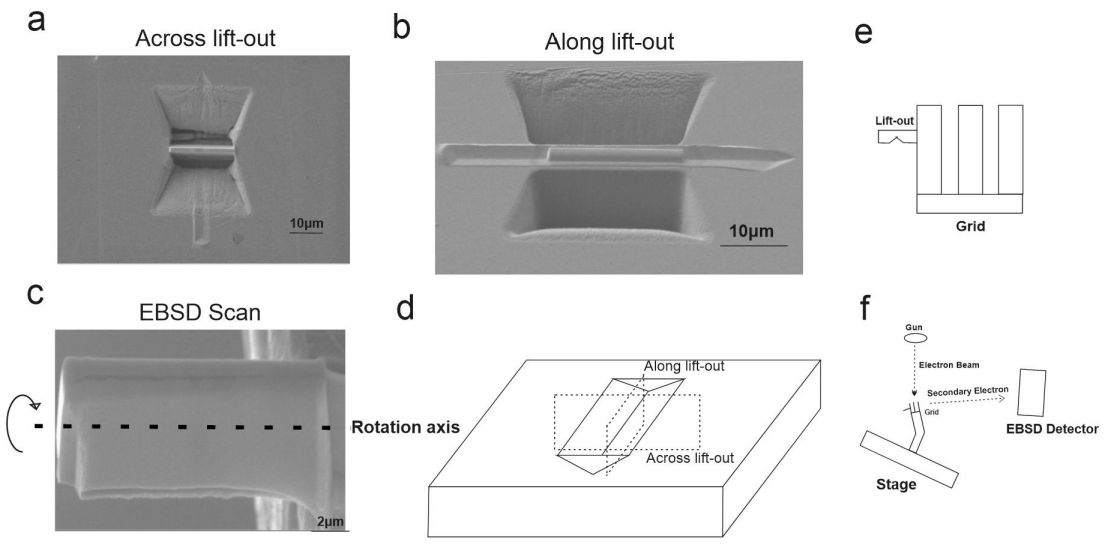



*Figure 38 Schematics of the lift-outs. a) 'Across' lift-out of an EF scratch, where the lift out is taken perpendicular to the scratch, b) 'Along' lift-out of an FF scratch, c) lift-out to be scanned with BESD (contact region facing downward), d) diagram illustration of lift out, e) schematic for lift-out mounting on the OmniProbe grid and f) positioning of holder relative to EBSD scanner. In this case, only across lift-out was taken.*

SEM image shown in Figure 39 was used to identify the scratch surface which is shown as the dark line.

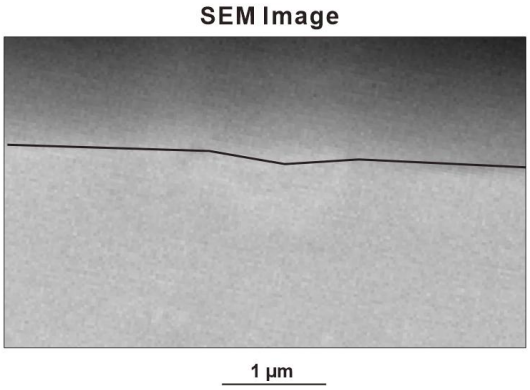



*Figure 39 SEM image of a 2 mN Berkovich tip edge-forward lift-out on Ni600. Dark line indicates where the sample surface is. Magnification is at 10000x, and the image has been rotated 180 degrees for ease of interpretation.*

Unfortunately, in reality, the stress zone caused by the 2 mN scratch was too small to be distinguished from the residual stress stored within the microstructure as shown in Figure 40 and similar problems have been found in strain and rotation results.

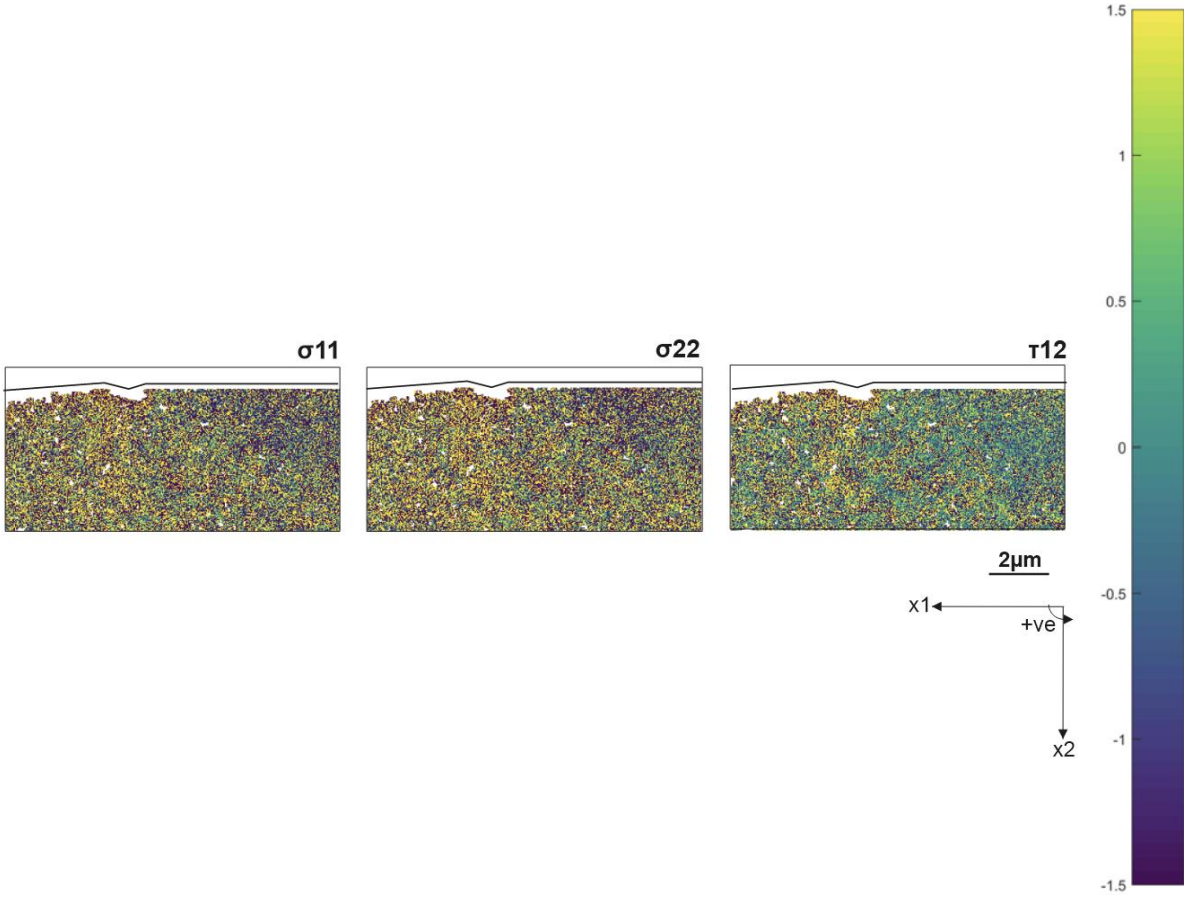



*Figure 40 HR-EBSD stress output of 2mN Berkovich tip 2 mN edge-forward scratch on Ni600. $\sigma_{11}$ map shows the stress in the horizontal direction, and the σ22 map shows stress in the vertical direction. $\tau_{12}$ map indicates the rotating shear stress from the horizontal to the vertical axis. Unit of the scale bar is GPa and the dark line indicates where the sample surface is.*

### *4.4.4 Discussion*

Low load scratches on Ni600 exhibited cross-sectional profiles closely matching the Berkovich geometry, implying that the residual grooves would form in similar way at near-surface region to scratches with higher penetration depths. This is contrary to the initial assumption that the field with higher stress concentration induced by the tip apex would lead the deformed material recover differently once the load has been removed. The lack of difference may suggest that the recovery process is purely elastic and does not induce additional geometry changes.

The Indentation Size Effect could be clearly observed for the Ni600 with almost a linear decrease in scratch hardness for the low normal loads measured. The pile-up instead grew more slowly at smaller depths and transited to a linear increase at higher normal loads. At low loads (0.5–2 mN), the slower pile-up growth is potentially due to ISE increasing the material's effective resistance to plastic flow, suppressing lateral displacement and limiting pile-up, while at higher loads (10–20 mN), the strain gradients relax as the scratch depth increases and bulk (statistically stored) dislocations dominate, allowing plasticity to scale linearly with load. This conforms with the initial expectation as for scratch/indentation depth below 100 nm, the material hardening from the Indentation Size Effect is often much more prominent [105] and less material is required to support the tip load. Pile-up heights are slightly different for two sides of the groove which could be due to the sample/tip alignment issue. However, the comparability of the test results is not compromised as the scratches are made in same batch at the same angle on the same grain As the pile-up right on the right is consistently higher for scratches made at locations far away from one another, it could also be caused by the grain being anisotropic and the relocated material has preferred moving direction. The pile-ups recorded by the AFM have been used to correct the correct

penetration depths as they also provide support to the tip during the scratch process and impact the actual contact areas.

For smaller loads (2 mN in this case), it was unable to distinguish between the deformation-induced and background stress in the HR-EBSD result, which suggests a need for simpler single crystal and single element substrates like single crystal copper free from the internal stress induced by the manufacturing process.

## 4.5 Scratching at different speeds

Speed was found to have a critical influence on the morphology of the chip formed in orthogonal cutting test simulations due to the softening of the material caused by the friction heat [65]. Nanoscratch tests were often done at much slower rates of microns per second in which the thermally enhanced softening is negligible as the heat is dissipated. However, even without the heat effect, it is worth investigating if an increase in scratch speeds leads to changes in scratch formation and scratch hardness measured to test if it is strain rate sensitive. Nanoscratch velocities were reported to have distinct effects on the deformation features of C-plane sapphire [55], in which increased scratch velocity led to a higher strain rate and hardness, which in turn limited crack formation and growth, resulting in more plastic deformation. However, the deformation mechanisms observed in sapphire (improved plasticity at higher velocities) likely wouldn't apply to nickel-based alloys as sapphire is a ceramic with ionic/covalent bonds that transition from brittle to plastic behaviour, while nickel alloys have metallic bonds and inherently ductile FCC structures that deform primarily through dislocation movement without brittle transition. Studies on Pd-based alloys and TiZrHfNb high-entropy alloys have shown that their wear resistance is independent of the scratch speed[58], [59]. In this section, a similar study has been conducted on Ni718, an alloy that is widely applied in engine turbine blades and subject to the wear caused by high-speed foreign objects [2].

Edge-forward scratches of 50 μm were performed at scratch speeds of 0.1 μm/s, 1 μm/s, 10 μm/s, and 20 μm/s on Ni718 at 50 mN normal load. Four repeated tests are performed at each scratch speed. Scratches were long enough to ensure that at least 10 grains were scratched through to minimise individual grain differences. The load was also high enough to ensure

that the tip penetrated deep enough to minimise the Indentation Size Effect and influence from the surface roughness, which is judged based on the threshold depth of 203.419 nm calculated in section 4.2 at which the hardness deviates less than 20% from the size-independent hardness. Figure 41 compares scratch profiles of a single scratch from each scratch speed and average penetration depths for repeated experiments are 619 nm, 614 nm, 634 nm and 606 nm for scratch speeds of 0.1 μm/s, 1 μm/s, 10 μm/s and 20 μm/s respectively. Contact Areas are corrected using the pile-ups measured with cross-section profile scans by nanoindenter. The fluctuations of penetration depth across the scratch distance are likely caused by the variability of grain hardness, which was also observed in the cross-section profiles that are less uniform than those measured in Ni600 scratches.

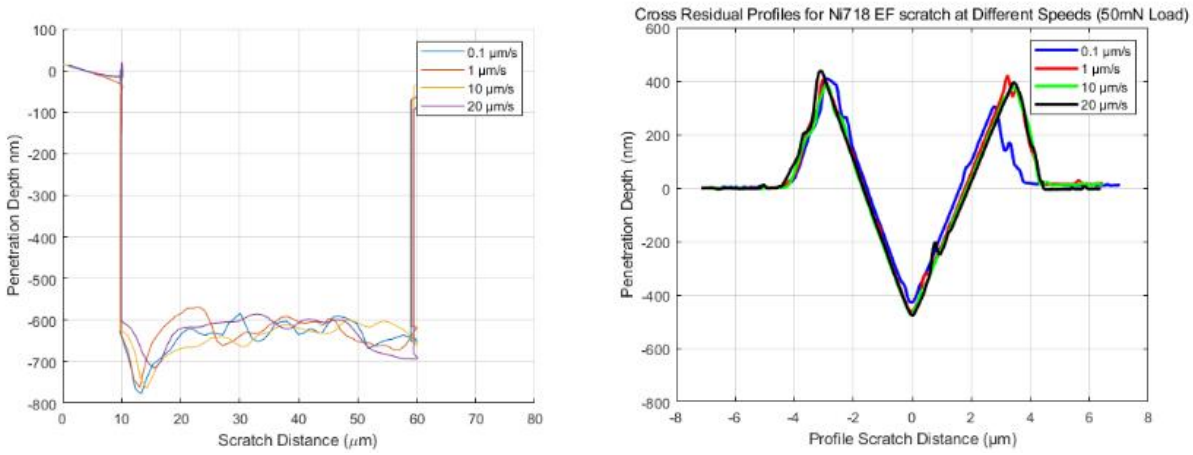



*Figure 41 a) Penetration depth profiles and b) cross-section profiles of edge-forward Berkovich tip nanoscratch tests with the different scratch speeds with normal load at 50 mN and scratch length of 50 μm (10 μm to 60 μm) on Ni718 using G200 nanoindenter. Penetration depths and pile-ups measured are from G200 output.*

### *4.5.1 Hardness Measurements*

The pile-up corrected mean scratch hardness values derived using the aforementioned method were 4.75 GPa, 4.67 GPa, 4.33 GPa, and 4.54 GPa, as illustrated in Figure 42. These results suggest that scratch speeds below 20 μm/s do not significantly influence the measured scratch hardness as no statistical differences have been observed, consistent with literature studies on Pd alloys and TiZrHfNb high entropy alloy[58], [59].

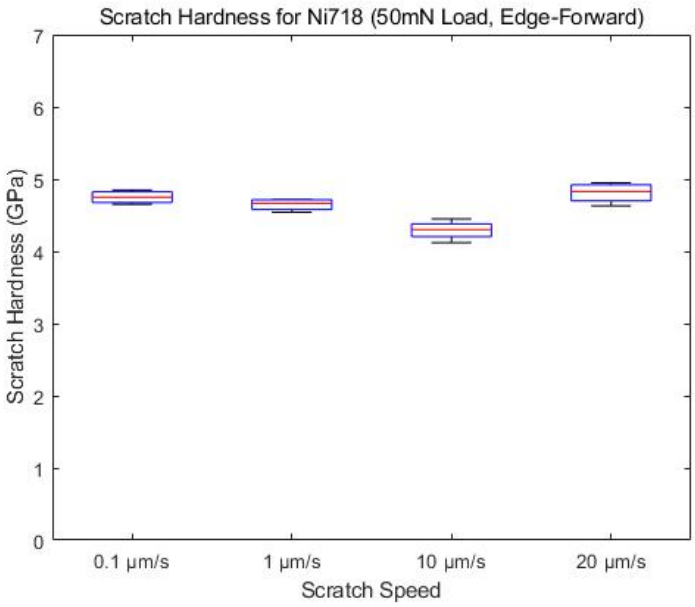



*Figure 42 Scratch hardness was measured for 50 μm long Berkovich edge-forward scratches on Ni718 at 50 mN normal load under scratch speed of 0.1 μm/s, 1 μm/s, 10 μm/s and 20 μm/s with 4 repeated tests for each speed. Error bars suggest the variance of scratch hardness measured in repeated experiments for each scratch speed. Pile-ups are corrected with cross-section scan output from the nanoindenter.*

### *4.5.2 Discussion*

Scratch velocities below 20 μm/s produced no discernible variation in stabilised penetration depth or scratch hardness measured. This sustained quasistatic behaviour potentially arises since even at 20 μm/s, the system can continuously re-establish equilibrium before contacting subsequent material sections except at the beginning when the tip endures high lateral acceleration. The strain rates for 0.1, 1, 10 and 20 μm/s speed tests would be roughly 0.04/s, 0.4/s, 4/s, and 8/s based on the Berkovich geometry, which is estimated by dividing the scratch speed with tip length in scratch direction. While elevated compared to default CSM nanoindentation strain rates (0.05/s), this remains orders of magnitude below rates characteristic of more dynamic loading regimes (100-1000/s) found in ballistic and orthogonal cutting tests [106], [107]. It is expected that higher scratch rates could have more influence on the nanoscratch measurements as the frictional heating at the contact interface can become significant and the temperature rise could ease dislocation glide. However, to avoid instrument damage, it is unlikely to perform such a test with a nanoindenter, and Finite Element Analysis is likely to be a viable solution. The nanoindenter typically has high frame stiffness in the vertical direction but not the lateral direction [108]. High lateral resistance experienced in the high strain rate experiment may also cause the bending of indenter shaft and torsion of the tip, which would make results hard to be compared with those from low strain rate experiments as the tip angle is different.

## 4.6 Scratching with Different Orientations:

Unlike a spherical tip, the geometry of a Berkovich tip has different faces and scratch orientation could have a major influence on the scratch hardness measured and the morphology of the groove formed. It was reported that for scratches on single crystal copper, under the same normal load, the tip penetrates slightly deeper in edge-forward orientation than in face-forward orientation (700 nm vs 800 nm under 20 mN normal load) but face-forward orientation had higher scratch hardness measured as there was less contact area used for calculation [97]. It was also reported that at the same normal load, the tip in the face-forward direction experiences notably higher lateral resistance [97]. Kareer explained that it was due to material accumulation in front of the tip in face-forward direction and hence more material needs to be rotated and relocated for tip to progress forward.

To investigate if a similar phenomenon can be found in nickel-based alloys, edge-forward and face-forward scratches were performed on Ni600 alloy under a normal load of 20 mN and scratch speed of 1 μm/s. It was observed that edge-forward scratches had sharp, straight groove edges similar to the low-load edge-forward scratches shown in the previous chapter, while face-forward had corrugated groove edges.

### *4.6.1 AFM Result*

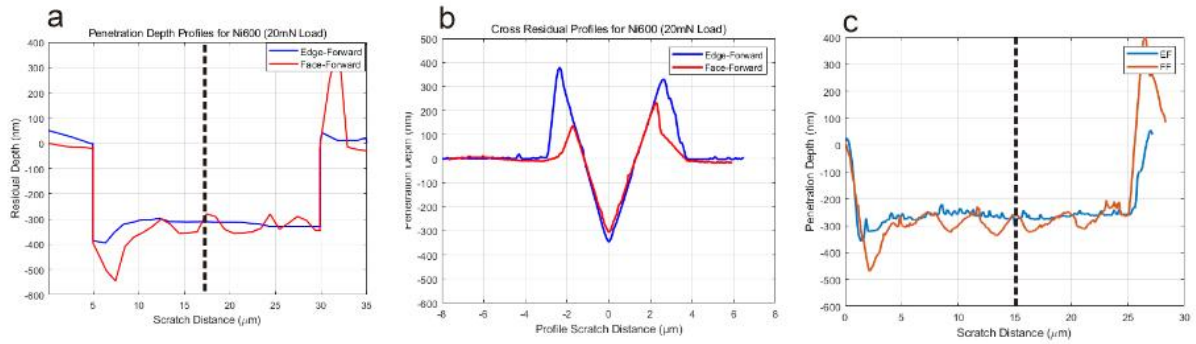



*Figure 43 a) Penetration depth vs scratch distance output from nanoindenter, b) cross-profile output from nanoindenter, and c) line profiles along the centreline of residual grooves taken by AFM. The dotted line indicates the position that the cross-section profile was taken. EF stand for edge-forward orientation and FF stands for face-forward orientation. Scratch was performed with 20 mN normal load at 1 μm/s scratch speed on a single Ni600 grain using a G200 nanoindenter.*

Line profiles along the groove centrelines obtained using AFM were shown in Figure 43 with the nanoindenter depth output, and it was found that in face-forward orientation, the tip sank deeper into the substrate before moving in the lateral direction which was explained that in face-forward direction, more facets of the tip lost contact with the substrate and the tip had to penetrate deeper to maintain the support [97]. A significantly bigger pile-up was formed at the end of the scratch in the face-forward direction, corroborating the hypothesis that material was pushed to the front of the tip in the face-forward direction, which was also reflected by a reduced side pile-up height compared to that measured in the edge-forward direction. It was observed that after the tip climbed out of the initial indentation, it formed a relatively flat, uniform bottom surface in the edge-forward direction but left a periodic wave-like structure at the bottom in the face-forward direction. Using the distance between two neighbouring crests, the 'wavelength' of the wave formed was approximately 5 μm. A similar pattern has been found in repeated experiments, and since the scratches were performed within a single grain, it is unlikely that the waves were caused by grain boundaries. It was also observed that within the groove there are periodic width changes as demonstrated by the AFM scans in Figure 43.

The average penetration depths for EF and FF scratches at 20 mN normal load were 487 nm and 425 nm, respectively. The scratch hardness calculated by assuming a 2/3 and 1/3 of indentation contact area corrected with the pile-up heights, presented in Figure 44, were 3.97 GPa and 5.32 GPa, with the scratch hardness for FF orientation being 29% higher than EF orientation due to less contact area, consistent with the scratch results from single crystal copper [97]. Compared to the nanoindentation hardness of 3.1 GPa, EF and FF scratch hardness were 28.1% and 72.6% higher, respectively. As explained in previous section, a more comparable material relocation mechanisms led to the smaller differences between EF scratch and nanoindentation hardness while FF scratch involves traversing through hardened material at front facet.

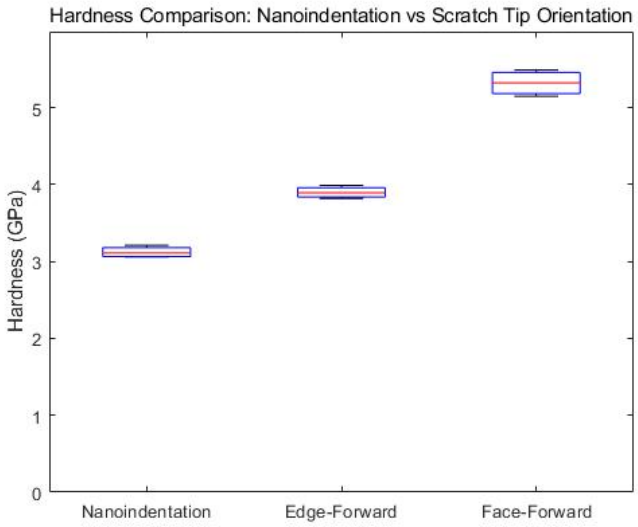



*Figure 44 A comparison of the scratch hardness measured in edge-forward and face-forward Berkovich tip scratches together with nanoindentation hardness. Scratches were made under 20 mN normal load at the scratch speed of 1 μm/s on the same Ni600 grain. Nanoindentation was made using Berkovich tip and standard CSM method in G200 nanoindenter.4 repeated tests were made for each method.*

### *4.6.2 HR-EBSD Analysis*

To investigate if the wave structure had any physical meanings, lift-outs were taken along the groove (along lift-out) as shown in Figure 45 using the same set-up in section 4.4.3 and HR-ESBD analysis was subsequently performed. Lift-out was taken in a way that the scratch direction on the map was from left to right.

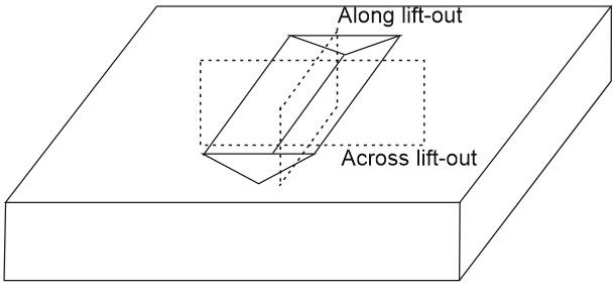



*Figure 45 Demonstration of two different lift-outs on the residual groove of a Berkovich tip nanoscratch test* [80].

SEM images shown in Figure 46 were used to identify the scratch surface and regions away from the initial normal load loading position are the cropped areas used for subsequent HR-EBSD analysis (boxed area). Scale bars were corrected for 70 degree tilt on horizontal and vertical directions.

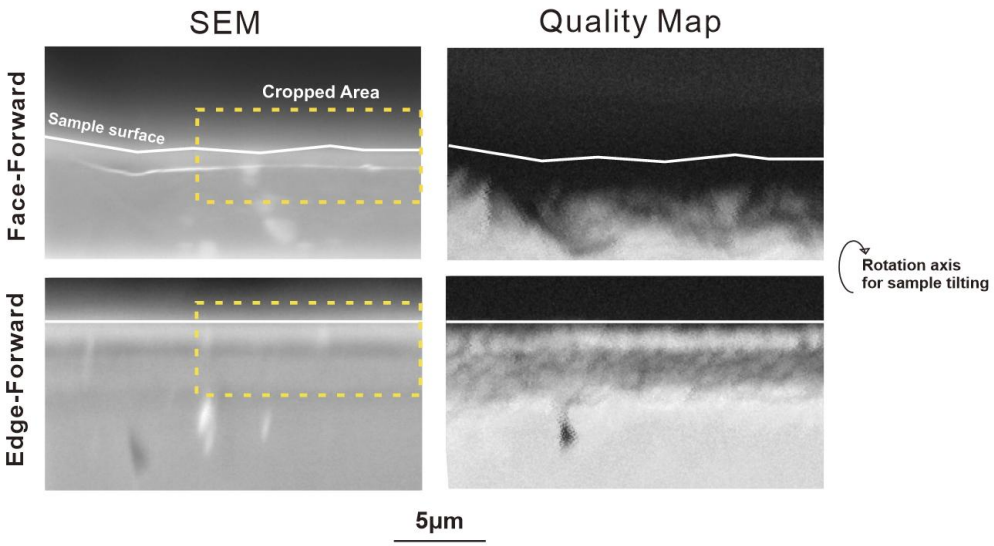



*Figure 46 SEM images and signal quality maps of 20 mN Berkovich tip nanoscratch along lift-outs on the same Ni600 grain. Boxed areas are selected for HR-EBSD analysis comparison and dark lines indicate the sample surface. The rotation axis indicates how the sample was titled during the EBSD scan (toward out of the page).*

The GND maps shown in Figure 47 suggested that in the edge-forward scratch, a dense, uniform layer of GND was formed at the bottom of the scratch, while in the face-forward scratch, there was a periodic increase and decrease of GND density along the wave-like structure.

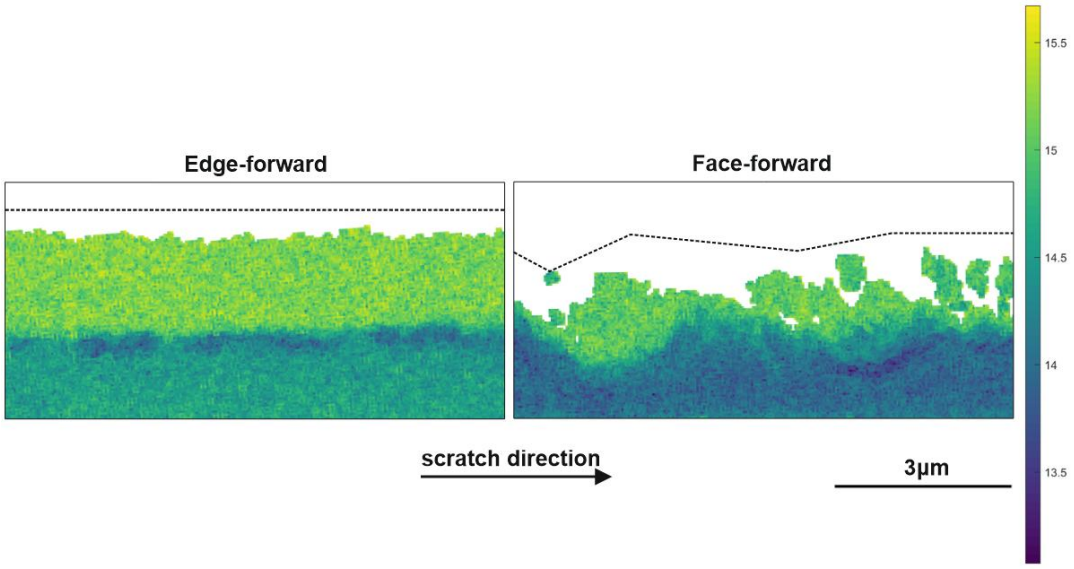



*Figure 47 GND distribution at the bottom of the residual groove of 20mN face-forward and edge-forward Berkovich scratch on the same Ni600 grain. Unit is in logarithmic scale and corresponds to $10^{13}$ to $10^{16}$ Geometrically Necessary Dislocations (GNDs) per square meter. Dotted line indicates where the scratch surface is. Lift-outs were taken from the areas away from the start of the scratch.*

Stress calculation results suggest that in the edge-forward orientation, beneath the dense GND layer where stress distribution was hard to recognise, existed a shallow layer where there was horizontal tensile stress, shown in Figure 48c (green region) and vertical tensile stress shown in Figure 48d (green region). Immediately beneath it, there was a thicker layer that exhibited stress of the opposite sign to the ones found in the shallow layer both in horizontal and vertical directions. In the face-forward scratch, horizontal compressive stress was found at the trough (dark blue region in Figure 48a); in the vertical direction, there was also a layer of compressive stress followed by a layer of tensile stress (dark blue region and yellow region beneath in Figure 48b). The magnitude of the relative compressive stress

identified was higher in the face-forward direction than in the edge-forward direction (1.5 GPa compared to 0.5 GPa).

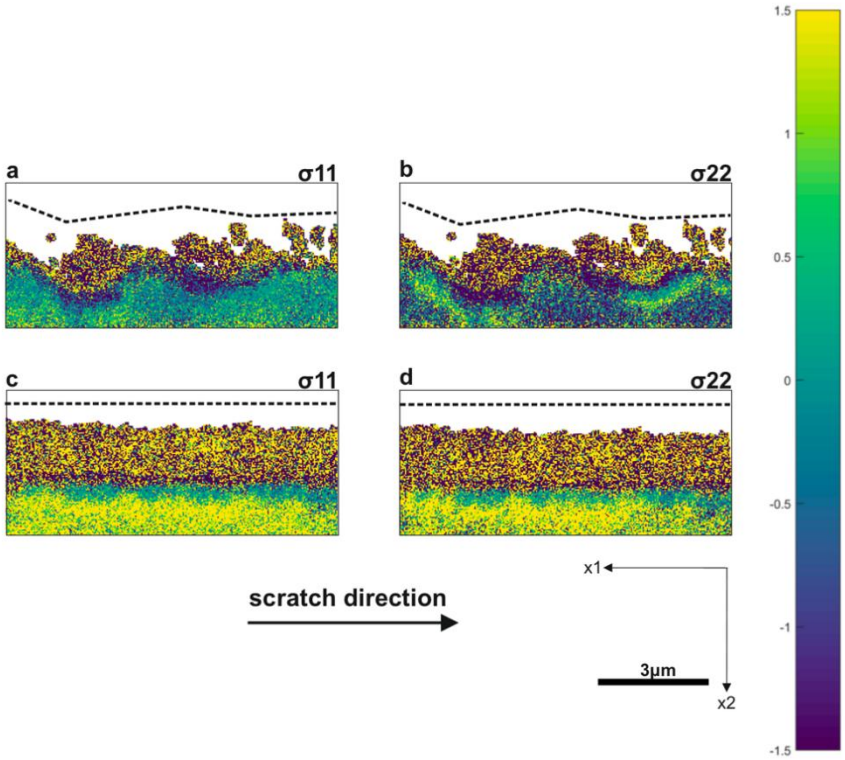



*Figure 48 Stress distribution at the bottom of the residual groove of 20mN face-forward and edge-forward Berkovich scratch on same Ni600 grain. σ11 map shows the stress in horizontal direction and σ22 map shows stress in vertical direction. Unit of the scale bar is GPa. A and c depicts the horizontal components of stress while b and d are related to vertical stress. Yellow indicates tensile stress while blue indicates compressive stress.*

From the rotation map shown in Figure 49, it can be seen that the material below the indenter tip was rotated toward the scratch direction (dark blue region). The rotation zone was uniform and thin in the edge-forward direction, while in the face-forward direction, the area of rotated material was larger at the bottom of the trough again. Rotations toward other axes (in and out of the plane) were not included as the lift-out cannot be perfectly along the centreline and the angle and the distance between the lift-out plane and the actual centreline could have a major influence on the magnitude and direction of the rotations measured which makes comparison hard, while for rotations about the $x_3$ axis, they were same for either side of the centreline due to the symmetry of Berkovich tip. It could also be observed in Figure 49b that there was a

more severe ‘ploughing’ deformation taking place in the FF scratch, while the EF scratch had a cleaner cutting behaviour.

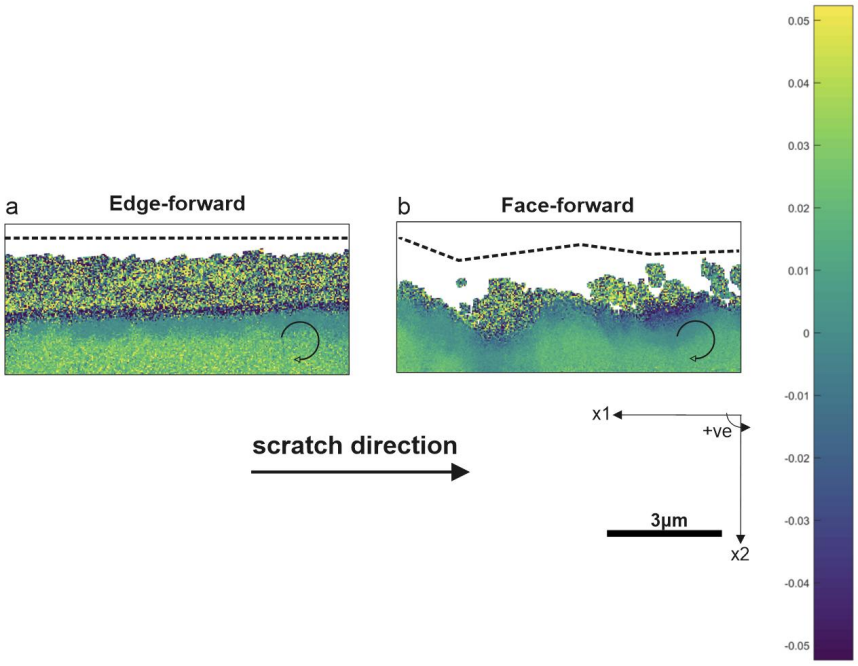



*Figure 49 Rotation maps showing rotations from the $x_1$ axis to the $x_2$ axis for 20mN face-forward and edge-forward Berkovich scratch on the same Ni600 grain. In this case, they correspond to the rotation of material along the scratch direction. The unit of scale bar is in radians. Blue colour indicates clockwise rotation toward scratch direction and yellow colour indicates counter-clockwise motion. Dotted lines indicate the position of the deformed sample surface.*

### *4.6.3 Discussion*

Scratch grooves exhibited distinct morphologies depending on tip orientation - edge-forward versus face-forward. Specifically, face-forward scratches contained an undulating, wave-like structure along the trough base similar to stick-slip phenomena resulting from kinetic to static frictional transitions. Possible explanatory mechanisms argue that lower kinetic friction enables slip initiation before re-adhering, creating discontinuities as this cycle repeats [108]. Moreover, differential material elasticities could focus stresses at contacting asperities during slip phases, further amplifying ripples. Recent literature also recognised the influence of instrument compliance in the formation of the oscillatory motion observed. It was suggested that for laterally applied forces, the measuring apparatus's dynamic characteristics become much more important compared to when forces are applied normally [109] and small oscillations within the measuring apparatus can influence the initiation of overall sliding [110] as well as the Coefficient of Friction measured [111]. However, consistency of all other testing variables implies such generalized stick-slip theories cannot fully explain the morphology differences here based solely on varied tip positioning.

Conceptually, the maximally stressed tip facet governs material flow directions, inducing rotations towards the facet normal. In edge-forward orientation, the side facets effectively "plough" material to either side in a manner similar to breaststroke swimming motions. This facilitates symmetrical extrusion of the groove edges, enabling steady transverse tip progression through uniform lateral clearing of the material.

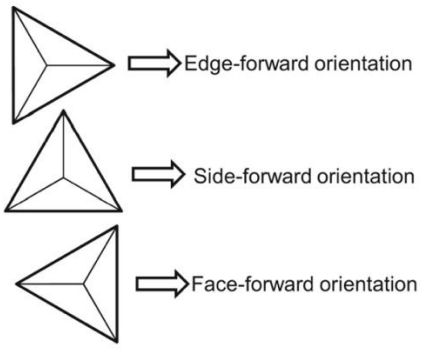



*Figure 50 Schematic representation of the Berkovich indenter with different tip orientations, including edge-forward, side-forward and face-forward [35].*

Additionally, a smaller volume of sub-tip material rotates towards the scratch direction, driven by frictional forces. Conversely, in face-forward scratches, material ahead of the contact either rotates upwards, constituting the “iceberg” like pile-up at the groove end, or shears beneath the facet, requiring subsequent tip travel through this strain-hardened material. Maintaining constant velocity likely facilitates an increase in lateral forces to penetrate the rotated, dislocation-dense material, as Figure 47 illustrates. This added friction could sequentially enable further material rotation and sticking ahead of the tip. However, once the driving friction force saturates, slippage can initiate, leaving the deformed material behind and perpetuating the periodic stick-slip phenomenon. Unfortunately, the nanoindenter employed in this study was not equipped with a lateral force gauge, rendering lateral force quantification impossible. Nevertheless, finite element analysis in the following chapter is

likely to provide additional insight into this issue. The instabilities during face-forward scratching may also potentially stem from instrument compliance – modern nanoindenters possess sufficiently high stiffness in vertical movement to minimise compliance, but this is not the case for lateral movement and torsion. Rotational moments applied to the contact can alter the locations of peak stresses at the interface, and in the case of multiple asperity contacts, these rotational moments can induce the phenomena of spragging and oscillatory stick-slip behaviour. The undulation observed in the face-forward groove could potentially ... come from spring bending and tip rotations, which again is likely to be verified in finite element simulation where rotation can be artificially limited.

The severe subsurface deformation likely disrupts the original lattice structures, as demonstrated by Liu et al. in α/β titanium alloy under fretting fatigue loading, where original grain structures shatter into smaller grains [112]. Unfortunately, for the regions that can be recognised by EBSD, there was only 1 grain identified in the IPF data and potentially fined grains cannot be recognised due to resolution limitation. The HR-EBSD determines the rotation by matching diffraction patterns based on cross-correlation. Nevertheless, the subset-based phase correlation algorithm cannot determine pattern shifts accurately when large rotations occurred [113], which is the case of the unidentifiable area within the trough. The more deformed grains exert a friction force that drives the smaller grains immediately below to rotate to the front, which is shown by the compressive stress in $\sigma_{11}$ maps of Figure 48, both in edge-forward and face-forward direction, together with the clockwise rotations shown in Figure 49. As the smaller grains rotate, a new layer of grain boundaries exerts stress on the adjacent material, which leads to the stacked layers of compressive and tensile stress shown in the $\sigma_{22}$ map of Figure 48, again both in edge-forward and face-forward directions.

## 4.7 General Discussion

This chapter initially addresses the hardness measurements of the three alloys used in this study. For a single Ni600 crystal, it was expected that the measured hardness could vary markedly with crystallographic direction (e.g., [100], [110], [111] directions), which was not assessed in this study due to time constraints. It was also suspected that the differences in stress concentration between the tip apex and side walls would result in differential material recovery. However, for the tested small normal load on Ni600, no alteration in the overall groove shape was observed. The scratching speed, which determines the strain rate, did not exhibit any influence on the measured scratch hardness within the tested speed range. However, due to limitations in apparatus stiffness, higher test speeds could potentially damage the instrument, highlighting the necessity of simulation work. Instrument compliance has also been reported as a potential cause of the periodic structures observed in the tip orientation section, further emphasising the need for simulation studies. The effect of strain rates has only been investigated on Ni718 due to time constraints, but the conclusion may vary for the other nickel-based alloys mentioned in this study.

## 4.8 Conclusions

Several loading conditions and tip orientations were tested on nickel alloys using Berkovich tip to study their effect on penetration depth and scratch hardness measured. A number of conclusions were derived.

1. Nickel alloys tested exhibited normal indentation size effect, and the moduli measured with CSM method were close to the literature values obtained from bulk tests and are similar for the three alloys tested due to significant presences of nickel element.
2. Strain rates under 8/s were found to have no influence on the scratch hardness measured in Ni718 using average penetration depths in stabilised scratch regions.
3. For Berkovich scratches on Ni600, scratches made with normal loads under 20 mN exhibited similar groove morphology. The difficulty in separating deformation-induced stress and internal stress variation from alloy processing indicates the necessity of using an initially stress-free alloy for residual stress analysis on nanoscratch with smaller normal loads (e.g. 2 mN).
4. Oscillatory stick-slip phenomenon was observed in face-forward scratches but not in edge-forward scratches. Strain-hardening of the material beneath the tip and instrument compliance were likely to be the causes of this phenomenon.

# 5. Multi-pass Scratches

## 5.1 Introduction

Nanoscratch testing conducted under controlled conditions in the laboratory provides valuable data on a material response to deformation at small length scales. However, relating the insights from these experiments directly to the complex tribological phenomena experienced in real-world applications remains a persistent challenge. Whereas nanoscratches in ductile metallic materials, the primary effect is plastic flow, which induces cracks on smooth surfaces. Actual components experience wear through multiple interdependent mechanisms: abrasion, adhesion, and surface fatigue, all operating under fluctuating loads, varied lubrication schemes, and the accumulation of wear debris over time.

Understanding the combined effects of these interdependent mechanisms necessitates a series of well-designed experiments and analytical techniques. Performing repeated nanoscratches at identical surface locations provides a starting point for characterising the progression of material response, as permanent deformation and damage cumulatively alter the subsurface structure. In this way, the incremental evolution of scratch texture, pile-up morphology, and subsurface cracks reflect the effects of repeated stress excursions and the surface deterioration caused by abrasive wear processes in wear applications.

## 5.2 Experiment

### *5.2.1 Nanoindenter Output*

Repeated 30 mN normal load, edge-forward oriented scratches were performed on Ni600. For each scratch pass, the tip was loaded to 30 mN at the starting point, and then the stage moved laterally to initiate the scratch process. Once the designated scratch length was reached, the tip was unloaded into the air and returned to the start position without load. It then loaded at the original starting position to 30 mN again and repeated the process for subsequent passes. A schematic of the experiment is provided in Figure 51a. Penetration depth of each pass was measured relative to the original sample surface as shown by the blue curve in Figure 51c and the increment of depth for each pass was measured relative to the pass prior.

As shown in Figure 51c, the first pass penetrated an average displacement of 515 nm at the stabilised region (blue line) with the second pass penetrating average of 509 nm (red line), using the original undeformed surface (dark line) as the reference. However, the increment of depth of the second pass was only 94 nm (509 nm – 415 nm) on average, significantly less than that of the first one. The increment of depth for each pass decreased steadily, and eventually, the tip almost stopped penetrating any further at the 10$^{th}$ pass (8 nm penetration depth on average).

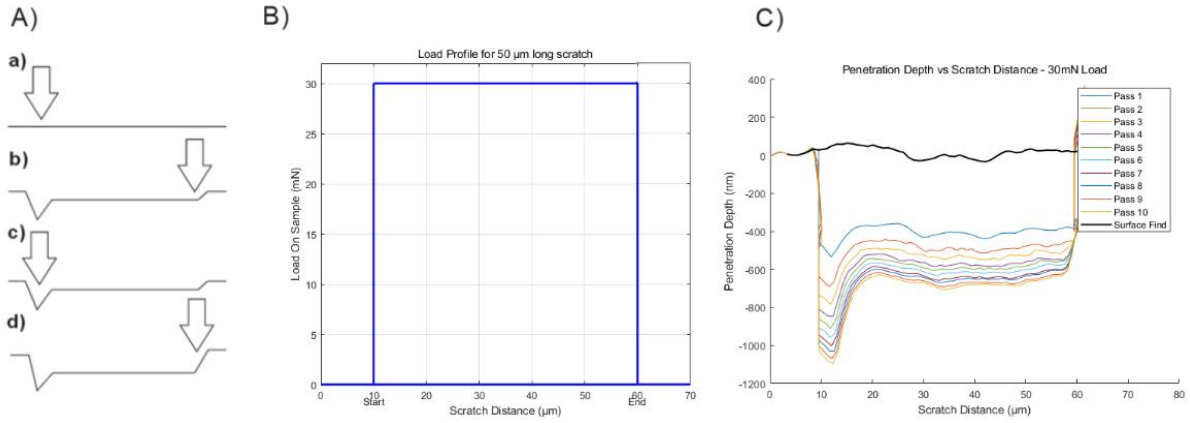



*Figure 51 Penetration depth profile of repetitive scratch on Ni600 from G200. Scratches were performed with a load of 30 mN and a scratch speed of 1 um/s in edge-forward orientation. A) is a schematic of the multi-pass nanoscratch process in*

*which the tip load(a), moves loaded laterally(b), unloads and returns to start unloaded (c) and repeat (d). B) is the load vs scratch distance from G200 for 1 pass from a 50 µm scratch and C) is the depth vs scratch distance measured by G200 relative to the initial surface for each pass. Scratch length is 50 µm in the multi-pass test (10 um to 60 um). Scratches were performed with load at the scratch speed of 1 µm/s in edge-forward orientation using Berkovich tip.*

Similar repetitive edge-forward scratches were performed with other normal loads of 20 mN, 50 mN and 80 mN. A wide range of normal loads was covered to investigate the load-dependency of this phenomenon and penetration vs load profiles for other loads are shown in Figure 52.

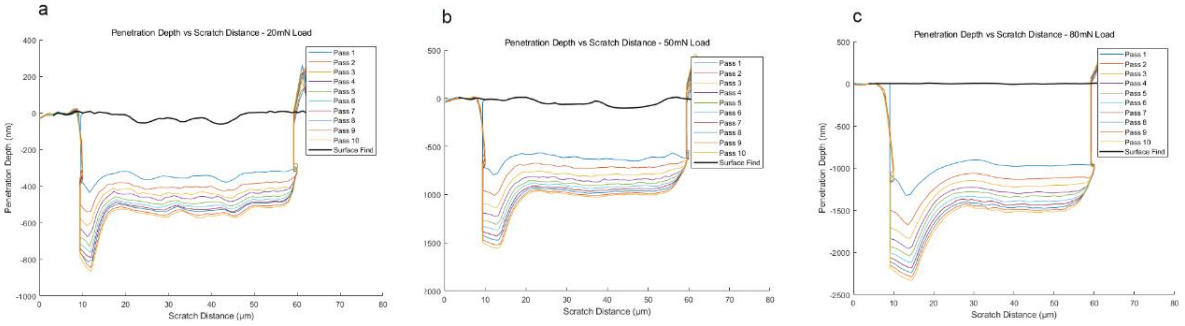



*Figure 52 A,b,c graphs are depth vs scratch distance profiles measured by G200 relative to the initial surface for each pass for 20mN, 50mN and 80mN normal loads. Scratch length is 50 µm in the multi-pass test (10 µm to 60 µm). Scratch directions are edge-forward using Berkovich tip.*

The total penetration depth charts (Figure 53) for each cycle suggest it was a common trend for all loads to stabilise to a certain penetration depth while the cycle times needed to stabilise increase with the load. The error bar indicates the variance in the average penetration depth of the repeated experiments under the same load. To determine the scratch hardness, the area of contact is considered to be two-thirds of the total Berkovich tip area, using the averaged penetration depth for edge-forward, as revised by Kareer to account for the actual area in contact during scratch tests [97]. A normal load was applied.  for the pressure calculation as the instrument used was not capable of measuring lateral resistance. Results were presented in Figure 53 - error bars represented the variance in scratch hardness measured using average penetration depths of repeated experiments under the same normal load, the depths were

averaged from the 10 to 50 µm scratch distance where the tip was seen to be stable after the climb-out region, a method that was explained and used in earlier chapters.

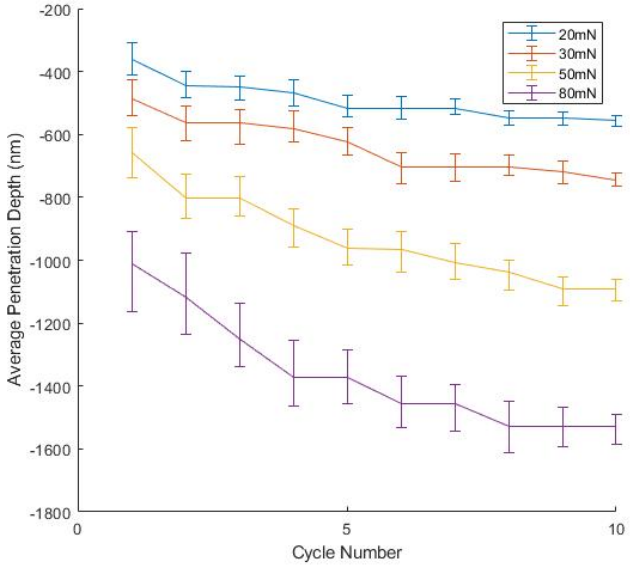



*Figure 53 Average penetration depths during tests from G200 output for each cycle in multi-pass nanoscratch tests under different normal loads. The depths are averaged for the depths recorded after climb-out region (the initial 10 µm). Tests were performed with Berkovich tip and Ni600. Tip orientation was edge-forward with scratch speed of 1um/s at length of 50um.*

Despite the differences in depth change after each cycle, the scratch hardness from four loads does indeed stabilise and converge in a similar manner, as shown in Figure 54. The scratch hardness was calculated using two-thirds of the contact area derived from the total penetration depth, corrected with the average pile-up heights measured from the cross-profile scan. However, profile scans were only performed at the end of each test, and for the pile-up heights for each pass before the final pass, a linear increase with the measured penetration depth was assumed to approximate the pile-up heights for passes prior to the final one. This approximation technique will be validated with AFM scans of 20 mN load scratch residual grooves in the next section. Shown in Figure 54, after 10 cycles, the scratch hardness measured under 20 mN decreased from 4.9 GPa to 2.65 GPa. For 30 mN, hardness dropped from 4.58 GPa to 1.92 GPa. For 50 mN, the value measured reduced from 3.62 GPa to 1.55 GPa while it was 2.67 GPa to 1.32 GPa for 80 mN scratch. The scratch hardness measured

between smallest to highest load decreased from 2.23 GPa at initial pass to 1.33 GPa at 10$^{th}$ pass. The error bars denote the variance of the hardness calculated at each cycle time between experiments under the same load.

.

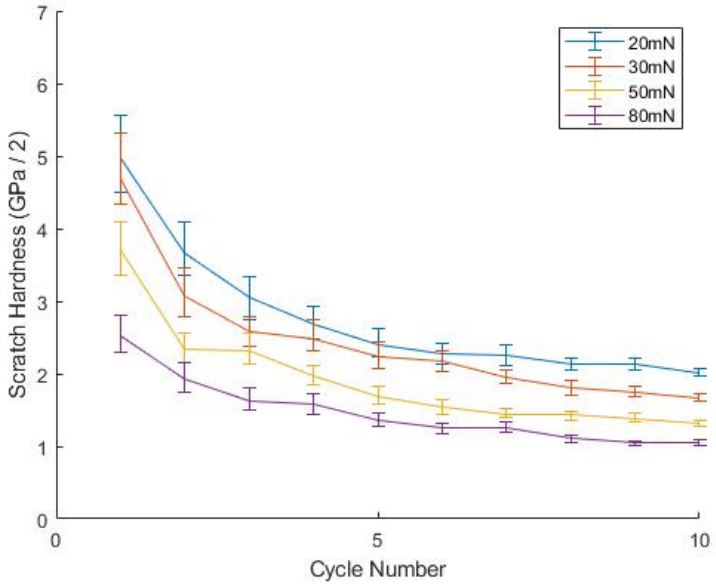



*Figure 54 Scratch hardness after each cycle in multi-pass test. Contact depth is defined as the total penetration depth after each cycle and contact area is 2/3 of the total area from area function calibrated with fused silica.*

However, it is unphysical that the material was softened by repeated scratches as strain hardening caused by the plastic deformation in the prior pass is expected. The decrease of scratch hardness calculated using total penetration depth was likely caused by the overestimation of the contact area – not the whole residual deformed surface was in contact with the tip at subsequent passes but only part of it, which could be the bottom of the groove where the tip penetrated further. An alternative way to calculate the area of contact was to use the difference in penetration depth after each pass, but as shown in Figure 52c, the tip penetrated less than 50 nm at final passes and hardness derived from the contact area using that depth increment would reach magnitude of thousand GPa which lacked physical interpretation. It was speculated that as well as the contact on the two faces pushing into the material up to the increment in depth, there was also contact along the two trailing edges of

the indenter over a narrow strip of material running all the way up the track height (i.e. over a height given by depth plus pile-up), which is illustrated in Figure 55.

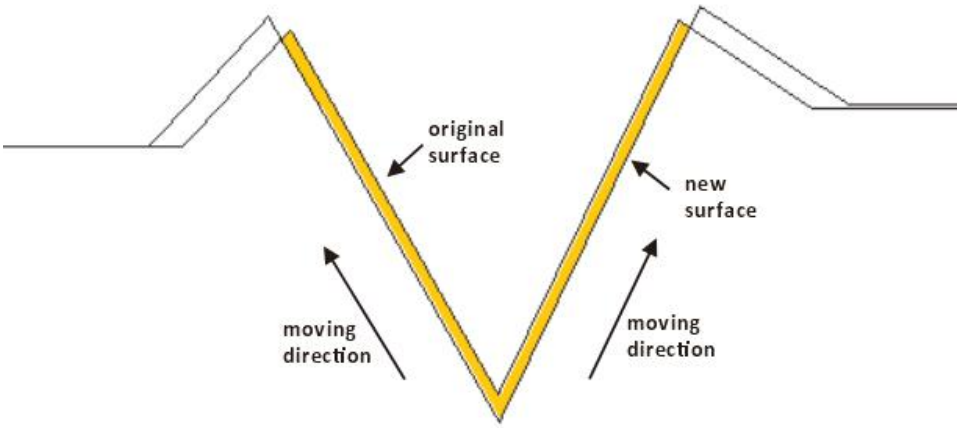



*Figure 55 A schematic showing how the material extruded by tip apex relocates and rotates to form the pile-up along two trailing edges (yellow region). Scratch direction for the Berkovich tip is out of the page.*

The strips of contact at the trailing edges and two side walls changed in area at each pass. The difficulty is to estimate the width of this contact to obtain an area, which this thesis hopes to address using Abaqus modelling seen in upcoming chapters.

To investigate the deformation mechanisms that leads to the stabilisation effect, edge-forward scratches of 1, 2, 5, 10 pass with the same load were made in the same direction on same grain with (0 0 1) orientation in z direction to minimise the grain difference and loading conditions. The normal load used was 20 mN and scratch speed was 1 μm/s and results are presented in upcoming chapters.

### *5.2.2 Residual Profiles*

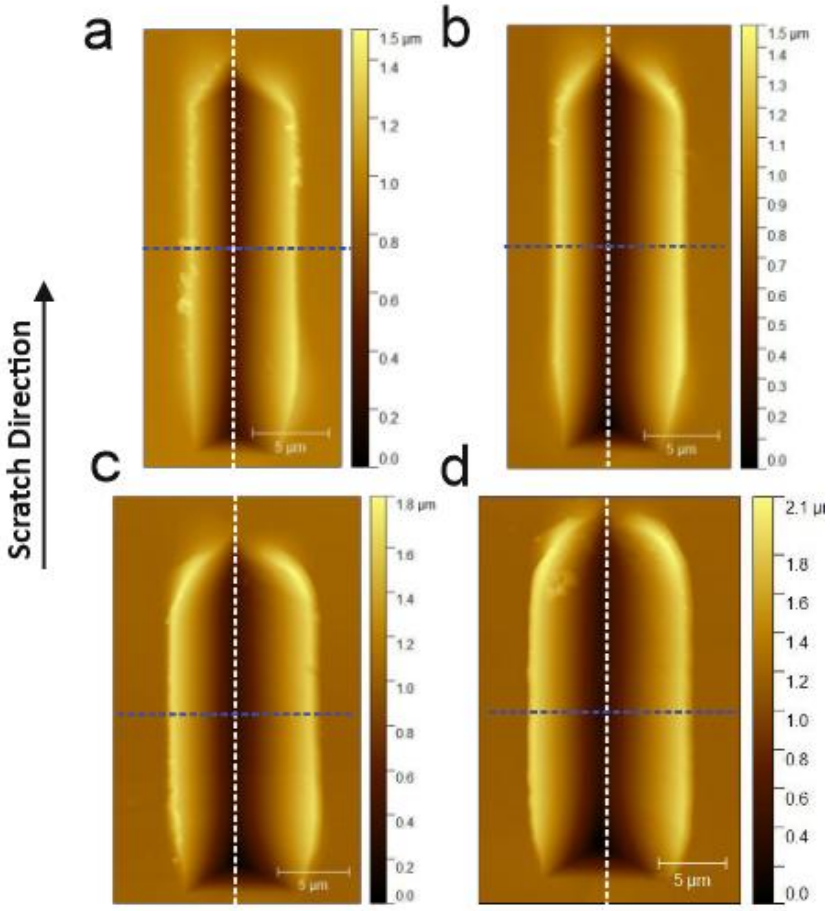



*Figure 56 AFM topography maps of 20mN edge-forward Berkovich tip nanoscratch tests with different number of passes using G200 nanoindenter. A, b, c, d correspond to scratch of 1 pass, 2 pass, 5 pass and 10 pass. 0 height plane were adjusted to the lowest point of the scratch groove. White and blue dotted lines indicate the position where AFM line profiles and cross-section profiles are taken.*

AFM scans were performed to record the residual morphology of the scratches as shown in Figure 56. Scratches under different cycles of loading appeared to maintain the Berkovich geometry similar to the observations made in single pass scratches with increased loading. Sharp and straight groove edges were maintained in all experiments. For 1, 2, 5, and 10 pass, the residual depths measured were 515 nm, 595 nm, 696 nm and 736 nm, and the groove widths measured from the widest part were 6.75 µm, 8.09 µm, 9.44 µm and 10.77 µm respectively, as shown by Figure 57. Displacement into the surface measured by the nanoindenter during scratches was 589 nm, 650 nm, 772 nm, and 809 nm respectively. These measurements were plotted alongside the residual depths to visualise the elastic recovery, as

shown in Figure 58. The AFM images were asymmetrical, likely due to poor alignment between the tip and the sample, as well as the grain being anisotropic, as suggested earlier sections. It should be noted that the Ni600 tested experienced cyclic loading during the multi-pass scratch process which potentially induced reverse plasticity and affected the measurements by altering the material's mechanical response during subsequent passes. The initial scratch introduced a high density of dislocations and residual stress within the alloy. At following passes, these pre-existing dislocations could rearrange in the reverse direction more easily due to the altered internal stress state and lead to changes in the observed residual depths and groove widths that were not solely attributable to the geometric effects of the tip or the applied load.

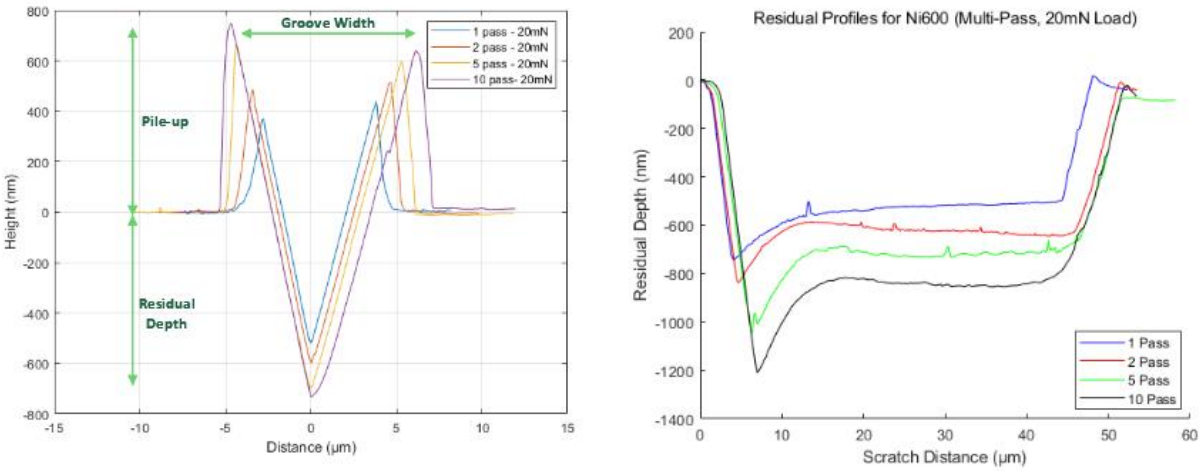



*Figure 57 Cross profiles and line profiles of repetitive scratches of different passes under 20mN normal load on same Ni600 grain in edge-forward Berkovich tip orientation. Heights were adjusted to align sample surface and profiles were taken with AFM.*

Discrepancies between the residual depth and penetration depth measured by nanoindenter and AFM are shown in Figure 58.

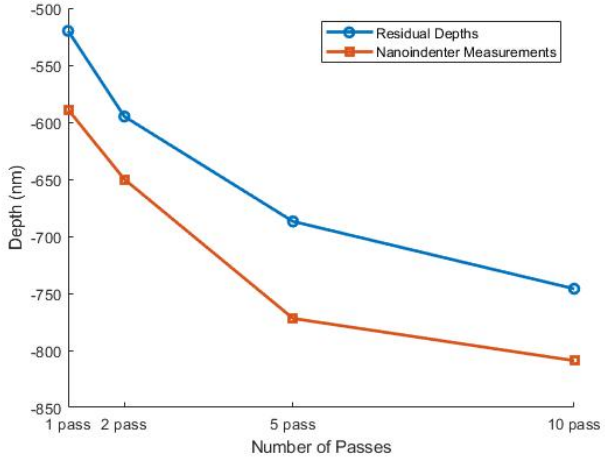



*Figure 58 Comparison of residual groove depth and experiment depth. The difference is due to the elastic recovery of the material. Depth is determined from the undeformed surface and does not include pile-up.*

An alternative method to calculate the contact area and scratch hardness has been attempted, which the new contact area (the strip of contact described in Figure 55) was defined as the difference between the total contact area of the current scratch and that of the previous scratch, which is illustrated in Figure 59 as the red regions.

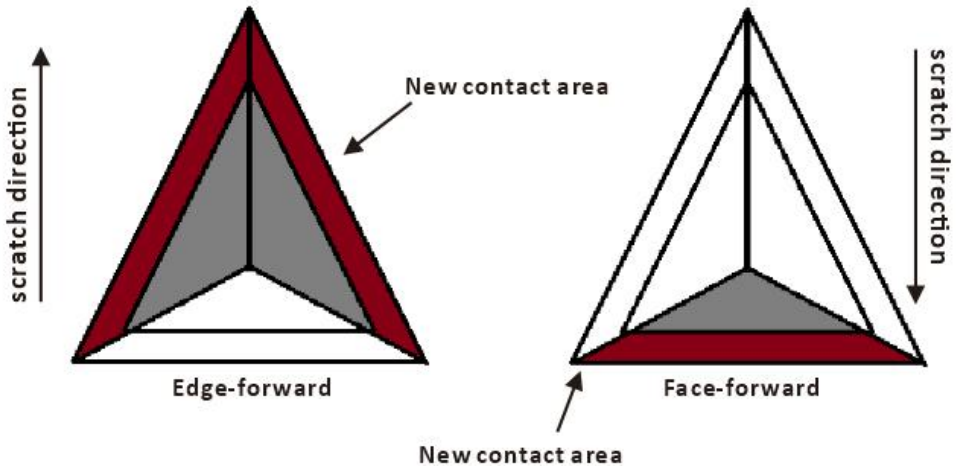



*Figure 59 A schematic showing how contact area is defined for subsequent passes in multi-pass experiments, which are the red regions that mark the difference between the total contact area in current scratch and total contact area in previous pass (grey region).*

However, for this method to be carried out, the pile-up heights at the 4th and 9th passes had to be estimated to ascertain the new contact area for the 5th and 10th passes, which

unfortunately were not directly measured in this study, as only one cross-profile scan was conducted at the end of the test, while the penetration depths at the 4th and 9th passes were recorded, as shown in Figure 52. This necessitates the approximation of the pile-up heights at the 4th and 9th passes to determine the total penetration depth using the penetration depths and pile-up heights measured for other passes. Shown in Figure 60, for the edge-forward Berkovich scratch at 20mN in this grain, a linear relationship between the penetration depth and pile-up heights was observed, although this relationship may not hold for scratches on other materials.

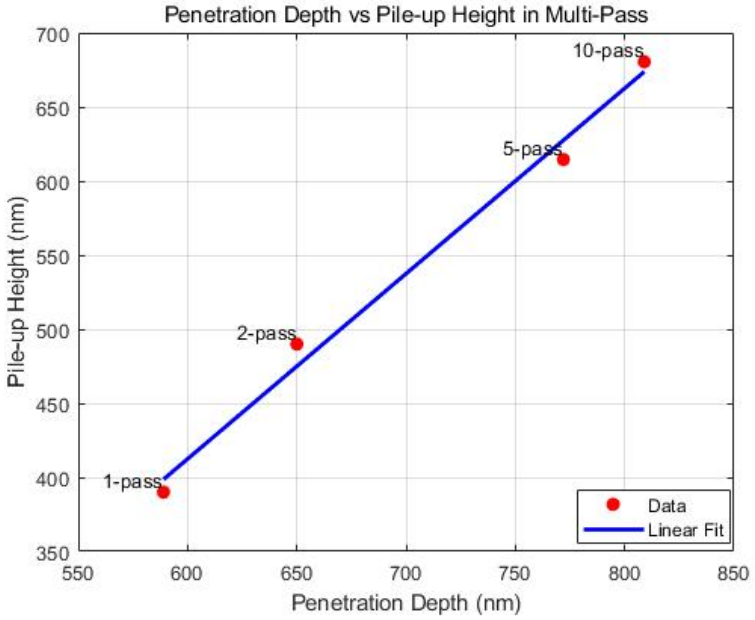



*Figure 60 Pile-up heights and penetration depths for the 20mN Berkovich tip edge-forward nanoscratch tests were measured on a single Ni600 grain. Pile-up heights were measured from AFM and penetration depths were recorded by nanoindenter.*

The measured pile-up heights were 396 nm, 493nm, 615 nm, and 681 nm for 1, 2, 5, and 10$^{th}$ passes, and the pile-up heights at 5$^{th}$ and 9$^{th}$ passes, approximated using the penetration depths of 731 nm and 780 nm measured were 584 nm and 635 nm, respectively.

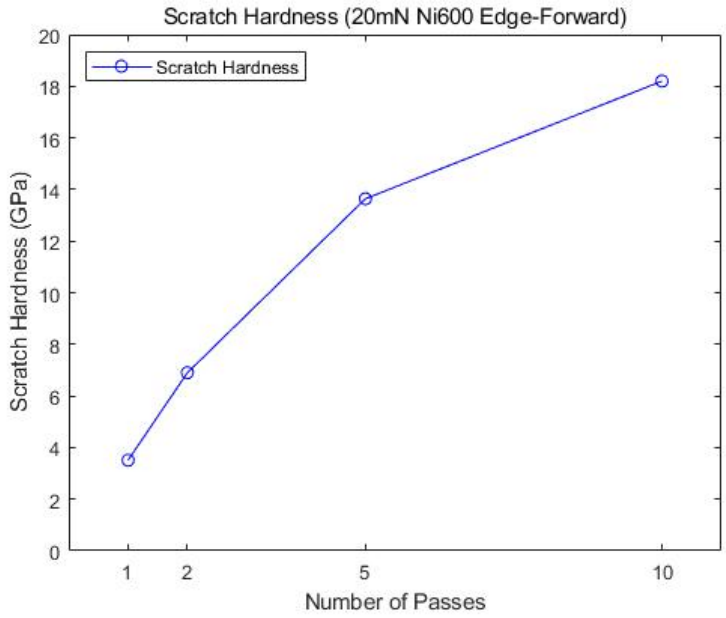



*Figure 61 Scratch hardness calculated using contact area defined as the difference between the total contact area of the current pass and the previous pass. Scratches were made with Berkovich tip at 20 mN normal load in edge-forward direction for 1, 2, 5 and 10 repeated scratch pass on same locations.*

Shown in Figure 61, the scratch hardness values calculated using this method for the 1$^{st}$, 2$^{nd}$, 5$^{th}$ and 10$^{th}$ pass were 3.8GPa, 6.9 GPa, 13.6 GPa, and 18.2 GPa. The scratch hardness measured in this way for the second pass was comparable to Ni718 scratch hardness measured in this study (around 5 GPa) and the scratch hardness at the 5$^{th}$ and 10$^{th}$ pass were comparable with the scratch hardness measured for ceramic materials in literature [114] which were in the range of tens of GPa. The discussion session presents an assessment of the physical implications of the new contact area defined and an interpretation of the hardness measured.

### *5.2.3 Discussion*

Observations of the scratch tip stabilising at a consistent depth after multiple loading cycles raise questions regarding the current definition of scratch hardness. Materials are understood to be hardened by prior mechanical deformation due to the accumulation of dislocations. Thus, the decreasing hardness values in multi-pass experiments obtained using accumulated penetration depth are unphysical and potentially suggest a new definition of the contact area that more accurately reflects the pressure experienced by the tip during subsequent passes to reconcile the contradiction.

A new definition of the contact area was proposed in this chapter which defined it as the difference between the total contact area of the current scratch and the previous scratch using total penetration depths. While using an area difference, this definition remains related to the total contact area of the current scratch which, physically, a higher penetration depth would decrease the current pressure experienced, while a bigger deformed area from the previous scratch would increase the pressure (measured hardness), reflecting the amount of surface hardening contributed by the previous scratches**.** It is hypothesized that the initial scratch induces grain refinement, generating dislocations that persist further deformation in the early stages, resulting in a hardness similar to Ni718, which has a finer-grained microstructure. As the number of scratch passes increases, the grains become increasingly refined and interlocked, forming a structure that, at a given load, the tip's ability to extrude new material and relocate it to become pile-ups through trailing edges is largely reduced.

It was suspected that the penetration depths measured in the final passes (typically in the tens of nanometres) were primarily due to elastic deformation, while any residual depth increase likely arises from localized reorganisation or annihilation of dislocations driven by the tip

load and residual stress within the deformed structure. To examine this theory, HR-EBSD analysis of the deformed structure would be performed to more thoroughly understand the microstructure changes [135].

## 5.3 Deformation zone analysis

### *5.3.1 HR-EBSD Output*

Cross-section (across) lift-outs and HR-EBSD analysis were prepared on each of the scratch was made under a normal load of 20 mN with edge-forward orientation, using the same lift-out preparation method described in Chapter 4.4, except that the EBSD scans for 1 pass and 2 pass were conducted at 10000x magnification, while those for 5 pass and 10 pass were performed at 8730x magnification. Figure 62 shows the secondary electron images of the lift-outs obtained and used for scratch surface identification.

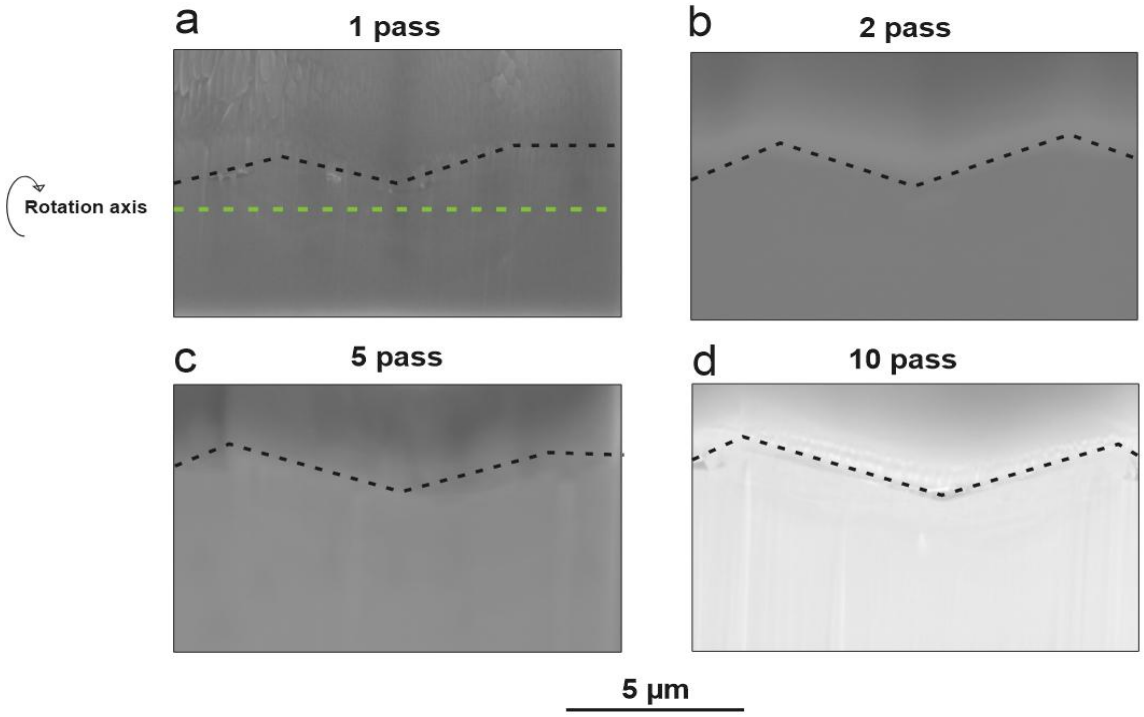



*Figure 62 SEM images of cross-section lift-outs of 20mN Berkovich tip edge-forward multi-pass nanoscratch experiments on same Ni600 grain. A,b,c,d represent results from 1 pass, 2 pass, 5 pass, 10 pass experiments. Dark dotted lines denote the scratch surfaces, and green dotted lines represent the axis that the lift-out was rotated around during the tilt process for the EBSD scan.*

IPFY maps shown in Figure 63 confirmed that lift-outs were made in regard to the same grain orientation. After 1 pass, shown in Figure 63a, some material close to the boundary of the plastic zone was identified as a grain of altered orientation by MTEX (bright yellow region),

which recognised misorientation by calculating the rotation matrix between the orientation matrices of adjacent grains and then extracting the misorientation angle and axis from this rotation matrix [115]. Plastic zones were not rigidly symmetrical against the middle of the image, which could be caused by an alignment issue that led to the tip not being perfectly normal to the sample surface.

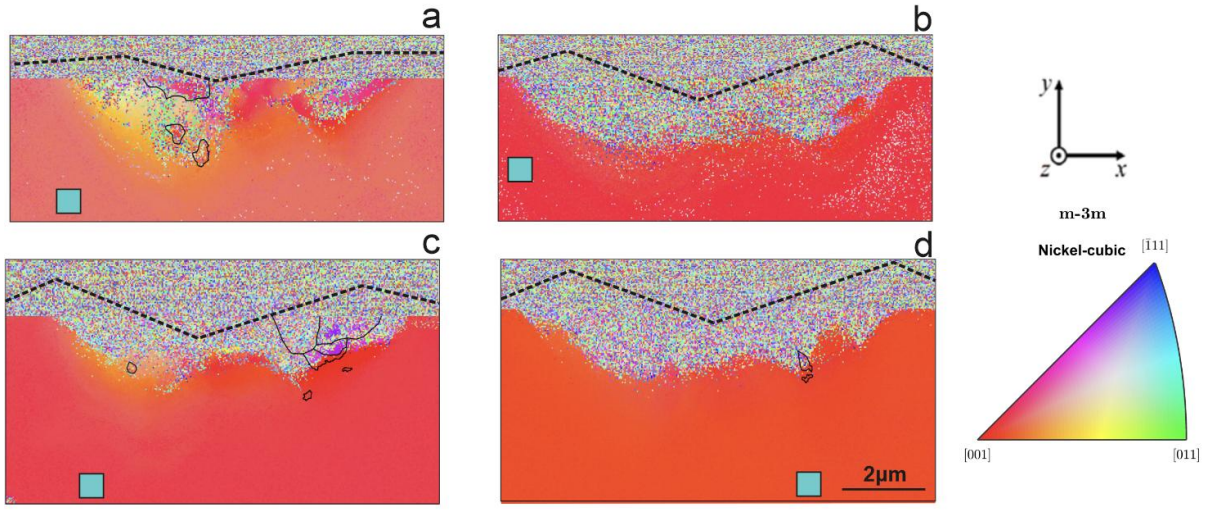



*Figure 63 IPFY maps of the lift-outs prepared from multi-pass 20mN edge-forward Berkovich tip scratches on same Ni600 grain. A, b, c, d images were taken from scratch times of 1 pass, 2 pass, 5 pass and 10 pass, respectively. Black lines reflected the automated grain boundary selection of HR-EBSD algorithm. Blue boxes were the referenced area used for cross-referencing (undeformed structure). Dotted lines indicate where the sample surface was.*

To estimate the depth of the plastic zone, pattern quality maps (Figure 64b) were used in conjunction with the secondary electron image shown in Figure 64a to recognise the boundary of residual morphology and plastic zone. The deformation caused by the scratch was considered the sole cause of the reduction in pattern quality as a Focused Ion Beam (FIB) does not induce additional stress as traditional machining methods do, though beam damage still occurs, which could be minimised by progressively reducing the current to remove the damage. Both residual penetration and plastic depths were estimated by measuring the deepest point of the plastic zone to the sample surface on both sides and averaged. The end of the plastic zone was taken as the point where the GND and signal quality returned to the

background level. Depth of the plastic zone estimated were 4.64 μm, 6.24 μm, 6.13 μm, and 5.58 μm for 1, 2, 5, and 10 passes. The plastic zone depth to residual depth ratio was from 7.6 to 10. The fluctuations were likely caused by the shape differences and material being regionally anisotropic. The depths of the plastic zones were measured to investigate if the increment depths in the following passes were due to more material being deformed and rotated or the evolution of previously deformed regions. As shown in Figure 66.2, there was still a substantial increase of deformed material in the second pass while the following passes had the size of the total plastic zone relatively unchanged between pass 5 and pass 10, which likely indicated that at the second pass, the tip was still able to rotate and deform new material while it was mainly altering the already deformed structure in later passes.

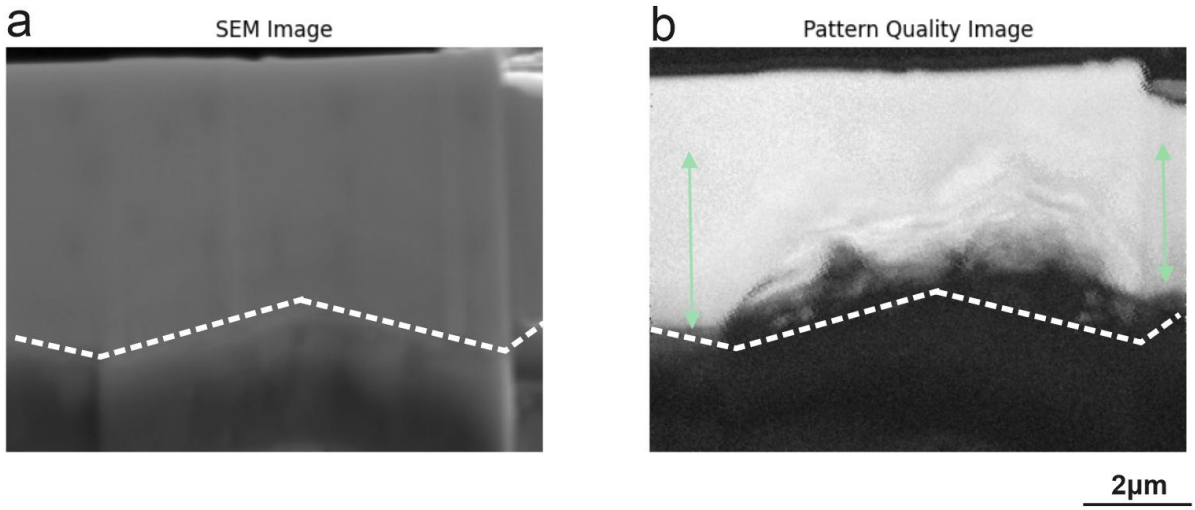



*Figure 64 Secondary electron image and pattern quality image of the 20mN 2 pass scratch lift-out on single Ni600 grain. Actual scratch edges are less discernible in pattern quality image and other output maps based on it due to severe deformation. Green lines indicate lengths used for plastic zone estimation. White dotted lines indicate the location of sample surface.*

The GND density measurements shown in Figure 65 were missing for the area closest to the indenter tip as the area was too deformed, and the measurement errors prohibited misorientation correlation. Similar recognition issues had been identified in stress and rotation maps. The GND maps were used as an aid to recognize how the material was subject

to plastic deformation: at the outer region of the second pass, shown in Figure 65b, a gradient of GND density decrease was observed which likely suggests that the deformations (rotations or recrystallisation) were 'passed' through layered structure while similar gradients were not observed for 5 or 10 passes (Figure 65c and Figure 65d).

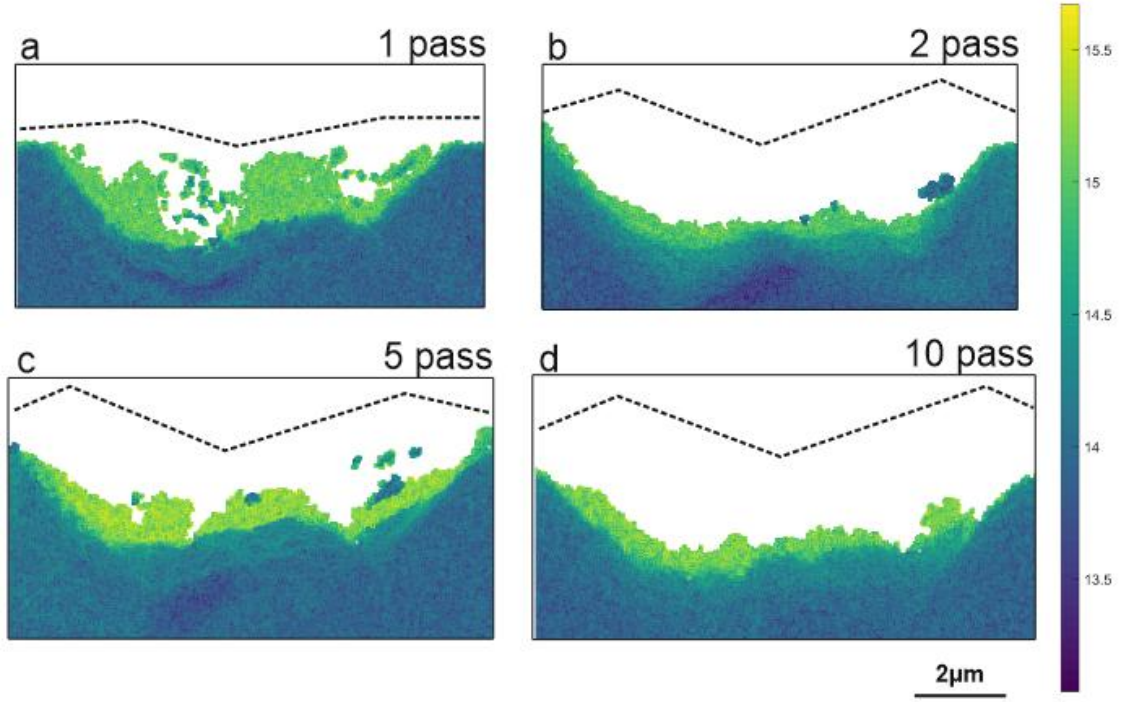



*Figure 65 GND density maps of 20mN Berkovich tip scratches under different cycles of loading on same Ni600 grain. A, b, c, d correspond to 1 pass, 2 pass, 5 pass and 10 pass. Unit was in logarithmic scale and corresponded to $10^{13}$ to $10^{16}$ Geometrically Necessary Dislocations (GNDs) per square meter.*

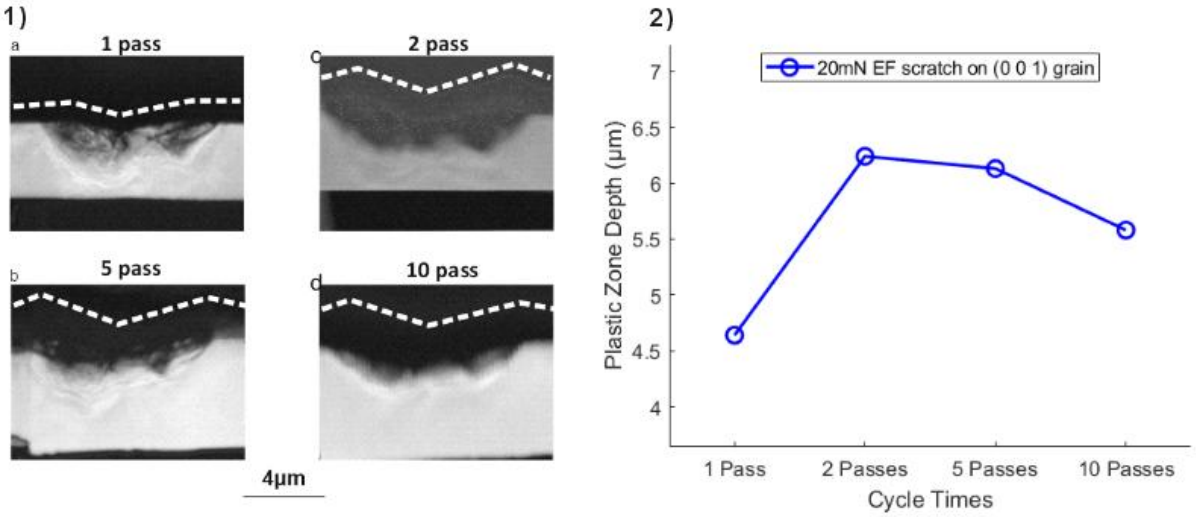


*Figure 66 1) Image quality maps of 20mN Berkovich tip scratch lift-outs under different cycles of loading on same Ni600 grain. White colour indicated area with best signal while dark black suggested no signal due to the severe deformation or presence of platinum protection layer. Dotted lines noted the location of the groove surface. 2) Depths of plastic zone plotted against number of scratch cycles measured using quality maps.*

Shown in Figure 67, after the initial pass, the lattice on both sides rotated away from the centreline both around the $x_3$ and $x_1$ axis as shown by the $\omega_{21}$ and $\omega_{32}$ maps (Figure 67a and Figure 67c), consistent with the suggestion above that the material was ploughed away from the indenter by the two side facets. For the 1 pass 20 mN edge-forward scratch, a clockwise rotation was observed in the $\omega_{13}$ map (yellow region in the Figure 67b), consistent with the HR-EBSD result from the single pass edge-forward along lift-out shown in Figure 48a, section 4.7.2. This suggested that the side facets of the Berkovich tip rotated the material around through friction at the initial pass.

After the second pass, $\omega_{21}$ map (Figure 67d) indicated that the material continued to rotate away from the tip about the $x_3$ axis (dark and bright yellow region on two sides). $\omega_{32}$ map (Figure 67f) showed no notable difference with that of the first pass except that the locations of rotations were further into the material. $\omega_{13}$ map (Figure 67e) suggested that the material recognized was rotating in a motion opposite to the motion identified for the initial pass (blue vs yellow area in 1$^{st}$ pass). It was likely that the 'yellow' region identified in the initial pass was still rotating in a similar manner, but the amplitude of rotation was too big to be cross-referenced by the HR-EBSD while the material with opposite motion was driven by the yellow region through friction instead of directly by the tip. The rotations maps suggested that at the second pass, while the tip could still deform new materials, the movement of the newly deformed materials was not influenced directly by the tip but by the previously deformed structure.

After five passes, 'zones' of material with the same direction of rotation were found next to the zones of opposite direction both in $\omega_{21}$ and $\omega_{32}$ maps as shown by the red and blue

boxes in Figure 67g and Figure 67i, and the locations of rotation The zones in the omega sub 21 map were found to correspond with the locations of opposite rotation zones in the omega sub 32 map. Compared to two passes, the area of clockwise rotation was enlarged in the omega sub 13 map, with the area of opposite rotation beneath (the thickened dark blue and bright yellow region in Figure 67h). After ten passes, the trends of rotations were indistinguishable in any of the maps. Starting from the fifth pass, the interactions between the deformed structures were more evident and likely the small increments of depth observed were due to the reorganization of the deformed structure.

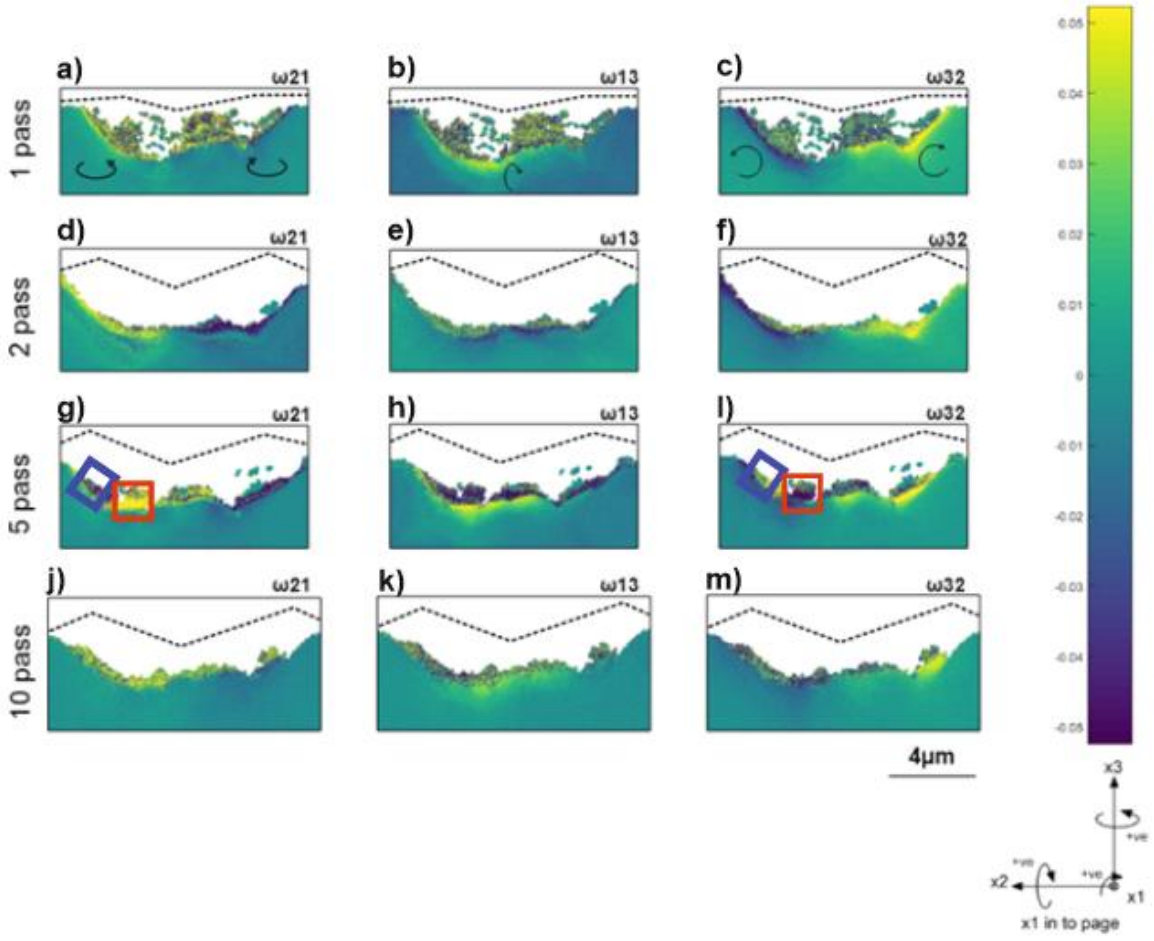



*Figure 67 HR-EBSD rotation maps of 20mN Berkovich tip scratches under different cycles of loading on same Ni600 grain. $\omega_{21}$ maps suggested horizontal rotations around vertical axis. $\omega_{13}$ maps characterised vertical rotation around $x_2$ axis and $\omega_{32}$ maps denoted in-plane rotation around $x_1$ axis. The yellow area indicated positive sign rotations, while the blue area suggested negative rotations. The unit of the scale bar was radian.*

Shown in Figure 68, $\sigma_{11}$ stress map (Figure 68a) suggested that after the initial pass, tensile stress was observed on both sides of the scratch groove (marked by the yellow region in Figure 68a). $\sigma_{22}$ map (Figure 68b) indicated that a layer of compressive stress was seen (dark blue region in Figure 68b) on top of another layer of tensile stress (yellow region in Figure 68b), again consistent with the side observation in Figure 48a at section 4.6.2. $\tau_{12}$ map (Figure 68c) suggested that a layer of anticlockwise shear stress was found right beneath the unidentifiable plastic zone with greater magnitude at the right-hand side. However, the layer of clockwise shear stress sitting beneath was found with greater magnitude at the left-hand side (dark blue region in Figure 68c). The shape of the shear stress distribution was found to match loosely with that of vertical stress distribution.

After the second pass, similar distributions were found in both vertical and horizontal stress: a thin layer of tensile stress was followed by a w-shaped compressive stress zone beneath, which was then surrounded by a bigger zone of tensile stress (dark blue region in Figure 68d and Figure 68e). For shear stress, the shape of distribution was almost identical to the previous two except that within the w-shape, multiple layers of opposite-sign stress were seen stacked on top of each other (alternating blue and yellow regions in Figure 68f), which further indicated that the originally deformed structure was driving the motion of the new deformed structure through shear stress. To illustrate, the tip likely exerted an anticlockwise shear stress on the material closest to it, while that material exerted a shear stress in the opposite direction to the surrounding material.

After five passes, similar to the observations in the rotation map, zones of stress with the same sign were located next to zones of opposite sign stress (boxed regions in (boxed regions in Figure 68g and Figure 68h). After 10 passes, the zones of stress with the same sign ceased

to exist, and stress became randomly distributed across all three maps (Figure 68j - l). Reference points were taken from the same locations as the GND maps shown above. Because of time limitations in the present HR-EBSD analysis, the grain rotation maps mainly depicted deformation related to sliding on certain crystallographic planes. As a result, additional crystal plasticity deformation methods like twinning or grain boundary sliding, not limited to conventional slip systems, were not completely addressed or included in the current analysis.

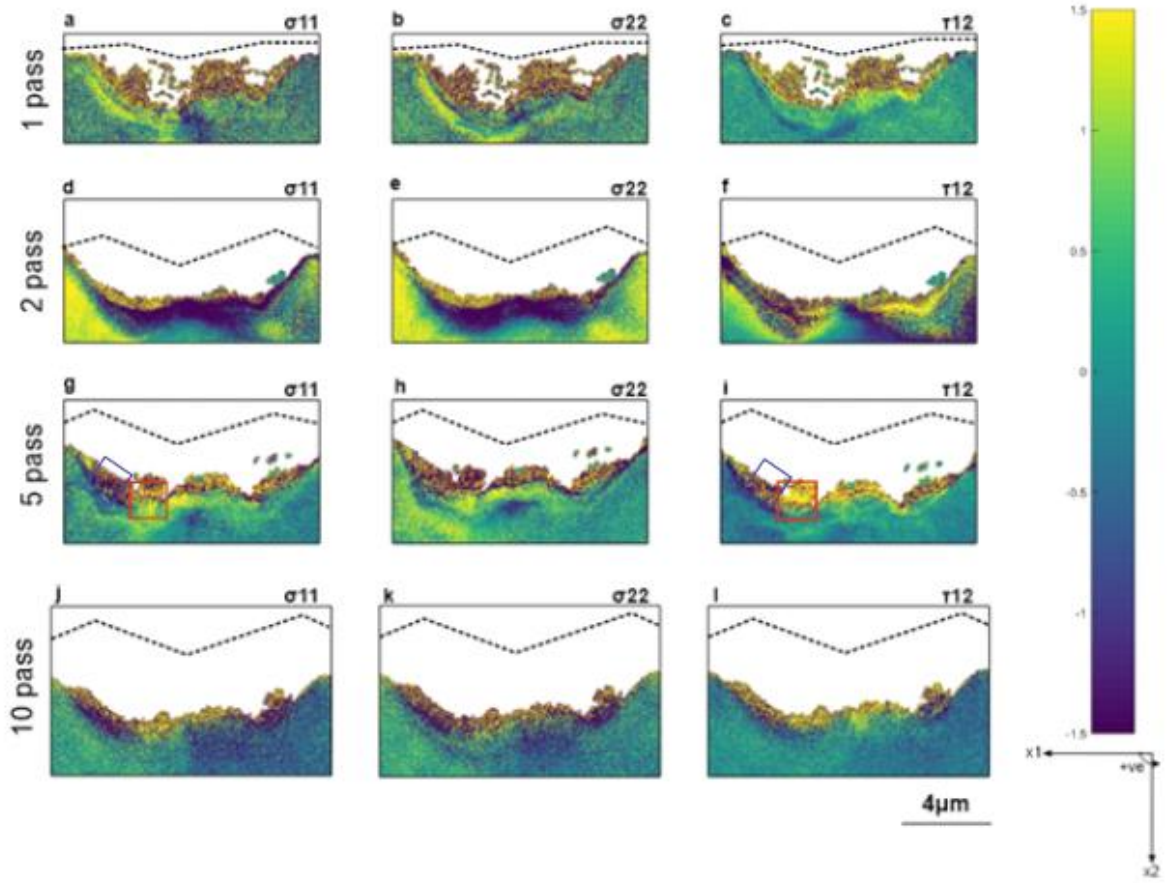



*Figure 68 Stress distribution of scratches under multiple passes of loadings. $\sigma_{11}$ map showed the stress in the horizontal direction and $\sigma_{22}$ map showed stress in the vertical direction. $\tau_{12}$ map indicated the rotating shear stress. The yellow area indicated tensile stress in $\sigma_{11}$ and $\sigma_{22}$ maps anticlockwise shear stress in. $\tau_{12}$ maps. The blue area suggested compressive and clockwise shear stress. The unit of the scale bar was GPa.*

### *5.3.2 Discussion*

HR-EBSD analysis was conducted on FIB machined lift-outs from the plastic zones of scratches subjected to varying cyclic loads. This aimed to reveal the mechanisms governing observed depth stabilization. As hypothesized previously, initial scratches may have induced crystalline shattering of single grains into nanocrystalline structures [137]. It was initially assumed based on the stress concentration theory that at the bottom tip apex there would exist a plastic zone bigger than that of the two flat side walls of the Berkovich tip in edge-forward scratches, however w-shaped plastic zones instead of V-shape plastic zones were observed in different experiments as shown in Figure 65 (GND map). A potential explanation is that the local abundance of GNDs at the tip apex in edge-forward scratches might have hardened the material near the bottom apex and prevented stress from propagating.

Rotation field maps at following passes suggest additional cycles further rotated the deformed material formed during initial plastic deformation. However, in the plastic zone, the high density of GNDs limits the volume of influence per cycle relative to the initial pass. Supporting this theory, alternating shear stress signs across layers appear in the $\tau_{12}$ map of 2nd pass. Anisotropic grain properties likely enabled easier rotation along certain orientations, giving more discernible outer rotation zones in $\omega_{21}$ map than in $\omega_{32}$ map after the second pass. Dislocations generated at interfaces between oppositely rotating zones exerted outward stresses on the surrounding material. This was manifested as stress separation lines between opposing layers in $\sigma_{11}$ and $\sigma_{22}$ maps. Despite the tendency for coordinated rotation, individual grain variations led to the formation of sub-zones of rotation and stress fields by the fifth pass which were seen as the zones with opposite colours adjacent to one another, shown in boxed areas of Figure 68g and Figure 68i. Further randomization of deformed material eventually interlocked each other, preventing additional penetration of the tip. With consistent tip

geometry, incremented load required proportional expansion of the randomized deformed material and their interactions to reach stabilization. This suggested a consistent “stabilised” hardness ratio between applied load and the volume of deformed material can be achieved. However, exceeding a threshold normal load for a given tip size likely enabled penetrating additional undeformed material during every cycle, preventing the deformed structure from fully balancing loads and a stabilised hardness might not be attained, which was yet to be testified and may require additional instrument as it likely exceeded the depth that the AFM in this study was able to probe into. This could be more of a macroscale wear process where run-in is achieved.

Despite efforts to minimise variations between scratches, lift-outs were taken from different sample locations. Therefore, the second pass did not strictly constitute continued evolution from the first. Notably, the 10-pass plastic zone in this case appeared slightly shallower than the 5 pass. An alternative approach is making an initial long scratch and then re-scratching sequential portions of this scratch to different total cycle counts. This better ensures identical initial loading conditions prior to additional cycles. For example, an initial scratch of 100 μm, length would be performed with the first 50 μm only scratched twice. This approach regrettably was not adopted as performing 1, 2,5 and 10 pass scratches on a single scratch would require a scratch with a length of at least a few hundred microns long, and it would be difficult to find one grain that is large enough to contain that and its repeats. Lift-outs taken were all subject to stress relaxation as the formerly compressed material on two sides was milled away. This potentially modified the stress and rotation distributions. However, the planar primary stresses and shear stresses analysed here were likely to be minimally affected by out-of-plane stresses.

Further verification of the hypothesized nanocrystal rotation mechanism requires higher resolution techniques like transmission Kikuchi diffraction (TKD) and transmission electron microscopy (TEM). Liu et al. demonstrated that near-surface wear-induced nanocrystals can measure just tens of nanometres [112] , while stacking faults occur on the nanometre scale [116]. SEM probes interaction volumes spanning hundreds of nanometres, encompassing multiple nanocrystals and makes EBSD analysis difficult. While TKD and TEM can better resolve local nanoscale features, subsequent HR-EBSD might be challenging. HR-EBSD cross-correlates the deformed region with a reference to highlight relative stress and rotation distribution, while stored strain and stress in the reference point directly impact the calculation of magnitudes and spatial profiles of stress. In the severely deformed near-surface region, selecting an appropriate reference area is difficult. An algorithm was proposed by Koko et al. [117]to automatically select reference points providing the most precise per-grain tensor measurement, which may aid rotation field analysis of scratch-induced nanocrystals.

This study assumed that the area function derived from indentation is maintained over the cycles with the only difference being penetration depth, while Li et al. recognized that face-forward scratch tests involve a reduced front and side facet contact area on subsequent passes as less material extrudes ahead or flows around the tip [116]. However, this conclusion is unlikely to be sustained for the metallic material used in this study as AFM scans of the residual groove suggest that smooth surfaces are constantly maintained, while in Li et al.'s study, voids were identified on the corrugated scratch surface, both of which reduced the contact area in following passes. Accurately determining contact area proves critical for quantifying scratch hardness but direct in-situ observation was not accessible. This study attempted to represent the effective contact area in subsequent passes with area difference in each pass, but the scratch hardness derived in this way is still hard to interpret. Simulation

constitutes the most viable route for tracking the evolution of contact areas by exporting history outputs.

While simulation enables otherwise inaccessible in-situ measurements, developing fully accurate models is challenging. Conventional FEA packages like Abaqus lack micro-scale dislocation representations. Instead, aggregate dislocation effects are represented through strain hardening in constitutive equations like Johnson-Cook. CPFEM approaches can incorporate dislocation features but rely heavily on precise material characterization - slip systems, directional critical resolved shear stresses, elastic constants, etc. This poses difficulties for complex multi-phase alloys like Ni718. Modelling cyclic scratch-induced phenomena like grain shattering and subsequent propagation of rotations across boundaries could be beyond the limit of existing frameworks. Simplified model systems such as single-grain copper could facilitate initial implementation, but the capability of CPFEM to capture grain refinement and their subsequent rotations has yet to be assessed.

While the repetitive nanoscratching conducted provides an improved representation of real-world wear processes, it remains a highly idealized model. In practice, subsequent scratch passes often occur at an angle or near existing tracks and work by Li et al., demonstrated that inter-scratch spacing affects elastic recovery rates [116]. More work is needed to bridge the gap between experiments and reality.

## 5.4 General Discussion

This chapter investigated the progressive surface deformation mechanisms in Ni600 under multi-pass nanoscratching, an attempt to bridge controlled laboratory experiments with real-world wear processes. It was shown that repeated scratching at the same location induces cumulative subsurface damage, with the incremental penetration depths of each pass consistently decreasing. It was further demonstrated that while initial passes generate significant plastic deformation and increase dislocation density (evidenced by GND maps), the size of the GND-dense zones stopped increasing, pointing to a shift from bulk plasticity to a redistribution of existing dislocations.

The decrease in scratch hardness, calculated using the conventional contact area definition based solely on total penetration depth, paradoxically suggests material softening. This contradiction potentially arises from an overestimation of the true contact area in later cycles, where the tip interacts primarily with rotating work-hardened regions relocated from the bottom apex. The proposed alternative contact area model—using the difference in contact areas calculated from the conventional definition—partially resolves this discrepancy but requires close observation of the microstructure beneath the deformed surface to account for the increased scratch hardness calculated.

HR-EBSD analysis described the microstructural evolution that led to the observed depth stabilization effect: initial passes induce pronounced grain rotations and shear stress gradients, while a correlation between the stress and rotation maps suggests that the energy in subsequent passes was likely dissipated through rotations driven by shear stress induced by friction between the tip and the deformed surface. However, the hypothesis of a transition

from dislocation-driven plasticity to reduced deformation led by grain rotations requires characterization tools with higher resolution, as grain refinement and the movements of the refined grains were not directly observed.

It is acknowledged that the multi-pass nanoscratch test applied is still a highly idealized experiment, far from being representative of real-world wear processes. Future studies should integrate in-situ characterization of the scratch process, as the transient wear process in this study was still deduced based on the results. A quantitative correlation between nanoscale dislocation dynamics and macroscale wear rates may be achieved through multi-scale modelling combining CPFEM with discrete dislocation dynamics.

## 5.5 Conclusions

1. An alternative definition of the effective contact area was proposed to address the decreasing hardness obtained using the traditional projected area based on total penetration depth, which contradicts the work-hardening theory.
2. GND maps from HR-EBSD analysis suggest that plastic zones expanded during initial passes but stopped after the fifth cycle, indicating a transition from bulk plastic deformation to localized dislocation reorganisation.
3. A grain rotational theory is raised to explain the evolving stress and rotation field observed in HR-EBSD results of the deformed region. It pointed to an interlocked nanocrystalline structure that persisted deformation through inter-grain frictions, which is to be further verified with characterisation tools with higher spatial resolution.

# 6. Retrieving material properties from nanoindentation tests with machine learning

## 6.1 Necessity of bespoke machine learning model for nanoindentation

The fast-developing topic of the machine learning model has proven effective in predicting the material constants from experimental data. However, no attempts have targeted specifically predicting Johnson-Cook (JC) constitutive constants using indentation experimental data. Conventional JC constant determination requires specialised sample preparation and testing under various conditions (e.g. strain rate, temperature etc). Nanoindentation provides an attractive alternative, requiring minimal material while confining surface damage to several microns, easily removed by polishing, and can achieve multiple strain rates in one test. The technique's accessibility and sample efficiency suggest merit in developing machine learning approaches to infer JC constants solely from nanoindentation results which would enhance flexibility in applying the JC model to new alloy systems.

Conventional approaches to derive Johnson-Cook parameters for new materials involve identifying the closest literature reference as an initial guess for feasible constant ranges. Finite element optimisation then iteratively refines constants until alignment with experimental indentation results. This manual calibration can be time-intensive for models with multiple fit parameters and is subject to user discretion – a perfect fit is not always obtainable, and the user needs to decide the preferred set of constants. HyperStudy [118] enables automated numerical optimization by coupling sensitivity analysis and design of experiments. This strategically selects simulation input combinations to maximize information gain per FEA evaluation. However, acquisition costs and software/FEA

compatibility issues can constrain adoption. Developing a machine learning model capable of retrieving material constants from nanoindentation results would greatly reduce the time and cost of building a Finite Element Model that accurately represents the experiment of interest.

## 6.2 Building Finite Element Analysis (FEA) Model

The FEA Model used in this study was built with Abaqus 2022, in which the engineering simulations are facilitated by several interconnected modules: Part (defines the geometry of the object under study), Properties (assigns material properties to the geometry), Assembly (organises multiple components into a cohesive system), Interaction (specifies the mechanical and physical interactions between components), Steps (divides the analysis into logical sequences for applying loads and boundary conditions) and Mesh (conversion of the continuous geometric domain into a finite set of elements for mathematical analysis).

### *6.2.1 Part Geometries and Material Properties*

The sample was represented by a 100 μm diameter, 50 μm tall cylinder in nanoindentation simulations. The sample in the FEA model is significantly smaller than the experimental sample, as in the experiment, only the region in the vicinity of the tip (usually up to 10 times the penetration distance) is deformed. Including the undeformed materials in the FEA model would substantially increase the computational cost. The diamond spherical tip with a nominal radius of 20 μm is characterised by a hemisphere with a 20 μm radius, while the Berkovich tip has a base length of 20 μm and a height of 2.66 μm from the apex to the base surface, as shown in Figure 69.

As the length dimension used in this model is μm, the material density used was set as 0.00847, representing 8470kg / $m^3$. Poisson's ratio and elastic modulus were 0.31 and 207GPa (input as 207000) from manufacturer spec sheet [101]. Johnson-Cook plastic hardening was selected, and a parametric study will be presented in the following chapters.

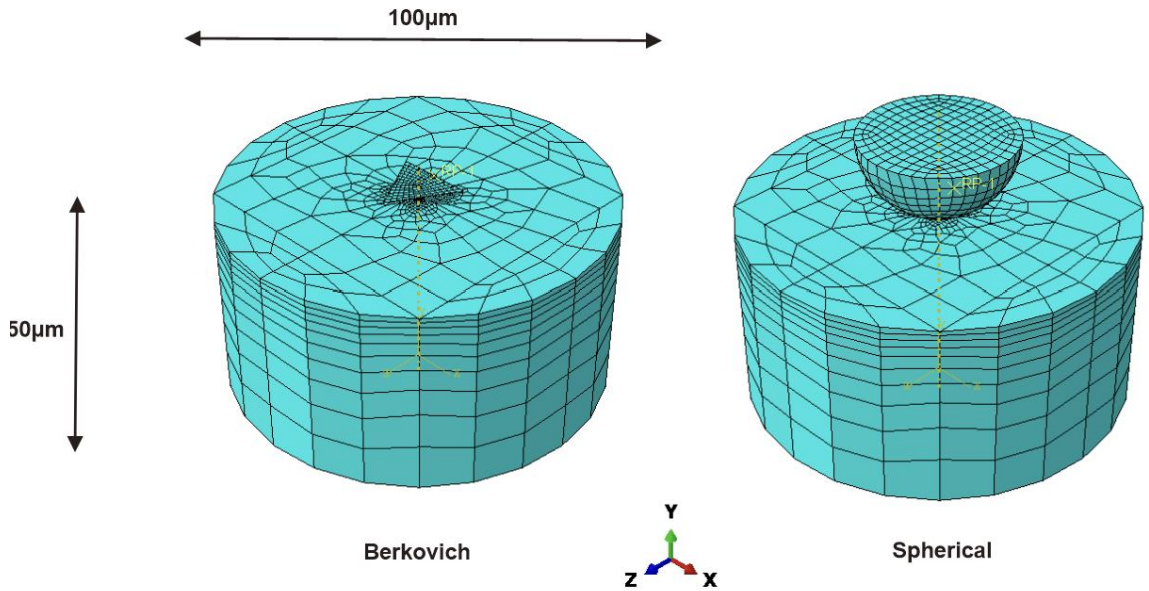



*Figure 69 Schematic of the nanoindentation model with Berkovich tip with base length of 20 µm and height of 2.66 µm and spherical tip of 20 µm nominal radius. Tips and samples are meshed.*

To verify the predictions made by the machine learning model, another nanoscratch model in Abaqus was made as shown in Figure 70. The assembly comprised a sample with dimensions of 50 µm x 14 µm x 10 µm and a Berkovich indenter with a base triangle side length of 20 µm and a height of 2.66 µm. Similar to a nanoscratch experiment, the tip would load to 20 mN at the starting position with a load time of 5 seconds, and then it starts moving laterally at a rate of 1 µm/s for a scratch length of 20 µm. A hard contact assumption was employed for the interaction between the sample and the tip.

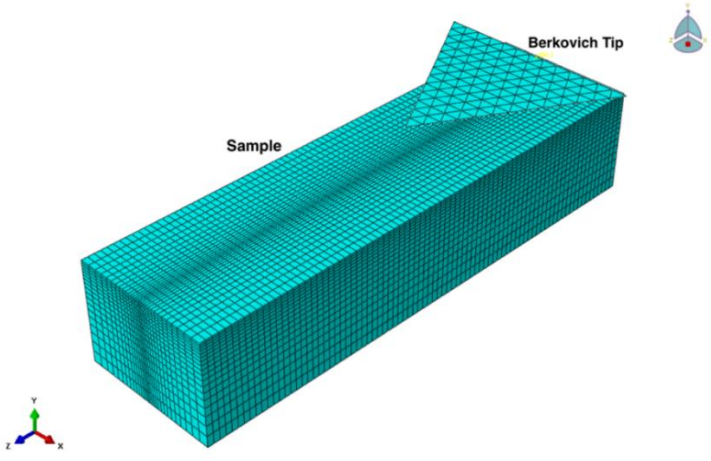



*Figure 70 Schematic of the Abaqus model in scratch test*

### *6.2.2 Steps*

In Abaqus, the solver used has a critical influence on the time it takes for simulation to complete and the outputs. Two primary solvers are incorporated in the Abaqus: the general (or standard) solver and the explicit solver. The Abaqus general solver employs an implicit integration scheme. This means the solver must solve a set of algebraic equilibrium equations at each time increment, relating forces to displacements. Specifically, it solves:

$$[K]\{u\} = \{F\} \#(24)$$

where $[K]$ is the stiffness matrix containing information about the stiffness of all elements, $\{u\}$ is the vector of nodal displacements, and $\{F\}$ is the applied load vector. This makes the general solver better suited for static or quasi-static processes, where inertial and damping effects are minimal. Another advantage is the general solver can use much larger time increments as the formulation does not require intermediate equilibrium states. However, the trade-off is that a set of simultaneous equations must be solved at each increment, requiring more memory and processing time per increment.

In contrast, Abaqus' explicit solver uses an explicit central difference integration rule. There is no need to solve a system of equations - instead, nodal accelerations can be calculated directly from the governing equations of motion:

$$m\{\ddot{u}\} = \{F\} - [C]\{\dot{u}\} - [K]\{u\} \#(25)$$

in which $m$ is the mass matrix, $\{\ddot{u}\}$ is nodal acceleration, $[C]$ is the damping matrix, and $\{\dot{u}\}$ and $\{u\}$ are the nodal velocity and displacement vectors, respectively. This formulation is ideal for complex nonlinear simulations with many short duration dynamic events, such as impact and blast problems. As no system of equations needs to be solved, there is much less memory is required. However, very small time increments are needed for stability, significantly increasing solution time for longer quasi-static processes.

This study initially selected a standard solver due to the quasi-static nature of the nanoindentation test but is subsequently changed to dynamics to create a larger database for subsequent machine learning model training – with the same model, the standard solver requires 5 minutes to finish one iteration while dynamics alternative takes 30 seconds. The computational time was reduced through mass scaling, in which the element mass was arbitrarily increased to increase the stable time step. It should be additionally noted that the use of the Johnson-Cook damage model is only allowed with a dynamics solver, while CPFEM only functions with a standard solver.

### *6.2.3 Assembly, Boundary Conditions, and Interactions*

In both models, the tips were positioned on top of the centre of the sample part as shown in Figure 69 and Figure 70 while a hard contact was defined where no penetration of the master surface (diamond tip surface) was allowed. The interfacial friction coefficient was adopted as 0.15 from previous literature [119]. For ease of computation, the tips were defined as rigid bodies that do not deform. Tips were loaded at 20 nm/s across a 100-second time span up to 2000 nm penetration depth, and no tip rotations were allowed. The bottom of the sample was defined as 'Encastre' which no rotations or movements were allowed. No boundary conditions were applied on the side walls of the sample but the sample was designed to be large enough that the walls at far end were close to stress free and had minimal impact on the material response.

### *6.2.4 Mesh and Convergence Study*

The indentation sample consisted of 7032 C3D8R elements (8-node bricks with reduced integration and hourglass control), and the scratch sample contained 31872 elements of the same type. The Berkovich tip and spherical tip used had 427 and 1100 C3D8R elements which were set as rigid and did not experience deformations. The finest 0.3 μm edge length meshing adjoined the tip, coarsening with distance. Increasing mesh density near contact areas was essential for accurately capturing stress concentrations and contact mechanics and ensuring numerical stability, as these regions exhibited more aggressive behaviours under load. Mesh convergence studies were performed for all three models used to ensure the results were not dependent on the mesh size but rather represented the actual physical behaviour of the model. The initial simulation was executed with a coarse mesh and the mesh was gradually refined until further refinement resulted in negligible changes in the measured

output. For the convergence study published by Johnson-Cook constants of Inconel 718 were used with $A$ = 1241 MPa, $B$ = 622 MPa, $n$ = 0.652 [120] The Johnson-Cook hardening model would be introduced with more details in the upcoming section.

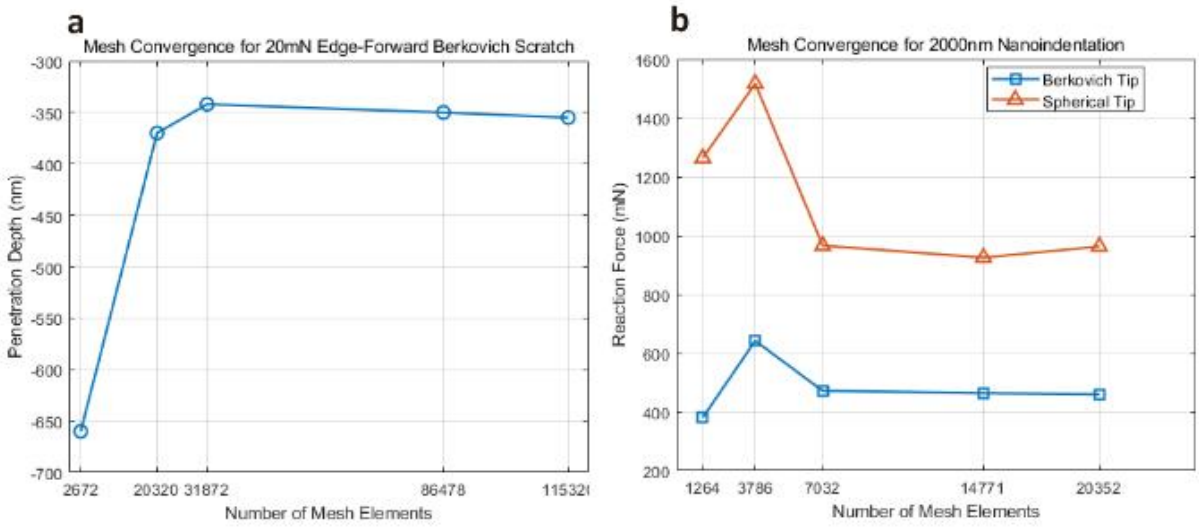



*Figure 71 Mesh convergence studies for 20mN edge-forward Berkovich tip nanoscratch simulation and nanoindentation simulation with Berkovich tip of spherical tip of 20-micron radius. Johnson-Cook constants for Inconel 718 were applied.*

## 6.3 Parametric Study of Johnson-Cook Constants in FEA model

Johnson-Cook constitutive equation consists of 5 parameters: *A* (yield stress), *B* (strain hardening coefficient), *C* (strain rate hardening coefficient), *n* (strain hardening exponent) and *m* (thermal softening exponent), additional to the *E* (elastic modulus) and *v* (Poisson Ratio).

$$\sigma = (A + B\varepsilon^{n})\left(1 + C\ln\dot{\varepsilon}^{*}\right)\left(1 - T^{*^{m}}\right)\#(26)$$

Each material has a unique combination that is capable of characterising its hardening/softening behaviour under loaded/heated conditions. In FEA, it is possible to alter the parameter individually to investigate its influence on load/displacement response in nanoindentation tests. To achieve this, published Ni601 Johnson-Cook constants are used as an initial guess of the material constants and varied over ±50% range, segmented over four intervals per variable to generate the 1024 distinct material parameter sets for simulations. Owing to the sufficiently low strain rates in nanoindentation testing, the strain rate coefficient parameter C was excluded from the parametric analysis. Nanoindentation simulations were performed with the spherical tip of 20 μm nominal radius.

It should be noted that this model does not inherently account for the plasticity size effect as it is fundamentally based on classical continuum mechanics, which assumes that material behaviour is independent of the size of the structure being analysed.

### *6.3.1 Influence of Yield Stress (A)*

Increasing the yield stress constant A from 212.15 MPa to 636.6 MPa in four equal intervals of 141.5 MPa incrementally raised the simulated resistance load, equivalent to indentation hardness, from 66 mN to 113 mN, as shown in Figure 72. The approximately linear 16 mN increase per yield stress step agrees with expectations, as the *A* parameter is a multiplier between the strain and equivalent stress in the Johnson-Cook constitutive relation.

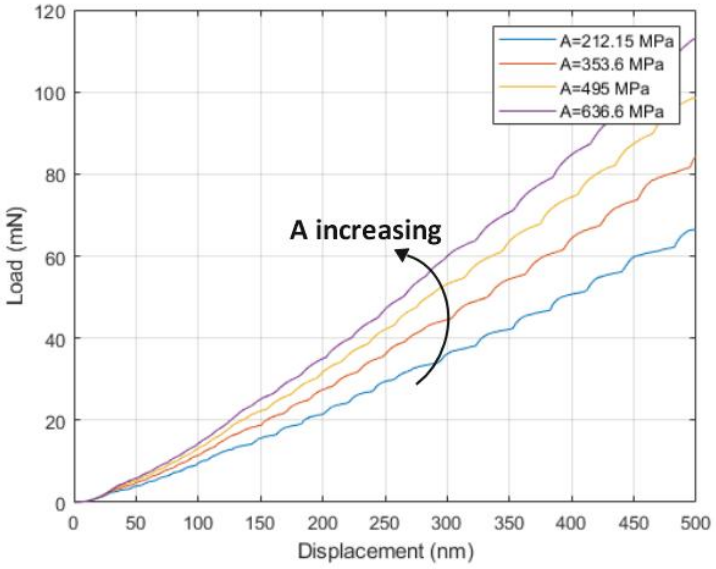



*Figure 72 Simulated load/Displacement curves of varying yield stress A. B=748.2MPa, v=0.258, E=104.6 GPa and n=0.419.*

### *6.3.2 Influence of Straining Hardening Exponent (B)*

The strain hardening exponent *B* plays a similar role to the yield stress *A* parameter in the Johnson-Cook equation. Systematically varying *B* induces an approximately linear increase in the simulated resistance force at maximum indentation depth, shown in Figure 73. However, its proportional influence proves lower in magnitude compared to yield strength. This agrees with the JC equation, as *B* serves as coefficient for the plastic strain term rather than contributing a direct stress component.

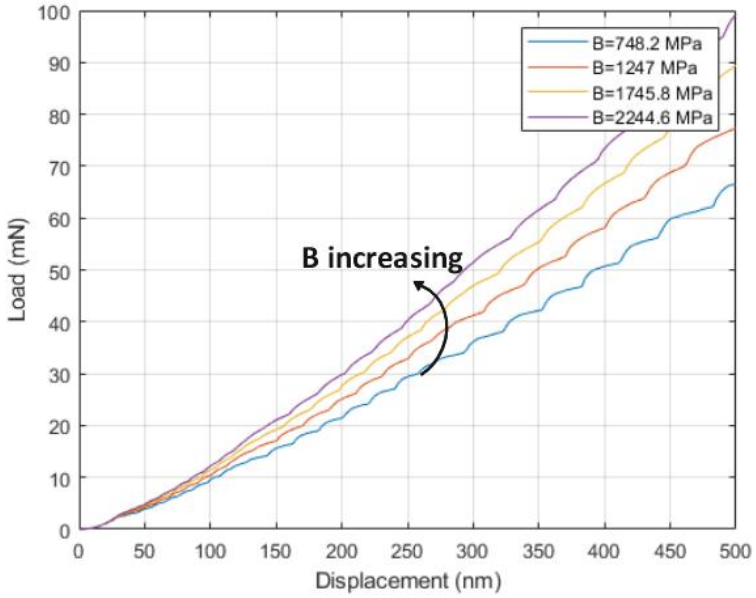



*Figure 73 Simulated load/Displacement curves of varying yield stress B. A=212.15MPa, v=0.258, E=104.6 GPa and n=0.419.*

### *6.3.3 Influence of Elastic Modulus (E)*

Young's modulus represents an independent input governing elastic material behaviour, rather than merely a parameter within the Johnson-Cook constitutive relation. While it imposes a threefold increase over the examined range, it results in only a 25% increase in the final load, as shown in Figure 74. This suggests that the plastic deformation mechanisms described by the Johnson-Cook equation more significantly influence indentation hardness predictions than elastic properties for a given displacement. Subsequently, it is not included in the machine learning training as it is well known for Nickel, being unaffected by the microstructure and low levels of alloying, as suggested by the measurements in the nanoindentation section.

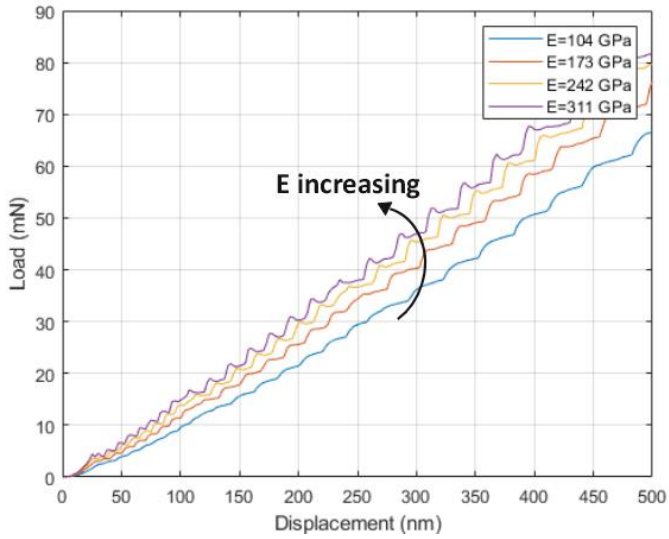



*Figure 74 Simulated load/Displacement curves of varying elastic modulus E. A=212.15MPa, B=748.2MPa, v=0.258, and n=0.419.*

### *6.3.4 Influence of Hardening exponent (n)*

The indentation hardness decreased nonlinearly with the increase of hardening exponent *n*, suggested by Figure 75. In reality, materials with high *n* are often associated with the continuous transition from elastic to plastic behaviour, while the changes are more abrupt for materials with low *n*. Ni601 has an *n* of 0.837, and that of copper is 0.31 [66].

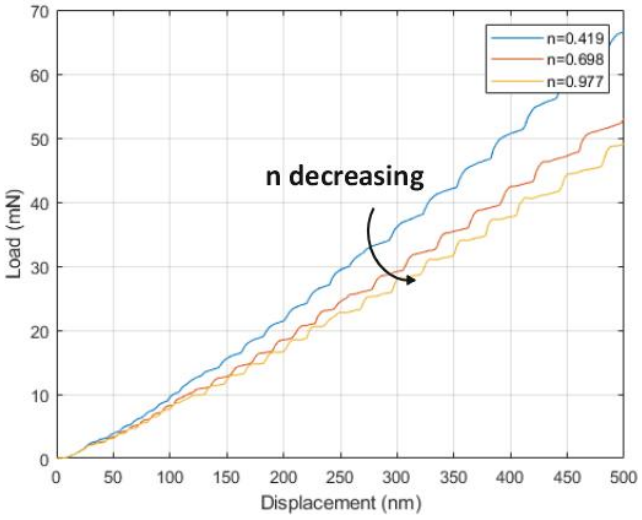



*Figure 75 Simulated load/Displacement curves of varying hardening exponent n. A=212.15MPa, B=748.2MPa, v=0.258, and E=106 GPa.*

### *6.3.5 Influence of Poisson's Ratio (v)*

Poisson ratios are often not discussed together with the material hardness and indeed, it shows minor influence on the loads measured except at $v$ = 0.465, where it is close to behaving in an incompressible manner when deformed elastically, as suggested by Figure 76.

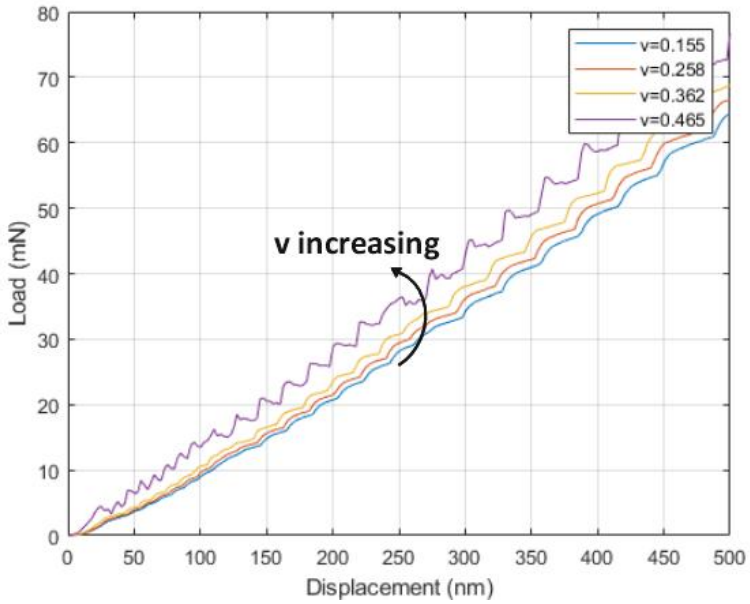



*Figure 76 Simulated load/Displacement curves of varying hardening exponent v. A=212.15MPa, B=748.2MPa, n=0.419 and E=106 GPa.*

Another key observation is the wave-like structure in the load-displacement curves, whose amplitudes were intensified with the increase in Poisson ratios and elastic modulus. This was likely caused by the 'contact stiffness oscillation' in finite element modelling, which occurs due to the discretised nature of the model's mesh and contacts. At each load increment, new elements reach the contact stress limit successively and are added to the contact interface, increasing the contact area and stiffness in a stepwise manner, which produces the non-smooth load-displacement behaviour. It was more obvious with higher elastic modulus since smaller displacements were needed to activate the step changes in the contact area and stiffness, and, at lower elastic modulus, the surface smoothly conforms to the indenter geometry with less discrete node pick-up and reduces the oscillation effects. Similarly, at a

higher Poisson's ratio, the mesh elements were near incompressible, which also magnifies the stepwise increments in contact stiffness due to localised stiffening. It is also not included in the subsequent machine learning training for a similar reason with elastic modulus.

## 6.4 Machine Learning Theories

Machine learning is a subfield of artificial intelligence that involves training computer algorithms to "learn" patterns and make predictions or decisions based on data. The goal is for the algorithms to improve their performance on a specific task as they are exposed to more data. In the context of material properties prediction, Gaussian Process Regression (GPR) and Artificial Neural Networks (ANN) are promising approaches that have been applied in the literature. In general, the main difference between GPR and ANN models is that GPR is a probabilistic, non-parametric method that uses kernel functions to measure similarity between data points and assumes a Gaussian distribution over functions, while ANN is a parametric method inspired by biological neural networks that learns by adjusting the weights of interconnected nodes and makes fewer assumptions about the underlying data distribution [121].

### *6.4.1 Gaussian Process Regression (GPR)*

GPR models the relationship between inputs *X* and outputs *y* as a Gaussian process which defines a distribution over functions f. This is formalised as:

$$y = f(X) + \varepsilon \#(27)$$

where $\varepsilon$ is Gaussian noise. Any finite number of samples from the function *f* are assumed to be jointly Gaussian distributed with some mean and covariance defined by a kernel function k *(x, x′):*

$$f(X) \sim GP\big(m(X), k(X, X')\big) \#(28)$$

A common kernel choice is the Radial Basis Function [122]:

$$k(x, x') = \exp\left(-\frac{1}{2}(x - x')^T \Sigma^{-1} (x - x')\right) \#(29)$$

, in which $k(x, x')$ measures the similarity between input vectors $x$ and $x'$, $(x - x')$ is their difference vector, $(x - x')^T$ denotes its transpose, $\Sigma^{-1}$ is the inverse covariance matrix that defines the kernel's shape and scale, and the exponential function transforms the scaled squared distance into a similarity score. This kernel encodes the inductive bias that function values closer together in the input space are more correlated. Making predictions at a new input *x** involves conditioning the prior GP distribution on the training data to obtain a Gaussian posterior distribution over *f(x*)* with mean and variance giving the predictive mean and uncertainty. The downsides of GPR are the computational cost of inverting the kernel matrix during training, and fragility to mispecifying the kernel for the application.

### *6.4.2 Artificial Neural Network (ANN)*

ANN model, on the other hand, mimics the functionality of biological neurons. Each neuron in an ANN receives a set of inputs, processes these inputs, and produces an output. Mathematically, this process is represented by a weighted sum of the inputs, augmented with a bias term, passed through a non-linear activation function. The output y of a neuron is given by [73]

$$y = f\left(\sum_{i=1}^{n} w_i x_i + b\right) \#(30)$$

where $x = [x_1, x_2, ..., x_n]$ represents the inputs, $w = [w_1, w_2, ..., w_n]$ are the weights, $b$ is the bias and $f$ is the activation function. Activation is crucial for introducing non-linearity into the network and enabling it to represent complex patterns. One of the most used is the Rectified Linear Unit (ReLU), expressed as

$$f(z) = \max(0, z) \#(31)$$

which gives an output of z if input z is positive and output of 0 if z is negative.

Figure 77 shows a simple 3-layer ANN model, in which the input layer receives experiment data, in this case, displacement and load, which is then processed in the hidden layer and returns results in the output layer. In this study, the desired output are the Johnson-Cook parameters.

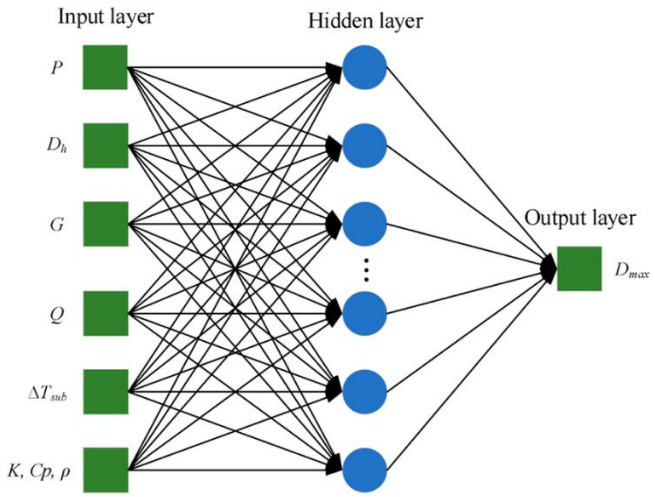



*Figure 77 Schematic diagram of the ANN model* [123].

The learning process in ANNs involves the use of a loss function, such as Mean Squared Error (MSE) for regression tasks or Cross-Entropy Loss for classification tasks, to quantify the difference between the predicted output and the actual output. The optimisation of these networks is typically performed using algorithms like Gradient Descent, where the weights are updated in the opposite direction of the gradient of the loss function.

## 6.5 Machine Learning (ML) Model Training

Artificial Neural Networks (ANNs) are selected as the preferred model for training due to their ability to generate a discrete set of Johnson-Cook (JC) constants as output predictions. In contrast, Gaussian Process Regression (GPR) produces a range of values with associated variances, which cannot be directly employed in subsequent Abaqus simulations without further processing. To facilitate the training process, a comprehensive database of simulation results is essential. The ranges of the JC constants used in these simulations are strategically maximised to encompass all feasible combinations for various alloy materials. This approach ensures that the trained model possesses the capability to accurately identify and characterise alloys belonging to different groups, thereby enhancing its predictive power and generalisation ability. ANN makes it easier to have a single model with multiple outputs, while basic GPR only supports one output, which fits the requirement for this study.

Ranges of JC constants used are $A$ (100 MPa to 1250 MPa), $B$ (200 MPa to 2500 MPa), and $n$ (0.245 to 0.999). Elastic parameters ($E$ and $v$) are excluded from training and prediction, as they are often readily available in the literature and exhibit limited variation within the same group of alloys. Removing variables would also improve the recognition of plasticity constants *A, B, and n*. Each constant range is divided into 15 intervals that end up with 3375 sets of training data sets. A Spherical tip was used in simulations as it covers a larger range of stress/strain during the nanoindentation process with an indentation speed of 20 nm/s to a maximum depth of 1000 nm in 50 seconds. The training process is achieved with TensorFlow 2.11 [124], an automated Machine Learning training platform provided by Google and the commanding codes are shown below in Figure 78:

```python
import os
import numpy as np
import pandas as pd
import pickle
from sklearn.model_selection import train_test_split
from sklearn.preprocessing import MinMaxScaler
from tensorflow.keras.models import Sequential
from tensorflow.keras.layers import Dense, LSTM

def load_data():
    X = []
    y = []
    for i in range(3375):
        df = pd.read_csv(f'converted_{i}.csv', names=['displacement', 'load'], header=None)
        # Check if the first line is empty data or headers
        if pd.isnull(df.iloc[0]['displacement']):
            df = df.iloc[1:] # Skip the first line
        material_constants = pd.read_csv('JC_Combinations_ML5M.csv').iloc[i]
        # Append entire DataFrame values for each simulation
        X.append(df.values)
        y.append(material_constants.values)
    return np.array(X), np.array(y)

# Load the data
X, y = load_data()

# Assume each simulation generates 'timesteps' number of data points
timesteps = X.shape[1]

# Normalize the data
scaler = MinMaxScaler()
X_normalized = scaler.fit_transform(X.reshape(-1, X.shape[-1])).reshape(X.shape)

# Save the scaler
with open('scaler_old_R5.pkl', 'wb') as f:
    pickle.dump(scaler, f)

# Split normalized data into training and testing sets
X_train, X_test, y_train, y_test = train_test_split(X_normalized, y, test_size=0.2, random_state=42)

# Define your model architecture
model = Sequential()
model.add(LSTM(32, input_shape=(timesteps, 2))) # 2 input features (displacement and load)
model.add(Dense(64, activation='relu'))
model.add(Dense(32, activation='relu'))
model.add(Dense(3, activation='linear')) # 3 output values (A, B, n)

# Compile your model
model.compile(loss='mse', optimizer='adam', metrics=['mae'])

# Split normalized data into training and testing sets
X_train, X_test, y_train, y_test = train_test_split(X_normalized, y, test_size=0.2, random_state=42)

history = model.fit(X_train, y_train, epochs=800, batch_size=64, validation_data=(X_test, y_test))

# Step 5: Evaluate the Model
loss, mae = model.evaluate(X_test, y_test)
print(f"Model Loss: {loss}")
print(f"MAE: {mae}")

# Save your model
model.save('trained_R5_Old.h5')
```

*Figure 78 Python code to be used as a command for TensorFlow. Variables and functions are highlighted.*

Prior to the training process, the Min-Max scaling method is employed to normalize the input features, namely load and displacement data, according to the following equation:$Normalized\ Value = \frac{Max-Min}{Value-Min} \#(32)$

where 'Value' represents the original value of the feature, while 'Min' and 'Max' denote the minimum and maximum values of that feature across the entire dataset. This normalisation procedure scales the features to a range between 0 and 1. The primary objective of this normalisation step is to mitigate the risk of the model becoming trapped in local minima and to accelerate convergence during the gradient descent optimization process by ensuring that each feature contributes equally to the decision-making process. The Mean Average Error (MAE) metric is used to evaluate the model's performance in each iteration, which calculates the error of all outputs:

$\text{MAE} = \frac{1}{n}\sum_{i=1}^{n} |y_i - \hat{y}_i| \#(33)$

However, it is important to note that this approach may inadvertently encourage the model to prioritize the minimization of large errors associated with high-magnitude targets at the expense of accuracy on smaller-magnitude targets, such as the parameter '$n$', which has a limited range from 0 to 1. To address this potential bias, the values of '$n$' are scaled by a factor of 1000 as target outputs, effectively matching the magnitude of the other two constants. The experimental data and training dataset are both pre-processed to minimise data discrepancies. The experiments are conducted with controlled strain rates, resulting in a higher density of measurements near the surface, while the simulations assume fixed depth intervals. To reconcile this difference, some of the experimental results corresponding to the near-surface region are excluded to align with the data collection intervals used in the simulations.

The architecture of the neural network comprises an input layer consisting of 32 neurons that receives the load and displacement data from simulations/experiments, followed by two hidden layers with 64 and 32 units which learns complex patterns and relationships within the data by adjusting connection weights during training. The output layer consists of 3 neurons, which predict the Johnson-Cook constants ($A$, $B$, and $n$). Number of neurons and layers are kept to minimum as having overcomplicated structure can lead to overfitting that cause the model unable accommodate the difference between experiment data and simulation data used for training while increasing computational complexity. The tuning parameters, such as the number of epochs, batch size, and training size, are selected based on literature that follows similar approaches [73]. Shown in Figure 79, MAE is recorded throughout the training process, and it was observed that with training iteration times of 800, learning was proved nonlinear - initial sharp error reductions later changed to stepwise descent and eventual stabilization at a ± 50 unit tolerance per predicted constant by the 160th cycle.

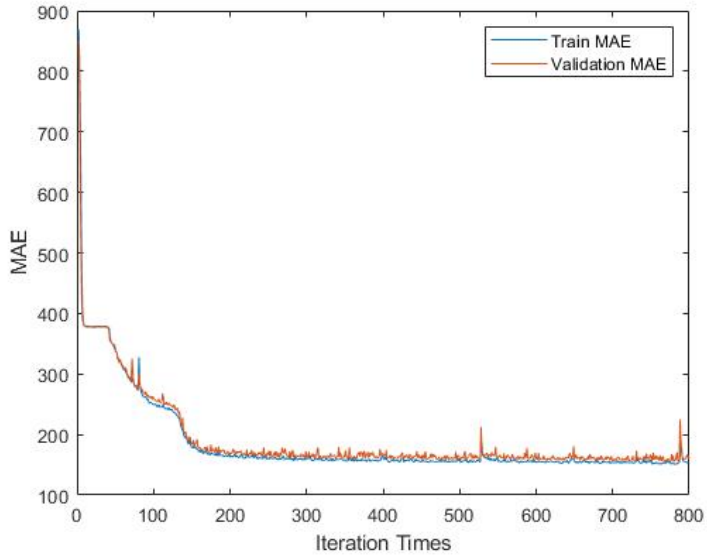



*Figure 79 Changes of Mean Absolute Error against iteration times in training and validation.*

## 6.6 Validation of the Artificial Neuron Network (ANN) Model

A simulation result with known Johnson-Cook constant inputs ($A$ = 250MPa, $B$ = 500 MPa, $n$ = 0.245) was used to test the accuracy of the trained model. The comparison between model predictions and simulation input is shown in Figure 80, in which the $n$ is magnified for 1000x for the convergence purpose. For the given simulation, the ANN model returns outputs of $A$ = 305 MPa, $B$ = 505 MPa, and $n$ = 312 (0.312).

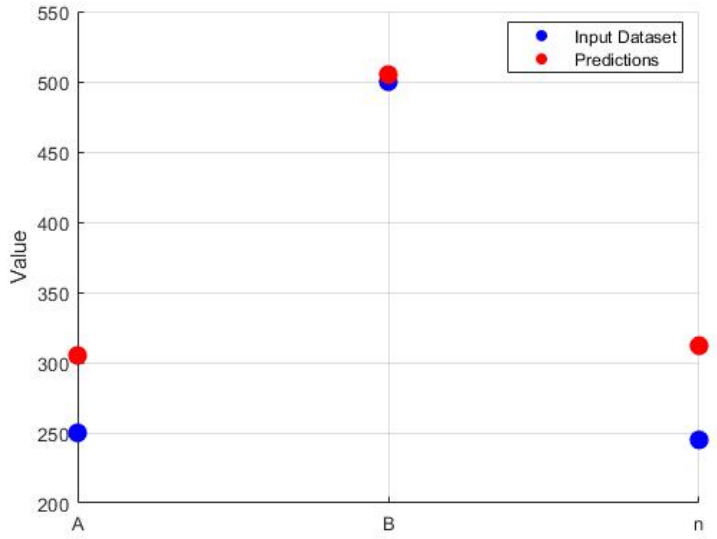



*Figure 80 A comparison of the Johnson-Cook constant predictions from Abaqus simulation results with material properties used.*

ANN model trained has overestimated all three variables A (yield strength), B (strain hardening coefficient) and n (strain hardening exponent) by 55 MPa, 5 MPa and 67, respectively. To investigate if this overestimation was systematic, 30 sets of predictions were plotted against their corresponding input datasets, as shown in Figure 81, with JC constant set ($A$ = 266 MPa, $B$= 616 MPa and $n$ = 0.747) used in simulation highlighted.

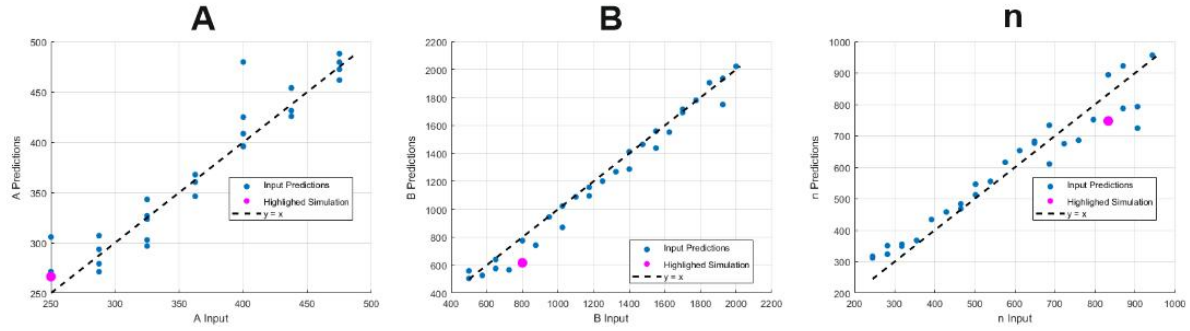



*Figure 81 Predictions of the A, B, and n constants are plotted against their input values, with a dotted line indicating perfect predictions. The model is trained using simulations with a spherical tip of 20 µm radius and tested on simulations employing a tip of the same radius.*

It can be concluded that the ANN model is capable of identifying the Johnson-Cook constants used in simulations with small uncertainty. Perfect predictions are not desired in this case as it would indicate that the model is overfitted and it is likely unable to deal with the discrepancies in experiment results.

However, the simulations used assumed a perfect spherical tip with a known radius, while in reality, spherical tips are rarely perfect spheres with claimed radius as the stiff and hard ceramic materials used in tip fabrication are anisotropic while the shape is crucial for determining the correct contact area. In literature, SEM scans suggested that the tip body is often closer to an ellipsoid shape instead of a spherical segment [125]. To examine the influence of shape deviation on identifying correct constants, the model trained with perfect spherical tip simulations is tested on simulations made with spherical tip subject ± 20% tip radii deviations, and the comparisons of predictions versus input values are shown in Figure 82 (Tip with -20% Radii) and Figure 83 (Tip with +20% Radii). Both Figure 82 and Figure 83 suggest that the model can no longer predict the correct Johnson-Cook constants if the tip geometry used in training differs significantly from the one used in experiment/test simulations. It is evident that accurately representing the tip geometry in the training process

is vital for prediction accuracy. However, it should be acknowledged that a 20% difference in recognised tip radius is severe, and tip calibration is often better than this. While this study represents the spherical tip with fixed radii for the ease of simulation and quantification, in reality, the radii for individual tips are often not constant and change with depth [126].

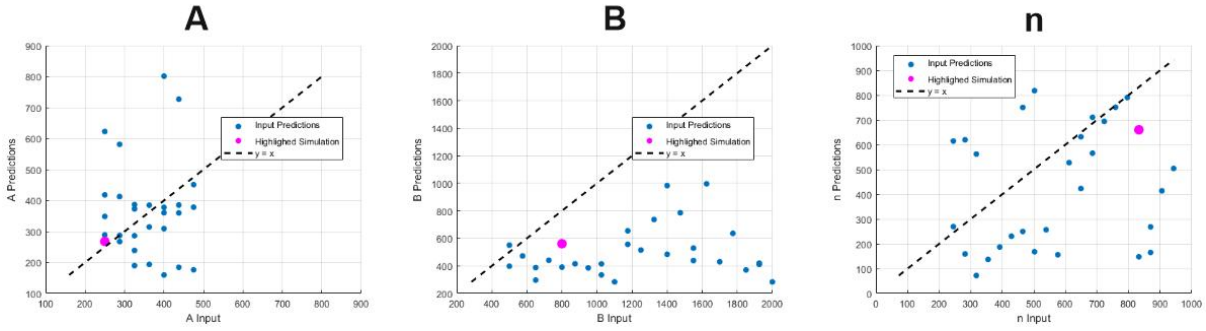



*Figure 82 Predictions of A, B, and n constants are plotted against their input values, with a dotted line indicating perfect predictions. The model is trained using simulations with a spherical tip of 20 µm radius and tested on simulations employing a tip of 16 µm radius.*

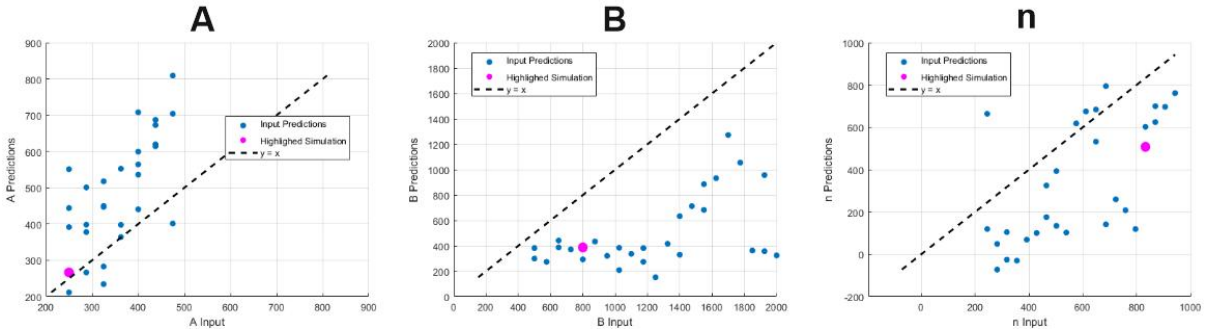



*Figure 83 Predictions of A, B, and n constants are plotted against their input values, with a dotted line indicating perfect predictions. The model is trained using simulations with a spherical tip of 20 µm radius and tested on simulations that utilise a tip with a radius of 24 µm.*

Similar training procedures have been performed with simulations using the perfect Berkovich tip. It should be noted that the Berkovich tip and spherical tip have different hardening characteristics: the sharp, self-similar Berkovich tip has a constant plastic strain while for the spherical tip, there is a progressive increase in strain with penetration depth [127].

A new ANN model was tested with CSM Berkovich tip indentation on Ni600 alloy made by G200 nanoindenter and returned a prediction of $A$ = 339 MPa, $B$ = 1246.5 MPa, $n$ = 0.75. Abaqus simulations using predicted Johnson-Cook constants had good agreement with experiment output in nanoindentation and nanoscratch tests, as shown by Figure 84 and Figure 85.

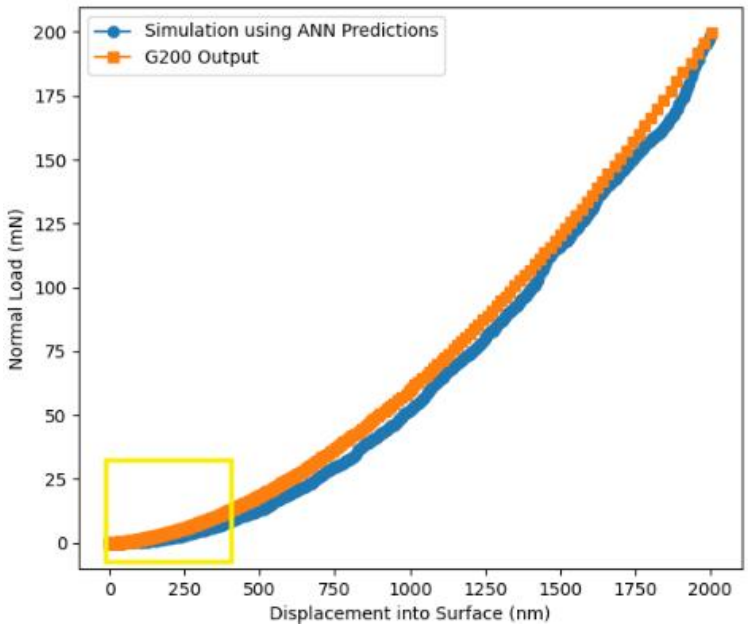



*Figure 84 Comparison of Ni600 Berkovich nanoindentation experiment with simulation using Johnson-Cook constants predicted by the ANN model. Yellow-boxed regions are the near-surface area where Abaqus have limited ability to predict due to the presence of the Indentation Size Effect.*

As shown by the yellow boxed region in Figure 84, Abaqus often underestimated the normal force experienced by the tip at near-surface region (depth below 200nm) as the standard Abaqus model was not able to account for the plasticity size effect since the classical continuum plasticity theories used assumed material behaviour was scale-independent, thereby lacking the necessary strain gradients or size-dependent mechanisms such as activation volume and dislocation nucleation to capture how plastic deformation behaviours change at the nanoscale (the Indentation Size Effect). Data points generated within that region likely would 'confuse' the model during the training process as it would not resemble the data points collected from the nanoindenter, and therefore, the penetration depth in simulations used for training has been intentionally increased to 2000 nm, a depth higher than

the depth experienced in 20mN Ni600 nanoscratch to increase the data points collected in regions away from the near-surface region. The data acquisition rate has also been increased in the experiment as the CSM nanoindentation tests were strain controlled, and fewer data points were collected at higher penetration depth.

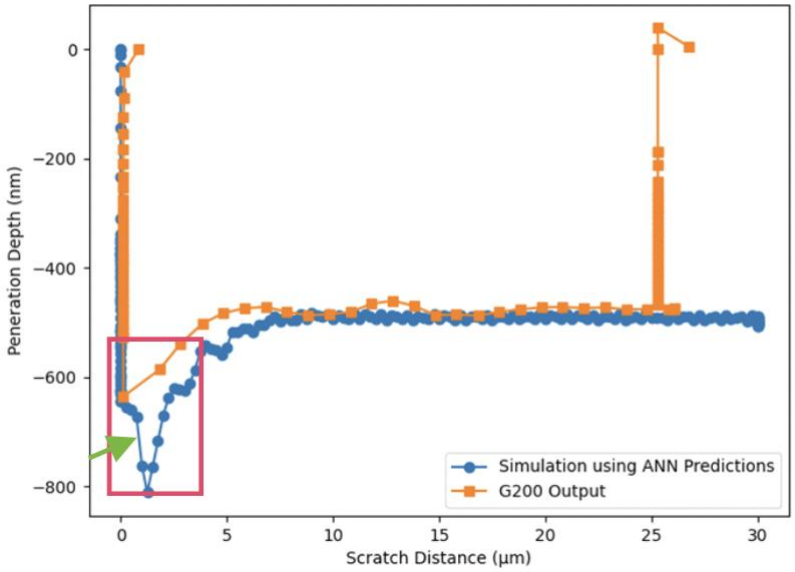



*Figure 85 Comparison of 20mN Ni600 Berkovich edge-forward nanoscratch experiment with Abaqus simulation using Johnson-Cook constants predicted by the ANN model from a single grain Ni600 indent. Red box denoted the discrepancy between the simulation and 20mN nanoscratch experiment in initial loading depth.*

Over-estimation of the maximum penetration depth was observed in the nanoscratch simulation, as shown by the red-boxed region in Figure 85. However, that could be caused by Abaqus being unstable in force-controlled experiments where the contact and movement changes [80]. This instability was likely caused by the massive acceleration that the tip endures when the back of the tip loses contact and begins lateral movement; momentum and inertia were considered in the dynamic solver, and 20mN can result in enormous acceleration on the micron-sized tip represented. A jump in penetration depth was indicated by the green arrow, and the contact gradually returned to equilibrium, which can be observed by the distance between data points. Shown in Figure 86, the residual groove profile from Abaqus output was compared with the residual groove profile from the 20 mN experiment scanned by

AFM, and it was confirmed that the residual profile matched the experiment result despite an overestimation during the scratch process.

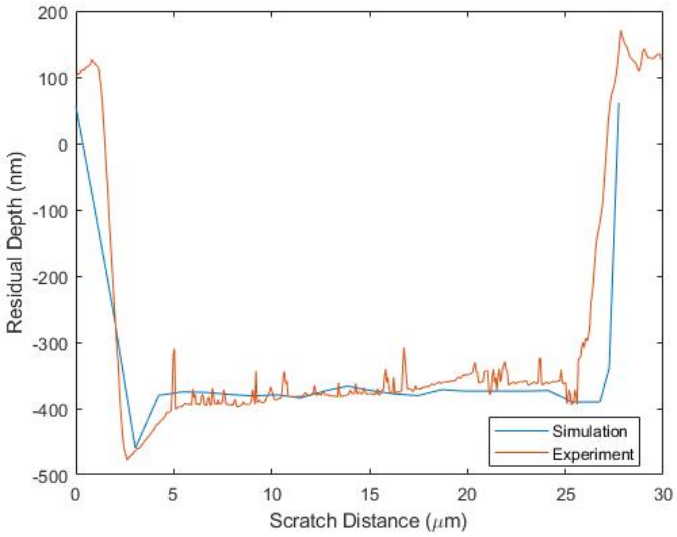



*Figure 86 Comparison of the residual profiles of 20mN Berkovich edge-forward scratch on Ni600 in Abaqus simulations and from experiment by G200 nanoindenter scanned with AFM.*

The ANN model has also been verified on Inconel 718. JC constants from literature are $A$ = 1241 MPa, $B$ = 622 MPa, $n$ = 0.652 [120] while predictions made by the model are $A$ = 1202.3 MPa, $B$ = 742.6 MPa, $n$ = 0.631. This suggest that the ANN model trained has adaptability to recognise the properties of other material that Johnson-Cook hardening law applies to and no over fitting problem has been observed (the phenomenon that a machine learning model can only work on a limited format of dataset (i.e. fixed length of data points).

## 6.7 General Discussion

The efficacy of machine learning in predicting material property is proven by the ANN model successfully identifying Johnson-Cook constants that align finite-element simulation with experiment. However, the capability of the ANN model is yet to be explored. [149]

The efficacy of this model's training was contingent upon the degree of similarity between the Berkovich tip used in the simulation and an ideal Berkovich tip, which is corroborated by the observation that models trained with a spherical tip of a nominal radius of 20 μm, it is not possible for it to accurately predict the Johnson-Cook constants from simulations involving tips subjected to radius deviation. While existing literature has successfully employed an ANN model trained with spherical indentations to predict material-specific parameters in Swift equation [73], the disparity observed in this study can be ascribed to two factors:

1. The prior study employed a considerably larger indenter tip with a radius of 250 μm, which likely bore a closer resemblance to the idealized spherical form assumed in simulations and is subject to less radii deviation.
2. The study used selected points from each simulation for model training rather than the entire data/displacement curve. This approach reduced the susceptibility of the model to deviations in sphericity.

Given these discrepancies, attempts are needed to incorporate tip imperfections into the training process. Such an adaptation would potentially enable the accurate identification of material constants from indentation data acquired using blunt tips.

The development of this model was based on an iterative process of trial and error. While this approach is practical for smaller models trained with a limited dataset, it is insufficient for more complex training objectives, such as the prediction of atomic structures. In these more advanced scenarios, a comprehensive understanding of how training parameters affect the efficiency of learning, and the rate of successful outcomes becomes crucial. For instance, the incorporation of Long Short-Term Memory (LSTM) neurons, known for their ability to retain sequential information, has led to a notable increase in training time. However, in the context of indentation testing, it is worth exploring whether the load/displacement data is intrinsically linked to preceding data or is solely dependent on the specific conditions of the experiment or simulation. Additionally, various other types of Artificial Neural Networks have demonstrated efficacy in the prediction of material properties, including Deep Feed-Forward Neural Networks (DFF), Radial Basis Function Neural Networks (RBFNN), and Recurrent Neural Networks (RNN) [128] while a comparative analysis of their effectiveness across different scenarios remains absent. The non-linear learning curve, as shown in the MAE map (Figure 79), highlights the need for a criterion to determine the optimal number of training iterations. This is essential to avoid undertraining, where the model stops learning too soon and doesn't perform as well as it could, or overtraining, where the model is trained for too many iterations and starts to memorize the training data instead of learning broader patterns. When this happens, it can lead to overfitting, meaning the model becomes too good at handling the training data but struggles with new, unseen data as it is too focused on the specific details of what it was trained on. Finding the right stopping point helps ensure the model performs well without wasting effort or losing its ability to adapt.

The accuracy of ANN predictions based on nanoindentation data is influenced by grain variability, which in turn contributed to a more precise correlation with Ni600 experiments,

as both the indentation and the verifying scratch were conducted within the same grain, which was unattainable for Inconel 718 with considerably smaller grain sizes. Therefore, methods are needed to integrate grain-specific information with the bulk properties the Johnson-Cook model intends to represent. The limitation of ANN in accounting for uncertainties is the ability to predict material responses based on known properties, which are often subject to variations. For this reason, the GPR model might serve as a better alternative. However, for it to be computationally viable, strategies must be devised to reduce the size of the data while preserving crucial information.

## 6.8 Conclusions

1. An artificial neural network (ANN) deep learning model was built to derive Johnson-Cook constants from nanoindentation data. Its efficacy was verified with nanoindentation and nanoscratch tests performed on material Ni600 and nanoindentation test on Inconel 718.
2. In the context of load/displacement output of nanoindentation simulation, individual influences of yield stress, strain hardening component, strain hardening exponent, elastic modulus and Poisson ratio were discussed, and plastic component were found to have bigger contribution to the indentation hardness measured.
3. The accuracy of machine learning predictions for Johnson-Cook constants from nanoindentation data is found highly sensitive to indenter tip geometry. Model with trained with Berkovich tip simulations may provide more reliable results than spherical tips as their manufacturing imperfections make harder to be characterised accurately in CAE.

# 7. Nanoscratch Simulations

## 7.1 Necessity of Abaqus simulations

Nanoscratch testing offers critical insights into nanoscale tribological interactions, yet experimental methods face inherent limitations that obscure mechanistic understanding. Surface contaminants, tip compliance (e.g., torsional bending [129]), and instrument constraints introduce uncontrolled variables, complicating efforts to isolate critical factors such as interfacial friction. These challenges are particularly evident in unresolved discrepancies between edge-forward and face-forward scratches: existing theories—ranging from adhesion-driven stick-slip mechanisms [108] to transient metallic welding [130] —fail to explain orientation-dependent friction behaviours observed in single-asperity contact scenarios. To address these ambiguities, computational frameworks like Abaqus provide a controlled environment to systematically investigate nanoscale phenomena. By eliminating experimental noise and enabling precise manipulation of variables, finite element simulations could help unravel the interplay between tip geometry, material response, and friction—a necessity for advancing predictive models of nanoscale wear and deformation.

Experimental approaches struggle to isolate the influence of individual variables due to overlapping contributing factors, while finite element simulations, like the Abaqus model, allow systematic decoupling of parameters such as the interfacial coefficient of friction (CoF). Within this framework, the CoF is defined as the ratio of local tangential stress to normal force at the nanoscale—a parameter that remains poorly characterized in physical experiments. A uniform CoF between the rigid indenter tip and the substrate surface is defined in the simulation and Bucaille et al. assumed its value to be 0.15 for diamond-to-metal contact in nanoindentation simulations [119] and concluded that for indenter tip angles exceeding 60°, the difference in reaction force between a friction coefficient (CoF) of 0 and

0.3 is approximately 3%. Nanoindentation and nanoscratch simulations conducted using CoFs of 0.1 and 0.15 yielded results aligned with experimental data [80], [131]. This suggested that nanoindentation might not be a particularly sensitive way to determine the CoF at the nanoscale and this chapter aims to examine if nanoscratch is a better alternative. It should be further noted that the CoF used in tribological applications is typically defined as the contact CoF: the overall ratio of the tangential and normal forces for the contact. This chapter also investigates the relationship between two commonly used CoFs with nanoscratch simulations.

## 7.2 Aim of Abaqus Simulations

The previous chapter demonstrated that nanoindentation and single-pass nanoscratch simulations could accurately match experimental results using appropriate Johnson-Cook material constants, as shown in Chapter 6. This chapter aims to further investigate the influence of the interfacial friction coefficient on scratch formation (section 7.3), specifically whether a coefficient of friction (CoF) above 0.15 can still yield simulations that align with experiments and its subsequent effect on the morphology of the residual grooves. Additionally, this chapter will explore the 'stick-slip' phenomenon observed in face-forward scratches to ascertain whether it is due to instrument compliance or purely by the change in contact mechanism.

This chapter also aims to investigate the effectiveness of Abaqus in simulating multi-pass nanoscratch experiments (section 7.4), where the interactions between deformed structures are believed to have a major influence on the hardening phenomenon observed. In Abaqus, this phenomenon is generalized only with an empirical stress-strain relationship denoted by Johnson-Cook equations and does not account for size-dependent plasticity. While this limitation may prevent the model from accurately predicting the depths in the following cycles, it still provides insights into the change in actual contact area—a parameter that is not directly measurable in experimental settings. The simulation can also illustrate the evolution of residual stresses on the grooves, which is directly linked to the extent of the strain-hardening effect. By identifying the causes of discrepancies between simulation and experimental outcomes, this approach enhances our understanding of the boundaries of FEA based on continuum theory and discretised elements.7.3 Single-pass Nanoscratch Simulations

### *7.3.1 Model Setup*

Using the same Abaqus nanoscratch model as the one shown in Section 6.2.1, simulations of edge-forward and face-forward nanoscratches were conducted with interfacial friction coefficients of 0, 0.15, 0.3, and 0.6. Material properties were Johnson-Cook constants predicted from the nanoindentation experiment on a single Ni600 grain: $A$ = 339 MPa, $B$ = 1246.5 MPa, $n$ = 0.75. Elastic modulus and Poisson's ratio used were 207GPa and 0.31 from manufacturer's spec sheet [101]. The sample was assumed to be isotropic as Abaqus dynamic solver only accepts material being isotropic.

### *7.3.2 Surface Friction – A parametric study*

Shown by Figure 87, the von Mises stress maps on residual grooves made with different assumed interfacial friction coefficients μ indicated that, in the case of edge-forward scratches, the maximum stress was uniformly distributed along the bottom of the scratch apex for μ ranging from 0 to 0.3. However, at a coefficient of 0.6, the peak stress extended to both sides of the scratch groove in addition to the bottom. For coefficients ranging from 0 to 0.3, the initial stress peak was located at the bottom of the initial indentation, but this peak shifted along the scratch direction as the surface friction increased. The maximum stress increased from 1.72 GPa to 2.81 GPa as the interfacial friction coefficient rose from 0 to 0.6.

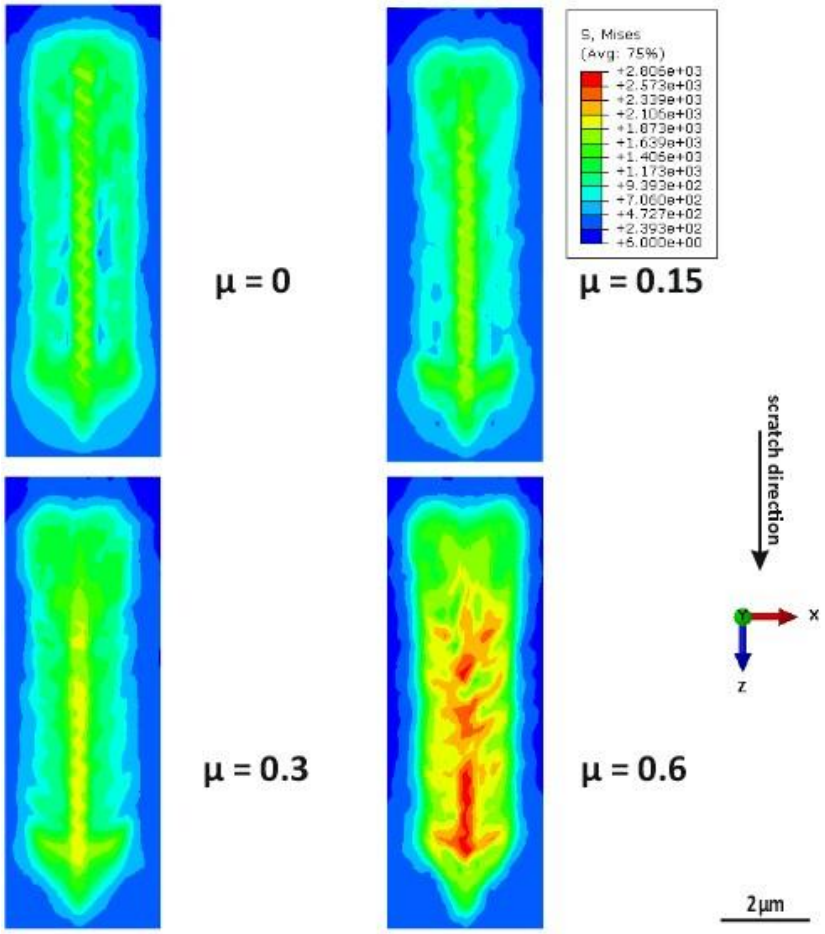



*Figure 87 Residual von Mises stress distributions on simulated edge-forward scratches with different interfacial friction coefficients. The unit of scale is MPa. 20 mN load edge-forward Berkovich tip nanoscratches of 20 μm length were simulated.*

As shown in Figure 88, depth vs scratch distance outputs along the scratch direction suggest that for edge-forward scratches, increasing the interfacial friction coefficients from 0 to 0.3 had a minimal impact on both the maximum initial indentation depths and the dip-in depths subsequent to the lateral movement of the tip. However, at μ of 0.6, there was an increase of 30 nm in the dip-in depth, with the scratch stabilizing approximately 3 μm later compared to the other three coefficients. For μ values of 0 and 0.15, the scratch profiles in the stabilized region were smooth, whereas at μ values of 0.3 and 0.6, oscillations indicative of the stick-slip phenomenon were observed. The average penetration depths in the stabilized region decreased from -550 nm to -450 nm as the μ values increased from 0 to 0.6. Results suggested that the initial indentation depth was less sensitive to interfacial CoF than the subsequent scratch depth response. An interfacial CoF of 0.15 yielded a depth vs scratch

distance profile that closely resembled the output from the experiment. The fluctuations in depth of penetration seen with increased interfacial friction coefficients were likely caused by the physical stick-slip phenomenon. When μ values were high, the greater frictional resistance between the tip and sample surface led to situations where the instrument switched back and forth between sticking, causing gradual material deformation as motion was resisted, and slipping, where sudden release and fast movement occurred as accumulated stress overcame static friction. This was supported by the fluctuations in the lateral force felt by the tip, as illustrated in Figure 89.

These oscillations were unlikely to be caused by mesh stiffness oscillations because they specifically emerged at higher friction coefficients, aligning with the expected physical behaviour of stick-slip dynamics rather than being a general numerical artefact. Mesh stiffness issues typically manifest across a range of simulation parameters and would likely diminish with finer mesh refinement. The simulations overestimated the maximum penetration depth of ‘dip-in’, and it was likely caused by the instability of load-controlled simulations when one facet lost contact, as explained in section 6.6.

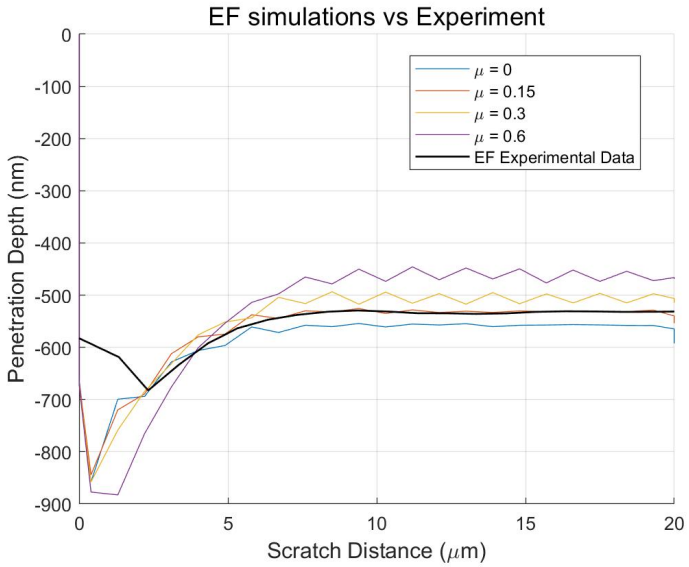



*Figure 88 Scratch profile of simulated edge-forward scratches in comparison with the 20mN Berkovich tip edge-forward experiment output by G200 on single Ni600 grain. Measurements were taken during the scratch process.*

The average lateral forces recorded for the four tested interfacial CoFs were 5 mN, 8 mN, 12 mN, and 20 mN, corresponding to overall contact CoFs of 0.25, 0.4, 0.6, and 1, respectively, using the stabilised section after tip climb out, and it was observed that the overall CoF increased with μ in a linear manner as shown in Figure 89. The lateral force measured at a μ of 0.15 agreed with CPFEM output in literature [80]. Smooth force measurements were observed for μ values of 0 and 0.15. However, oscillations were noted in the force readings for μ values of 0.3 and 0.6. Due to instrument limitation, the actual overall CoF of the Ni600 used in this study has not been tested in the experiment, but an overall CoF of 0.4 is the value found in literature experiments on metal and alloys [97], [132].

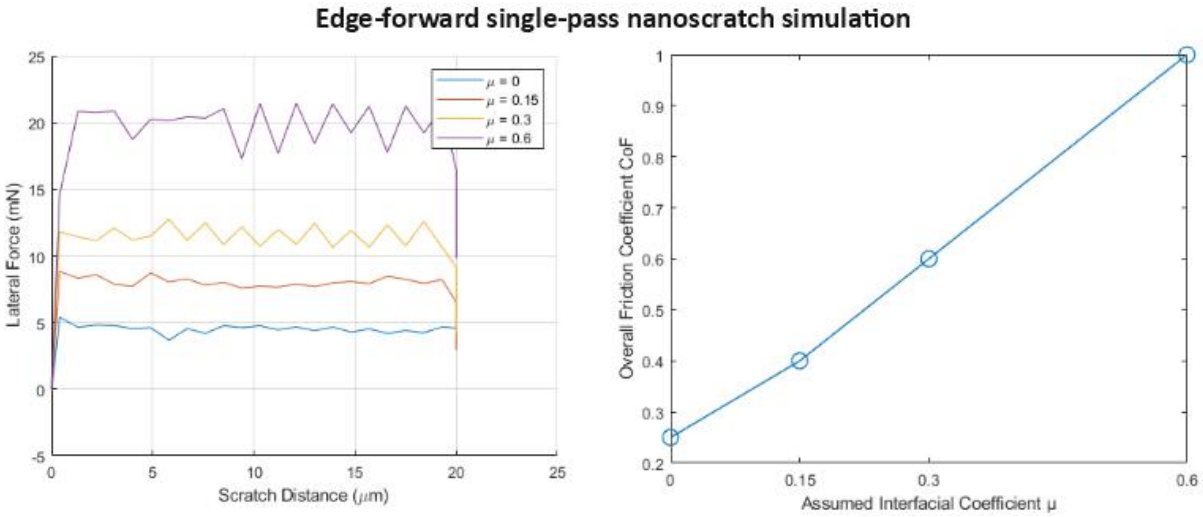



*Figure 89 Lateral force measurements and overall CoFs against different assumed interfacial friction constants in 20 mN edge-forward Berkovich nanoscratch simulations.*

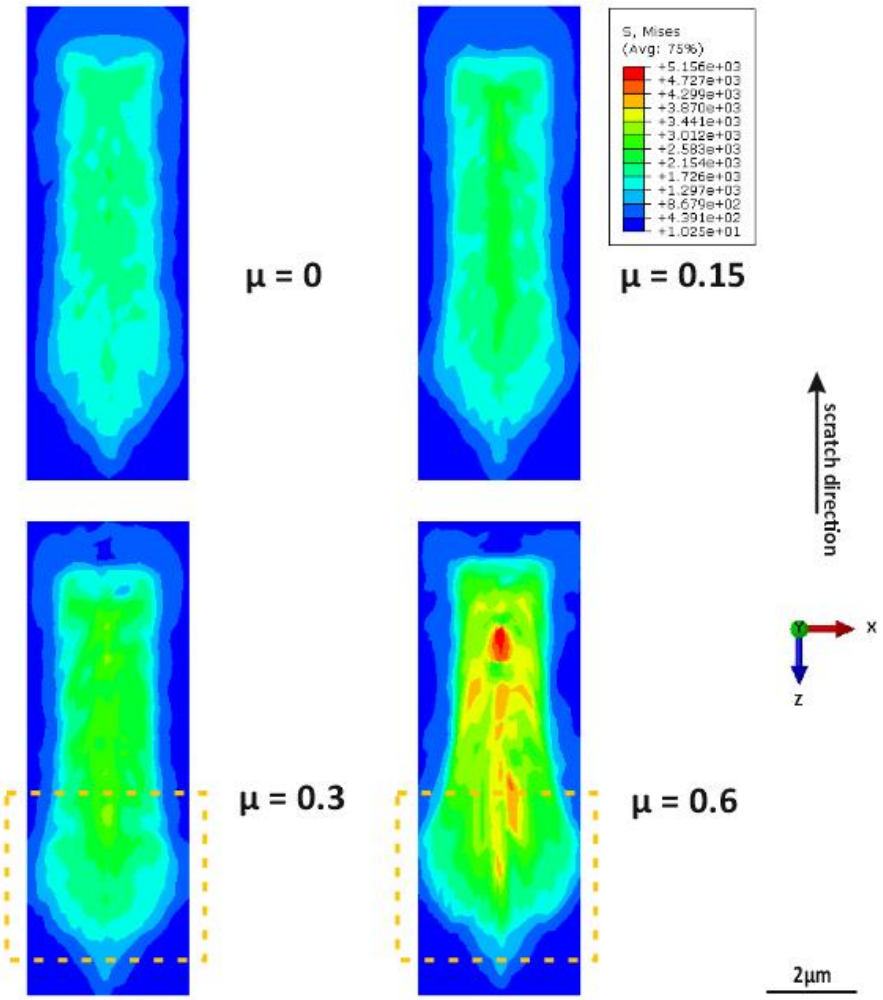



*Figure 90 Residual von mises stress distributions on simulated face-forward scratches with different interfacial friction coefficients. The unit of scale is MPa. 20 mN load face-forward Berkovich tip nanoscratches of 20 μm length were simulated. Boxed regions indicate where the start of the scratch no longer resembles a Berkovich triangle indent.*

As shown in Figure 90, stress distributions in face-forward scratches were more varied. At μ = 0, stress maxima distributed across the groove surface after the initial indent while at μ = 0.15, stress maxima were positioned along the groove bottom, similar to the distributions found in edge-forward scratches except with increased spread on two sides. At μ = 0.3, the maxima appeared as intermittent spots along the groove bottom, while at μ = 0.6, only one stress maxima was found within the 20 μm scratch created. Triangular residual shapes were observed at initial indentation locations in μ = 0 and μ = 0.15, while in μ = 0.3 and μ = 0.6 simulations, these features become rounded shapes, as shown by the boxed areas in Figure 90.

The magnitude of maximum von Mises stress was 30% bigger than that of EF at μ = 0 and 90% bigger at μ = 0.6.

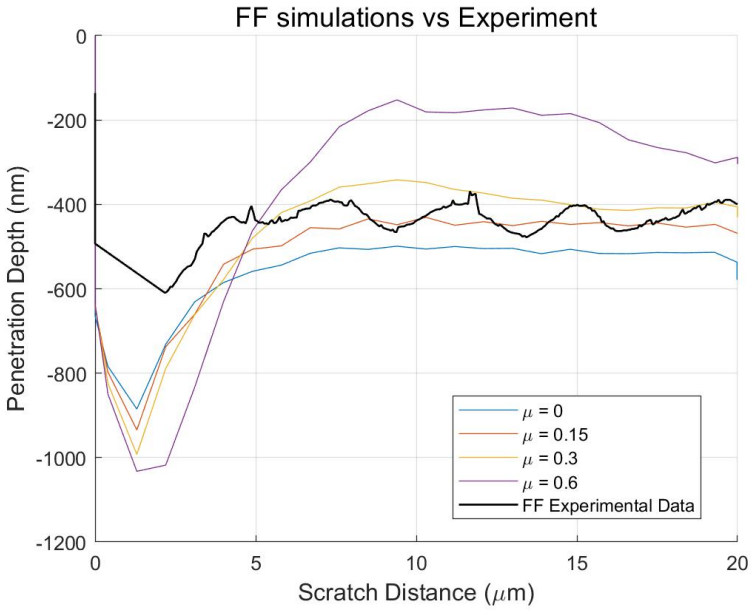



*Figure 91 Scratch profiles of the simulated 20mN Berkovich tip face-forward scratches using varied interfacial friction coefficients and experiment output from G200 nanoindenter.*

In the scratch depth profiles shown in Figure 91, negligible oscillations were observed in the stabilized region for μ of 0 and 0.15 (at the scratch distance between 10 to 20 μm), while oscillations notably expanded at μ values of 0.3 and 0.6. The average penetration depths experienced a sharp decrease, falling from 500 nm for μ = 0 to 210 nm for μ = 0.6 with an increase of 150 nm in dip-in depth. For μ values of 0 and 0.3, the difference in dip-in depths was recorded for 100 nm, a contrast to the negligible variation observed in edge-forward scratches. The location of the stress maxima matches with the regional minima in penetration depth, a finding that aligned with observations from HR-EBSD analysis of the side sections, where GNDs and stress concentrate at the troughs.

Compared to the experiment output, simulation using μ of 0.15 again most accurately predicted the average penetration depth in stabilised regions, but the magnitude and distance

between the oscillations had not been clearly predicted, while the oscillations at higher μ are too large compared to ones observed in the experiment. Negligible oscillation is expected at μ = 0, as a stick should not happen if there is no interfacial friction.

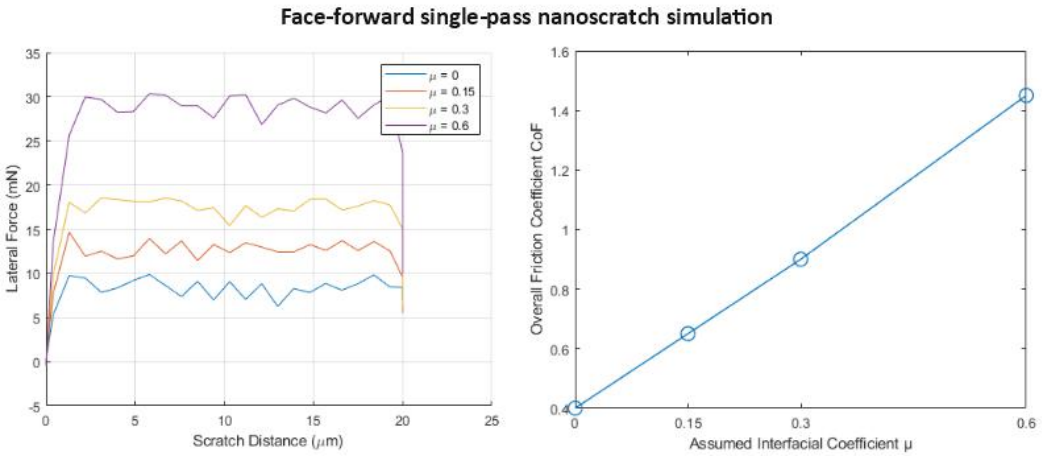



*Figure 92 Lateral force measurements and overall CoFs against different assumed interfacial friction constants in 20 mN face-forward Berkovich nanoscratch simulations. A CoF above 1 indicates that the lateral resistance experienced by the tip exceeded the normal load applied.*

Shown in Figure 92, for face-forward scratches, average lateral forces experienced by the tip were 8 mN, 13 mN, 18 mN, and 29 mN for the 4 interfacial friction coefficients examined that led to overall friction coefficient of 0.4, 0.65, 0.9 and 1.45 with a similar linear increase observed in edge-forward scratches. Again μ = 0.15 led to an agreement with CPFEM simulation and experiments in literature. Oscillations in the measurement of lateral force were observed at all levels of friction. The rise potentially indicated increased resistance caused by the formation of a pile-up at the front facet, while the drop suggested the relocation of the pile-up to either side.

### *7.3.3 Effect of Normal Loads*

Simulations of single-pass, edge-forward nanoscratch testing were conducted employing normal loads of 0.5 mN, 2 mN, 10 mN, and 20 mN, using ANN-model predicted Ni600 Johnson-Cook material parameters from Chapter 6. It aimed to explore whether Abaqus simulations across a spectrum of normal loads would correspond with the experimental findings depicted in Figure 35 and Figure 36. The alterations in the overall Coefficients of Friction (CoF) would also be examined in response to variations in the applied normal load during simulations. For the purposes of these simulations, the interfacial surface friction constant (μ) was presupposed to be 0.15, a value that yielded CoF estimates congruent with those observed in empirical measurements for both 20 mN edge-forward and face-forward scratches.

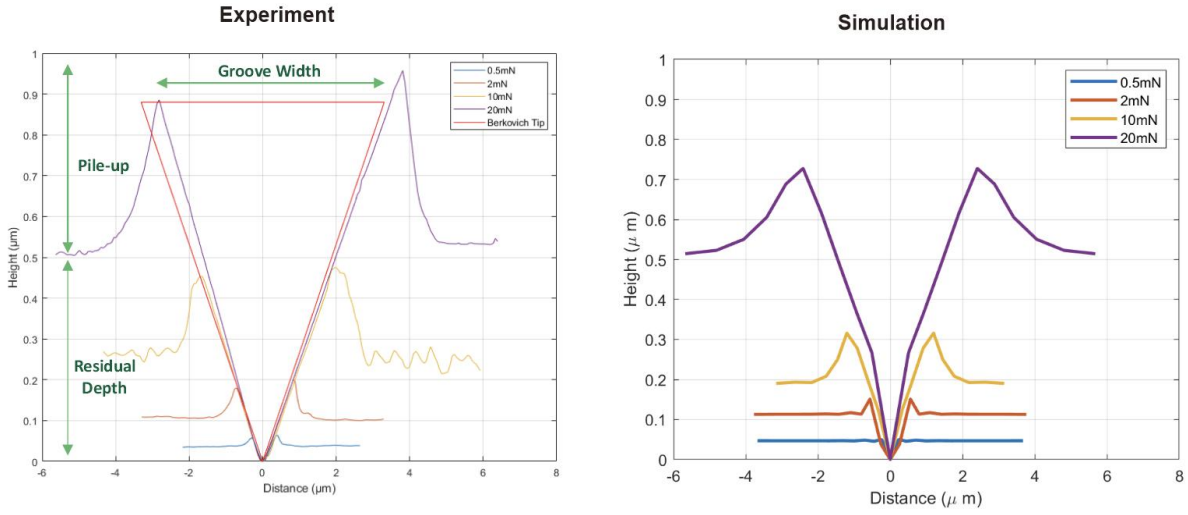



*Figure 93 A comparison of the cross-section profiles of residual groove in Abaqus simulations and experiments of edge-forward Berkovich nanoscratch at 0.5 mN, 2 mN, 10 mN, 20 mN normal loads on single Ni600 grain.*

Figure 93 indicates that the maximum penetration depths of the groove were in alignment with the experimental outcomes across the four tested normal loads with a single scratch pass. However, discrepancies in the morphology of the grooves may be attributable to the discrete

configuration of mesh elements. Specifically, the cross-sectional profile generated in the simulation was delineated based on the nodes of the mesh elements, which might deviate from the central axis of the groove subsequent to deformation. The difference in pile-up heights on two edges in the experiment was not observed in simulations because the tip remained perfectly vertical to the sample surface and the material was isotropic. The pile-up heights in simulations for 0.5 mN, 2 mN, 10 mN, and 20 mN were 4 nm, 38 nm, 114 nm, and 223 nm, consistently lower than the 31.7 nm, 97.5 nm, 276.3 nm, and 494.8 nm observed in the experiment. The underestimation was most pronounced at 0.5 mN, where pile-up was scarcely observed in the simulations. In the 0.5 mN scratch experiment, the tip penetrated only 30 nm into the surface, and the hardening of the surface beneath the indenter tip, caused by strain gradient and indentation size effects, was significant. This made material relocation to the free surface as pile-up a preferred deformation mechanism, which is not represented in the standard Abaqus model. Abaqus simulations often impose restrictions on the rotational freedom of the material (one mesh cannot detach and rotate against the neighbouring mesh), preventing it from freely rotating as it might in a real-world scenario. This limitation restricted the natural redistribution of material around the indentation site, further contributing to the underestimation of pile-up heights.

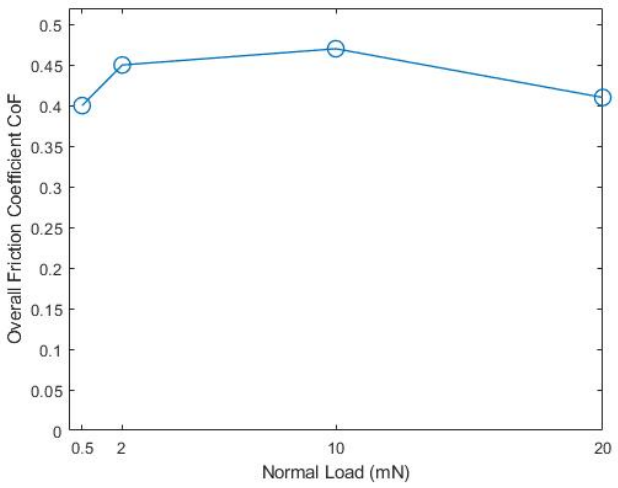



*Figure 94 Overall Coefficient of Friction for edge-forward Berkovich nanoscratch simulations with 0.5 mN, 2 mN, 10 mN and 20 mN normal loads.*

Figure 94 presents the average Coefficients of Friction (CoFs) derived from the single-pass edge-forward simulations under varied loads, which fluctuated between 0.4 and 0.47. These values were consistent with experimental findings reported in the relevant literature [97].

Figure 95 depicts the residual von Mises stress distributions of the simulations performed. The stress distribution exhibited a consistent pattern, with the peak stress occurring at the apex of the tip and dispersing uniformly along the central axis.

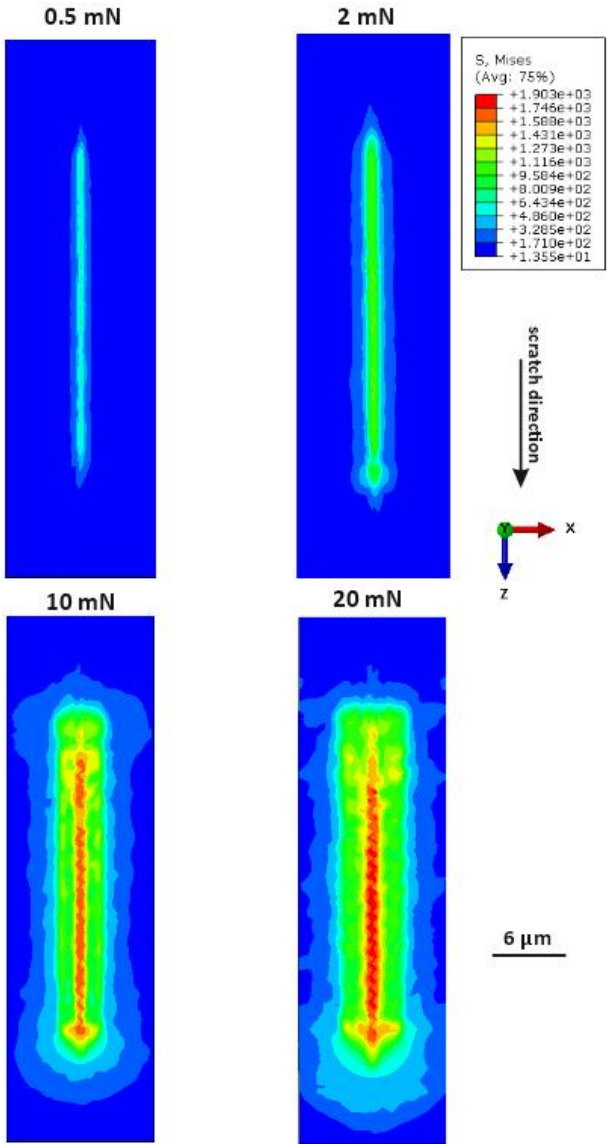



*Figure 95 Top views of the residual von Mises stress distribution. Edge-forward Berkovich tip nanoscratches of 30 µm length under 0.5 mN, 1 mN, 10 mN and 20 mN normal loads were simulated.*

### *7.3.4 Comparison of Edge-Forward and Face-Forward Simulations*

As evidenced by Figure 90 and Figure 91, the occurrence of the stick-slip phenomenon and the undulating morphology of the residual groove were observed in face-forward simulations, even when the tip was exempt from torsional and bending deflections. This observation suggested that the root cause of the phenomenon in this case is likely attributable to the geometry of the contact surface rather than to the compliance of the instrument. Tip bending/torsional compliance might still play a role in experiments but has been ruled out in these simulations. Furthermore, the distributions of von Mises stress during the scratch formation process, as illustrated in Figure 96, indicates that in face-forward scratches, a higher stress was exerted on the sample surface than the case in edge-forward scratch, which potentially led to a higher strain-hardening.

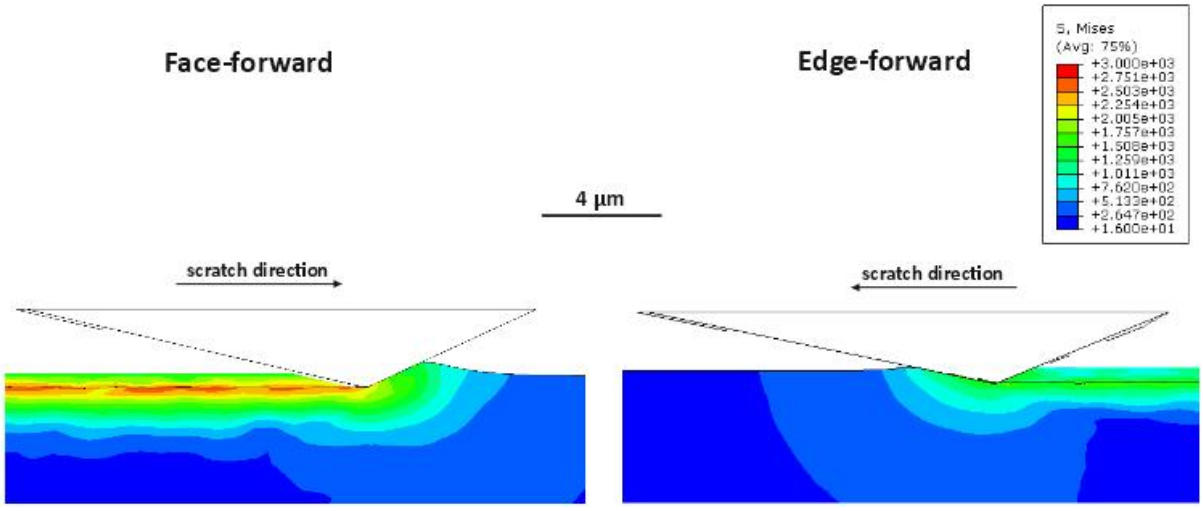



*Figure 96 Stress distribution in two ongoing simulated Berkovich tip scratches with 20 mN normal load at 1 µm/s scratch speed.*

Establishing a direct linkage between HR-EBSD outcomes and Abaqus simulation results presents a challenge due to the fundamental disparities in their underlying principles. HR-EBSD determines the stress state by correlating measured elastic strains with stress through

Hooke's law, effectively accommodating the anisotropic characteristics of single crystals and facilitating localized stress measurements. Conversely, standard Abaqus simulations presuppose material homogeneity and isotropy, with constitutive equations derived from the principles of continuum mechanics. The crystallographic influence on anisotropy in both elastic and plastic responses can be profound and is not captured in the simulations. The more isotropic engineering level approach used in the simulation was required to complete the simulations in a reasonable timeframe.

In experimental settings, strain-hardening of materials is likely achieved through multiple mechanisms, including the formation of GNDs, recrystallization, and the interlocking of grain boundaries. However, the standard version of Abaqus lacks the capacity to capture these complex phenomena. Instead, strain hardening is represented through empirical stress-strain relationships, such as the Johnson-Cook relationship employed in this study. The graphical representation of the material's strain hardening behaviour is depicted using the plastic strain component (PE) map, but plasticity size effects are not incorporated.

Figure 97 presents a comparison between the PE map (maximum principal strain) obtained from Abaqus simulations and the GND density map derived from HR-EBSD analysis. The two metrics are fundamentally different, but we might expect some qualitative correlation between them as higher plastic strains generally lead to greater dislocation storage within the material. This comparison reveals the volume and distribution of hardened material on the deformed sample surface. The two outputs exhibit similar hardening behaviours. In face-forward scratches, the GND reached its highest density at the top of the groove, as illustrated in Figure 97c, while the maximum plastic strain is also observed at a similar location, indicated by the red region in Figure 97a. In edge-forward scratches, both the maximum

principal plastic strain and GND density follow a uniform distribution in the region closest to the indenter tip, as demonstrated in Figure 97b and Figure 97d.

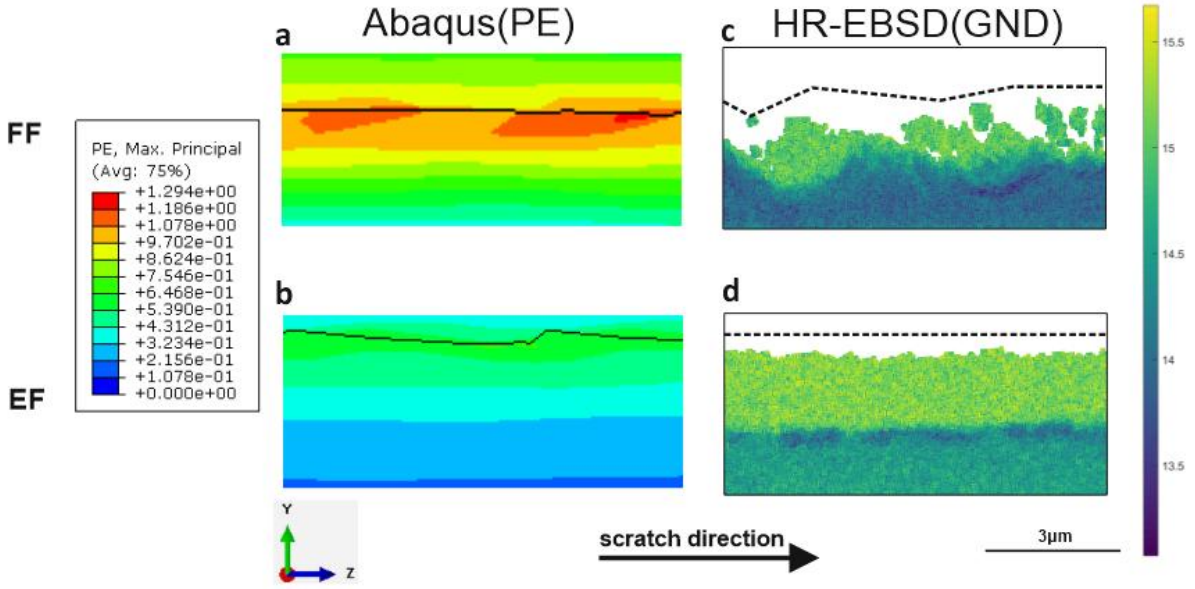



*Figure 97 A comparison of the plastic strain component maps from Abaqus simulation with HR-EBSD GND analysis on the residual groove of 20 mN Berkovich nanoscratch tests on single Ni600 grain in edge-forward (EF) and face-forward (FF) orientations. The unit of GND density was on logarithmic scale and corresponded to $10^{13}$ to $10^{16}$ Geometrically Necessary Dislocations (GNDs) per square meter.*

## 7.4 Multi-pass Nanoscratch Simulations

### *7.4.1 Experiment Findings and Simulation Aims*

The repeated nanoscratch experiment conducted in Chapter 5, employing a constant normal load at identical locations, revealed that Ni600 experienced progressive hardening with an increasing number of passes until the tip could no longer penetrate further into the surface. This phenomenon was observed to occur regardless of the applied normal load, with the only difference being that the number of passes required to achieve stabilization increased with elevated normal loads.

Given the effective representation of stress/strain hardening distribution in single-pass simulations, it is worth investigating whether the FE simulations based on our simple Johnson-Cook material model can capture this phenomenon. Simulation results were compared with the experimental observations to assess the ability of the standard Abaqus software to capture the progressive hardening and stabilisation phenomena observed in the repeated nanoscratch experiments.

### *7.4.2 Construction of the FEA model*

In simulations of repetitive scratching, the sample dimensions were expanded to 75 μm x 21 μm x 15 μm, accommodating the increased plastic zone and groove formation. The scratch rate was elevated to 2 μm/s, completing a 30 μm scratch in 15 seconds to reduce the computation time. The indenter tip was programmed to unload over a period of 1 second and then return to the original position in another second. Each cycle was thus completed in 22 seconds, culminating in a 10-pass process over a total duration of 220 seconds. The number

of mesh elements, material constants used, and remaining boundary conditions were unchanged. An interfacial CoF of 0.15 was used throughout.

### *7.4.3 Effects of Repeated Passes*

#### 7.4.3.1 Residual Stress Distribution

Repeated scratches were performed with 20 mN normal load, and the surface stress distribution observed after the initial pass displayed patterns akin to those seen in the edge-forward scratch example– with peak stress forming a straight line at the groove's bottom, shown in Figure 98. During the second pass, an overall increase in surface stress was noted, with the peak stress beginning to extend to both sides of the bottom apex. After 5 passes, the peak stress became less pronounced on the surface, which assumed a corrugated appearance reminiscent of aged, folded paper, in contrast to the initially flat and smooth surface. After 10 passes, the stress distribution approached a near-uniform state across the surface.

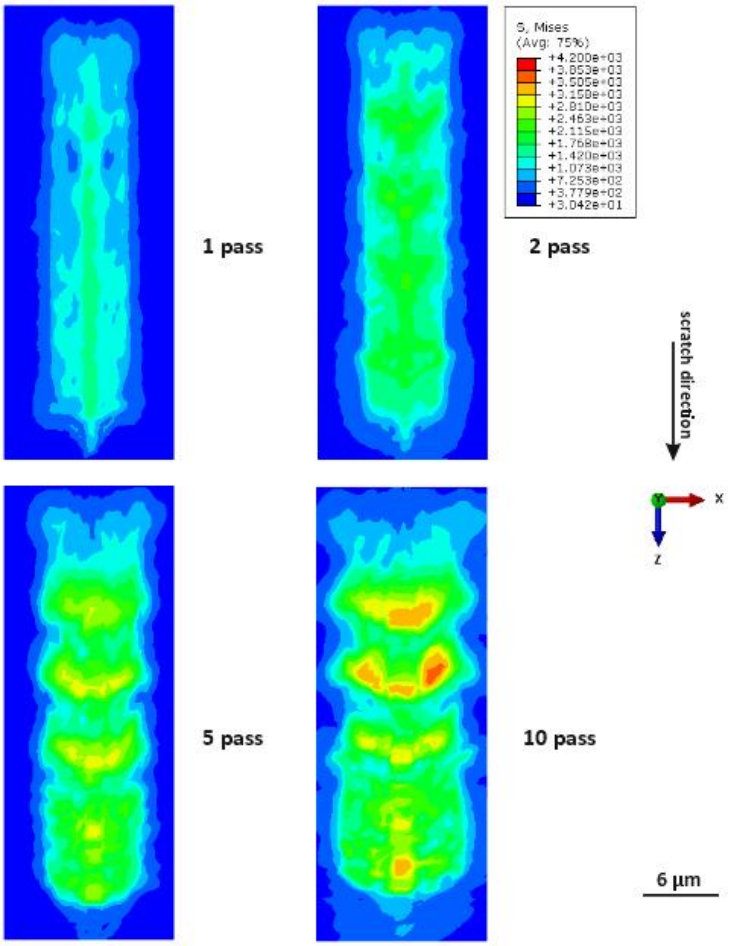



*Figure 98 Residual von Mises stress distribution at groove surface after different numbers of loading cycles. 20 mN normal load edge-forward Berkovich tip nanoscratches of 30 µm length under 1, 2, 5 and 10 scratch passes were simulated.*

7.4.3.2 Residual Groove Profiles and Elastic Recovery

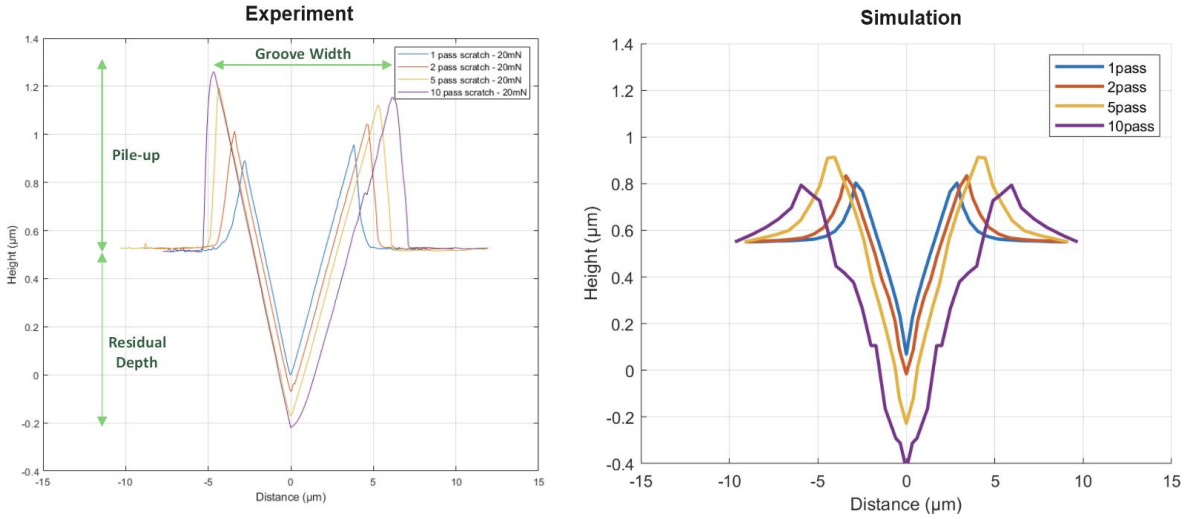



*Figure 99 A comparison of the residual cross profiles of 20 mN Berkovich nanoscratch s in edge-forward orientation after 1, 2, 5 10 passes in both FE simulations and experiment residual profiles on Ni600, scanned by AFM.*

Figure 99 suggests that the standard Abaqus software adequately predicted the residual groove depth at a lower number of passes. However, the residual groove depth at the 10th pass was overestimated by approximately 200 nm (1 µm in simulation to 800 nm in experiments), with the pile-up height and shape differing significantly from the experiment – the pile-up from experiments was much steeper. It was also observed that the groove of the 10th pass exhibited a rugged final surface, indicating varied strain hardening at different locations due to the discrete nature of the mesh elements, and the tip might no longer be in full contact at later passes as the surface did not fully conform to the tip shape. Compared to the experiment in which the formation of pile-up is a preferred way of deformation in subsequent passes as shown in section 5.2.2 compared to further surface penetration in simulations, the grooves were constantly widened and deepened as there was no saturation of dislocations and size effects that impeded further tip penetration while rotation and relocation of the material were constrained, which resulted in the pile-up from 10 pass appearing lower than that of 5 pass, potentially caused by the material overly extruded to two sides and groove geometries were no longer self-similar as they appeared in the experiment.

The elastic recoveries observed in the simulations were found to be similar to the experimental results, with recovery distances ranging from 40 nm to 60 nm for different numbers of passes, as shown in Figure 100.

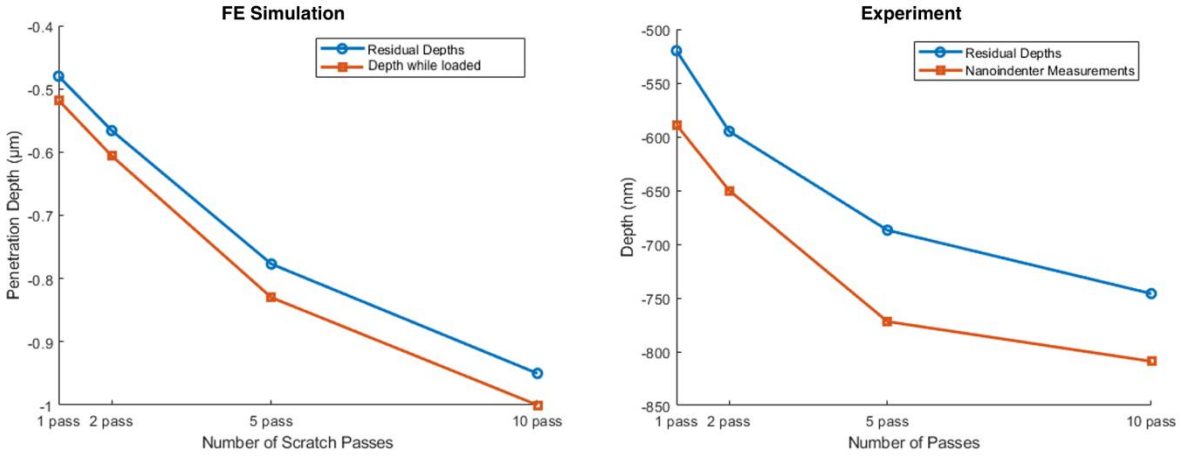



*Figure 100 A comparison of average residual groove depth and vertical displacements during FE simulations of 20 mN edge-forward Berkovich nanoscratch tests with changing number of scratch passes on single Ni600 grain. Experiment results are displayed on the right for comparison.*

### 7.4.3.3 Lateral Resistance and Coefficient of Friction

The lateral forces experienced by the tip were averaged along the scratch distance to obtain the overall CoFs for different numbers of scratch passes, as shown in Figure 101. The results indicate a small decrease in the coefficient of friction from 0.42 at the first pass to 0.32 at the 10th pass. However, a closer examination of the lateral resistance changes along the scratch distance, as presented in Figure 102, suggests that the coefficient of friction might not be sufficient to characterise the tribological behaviour at higher numbers of passes, where the lateral resistance fluctuated acutely due to non-uniform strain hardening at the sample surface, as depicted in Figure 98.

In reality, these localised hardened regions could lead to changes in the contact conditions between the tip and the sample surface: the tip may become blunt, resulting in an increased

contact area. These changes in contact conditions can potentially influence the wear mode both at the nano and macro levels.

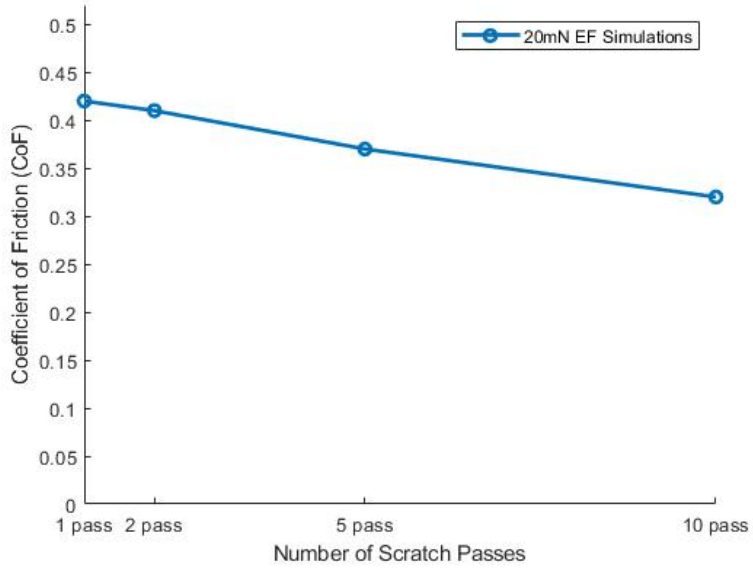



*Figure 101 Change of overall friction coefficient for 20 mN load edge-forward nanoscratch simulations under changing number of passes.*

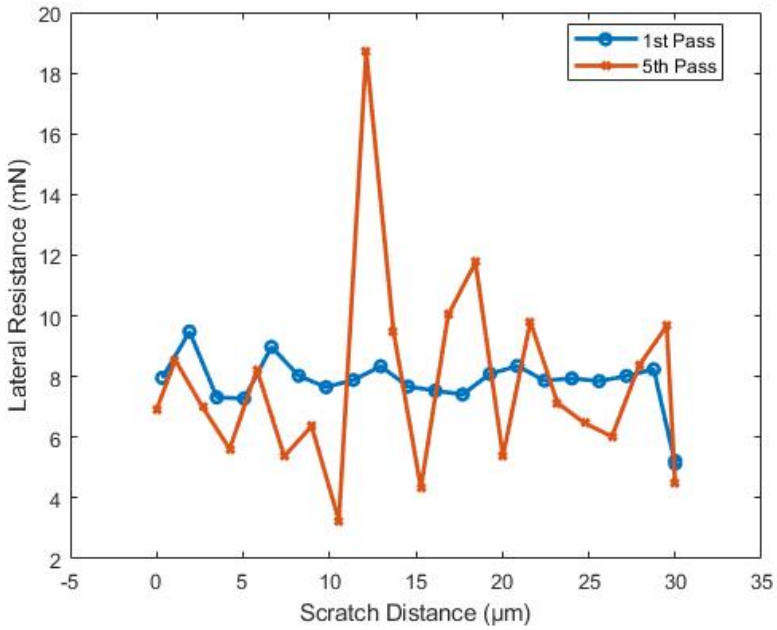



*Figure 102 Changes of lateral resistance on the tip during the first and fifth pass of repeated 20 mN load edge-forward Berkovich nanoscratch simulations.*

### *7.4.4 Effect of Normal Loads*

7.4.4.1 Change of Penetration Depths

Shown in Figure 103, average penetration depths of the edge-forward Berkovich nanoscratch simulations were measured for 10 passes under simulated normal loads of 20 mN, 30 mN, and 50 mN to be compared with the experimental results obtained in section 5.2. Simulations under 80 mN were not performed due to the requirement of significantly larger tip and sample sizes to accommodate the increased deformed area, as major changes in the mesh and sample layout could have a critical influence on the results. Penetration depths were obtained by averaging the depth measurements within the stabilized region after the tip climb out.

Simulation results in Figure 103 indicates that the material surface experienced strain hardening, with the second pass penetrating significantly less than the initial pass at the three different simulated normal loads. However, the average penetration depth increased almost linearly for each subsequent pass, contrasting with the diminishing depth increment for each pass observed in the experiments, leading to an overestimation of the average penetration depth at higher passes. It is unlikely that the reverse plasticity was predicted by the model as that would require kinematic hardening which the yield surface, instead of expanding, translates in stress space without changing its size or shape, essential for capturing the Bauschinger effect, while the Johnson-Cook hardening assumed in this model is isotropic hardening in which the yield surface expands uniformly in all directions in stress space and the yield stress increases equally in all loading directions.

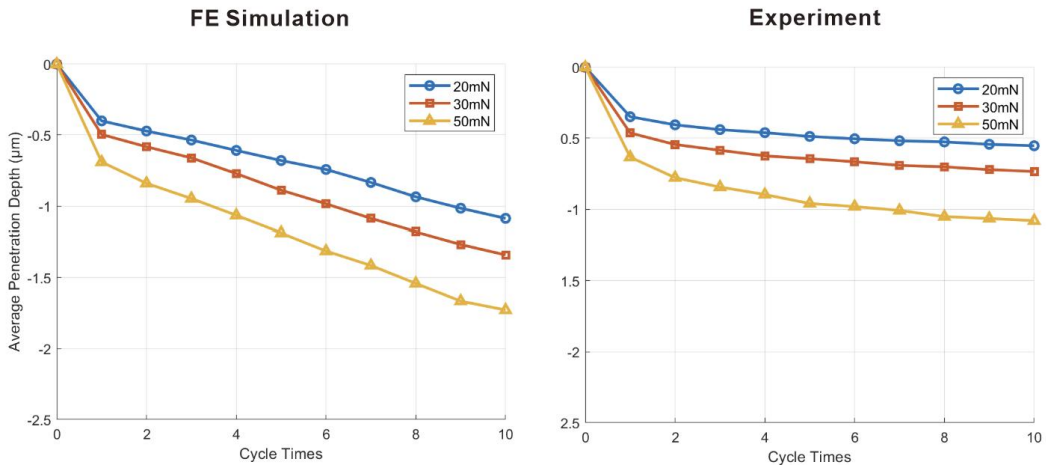



*Figure 103 Change of average penetration depth with different number of passes on edge-forward Berkovich edge-forward nanoscratch simulations on Ni600 described with Johnson-Cook hardening under changing normal loads. Experiments results from G200 nanoindenter measurements are shown on the right for comparison.*

### 7.4.4.2 Contact Area and Scratch Hardness

In both nanoindentation and nanoscratch experiments, the contact area is crucial for determining the correct hardness, and area functions are frequently employed to account for tip imperfections and deduce the contact area at a given penetration depth. One of the key benefits of Abaqus is its ability to derive contact area as an output along the scratch distance for specific pass and tip face as well as to visualise the contact geometry, which is not possible to be observed directly in experiments as the tip is beneath the material surface. However, limitations still exist: for the contact area to be properly accounted for, the submissive surface needs to be fully deformed to the shape of the tip, while the discrete nature of the mesh elements may limit this. The elements can only be in contact with the tip at the node points, which can lead to an underestimation of the contact area, an issue that may be even more pronounced in spherical tip scratch simulations due to the complex tip geometry.

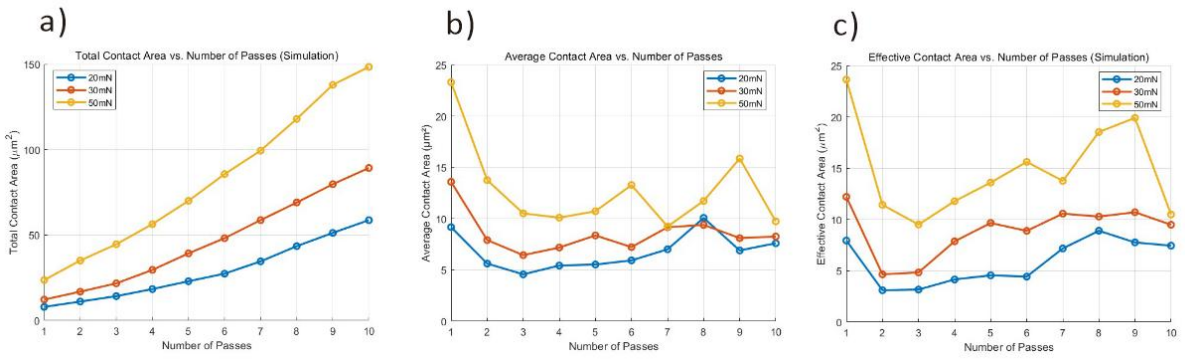



*Figure 104 Change of average contact area with number of passes in Berkovich nanoscratch simulations under normal loads of 20 mN, 30 mN and 50 mN. Contact areas are obtained differently, in which a) is estimated from total penetration depth, b) is from direct Abaqus output, and c) is estimated using the difference between the total contact areas in two neighbouring passes, defined as an 'effective contact area' in the previous section.*

Figure 104 compares the 'true' contact areas from direct Abaqus output with areas estimated using total penetration depth and the effective contact areas defined in the experiment section 5.2, in which the effective contact area is described as the difference between the contact areas calculated with total penetration depths for two neighbouring passes. It was observed

that the true contact area is the same as the estimation at the initial pass and becomes smaller than the values derived from the total penetration and area subtraction method for the following passes. It was observed that the true contact area reduces over the initial few passes and then becomes relatively stable, a potential indication that under the J-C model, the material surface hardening increased for the first few contacts and maintained at a given state for the later rounds. However, the use of average contact area could omit important features: in Figure 105 the contact area was plotted across the scratch distance for the 1st and 5th passes of 20 mN load nanoscratches, and it was observed that the area changes dramatically along the scratch distance at higher numbers of passes, potentially again caused by localized material hardening.

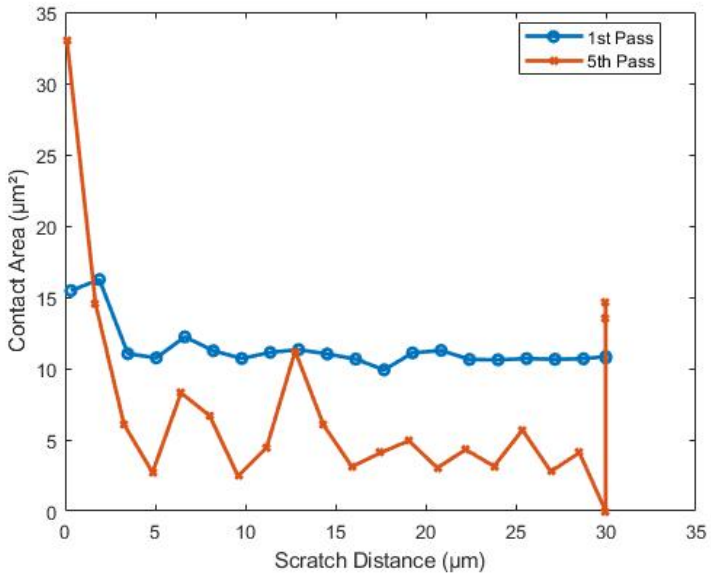



*Figure 105 Change of tip contact area across the scratch distance for first and fifth pass of edge-forward nanoscratch simulation with 20 mN normal load.*

Figure 106a revealed that the scratch hardness, calculated using the contact area output, increased during the initial three passes due to strain hardening and showed consistent values for all three normal loads tested. However, after three passes, the scratch hardness fluctuated too severely to allow for any generalization. This fluctuation was potentially caused by the

severely deformed surface and the almost complete loss of contact with the tip at certain locations, as depicted by the drop in contact area in Figure 105.

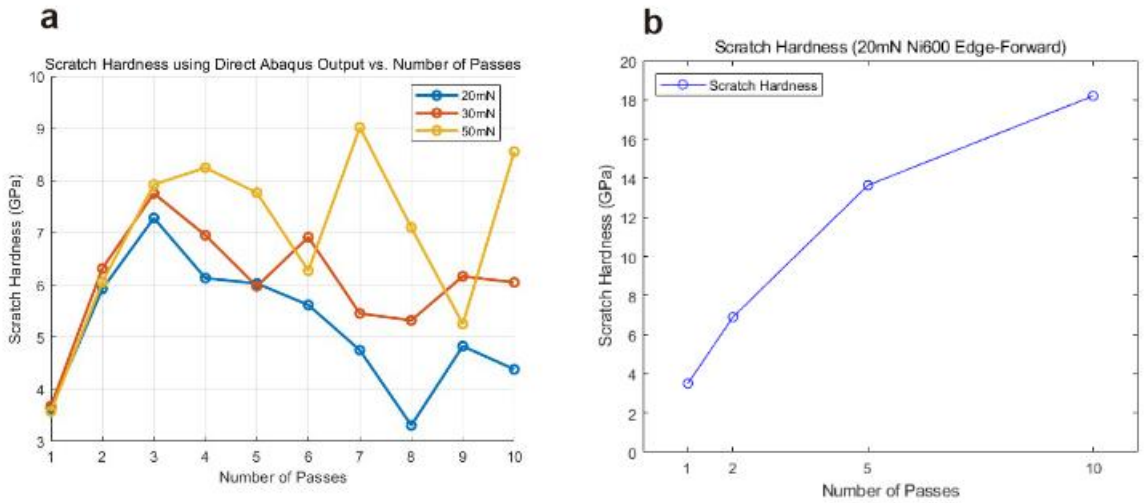



*Figure 106 a) change of scratch hardness with the increased number of nanoscratch passes under different normal loads. Contact areas used to derive hardness are directly derived from Abaqus Output b) Change of scratch hardness in 20 mN Berkovich tip edge-forward nanoscratch on Ni600. Contact areas used in the experiment are defined as the differences in total projection area between passes.*

Figure 106b shows the changes in scratch hardness during repeated 20 mN edge-forward nanoscratch experiments on a single grain Ni600. The hardness was estimated using the effective contact area defined in section 5.2. Compared with Figure 106a, Abaqus adequately reflected the bulk strain-hardening behaviour in the initial two passes but cannot simulate the surface protection from size effect, a theory that was raised in section 5.2. The ups and downs in the contact area in simulations may indicate that the surface was no longer flat and some of the higher asperities on the deformed surface contacted the tip and were pushed outward. In the next pass, asperities that were not in contact during the previous pass become the new points of contact and were pushed outward again, demonstrated in Figure 107, which explained why the groove became much wider at the end.

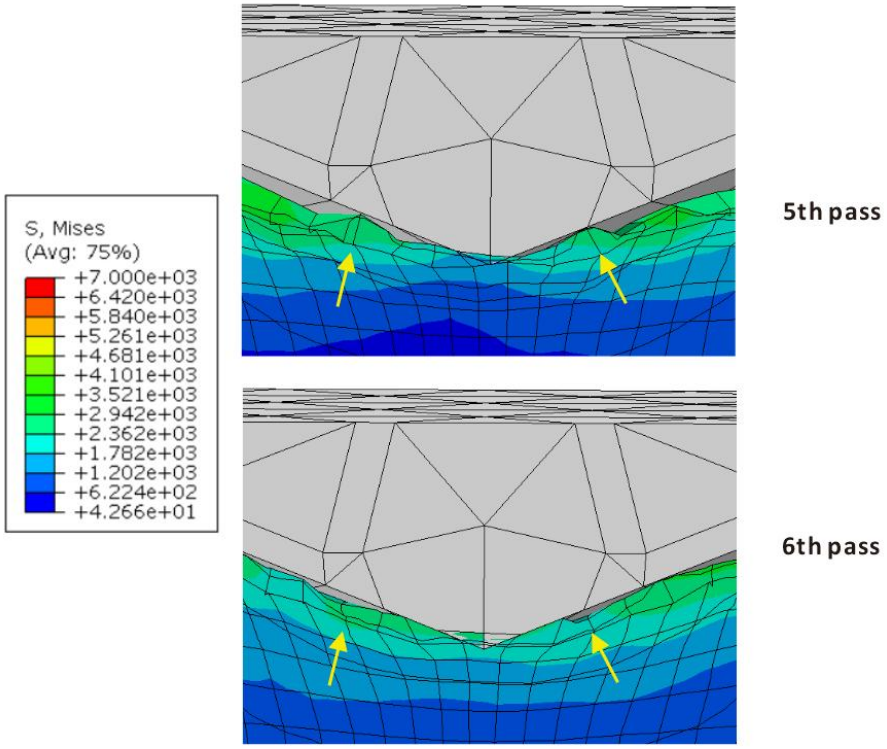



*Figure 107 Cross-sections of 20mN Berkovich tip edge-forward nanoscratches at the 5th and 6th pass at the same scratch distance. Arrows indicate the positions where the elevated asperities are no longer in contact with the tip in the following pass.*

Figure 108 indicates that even for the second pass, where the groove surface was still flat, the residual groove from the initial pass was still not in full contact with the tip. Instead, only the further penetrated area with some neighbouring regions supported the tip. However, this was still likely not a fully accurate depiction of the real-world scenario as the relocation and rotation of the material was restricted in standard Abaqus, and the mesh was still relatively coarse compared to the tip dimension (with only ~10 elements across the tip edge length).

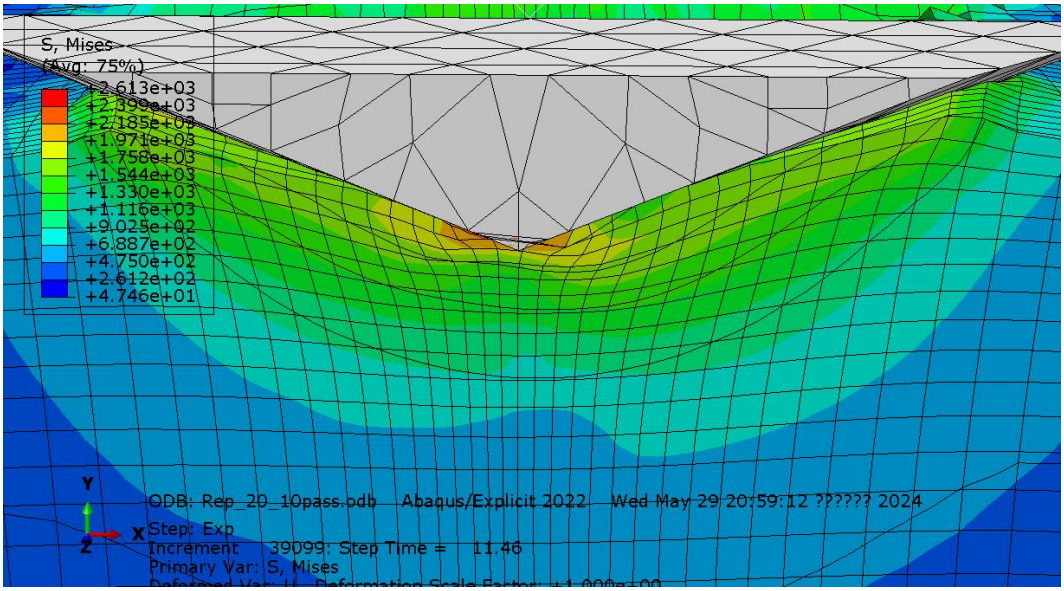



*Figure 108 Cross-section of a 20mN Berkovich tip edge-forward repeated nanoscratch simulation. The frame shown is in the middle of the second pass on the same scratch location.*

In the experimental case, it is likely that new material was 'excavated' from the bottom groove by the tip apex and rotated evenly along the side tip surfaces, which then became the new flat groove surface and pile-ups.

Scratch hardness from the multi-pass experiments has been recalculated using the effective contact area for tested loads, in which a linear relationship between penetration depth and pile-up height was assumed to estimate the pile-up height and total penetration depths for the 2$^{nd}$ to 9$^{th}$ pass. The linear relationship has been demonstrated with AFM scans of 20mN multi-pass edge-forward nanoscratches on single Ni600 grain in section 5.2. Scratch hardness has also been calculated using a similar method for simulation results. Shown in Figure 109, the scratch hardness increased for all normal loads in the following passes in the experiment while the hardness calculated decreased in simulation, which is likely caused by the uneven surface shown in Figure 107, that the effective area calculated essentially included the empty space between the tip surface and groove surface, causing the contact area to be overestimated.

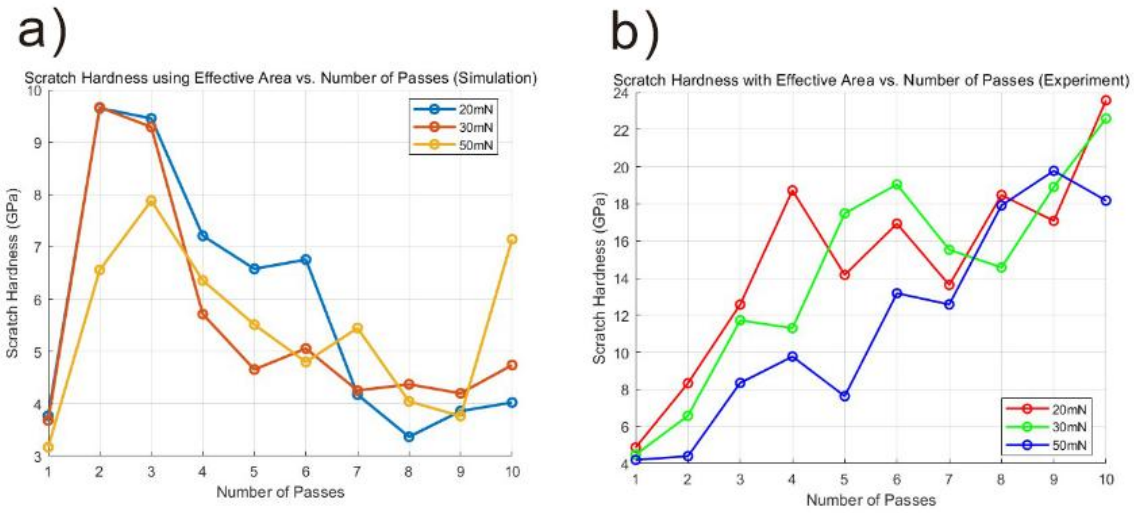



*Figure 109 Comparison of scratch hardness calculated using effective contact area defined in Section 5.2 for a) Abaqus simulation and b) G200 penetration depths measurement for edge-forward Berkovich nanoscratches under 20 mN, 30 mN, and 50 mN. For ease of comparison, the result for 1 test/simulation for each load was shown.*

### 7.4.4.3 Comparison of Abaqus and HR-EBSD Results

Attempts have been made to correlate the HR-EBSD results on multi-pass experiment with Abaqus stress map output, which is proven difficult as the stress/rotation maps (Figure 67 and Figure 68 in section 5.3.1) from HR-ESBD denotes regions with opposing and eventually randomised motions within the material, while Abaqus, which works on continuum theory, does not allow free mesh element rotation. Additionally, Abaqus calculates body rotation, while HR-EBSD calculates lattice rotation. Despite these limitations, a close examination of the Abaqus output would allow us to better understand the limitations of this engineering software in simulating nanoscale experiments and how good convergence with the experiment was obtained in the initial pass but not in the following passes.

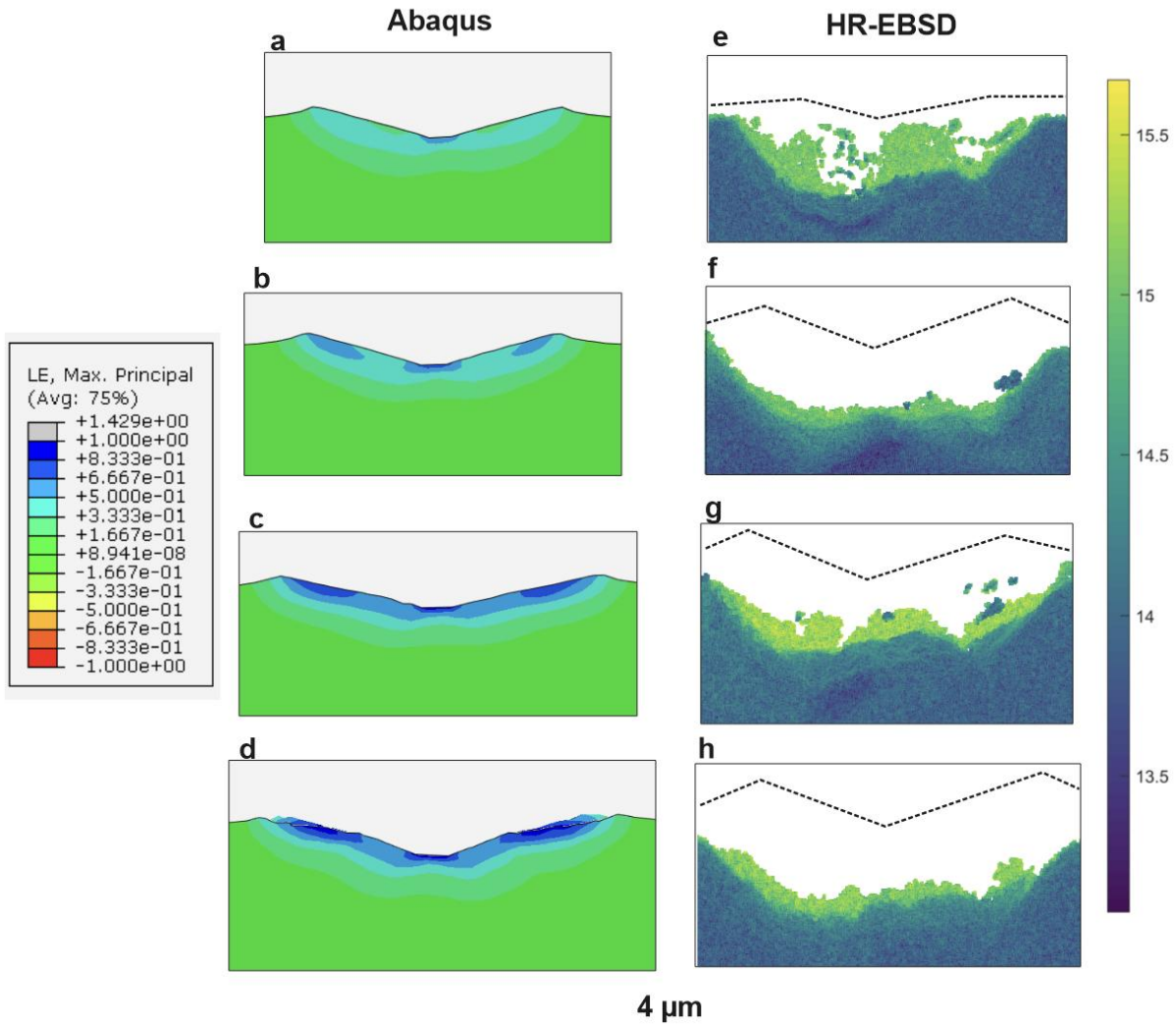



*Figure 110 A comparison of the Abaqus plastic strain output and GND map from HE-EBSD on repeated nanoscratch experiment lift-out. Unit of the GND is in logarithmic scale and corresponds to $10^{13}$ to $10^{16}$ Geometrically Necessary Dislocations (GNDs) per square meter*

In the plastic strain map shown in Figure 110 a-d, strain hardening was seen to increase at the locations where the geometry change concentrates stress, likely at the tip apex and pile-up but the areas affected by the strain hardening did not substantially increase as exemplified by the growth of unidentified (severely deformed) areas in Figure 110 e-h. The extended strain hardening possibly caused the tip to be unable to penetrate through these regions at a given normal load, eventually leading to sharp fluctuations in the contact area and lateral resistance. Such over-hardening is unphysical in the real world, as stress cannot indefinitely accumulate within the same location; instead, it would be relieved through mechanisms like slip, GND

formation, and recrystallization, which were not available in the Abaqus simulations. Variants of the Johnson-Cook model, such as the JC damage model, allow mesh elements to fail when subjected to excessive deformation, but this is often applied in scenarios where the material is removed from the surface in cutting tests. Abaqus with the JC model was able to accurately simulate the first pass, as the plastic hardening effects were represented in empirical stress-strain relations. However, as the deformation microstructure becomes increasingly complicated in the following passes, the empirical formula no longer applies, as it does not allow for further relief of stress.

## 7.5 General Discussion

The oscillations observed in the scratch profile from face-forward simulations at zero friction levels indicate that the stick-slip phenomenon noted in experiments was not solely due to instrument compliance or surface effects. Instead, it appeared to be more closely associated with strain hardening induced by material compression and the indenter's front flat facet. This interpretation was corroborated by the observation of stick-slip motion in edge-forward scratches at sufficiently high friction coefficients, where the side facets accumulated and hardened the neighbouring material through shear stress. At elevated friction coefficients ($\mu$), the material behaviour resembled a dough-kneading process, where it was elongated, and the triangular indents were rounded due to the elevated lateral force exerted by the flat facet. The distance required to complete one stick-slip cycle likely increased with the surface's ability to accumulate material.

The distinction between the interfacial coefficient of friction (CoF) and overall CoF, established earlier in this chapter, revealed that nanoscratch simulation outputs were significantly more sensitive to interfacial CoF. In both edge-forward and face-forward scratches, an increase in interfacial CoF from 0 to 0.3 led to a doubling of lateral resistance and CoF, compared to a negligible 3% reaction force difference in literature nanoindentation simulations [119]. It is likely that sliding contact is more prominent in the dynamic process of nanoscratch, while in the quasi-static process of nanoindentation, resistance mainly arises from compression on sample surfaces rather than sliding motions. An increased interfacial CoF might cause the tip to plough the material differently, as shown in Figure 91 - the tip can stick longer at increased friction levels before slipping, while nanoindentation mainly involves material extrusion and pile-up around the indenter tip. An interfacial CoF of 0.15

was found to yield an overall CoF matching experimental results in Abaqus nanoscratch simulations.

Investigating the effect of a compliant tip and indenter shaft on nanoscratch results by allowing the tip a certain degree of rotational freedom would require a complete redesign of the model. The simulated tip must possess inertia similar to the real-world tip to limit angular acceleration to avoid destabilizing the system, unlike the micron-sized tip model currently used.

Repetitive scratch simulations highlighted certain limitations of standard Abaqus in modelling nanoscale phenomena. The mesh in these simulations cannot rotate and interact with other segments as separate entities, despite such rotations being crucial for stress and energy release observed experimentally. This restriction led to continuous stress accumulation and excessive surface material hardening at certain nodes, ultimately resulting in a corrugated morphology. The material became too rigid to be uniformly deformed by the tip, causing the tip to periodically lose contact with the sample surface across the scratch distance after a higher number of passes. The Johnson-Cook model allowed the material surface to harden only to a certain extent in nanoscratch simulations, as suggested by Figure 103. Here, the depth increment was reduced for the second and third pass, but the tip continued to penetrate at the same magnitude in subsequent passes, whereas, in experiments, the increments in penetration depth kept decreasing for each pass. This suggested that scratch hardness in Abaqus simulations could only be calculated from the contact area output during individual scratches, as the contact area derived from penetration depth would be too large and include areas not in contact due to the lack of sample surface compliance with the tip. Despite these limitations, alignment with single-pass experiments indicates that the standard

model of Abaqus remained effective in predicting simple tribological phenomena and studying individual variables that cannot be isolated in experimental settings.

## 7.6 Conclusions

1. Consistent with experimental observations, the stick-slip phenomenon was predominantly found in face-forward scratch simulations at low surface friction levels, which suggested that the phenomenon was more closely related to the orientation-specific interaction between the tip and the substrate, rather than external factors.
2. It was observed that increased surface friction ($\mu = 0.6$) could trigger instabilities akin to stick-slip in edge-forward scratches and elongate the stick-slip cycle in face-forward scratches, thereby impacting the scale of this phenomenon. While this friction level is uncommon for metal-diamond contact, surface modification (i.e. adding glue) can potentially be performed in experiments to verify the friction effect.
3. Surface friction level had a major influence on the overall friction coefficient measured in scratch simulations while this effect was minimal in indentation simulations which indicated that lateral force measured in nanoscratch tests might be a more dynamic indicator of the surface friction level.
4. Standard implementations of Abaqus were identified as insufficient for accurately simulating repetitive nanoscratch test due to the constraints on the movement of discretised elements and limited their ability to replicate the dynamics observed in physical experiments.

# 8. Summary and Outlook

This thesis investigates the early wear formation mechanisms in nickel-based alloys (Ni201, Ni600, Ni718) through nanoindentation, nanoscratch experiments, and complementary techniques such as AFM, HR-EBSD, and finite element simulations, with an aim to explore connections between nanoscale deformation and macroscopic material behaviour. It also highlights unresolved questions and methodological challenges that underscore the complexity of bridging scales in tribology.

Experimental results show correlations between nanoscale hardness profiles and macroscopic yield strength, with scratch hardness exceeding indentation hardness due to dynamic deformation hardening effects. The disparity between nanoindentation and nanoscratch hardness was explained by suggesting that scratch hardness represents a dynamic response involving strain hardening and directional material flow, while indentation hardness primarily reflects the material's resistance to static compression, indicating why scratch tests provide a more representative measure of wear resistance under sliding contact conditions. Berkovich tip orientation was found to influence scratch resistance and groove morphology, where face-forward scratches exhibited periodic stick-slip patterns linked to strain hardening. Multi-pass nanoscratch tests revealed stabilization in penetration depth, attributed to microstructural changes such as dislocation accumulation and potential grain refinement. HR-EBSD analyses provided tracing evidence of these subsurface alterations, but observations made with experimental tools of higher resolution are still needed to corroborate the proposed theory.

A key aspect of the research involves developing an Artificial Neural Network (ANN) to predict Johnson-Cook constitutive constants from nanoindentation data. While the model successfully linked microscale measurements to macroscale properties—validated by finite

element simulations in Abaqus for single-pass tests—its limitations became apparent. Predictions were sensitive to tip geometry deviations and material anisotropy, highlighting a need for expanded training datasets that account for real-world variabilities. Similarly, standard Abaqus simulations, though effective for single-pass scenarios, struggled to replicate microstructural evolution in multi-pass tests. Overestimations of penetration depth and discrepancies in groove morphology at higher passes suggest inherent constraints in modelling material rotation and plasticity size effects. The discretized finite elements struggle to maintain contact with curved geometries at higher stress states, compromising stress and strain accuracy at the interface. Numerical approximations used in finite element analysis could introduce artificial dynamics by transforming steady-state problems into time-dependent ones, obscuring true material behaviour. These challenges suggest the need for advanced techniques—like adaptive mesh refinement—to enhance the model's ability to predict local surface response in future research.

An alternative method of defining contact area was proposed to address the paradoxical hardness decrease when using contact area calculated from total penetration depth. By applying this method to both simulation and experimental measurements, a more sensible characterization of the hardness increase in multi-pass tests was achieved, and an overestimation of contact area in simulations was observed when normal projected areas were applied to evaluate scratch hardness.

While this thesis advances methodologies for studying nanoscale wear, its findings emphasize the need for targeted experiments—such as single-crystal or controlled polycrystalline studies—to further clarify the role of grain boundaries and residual internal stress in deformation. Computationally, hybrid approaches combining crystal plasticity,

discrete dislocation dynamics, and adaptive meshing could address current simulation limitations. By framing both progress and unresolved questions, this work provides a foundation for future research to refine predictive models and expand our understanding of wear across scales.

# 9. References


[1] U.S. Nuclear Regulatory Commission (NRC), 'San Onofre Nuclear Generating Station - NRC Inspection Report 050-00361/2024-004 and 050-00362/2024-004', San Clemente, Aug. 2024. Accessed: Oct. 01, 2024. [Online]. Available: https://www.nrc.gov/docs/ML2421/ML24215A313.pdf

[2] T. J. Carter, 'Common failures in gas turbine blades', *Eng Fail Anal*, vol. 12, no. 2, pp. 237–247, Apr. 2005, doi: 10.1016/J.ENGFAILANAL.2004.07.004.

[3] M. F. Ashby and S. C. Lim, 'Wear-mechanism maps', *Scripta Metallurgica et Materialia*, vol. 24, no. 5, pp. 805–810, May 1990, doi: 10.1016/0956-716X(90)90116-X.

[4] J. F. Archard, 'Contact and Rubbing of Flat Surfaces', *J Appl Phys*, vol. 24, no. 8, pp. 981–988, Aug. 1953, doi: 10.1063/1.1721448.

[5] D. Tabor, 'The Hardness of Metals', *The Hardness of Metals*, Aug. 2000, doi: 10.1093/OSO/9780198507765.001.0001.

[6] W. C. Oliver and G. M. Pharr, 'An improved technique for determining hardness and elastic modulus using load and displacement sensing indentation experiments', *J Mater Res*, vol. 7, no. 6, pp. 1564–1583, 1992, doi: 10.1557/JMR.1992.1564.

[7] J. Xiaoyu, B. Lauke, and T. Schueller, 'Frictional contact analysis of scratch test for elastic and elastic–plastic thin-coating/substrate materials', *Thin Solid Films*, vol. 414, no. 1, pp. 63–71, Jul. 2002, doi: 10.1016/S0040-6090(02)00428-5.

[8] B. Briscoe and A. C. Smith, 'Time dependence effects in the shear of thin polymeric films', *J Phys D Appl Phys*, vol. 15, no. 4, pp. 579–594, 1982, doi: 10.1088/0022-3727/15/4/010.

[9] 'G171 Standard Test Method for Scratch Hardness of Materials Using a Diamond Stylus'. Accessed: Oct. 02, 2024. [Online]. Available: https://www.astm.org/g0171-03r17.html

[10] B. J. Briscoe, 'Friction of Organic Polymers', *Fundamentals of Friction: Macroscopic and Microscopic Processes*, pp. 167–182, 1992, doi: 10.1007/978-94-011-2811-7_9.

[11] J. A. Williams, 'Analytical models of scratch hardness', *Tribol Int*, vol. 29, no. 8, pp. 675–694, Dec. 1996, doi: 10.1016/0301-679X(96)00014-X.

[12] S. Graça, R. Colaço, and R. Vilar, 'Micro-to-nano indentation and scratch hardness in the Ni-Co system: Depth dependence and implications for tribological behavior', *Tribol Lett*, vol. 31, no. 3, pp. 177–185, Sep. 2008, doi: 10.1007/S11249-008-9350-1.

[13] I. P. Shakhverdova, M. Reibold, W. Kochmann, and P. Paufler, 'Nanoscratching meets nanoindentation', *Z Kristallogr Cryst Mater*, vol. 231, no. 6, pp. 351–363, Jun. 2016, doi: 10.1515/ZKRI-2016-1934/MACHINEREADABLECITATION/BIBTEX.

[14] F. P. Bowden and D. Tabor, *The Friction and Lubrication of Solids*, 1st ed. Oxford: Oxford University Press, 2001.

[15] M. F. Ashby, *Materials Selection in Mechanical Design*, 3rd ed. Butterworth-Heinemann, 1999.

[16] B. Bhushan and B. K. Gupta, *Handbook of Microscopy for Nanotechnology*, 1st ed. New York: Springer, 2004. doi: https://doi.org/10.1007/1-4020-8006-9.

[17] K. Holmberg, H. Ronkainen, A. Laukkanen, and K. Wallin, 'Friction and wear of coated surfaces - scales, modelling and simulation of tribomechanisms', *Surf Coat Technol*, vol. 202, no. 4–7, pp. 1034–1049, Dec. 2007, doi: 10.1016/j.surfcoat.2007.07.105.

[18] N. P. Suh, 'An overview of the delamination theory of wear', *Wear*, vol. 44, no. 1, pp. 1–16, Aug. 1977, doi: 10.1016/0043-1648(77)90081-3.

[19] D. A. Rigney, L. H. Chen, M. G. S. Naylor, and A. R. Rosenfield, 'Wear processes in sliding systems', *Wear*, vol. 100, no. 1–3, pp. 195–219, Dec. 1984, doi: 10.1016/0043-1648(84)90013-9.

[20] J. Schell, P. Heilmann, and D. A. Rigney, ‘Friction and wear of Cu-Ni alloys’, *Wear*, vol. 75, no. 2, pp. 205–220, Jan. 1982, doi: 10.1016/0043-1648(82)90149-1.
[21] C. Greiner, Z. Liu, L. Strassberger, and P. Gumbsch, ‘Sequence of Stages in the Microstructure Evolution in Copper under Mild Reciprocating Tribological Loading’, *ACS Appl Mater Interfaces*, vol. 8, no. 24, pp. 15809–15819, Jun. 2016, doi: 10.1021/ACSAMI.6B04035.
[22] P. J. Blau, *Friction Science and Technology: From Concepts to Applications*, 2nd ed. Boca Raton: CRC Press, 2008.
[23] A. G. Quarrell, ‘The Hardness of Metals’, *Nature*, vol. 170, no. 4333, p. 818, 1952, doi: 10.1038/170818b0.
[24] M. Sakai, ‘The Meyer hardness: A measure for plasticity?’, *J Mater Res*, vol. 14, no. 9, pp. 3630–3639, 1999, doi: 10.1557/JMR.1999.0490.
[25] D. Tabor, ‘Indentation hardness: Fifty years on a personal view’, *Philosophical Magazine A*, vol. 74, no. 5, pp. 1207–1212, 1996, doi: 10.1080/01418619608239720.
[26] D. Chicot, F. Roudet, A. Zaoui, G. Louis, and V. Lepingle, ‘Influence of visco-elasto-plastic properties of magnetite on the elastic modulus: Multicyclic indentation and theoretical studies’, *Mater Chem Phys*, vol. 119, no. 1, pp. 75–81, 2010, doi: https://doi.org/10.1016/j.matchemphys.2009.07.033.
[27] R. B. King, ‘Elastic analysis of some punch problems for a layered medium’, *Int J Solids Struct*, vol. 23, no. 12, pp. 1657–1664, 1987, doi: https://doi.org/10.1016/0020-7683(87)90116-8.
[28] D. Chicot *et al.*, ‘A contact area function for Berkovich nanoindentation : Application to hardness determination of a TiHfCN thin film’, *Thin Solid Films*, no. 558, pp. 259–266, 2014.
[29] A. C. Fischer-Cripps, ‘Critical review of analysis and interpretation of nanoindentation test data’, *Surf Coat Technol*, vol. 200, no. 14, pp. 4153–4165, 2006, doi: https://doi.org/10.1016/j.surfcoat.2005.03.018.
[30] A. J. Wilkinson, G. Meaden, and D. J. Dingley, ‘High resolution mapping of strains and rotations using electron backscatter diffraction’, *Materials Science and Technology*, vol. 22, no. 11, pp. 1271–1278, 2006, doi: 10.1179/174328406X130966.
[31] J. Hay and B. Crawford, ‘Measuring substrate-independent modulus of thin films’, *J Mater Res*, vol. 26, no. 6, pp. 727–738, Mar. 2011, doi: 10.1557/JMR.2011.8.
[32] S. Verma, P. Sarkar, and P. Pant, ‘Thermal drift in room temperature nanoindentation experiments: Measurement and correction’, *J Mater Res*, vol. 36, no. 17, pp. 3436–3444, Sep. 2021, doi: 10.1557/S43578-021-00386-0.
[33] M. Galetto, G. Genta, and G. Maculotti, ‘Single-step calibration method for nano indentation testing machines’, *CIRP Annals*, vol. 69, no. 1, pp. 429–432, Jan. 2020, doi: 10.1016/J.CIRP.2020.03.015.
[34] Y. V Milman, A. A. Golubenko, and S. N. Dub, ‘Indentation size effect in nanohardness’, *Acta Mater*, vol. 59, no. 20, pp. 7480–7487, 2011, doi: https://doi.org/10.1016/j.actamat.2011.08.027.
[35] A. Kareer, X. D. Hou, N. M. Jennett, and S. V. Hainsworth, ‘The existence of a lateral size effect and the relationship between indentation and scratch hardness in copper’, *Philosophical Magazine A*, vol. 96, no. 32–34, pp. 3396–3413, Mar. 2016, doi: 10.1080/14786435.2016.1146828.
[36] K. Sangwal, ‘On the reverse indentation size effect and microhardness measurement of solids’, *Mater Chem Phys*, vol. 63, no. 2, pp. 145–152, Feb. 2000, doi: 10.1016/S0254-0584(99)00216-3.
[37] J. Strader, ‘A Study of the Indentation Size Effect in Copper’, *Doctoral Dissertations*, Dec. 2008, Accessed: Oct. 25, 2024. [Online]. Available: https://trace.tennessee.edu/utk_graddiss/526

[38] J. G. Swadener, E. P. George, and G. M. Pharr, 'The correlation of the indentation size effect measured with indenters of various shapes', *J Mech Phys Solids*, vol. 50, no. 4, pp. 681–694, Apr. 2002, doi: 10.1016/S0022-5096(01)00103-X.
[39] W. D. Nix and H. Gao, 'Indentation size effects in crystalline materials: A law for strain gradient plasticity', *J Mech Phys Solids*, vol. 46, no. 3, pp. 411–425, 1998, doi: https://doi.org/10.1016/S0022-5096(97)00086-0.
[40] S. J. Bull, 'On the origins and mechanisms of the indentation size effect', *International Journal of Materials Research*, vol. 94, no. 7, pp. 787–792, Jul. 2003, doi: 10.3139/IJMR-2003-0138.
[41] C. A. Schuh, J. K. Mason, and A. C. Lund, 'Quantitative insight into dislocation nucleation from high-temperature nanoindentation experiments', *Nature Materials 2005 4:8*, vol. 4, no. 8, pp. 617–621, Jul. 2005, doi: 10.1038/nmat1429.
[42] A. Bolshakov and G. M. Pharr, 'Influences of pileup on the measurement of mechanical properties by load and depth sensing indentation techniques', *J Mater Res*, vol. 13, no. 4, pp. 1049–1058, Jan. 1998, doi: 10.1557/JMR.1998.0146.
[43] J. S. Field and M. V. Swain, 'Determining the mechanical properties of small volumes of material from submicrometer spherical indentations', *J Mater Res*, vol. 10, no. 1, pp. 101–112, Mar. 1995, doi: 10.1557/JMR.1995.0101.
[44] B. D. Beake, A. J. Harris, and T. W. Liskiewicz, 'Review of recent progress in nanoscratch testing', *Tribology - Materials, Surfaces and Interfaces*, vol. 7, no. 2, pp. 87–96, 2013, doi: 10.1179/1751584X13Y.0000000037.
[45] J. Y. Kim, B. W. Lee, D. T. Read, and D. Kwon, 'Influence of tip bluntness on the size-dependent nanoindentation hardness', *Scr Mater*, vol. 52, no. 5, pp. 353–358, Mar. 2005, doi: 10.1016/J.SCRIPTAMAT.2004.10.036.
[46] O. Brazil, J. B. Pethica, and G. M. Pharr, 'The contribution of plastic sink-in to the static friction of single asperity microscopic contacts', *Proceedings of the Royal Society A*, vol. 477, no. 2256, Dec. 2021, doi: 10.1098/RSPA.2021.0502.
[47] D. Linsler, F. Ruebeling, and C. Greiner, 'Subsurface microstructural evolution during scratch testing on bcc iron', *Metals (Basel)*, vol. 11, no. 8, p. 1258, Aug. 2021, doi: 10.3390/MET11081258/S1.
[48] G. Prieto, K. D. Bakoglidis, W. R. Tuckart, and E. Broitman, 'Nanotribological behavior of deep cryogenically treated martensitic stainless steel', *Beilstein J. Nanotechnol*, vol. 8, pp. 1760–1768, 2017, doi: 10.3762/bjnano.8.177.
[49] D. Kumar, J. Jain, and N. N. Gosvami, 'Anisotropy in Nanoscale Friction and Wear of Precipitate Containing AZ91 Magnesium Alloy', *Tribol Lett*, vol. 67, no. 2, pp. 1–8, Jun. 2019, doi: 10.1007/S11249-019-1160-0/FIGURES/7.
[50] K. Wasmer, R. Gassilloud, J. Michler, and C. Ballif, 'Analysis of onset of dislocation nucleation during nanoindentation and nanoscratching of InP', *J Mater Res*, vol. 27, no. 1, pp. 320–329, Jan. 2012, doi: 10.1557/JMR.2011.305.
[51] S. W. Youn and C. G. Kang, 'Effect of nanoscratch conditions on both deformation behavior and wet-etching characteristics of silicon (1 0 0) surface', *Wear*, vol. 261, pp. 328–337, 2006, doi: 10.1016/j.wear.2005.11.007.
[52] D. Mulliah, D. Christopher, S. D. Kenny, and R. Smith, 'Nanoscratching of silver (100) with a diamond tip', *Nucl Instrum Methods Phys Res B*, vol. 202, pp. 294–299, 2003, doi: https://doi.org/10.1016/S0168-583X(02)01872-4.
[53] S. R. Pergande, A. A. Polycarpou, and T. F. Conry, 'Use of Nano-Indentation and Nano-Scratch Techniques to Investigate Near Surface Material Properties Associated With Scuffing of Engineering Surfaces', in *Air Conditioning and Refrigeration Project*, University of Illinois at Urbana-Champaign, Dec. 2001, pp. 1–157.

[54] O. Shikimaka and A. Prisacaru, ‘Deformation mechanisms under nanoscratching of Si: Effect of scratching speed, load and indenter orientation’, *Mater Res Express*, vol. 6, no. 8, 2019, doi: 10.1088/2053-1591/ab1a0d.
[55] P. Feng, C. Zhang, Z. Wu, and J. Zhang, ‘Effect of scratch velocity on deformation features of c-plane sapphire during nanoscratching’, *Strojniski Vestnik/Journal of Mechanical Engineering*, vol. 59, no. 6, pp. 367–374, 2013, doi: 10.5545/SV-JME.2012.679.
[56] K. Tang *et al.*, ‘Material Removal Characteristics of Single-Crystal 4H-SiC Based on Varied-Load Nanoscratch Tests’, *Chinese Journal of Mechanical Engineering (English Edition)*, vol. 36, no. 1, pp. 1–14, Dec. 2023, doi: 10.1186/S10033-023-00944-Z/FIGURES/13.
[57] R. Gassilloud, C. Ballif, P. Gasser, G. Buerki, and J. Michler, ‘Deformation mechanisms of silicon during nanoscratching’, *Physica Status Solidi (A) Applications and Materials Science*, vol. 202, no. 15, pp. 2858–2869, Dec. 2005, doi: 10.1002/PSSA.200521259.
[58] A. M. Hodge and T. G. Nieh, ‘Evaluating abrasive wear of amorphous alloys using nanoscratch technique’, *Intermetallics (Barking)*, vol. 12, no. 7–9, pp. 741–748, Jul. 2004, doi: 10.1016/J.INTERMET.2004.02.014.
[59] Y. X. Ye, C. Z. Liu, H. Wang, and T. G. Nieh, ‘Friction and wear behavior of a single-phase equiatomic TiZrHfNb high-entropy alloy studied using a nanoscratch technique’, *Acta Mater*, vol. 147, pp. 78–89, Apr. 2018, doi: 10.1016/J.ACTAMAT.2018.01.014.
[60] S. Zhang, X. Guo, Z. Jin, R. Kang, D. Guo, and W. C. Tang, ‘Surface morphologies and corresponding hardness evolution during nanoscratching’, *Journal of Materials Research and Technology*, vol. 9, no. 3, pp. 3179–3189, May 2020, doi: 10.1016/J.JMRT.2020.01.064.
[61] S. Sanyal, S. Chabri, S. Chatterjee, N. Bhowmik, A. K. Metya, and A. Sinha, ‘Tribological behavior of thermomechanically treated Al–Mg–Si alloy by nanoscratch measurements’, *Tribol Int*, vol. 102, pp. 125–132, Oct. 2016, doi: 10.1016/J.TRIBOINT.2016.05.029.
[62] L. Chen, Q. Du, M. Yu, X. Guo, and W. Zhao, ‘Measuring the effect of residual stress on the machined subsurface of Inconel 718 by nanoindentation’, *PLoS One*, vol. 16, no. 1 January, pp. 1–15, 2021, doi: 10.1371/journal.pone.0245391.
[63] J. Kluczyński *et al.*, ‘Crack Growth Behavior of Additively Manufactured 316L Steel—Influence of Build Orientation and Heat Treatment’, *Materials 2020, Vol. 13, Page 3259*, vol. 13, no. 15, p. 3259, Jul. 2020, doi: 10.3390/MA13153259.
[64] Y. Zhanwei, L. Fuguo, and J. Guoliang, ‘A Modified Johnson Cook Constitutive Model for Aermet 100 at Elevated Temperatures’, *High Temperature Materials and Processes*, vol. 37, no. 2, pp. 163–172, 2018, doi: 10.1515/htmp-2016-0096.
[65] K. B. Park, Y. T. Cho, and Y. G. Jung, ‘Determination of Johnson-Cook constitutive equation for Inconel 601’, *Journal of Mechanical Science and Technology*, vol. 32, no. 4, pp. 1569–1574, 2018, doi: 10.1007/s12206-018-0311-9.
[66] V. Kumar Reddy Sirigiri, V. Yadav Gudiga, U. Shankar Gattu, G. Suneesh, and K. Mohan Buddaraju, ‘A review on Johnson Cook material model’, *Mater Today Proc*, vol. 62, pp. 3450–3456, 2022, doi: 10.1016/j.matpr.2022.04.279.
[67] R. Eisseler, K. Drewle, K. C. Grötzinger, and H. C. Möhring, ‘Using an inverse cutting simulation-based method to determine the Johnson-Cook material constants of heat-treated steel’, *Procedia CIRP*, vol. 77, no. March, pp. 26–29, 2018, doi: 10.1016/j.procir.2018.08.198.
[68] M. Murugesan and D. W. Jung, ‘Johnson cook material and failure model parameters estimation of AISI-1045 medium carbon steel for metal forming applications’, *Materials*, vol. 12, no. 4, 2019, doi: 10.3390/ma12040609.
[69] J. Wang, J. Wang, R. Schmid-Fetzer, S. Liu, Y. Du, and Z. Jin, Eds., ‘Fundamentals of Crystal Plasticity Finite Element Method’, in *Computational Design of Engineering Materials: Fundamentals and Case Studies*, Cambridge: Cambridge University Press, 2023, pp. 95–112. doi: DOI: 10.1017/9781108643764.006.

[70] D. Depriester and R. Kubler, ‘MTEX2Gmsh: a tool for generating 2D meshes from EBSD data’, *J Open Source Softw*, vol. 5, no. 52, p. 2094, 2020, doi: 10.21105/joss.02094.
[71] S. Chibani and F. X. Coudert, ‘Machine learning approaches for the prediction of materials properties’, *APL Mater*, vol. 8, no. 8, 2020, doi: 10.1063/5.0018384.
[72] J. D. Evans and F. X. Coudert, ‘Predicting the Mechanical Properties of Zeolite Frameworks by Machine Learning’, *Chemistry of Materials*, vol. 29, no. 18, pp. 7833–7839, 2017, doi: 10.1021/acs.chemmater.7b02532.
[73] Y. Kim *et al.*, ‘Novel deep learning approach for practical applications of indentation’, *Mater Today Adv*, vol. 13, p. 100207, 2022, doi: 10.1016/j.mtadv.2022.100207.
[74] A. Burleigh *et al.*, ‘Artificial intelligence based analysis of nanoindentation load–displacement data using a genetic algorithm’, *Appl Surf Sci*, vol. 612, p. 155734, Mar. 2023, doi: 10.1016/J.APSUSC.2022.155734.
[75] N. Thakur, P. Kumar, and R. S. Bharj, ‘Effect of Variation of Johnson-Cook Parameters on Kinetic Energy and Simulation of 4340 Steel Projectile’, *Mater Today Proc*, vol. 5, no. 14, pp. 27884–27892, Jan. 2018, doi: 10.1016/J.MATPR.2018.10.027.
[76] M. Daoud, J. F. Chatelain, and A. Bouzid, ‘Effect of rake angle on Johnson-Cook material constants and their impact on cutting process parameters of Al2024-T3 alloy machining simulation’, *International Journal of Advanced Manufacturing Technology*, vol. 81, no. 9–12, pp. 1987–1997, Dec. 2015, doi: 10.1007/s00170-015-7179-y.
[77] P. W. Liu *et al.*, ‘Integration of phase-field model and crystal plasticity for the prediction of process-structure-property relation of additively manufactured metallic materials’, *Int J Plast*, vol. 128, May 2020, doi: 10.1016/j.ijplas.2020.102670.
[78] C. Zhang, L. W. Zhang, W. F. Shen, Y. N. Xia, and Y. T. Yan, ‘3D crystal plasticity finite element modeling of the tensile deformation of polycrystalline ferritic stainless steel’, *Acta Metallurgica Sinica (English Letters)*, vol. 30, no. 1, pp. 79–88, Jan. 2017, doi: 10.1007/s40195-016-0488-9.
[79] H. R. Chamani and M. R. Ayatollahi, ‘The effect of Berkovich tip orientations on friction coefficient in nanoscratch testing of metals’, *Tribol Int*, vol. 103, pp. 25–36, 2016, doi: https://doi.org/10.1016/j.triboint.2016.06.036.
[80] A. Kareer, E. Tarleton, C. Hardie, S. V Hainsworth, and A. J. Wilkinson, ‘Scratching the surface: Elastic rotations beneath nanoscratch and nanoindentation tests’, *Acta Mater*, vol. 200, pp. 116–126, 2020, doi: https://doi.org/10.1016/j.actamat.2020.08.051.
[81] D. Feichtinger, P. M. Derlet, and H. Van Swygenhoven, ‘Atomistic simulations of spherical indentations in nanocrystalline gold’, *Phys Rev B Condens Matter Mater Phys*, vol. 67, no. 2, Jan. 2003, doi: 10.1103/PhysRevB.67.024113.
[82] I. Szlufarska, R. K. Kalia, A. Nakano, and P. Vashishta, ‘Nanoindentation-induced amorphization in silicon carbide’, *Appl Phys Lett*, vol. 85, no. 3, pp. 378–380, Jul. 2004, doi: 10.1063/1.1774252.
[83] L. Zhao, M. Alam, J. Zhang, R. Janisch, and A. Hartmaier, ‘Amorphization-governed elasto-plastic deformation under nanoindentation in cubic (3C) silicon carbide’, *Ceram Int*, vol. 46, no. 8, pp. 12470–12479, Jun. 2020, doi: 10.1016/j.ceramint.2020.02.009.
[84] I. N. Remediakis, G. Kopidakis, and P. C. Kelires, ‘Softening of ultra-nanocrystalline diamond at low grain sizes’, *Acta Mater*, vol. 56, no. 18, pp. 5340–5344, 2008, doi: https://doi.org/10.1016/j.actamat.2008.07.014.
[85] T. J. Rupert, ‘Strain localization in a nanocrystalline metal: Atomic mechanisms and the effect of testing conditions’, *J Appl Phys*, vol. 114, no. 3, p. 33527, 2013, doi: 10.1063/1.4815965.
[86] D.-Q. Doan, T.-H. Fang, and T.-H. Chen, ‘Influences of grain size and temperature on tribological characteristics of CuAlNi alloys under nanoindentation and nanoscratch’, *Int J Mech Sci*, vol. 185, p. 105865, 2020, doi: https://doi.org/10.1016/j.ijmecsci.2020.105865.

[87] A. Shugurov, A. Panin, A. Dmitriev, and A. Nikonov, 'The effect of crystallographic grain orientation of polycrystalline Ti on ploughing under scratch testing', *Wear*, vol. 408–409, pp. 214–221, 2018, doi: https://doi.org/10.1016/j.wear.2018.05.013.
[88] D. Xu *et al.*, 'Revealing Nanoscale deformation mechanisms caused by shear-based material removal on individual grains of a Ni-based superalloy', *Acta Mater*, vol. 212, p. 116929, 2021, doi: https://doi.org/10.1016/j.actamat.2021.116929.
[89] G. Aggag and A. Abu-Elezz, 'Effect of loading rate and duration time on indentation hardness measurements', *18th IMEKO World Congress 2006: Metrology for a Sustainable Development*, vol. 3, Jan. 2006.
[90] A. Yacoot and L. Koenders, 'Aspects of scanning force microscope probes and their effects on dimensional measurement', May 21, 2008. doi: 10.1088/0022-3727/41/10/103001.
[91] J. V. Bernier, R. M. Suter, A. D. Rollett, and J. D. Almer, 'High-Energy X-Ray Diffraction Microscopy in Materials Science', *Annu Rev Mater Res*, vol. 50, pp. 395–436, 2020, doi: 10.1146/annurev-matsci-070616-124125.
[92] A. J. Wilkinson and T. Ben Britton, 'Strains, planes, and EBSD in materials science', *Materials Today*, vol. 15, no. 9, pp. 366–376, 2012, doi: 10.1016/S1369-7021(12)70163-3.
[93] J. F. Nye, 'Some geometrical relations in dislocated crystals', *Acta Metallurgica*, vol. 1, no. 2, pp. 153–162, Mar. 1953, doi: 10.1016/0001-6160(53)90054-6.
[94] T. B. Britton *et al.*, 'Factors affecting the accuracy of high resolution electron backscatter diffraction when using simulated patterns', *Ultramicroscopy*, vol. 110, no. 12, pp. 1443–1453, 2010, doi: 10.1016/j.ultramic.2010.08.001.
[95] A. J. Wilkinson, 'A new method for determining small misorientations from electron back scatter diffraction patterns', *Scr Mater*, vol. 44, no. 10, pp. 2379–2385, 2001, doi: 10.1016/S1359-6462(01)00943-5.
[96] Agilent Technologies, 'Nanoindentation, Scratch, and Elevated Temperature Testing of Cellulose and PMMA Films', 5990–5761EN, Apr. 2010. Accessed: Oct. 05, 2024. [Online]. Available: https://www.keysight.com/ch/de/assets/7018-02534/application-notes-archived/5990-5761.pdf
[97] Anna Kareer, 'Nano-scratch hardness and the Lateral Size Effect (LSE)', University of Leicester, Leicester, 2015. Accessed: Oct. 05, 2024. [Online]. Available: https://figshare.com/articles/thesis/Nano-scratch_hardness_and_the_Lateral_Size_Effect_LSE_/10157198?file=18305099
[98] C. Berger *et al.*, 'Plasma FIB milling for the determination of structures in situ', *Nat Commun*, vol. 14, no. 1, pp. 1–12, 2023, doi: 10.1038/s41467-023-36372-9.
[99] Annalena Wolff, 'Focused ion beams: An overview of the technology and its capabilities', Wiley Analytical Science. Accessed: Oct. 05, 2024. [Online]. Available: https://analyticalscience.wiley.com/content/article-do/focused-ion-beams-overview-technology-and-its-capabilities#was.auth.WolffA
[100] N. Ni, 'Nickel 200 & 201', *Alloy Digest*, vol. 11, no. 10, pp. 200–201, 1962, doi: 10.31399/asm.ad.ni0075.
[101] Special Metals Corporation, 'INCONEL® Alloy 600', Hereford, SMC-027, Sep. 2008. Accessed: Oct. 05, 2024. [Online]. Available: https://www.specialmetals.com/documents/technical-bulletins/inconel/inconel-alloy-600.pdf
[102] N. Fang, Z. Zhou, and B. Britton, 'The Performance of Different Etchants on the Carbides of Ni600 and Ni625', *Metals 2024, Vol. 14, Page 91*, vol. 14, no. 1, p. 91, Jan. 2024, doi: 10.3390/MET14010091.
[103] Special Metals, 'INCONEL® alloy 718', Hereford, SMC-045, Sep. 2007. Accessed: Oct. 03, 2024. [Online]. Available: https://www.specialmetals.com/documents/technical-bulletins/inconel/inconel-alloy-718.pdf

[104] X. Li *et al.*, 'Indentation size effect: an improved mechanistic model incorporating surface undulation and indenter tip irregularity', *Journal of Materials Research and Technology*, vol. 23, pp. 143–153, Mar. 2023, doi: 10.1016/J.JMRT.2023.01.001.
[105] R. Yang, Q. Zhang, P. Xiao, J. Wang, and Y. Bai, 'Two opposite size effects of hardness at real nano-scale and their distinct origins', *Scientific Reports 2017 7:1*, vol. 7, no. 1, pp. 1–8, Nov. 2017, doi: 10.1038/s41598-017-14734-w.
[106] A. Sela, G. Ortiz-De-Zarate, D. Soler, G. Germain, P. Aristimuño, and P. J. Arrazola, 'Measurement of plastic strain and plastic strain rate during orthogonal cutting for Ti-6Al-4V', *Int J Mech Sci*, vol. 198, p. 106397, 2021, doi: 10.1016/j.ijmecsci.2021.106397.
[107] D. Ma, Z. Wang, M. Giglio, S. Campos Amico, and A. Manes, 'Influence of strain-rate related parameters on the simulation of ballistic impact in woven composites', *Compos Struct*, vol. 300, p. 116142, Nov. 2022, doi: 10.1016/J.COMPSTRUCT.2022.116142.
[108] W. W. Yao, X. P. Zhou, D. Dias, Y. Jia, and Y. J. Li, 'Frictional contact and stick-slip: Mechanism and numerical technology', *Int J Solids Struct*, vol. 274, no. January, p. 112289, 2023, doi: 10.1016/j.ijsolstr.2023.112289.
[109] J. B. Pethica, 'Nanoindentation in more than one dimension – Experimental challenges and opportunities', *Curr Opin Solid State Mater Sci*, vol. 27, no. 4, p. 101100, Aug. 2023, doi: 10.1016/J.COSSMS.2023.101100.
[110] V. C. Kumar and I. M. Hutchings, 'Reduction of the sliding friction of metals by the application of longitudinal or transverse ultrasonic vibration', *Tribol Int*, vol. 37, no. 10, pp. 833–840, Oct. 2004, doi: 10.1016/J.TRIBOINT.2004.05.003.
[111] G. G. Adams, 'Self-Excited Oscillations of Two Elastic Half-Spaces Sliding With a Constant Coefficient of Friction', *J Appl Mech*, vol. 62, no. 4, pp. 867–872, Dec. 1995, doi: 10.1115/1.2896013.
[112] H. Liu *et al.*, 'Microstructural evolution and oxidation in α/β titanium alloy under fretting fatigue loading', *Friction*, vol. 11, no. 10, pp. 1906–1921, 2023, doi: 10.1007/s40544-022-0729-z.
[113] W. Li *et al.*, 'Measurement of the pattern shifts for HR-EBSD with larger lattice rotations', *Ultramicroscopy*, vol. 247, no. February, p. 113697, 2023, doi: 10.1016/j.ultramic.2023.113697.
[114] S. Zhang, X. Guo, Z. Jin, R. Kang, D. Guo, and W. C. Tang, 'Surface morphologies and corresponding hardness evolution during nanoscratching', *Journal of Materials Research and Technology*, vol. 9, no. 3, pp. 3179–3189, May 2020, doi: 10.1016/J.JMRT.2020.01.064.
[115] R. Hielscher and H. Schaeben, 'A novel pole figure inversion method: specification of the MTEX algorithm', *J. Appl. Cryst*, vol. 41, pp. 1024–1037, 2008, doi: 10.1107/S0021889808030112.
[116] C. Li, F. Zhang, X. Wang, and X. Rao, 'Repeated nanoscratch and double nanoscratch tests of Lu2O3 transparent ceramics: Material removal and deformation mechanism, and theoretical model of penetration depth', *J Eur Ceram Soc*, vol. 38, no. 2, pp. 705–718, 2018, doi: 10.1016/j.jeurceramsoc.2017.09.028.
[117] A. Koko, V. Tong, A. J. Wilkinson, and T. J. Marrow, 'An iterative method for reference pattern selection in high-resolution electron backscatter diffraction (HR-EBSD)', *Ultramicroscopy*, vol. 248, no. February, p. 113705, 2023, doi: 10.1016/j.ultramic.2023.113705.
[118] A. I. Constantin and V. Fireteanu, 'HyperStudy Optimization of Induction Motors Finite Element Assisted Design', *2021 International Aegean Conference on Electrical Machines and Power Electronics, ACEMP 2021 and 2021 International Conference on Optimization of Electrical and Electronic Equipment, OPTIM 2021*, pp. 191–197, Sep. 2021, doi: 10.1109/OPTIM-ACEMP50812.2021.9590030.

[119] J. L. Bucaille, S. Stauss, E. Felder, and J. Michler, ‘Determination of plastic properties of metals by instrumented indentation using different sharp indenters’, *Acta Mater*, vol. 51, no. 6, pp. 1663–1678, 2003, doi: 10.1016/S1359-6454(02)00568-2.
[120] T. Ozel, I. Llanos, J. Soriano, and P. J. Arrazola, ‘3d finite element modelling of chip formation process for machining inconel 718: Comparison of FE software predictions’, *Machining Science and Technology*, vol. 15, no. 1, pp. 21–46, Jan. 2011, doi: 10.1080/10910344.2011.557950.
[121] D. Bodana, N. K. Tiwari, S. Ranjan, and U. Ghanekar, ‘Estimation of the depth of penetration in a plunging hollow jet using artificial intelligence techniques’, *Archives of Materials Science and Engineering*, vol. 103, no. 2, pp. 49–51, 2020, doi: 10.5604/01.3001.0014.3354.
[122] E. Schulz, M. Speekenbrink, and A. Krause, ‘A tutorial on Gaussian process regression: Modelling, exploring, and exploiting functions’, *J Math Psychol*, vol. 85, pp. 1–16, 2018, doi: 10.1016/j.jmp.2018.03.001.
[123] X. Dong, H. Chen, C. Li, M. Yang, Y. Yu, and X. Huang, ‘An Evaluation of the Data-Driven Model for Bubble Maximum Diameter in Subcooled Boiling Flow Using Artificial Neural Networks’, *Front Energy Res*, vol. 10, p. 903464, Aug. 2022, doi: 10.3389/fenrg.2022.903464.
[124] A. Martín, ‘TensorFlow: learning functions at scale’, *ACM SIGPLAN Notices*, vol. 51, no. 9, pp. 1–1, Sep. 2016, doi: 10.1145/3022670.2976746.
[125] A. Leitner, V. Maier-Kiener, and D. Kiener, ‘Essential refinements of spherical nanoindentation protocols for the reliable determination of mechanical flow curves’, *Mater Des*, vol. 146, pp. 69–80, 2018, doi: 10.1016/j.matdes.2018.03.003.
[126] D. Avadanii, A. Kareer, L. Hansen, and A. Wilkinson, ‘Calibration and data-analysis routines for nanoindentation with spherical tips’, *J Mater Res*, vol. 38, no. 17, pp. 4042–4056, Sep. 2023, doi: 10.1557/s43578-023-01041-6.
[127] I. J. Spary, A. J. Bushby, and N. M. Jennett, ‘On the indentation size effect in spherical indentation’, *Philosophical Magazine*, vol. 86, no. 33-35 SPEC. ISSUE, pp. 5581–5593, Nov. 2006, doi: 10.1080/14786430600854988.
[128] P. H. Thike, Z. Zhao, P. Shi, and Y. Jin, ‘Significance of artificial neural network analytical models in materials’ performance prediction’, *Bulletin of Materials Science*, vol. 43, no. 1, pp. 1–22, 2020, doi: 10.1007/s12034-020-02154-y.
[129] A. F. Bower and K. L. Johnson, ‘The influence of strain hardening on cumulative plastic deformation in rolling and sliding line contact’, *J Mech Phys Solids*, vol. 37, no. 4, pp. 471–493, Jan. 1989, doi: 10.1016/0022-5096(89)90025-2.
[130] F. P. Bowden and L. Leben, ‘The nature of sliding and the analysis of friction’, *Proc R Soc Lond A Math Phys Sci*, vol. 169, no. 938, pp. 371–391, Feb. 1939, doi: 10.1098/RSPA.1939.0004.
[131] C. J. Adam and M. V. Swain, ‘The effect of friction on indenter force and pile-up in numerical simulations of bone nanoindentation’, *J Mech Behav Biomed Mater*, vol. 4, no. 7, pp. 1554–1558, 2011, doi: 10.1016/j.jmbbm.2011.03.026.
[132] K. P. Marimuthu, J. Han, U. Jeong, K. Lee, and H. Lee, ‘Study on tribological characteristics of Zr-based BMG via nanoscratch techniques’, *Wear*, vol. 486–487, p. 204067, Dec. 2021, doi: 10.1016/J.WEAR.2021.204067.